Very-High-Energy and Ultraviolet Studies of Markarian 421 during 2007-2008

Andrea Cesarini M.Sc.Eng

Supervisors:
Dr. Mark Lang
Dr. Gary Gillanders

Thesis submitted in the
School of Physics
for the award of

Ph.D.

National University of Ireland Galway - NUIG
June 2012

To my fantastic father Luis (Luigi) that works so hard every day of his life for making all possible.

To my tireless mother Francesca, who has a big heart, who is pervaded of the big Spirit of compassion, who patiently takes care of everybody, and who has supported in every aspect of our lives my father, myself and, lately, also my own family.

To my wife Filomena, who has enriched and changed my life, fast and strongly, in such a marvelous way. She teaches me constantly the way of temperance. Also, she helps me to be day-by-day more patient and supports me when I am forced to take part to unethical social rites.

To my son Thomas Nicola, who, since his early age, has already clearly begun to disappoint his mother by growing up fast without even asking for an approval that, from myself, would have been granted anyway.

To Giovanna with her bright intuitions and to Nicola with his infinite creativity.

To Daniele, Valentina and Sean, that I always consider as my own family.

Declaration of work

This thesis concerns ultraviolet and very-high-energy γ-ray observations of the active galaxy Markarian 421. The work is part of a larger multiwavelength study led by the VERITAS Collaboration.

The VERITAS (Very Energetic Radiation Imaging Telescope Array System) Collaboration is comprised of about a hundred scientists from 23 different institutions in the United States, Canada, Germany, England and Ireland. The Astrophysics Group at the National University of Ireland Galway (NUIG) is part of the VERITAS Collaboration.

The VERITAS array consists of four 12 m imaging atmospheric Cherenkov telescopes (IACTs) for γ-ray astronomy located at the Fred Lawrence Whipple Observatory (FLWO) in southern Arizona.

The results of the full multiwavelength study have been published as a multiauthor collaboration paper in the Astrophysical Journal (Acciari *et al.* 2011).

I was responsible for the analysis of the ultraviolet observations presented in the paper. The observations were public source Swift/UVOT data. I analyzed the data using the standard public UVOT pipeline. I also extended the public pipeline as described in Chapter 3 in order to deal with bright foreground stars in the field of view. In Chapter 5, I independently verified the VERITAS data analysis published in Acciari *et al.,* (2011). I applied existing techniques in time-domain and correlation analyses (Chapter 6), and developed new simulations to determine power spectral density index from variability analysis. All the analyses described in Chapters 3, 5 and 6 were carried out by me personally at NUIG.

During my Ph.D., I was periodically relocated and employed at FLWO and, with

my four extended working placements, I contributed to the VERITAS observation programme. For my first and second placements, I was a Visiting Graduate Student in the Internship Program at SAO (Smithsonian Astrophysical Observatory) supervised by Dr. Trevor C. Weekes for a total time of 6 months (5^{th} March 2007 to 4^{th} May 2007 and 22^{nd} November 2007 to 21^{st} February 2008). My third and fourth placements, for VERITAS observational shifts were from 1^{st} March 2009 to 21^{st} April 2009 and 17^{th} May 2010 to 19^{th} June 2010.

During my first and second working periods at VERITAS basecamp, I was also directly involved in taking the Markarian 421 observations analyzed in this work.

I carried out the initial optical alignment of the 'Telescope 4' ('Tel. 4') and the periodic realignments of the mirror facets of the other telescopes of the array. I also participated in carrying out the mirror bias measurements of 'Tel. 3' and 'Tel. 4' (described in Section 4.3.3).

I coauthored 47 Collaboration papers. This reflects my general contributions to the observing programme. Although this is not discussed in this thesis, I have been also directly involved in 10 VERITAS Collaboration papers by providing optical and ultraviolet data results and by participating in the consistency process of the analyses made by different telescopes.

I have also coauthored two non-VERITAS Collaboration papers. Selected VERITAS and non-VERITAS publications which I have co-authored are listed in Appendix B. As co-author in these publications, I provided optical and ultraviolet data results and interpretation and participated in the analysis and in the jet modeling.

Acknowledgements

My first thought must go to my supervisors, Dr. Gary Gillanders and Dr. Mark Lang, for everything and especially for the opportunity they gave me a few years ago. During the course of my Ph.D., I have learned from them more than just what it means to be a scientist. Through their acquaintance, I have learned how to significantly tame my instincts and attitudes in the professional realm. In my own department, I must thank Dr. Leon Harding, one of the youngest and most talented MF Jedi (Astronomy) Masters in the Council of the Republic and my personal Frater. I have also to thank my personal friend Dr. Navtej Singh, for providing continuous bursts of inspiration and for being a very kind friend. Congratulation to you and Manjyot !! Also, I wish to thank Dr. John Toner (or Dott. Giovanni Tonegro), who introduced me to the Whipple data analysis and helped me with his suggestions when I was away and lonely up on a high mountain (meditating about "10m or not 10m? this is the (tele)scope!!"). I still remember the day I met Conor Mc Brierty and P.J. Walsh, the two most intelligent and most philosophically/musically and electronically minded people I have ever met (one of them also speaking a really funny Chinese-Donegal English he had learned, perhaps, through many years of buying electronic devices with Chinese vendors via internet). I am also indebted to James "Wizard" Nallen for his mysterious managing of information resources, which, when he passes, show up in to the living world. From the computer office, thanks to Tom Regan and Wesley Reilly, without their help I would have had no chance to connect my server outside the NUIG "Chinese" (fire)wall. Thanks to Padraic Moran for introducing me to the world of vegetable gardens, which soon led to an interest in botanical gardens. I also wish to thank especially the secretary of our department, Tess Mahoney for her invaluable help. Moreover, I had very interesting chats with Prof. Thomas J. Glynn, whom I must thank for his encouraging words, and Prof. George F. Imbusch, whom I must thank for his fantastic lecture notes, and Prof. Mike Redfern. I must thank also: Dr. Mark Foley, from whom I have learned the first idiomatic sentences in English (without great results), and the concept that "Physics is fun!", Dr. Alan Fergus, who is a splendid person and his father will be always proud of him. I thank also my colleagues and friends Niall Clyne, with whom I have shared many nights of work and who has always provided me with a positive energy. I would like to thank also Margaret Toohey, who very kindly stole my desk :-) and Lisa-Marie Browne, for her kindness and goodwill, things that come along with very talented people. I also thank Brandon "Giuba" Wiles, my compadre in Capoeira (always willing to talk and solve complex questions), Aonghus "99.99%" Mullins (lethal opponent in a bat-and-ball game [he lets you chose it]), Ronan "4D Manifold" Rochford (an unleashed beast at 64 bits) and Diarmaid "Chessmate" De Burca (you are already in his underwater white & black "grid").

Moreover, I must thank former VERITAS P.I., Dr. Trevor Weekes, and the current one, Dr. Wystan Bembow, for the chance they gave me to work in such a stimulating collaboration. I must thank many others. In chronological order: Andy Smith,

John Kildea, Amanda Weinstein, Jamie Holder, (Yeuk Chun) Ken Chow, Henric Krawczynski, Matthias Beilicke and last, but not least, a big hug to Angelo "Binary" Varlotta and Nicola "Wind Flying" Galante. A very kind embrace for two very kind and brainy friends: Ana Pichel and Tulun Ergin.

I wish to send a hello to the end (or the beginning) of the Cosmos to Simon Swordy with whom I really would have had a jam session based on Paco de Lucia's music.

Thank you kindly to Gene Gardner, Kenneth Gibbs and his fantastic doggy dog, Stephen Criswell, Emilio Falco, Grace Alegria, Karen Myres, Emmet Roache, Jack Musser, Dan Brocious, Danny West, Cesar Lopez, Ryan Irvin and Ginny. Also, a particular hand shake goes to Michael Calkins, Perry Berlind and Gil Esquerdo, with whom I shared several nights of observation and (working) holydays sharing warm chocolate cakes and candies.

Finally, I really must to thank Prof. Alberto De Santis, who teaches to his student how be Men and Engineers. I really won't forget his lectures. A special thank to Dr. Marcello Giroletti and an embrace to his family.

A scientist who does not care about participating in building a wiser world, at the service of the people and not the economy, is not a Scientist; he/she is only one of the "ever old" cold bureaucrats only worthy of Eichmann's professional admiration.

I owe a lot to "Mamma Irlanda" and perhaps one day I will give back some of it !! In Ireland I met Dr. Enrico Dal Lago, one of the most encyclopedic and enlightened minds, a modern time BVZM, a knight who fights against the ignorance of this darkest of nights, a true north american history lecturer. I also found a very kind friend, generous and noble. Thanks to Enrico my brain was never caught sleeping when thinking just about numbers; with his guide, I looked for meaning behind those numbers, and I rediscovered the humanities (my first true passion). Thanks also to the group of Masons which, during these years, indirectly via Enrico, so profoundly inspired my vision.

It is not possible for me to forget to say thanks to my compadres of Capoeira. My first thanks goes to my irmao Oisin Mac Aodha "Farinha", of whom I'm very fond. A very big hug (with no beju!!) goes to my first Capoeira Mestre and my personal friend, CM Mola, aka Keine Mendez. I own him too much, since Capoeira changed my life; I see now the ancient Orishas, I feel the trembling of the ground made by the atabaque, «cai a chuva vai u ventu, pasa agua na peneira» and I hear the true rhythm of Life that sounds like "Tich Tich, Dom, Dim, ( ) ". This is called Angola, the first of the traditional Capoeira toques, firstly played 4000 B.C., likely before... long before... at the Dawn of humanity. When I do Capoeira, sometimes my thoughts holds about my son: « Ai meu Deus cuando eu partir, desse mundo enganador , pra meu filho eu deixarei uma coisa de valor e'... Não e' dinhairo, não e' ouro nem e' prata. E' um berimbau maneiro que eu ganhei do meu avô». Since it worked for myself, I really hope that one day my son will envision this deep meaning and will find his way for his own Happiness.

Moreover, it is a pleasure to embrace my Capoeira compadres in Viareggio. I owe

Jacopo “Alba” and Fabien “Grillo” too much. They are very special to me. Also I thank them for our common love for the ocean and for our common interests in the Hawaiian coralline reef. Even more, I owe M Puma and CM Delfino. Their positivity pervades the life of their students, something that is only possible to summarize in the word “Cosmic”, all together making a very enjoyable cosmic family.

I would like to thank also Yarek and Carmen for their friendship during this long path. Also, I really enjoyed our long chats about everything was Polish, Italian and Romanian. Thanks to Tiger for our long tennis games :-) !!!

I wish to clarify that the present work could not have begun without Silvana Falasca’s and Stefania Gianmanco’s kindness and help. It proves that a few very good friends make an actual difference in one’s life. I am really lucky for having Silvana as my good friend. I really appreciate her positive big Soul. Thanks to Massimo Sartori another very good friend, who was always interested in sharing life experiences and kind words. Thanks to Renzo Colameo for his friendship during this long time.

In Ireland I also met my good friend Dr. Victor Abelardo Acciari. To him, I owe my first genuine love for Latino America. Thanks also to Marcelo Alberto Echeverria, Arturo Hernandez Martinez and Mestre Augustinho. Un saludo desde Cuernavaca, Xochicalco hasta la Tierra Madre, Patagonia, hasta el final del mundo. Thanks to all the people who entered my life, crossing my Italian/Irish/South American path, my road, the migrants’ road ...

A big hug to the immense intellectual and writer Edoardo Galeano for disclosing the real face of history through his inspiring books, the real poetry of fighting to the end, fighting for one’s land,fighting with the Land (Earth, Terra, Gea, Gaia, Tiamat). Y gracias por detenernos agarrados “al viento con las unas” !!

During the years, I had the chance to live in many countries for extended periods and I met many cultures and peoples. No one is 100% good or bad. Some places are more evil than others. Few of them, though, still brings hope to humankind. I remember warmly Latin America. “Que viva la Tierra” !!

Thanks to everybody that fights like Sandino hearing the breath of the Earth. Thanks to who is preserving the flame of Bolivar’s Hope and to who, led by compassion for humankind, had lit that flame again almost a century and a half after Bolivar’s death. Thanks to who proved to the world that injustice is injustice even if masked under the pretext of quasi-law (based on violence).

A warm hug to Vittorio Arrigoni that repeatedly faced the brutality. Facing it, we should always remind our Compassion. Vittorio, everybody is missing you, even more while you were used to repeat «Stay human» !! («Restiamo Umani» !!)

What a piece of work is a man, how noble in reason, how infinite in faculties, in form and moving how express and admirable, in action how like an angel, in apprehension how like a God the beauty of the world, the paragon of animals — and yet, to me, what is this **quintessence of dust***?*

Hamlet, *Act 2, Scene 2*

Who's going far from his home seeking knowledge (walks) in the path of God —

At-Tirmidhi, *Sayings*

Abstract

We have investigated the very-high-energy (VHE) γ-ray emission and the ultraviolet emission of Markarian 421 recorded during 2007-2008. The VHE dataset is reasonably spread out over nine successive months of observation, with the presence of periodic time gaps due to the moon phase. During this observational season, VERITAS recorded the Markarian 421 averaged emission ($F_{mean} = 2.71 \times 10^{-10}$ erg/cm^2/s) and its historically largest known VHE flare ($F_{max} = 1.18 \times 10^{-9}$ erg/cm^2/s). The Swift/UVOT ultraviolet dataset consists primarily of three intensive observational periods corresponding to the VHE active emission states of Markarian 421. The analysis of this dataset has returned the averaged emissions (F_{mean}: 11.9, 12.6, 11.6 mJy) and the maximum seasonal emissions (F_{max}: 14.7, 19.4, 17.8 mJy) of Markarian 421 in the three Swift/UVOT ultraviolet bands (UVW1, UVM2, UVW2), respectively. For VHE flux variations, there is evidence of correlation between flux increases and spectral hardening, obtaining a proportionality constant of 0.86 ± 0.42 over the VHE portion of the spectrum. We find no conclusive evidence for any correlation between the VHE and UV datasets. A multiwavelength study of the typical flare profiles has also been carried out by introducing structure function analysis and obtaining a value for the ratio of the rise and fall timescales of $\tau_{ratio,\mathrm{VERITAS}} = 2.7 \pm 0.7$. We measure a significantly different profile for the flares at ultraviolet bands ($\tau_{ratio,\mathrm{UVOT}} = 0.9 \pm 0.3$). At both VHE and in the ultraviolet band, the power spectral density of Markarian 421 is effectively described by $P(f) \propto f^{-\alpha}$ with $\alpha = 2.6 \pm 0.1$, thus, located between the random walk noise ($\alpha = 2$) and the flicker random noise ($\alpha = 3$) behaviors.

Contents

Chapter 1

Introduction

This thesis presents the result of the investigation of ultraviolet and very-high-energy observations of the active galaxy Markarian 421. We have analyzed the data recorded during the 2007-2008 monitoring campaign by the UVOT (UltraViolet and Optical Telescope), which is one of the three technological payloads aboard the Swift satellite, and by the VERITAS (Very Energetic Radiation Imaging Telescope Array System) γ-ray telescope array.

At the beginning of each chapter, we provide a brief summary of the specific content. The Dissertation consists of seven chapters, of which Chapter 1 is the Introduction. Chapter 2 deals with the basics of very-high-energy (VHE) astrophysics.

In Chapter 3 a short and general overview of the UVOT telescope is provided. In 2007, a reduction pipeline for UVOT data was not available; we overcame this difficulty by developing our reduction analysis. Our efforts were mainly aimed at reducing observations with bright foreground stars in the field of view (see Section 3.3). Moreover, we developed an automatic code by implementing a number of data quality

checks and introducing refinements that account for the interaction of radiation with matter and cosmological effects.

In Chapter 4, we introduce the principles of the atmospheric Cherenkov imaging telescope operation and the specific design of the VERITAS array. In Chapter 5, we present the reduction of the VERITAS dataset using the VEGAS (VEritas Gamma-ray Analysis Suite) analysis software. Since each extensive air shower is different and results from a series of random processes, the VEGAS package involves simulations of particle showers originating from γ-rays and particles.

Chapter 6 focuses on the temporal analysis, which we performed by writing a dedicated software suite. We developed this time-domain analysis both by integrating already known approaches with new techniques, and also by presenting some new aspects of the time-domain approach. These included a variability study with particular emphasis on the identification of noise-like characteristics of the signal produced by the blazar processes. Moreover, we carried out the cross-correlation and autocorrelation analyses of the UVOT and the VERITAS lightcurves. Finally, with the structure function analysis, we determined the ranges of some characteristic timescales that contribute to the temporal variability of the UVOT and VERITAS lightcurves.

In Chapter 7, we provide a brief summary of the entire work, and we discuss the conclusions. We end the present work providing this final chapter with a section dedicated to the future of the VHE astrophysics. We also introduce the VERITAS hardware upgrade plan and we provide an overview of the CTA (Cherenkov Telescope Array).

Chapter 2

Review of γ-ray Astronomy

Traditionally, very-high-energy (VHE) γ-ray astronomy is defined as observations at energies above 300 GeV and below 100 TeV (Catanese & Weekes, 1999; Weekes *et al.*, 1989). The Whipple 10 m γ-ray telescope was built on Mount Hopkins in 1968 to search for sources of γ-rays. However, it was not until many years later that scientists began to see tangible results. With the detection of the Crab Nebula (Weekes *et al.*, 1989), the Whipple Group led by Dr. Trevor Weekes, which subsequently became the VERITAS Collaboration, showed that it was possible to statistically select the γ-ray initiated showers (circa 0.1% of the detected showers) from the much more numerous cosmic ray initiated showers (Hillas, 1981, 1996).

Presently, VHE γ-ray astronomy plays an important role in astroparticle studies. Astrophysics researchers investigate the existence of Lorentz invariance violation, observing flares of distant sources (Coleman & Glashow, 1999; Stecker & Glashow, 2001). Moreover, they probe cosmic ray origin by studying the γ-ray emission of starburst galaxies (Acciari *et al.*, 2009c).

2.1 VHE Astrophysics

Gamma-rays, denoted as γ, are the most energetic known forms of electromagnetic radiation, with each γ-ray being at least one hundred thousand times more energetic than an optical light photon. γ-rays have energies above 100 keV (10^{19} Hz) and VHE γ-rays have a frequency $\simeq 10^{25}$ Hz (corresponding to an energy in the TeV range). They are produced either by subatomic particle interactions such as $e^- e^+$ annihilation, neutral pion (π^0) decay, radioactive decay, fusion and fission or, in astrophysical processes, by inverse Compton (IC) scattering. The reconstruction of the direction from which such very-high-energy γ-rays come reveals the sky position of the strong cosmic accelerators from where they originate. γ-rays production mechanisms can be easily separated into two classes: line emission mechanisms and continuum emission mechanisms.

2.2 Line Emission Mechanisms

Usually, emission lines are produced by low-energy processes, explained below:

- **Particle/Antiparticle Annihilation**

  When a particle collides with a matching antiparticle, both particles annihilate. Then, their energy produces fundamental bosons that subsequently decay and produce other particles and antiparticles (Figure 2.1). As a results, positron-electron pair collision and annihilation is likely to produce a γ-ray photon pair. This decay preserves the total net charge of the annihilating particles, that is zero. The angular momentum is conserved and more importantly, the linear

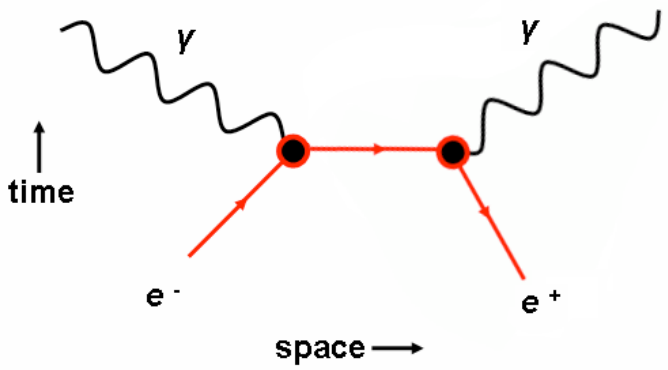

Figure 2.1: Feynman diagram showing spacetime vectors of electron-positron annihilation – (Toner, 2008) and modified from Ford (1963).

momentum and the total energy are also conserved, thus preventing the creation of a single γ-ray. γ-rays are produced, *e.g.*, as follows: $e^+ + e^- \rightarrow 2\gamma$. If the electrons are at rest (low-energy case), each of the produced γ-rays will have an energy of 511 keV. However, since neutrinos also have smaller mass than electrons, the production of one (or more) neutrino/antineutrino pairs is still possible (but less likely). If the annihilating particles are in motion (high-energy case) at the moment of collision, a continuous energy distribution will be produced, and the energy of a collision will be shared equally between the two emerging photons. Eventually, other particles that possess larger mass can also be produced, since there is a significant amount of kinetic energy from the relative particle velocities that might provide the rest energy for the produced particles.

- **Collisions of energetic particles**

  Energetic particle collisions can excite or de-excite nuclei, producing γ-ray line

emission. The interstellar medium commonly shows line-emission processes, mainly when radioactive products of stellar ejecta material de-excite. The radiation field of the interstellar gas is typically much weaker than the field of a medium in thermodynamic equilibrium.

- **Landau transitions**

  When a strong magnetic field is present, discrete cyclotron orbits may be occupied by charged particles (*e.g.* electrons), producing cyclotron emission lines. The γ-ray emission is at an energy of 11.6×10^3 B TeV (where the magnetic field B is in Gauss) beginning at $E > 511$ keV. The energies, E_n, of the Landau levels n are uniformly spaced:

$$E_n = \frac{(n + 0.5)\hbar\ \omega}{(1 + z)}, \tag{2.1}$$

  where $\hbar$ is the reduced Planck constant $h/2\pi$, ω is the angular cyclotron frequency, and z is the gravitational redshift of the object producing the high magnetic field. The magnetic field strength B and the charge-to-mass ratio, q/m, of the particle in motion determine the cyclotron angular frequency.

- **Particle decay**

  The decay of elementary particles may produce γ-rays since neutral pions (π^0) decay into two γ-rays with a probability of 98.8%. If the decay happens while the pion is at rest, each of the resultant γ-rays will have an energy of 0.5 $m_{\pi^0}c^2$, where m_{π^0} is the mass of the neutral pion. It is much more common for the pion to decay while moving at relativistic speeds, producing γ-rays at energies

>GeV. Usually, π^+ and π^- decay without gamma emission. However, there is still a slight chance (10^{-4}) that charged pions decay producing a γ-ray.

2.3 Continuum Emission Mechanisms

- **Bremsstrahlung**

  Bremsstrahlung, or "braking radiation", is the electromagnetic radiation produced by an accelerated charged particle, such as an electron, which is deflected when passing through an electric field. As the electron moves through the electric field, it loses a large amount of energy, producing a continuous emission spectrum (unlike atomic spectra, which contain sharp spectral lines). Sometimes this radiation is referred to as 'free-free' radiation, because the incident electrons are not bound to an atom or ion, either before or after the braking. The deceleration of the incident electrons provokes the emission of γ-rays at wavelength

$$\lambda = \frac{h \cdot c}{\Delta E} \tag{2.2}$$

  where ΔE is the change in the kinetic energy of the charged particle due to acceleration/deceleration, h is Planck's constant and c is the speed of light. *Bremsstrahlung* occurs when electrons move through interstellar clouds where a high concentration of ionized (charged) gas is present. The γ-ray flux produced is directly proportional to the product of the density of the ionized gas by the electron flux. It is possible to retrieve the original power-law spectrum of an electron population knowing just its γ-ray *bremsstrahlung* spectrum, but only if other major processes are not involved.

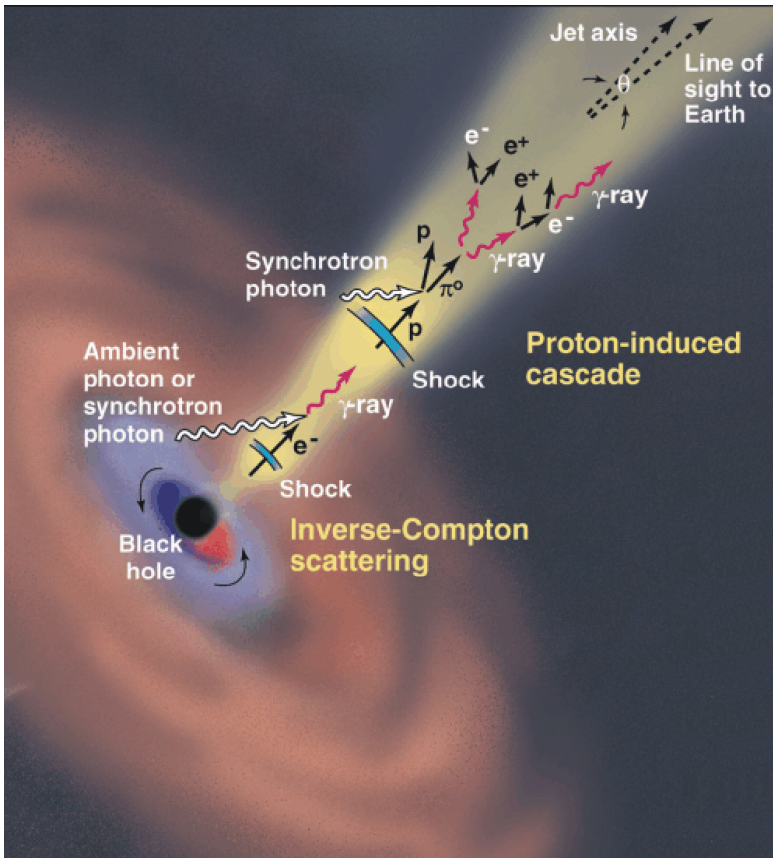

Figure 2.2: Collimated ejection of electrons from a supermassive black hole that experience multiple interactions with ambient photons along the observer's line of sight (Buckley, 1998).

- **Synchrotron radiation**

  The synchrotron-emission mechanism is dominant in high-energy astrophysics (Figure 2.2). Synchrotron radiation occurs when ultrarelativistic electrons follow a spiral path driven along the magnetic field lines. This process produces strongly polarized radiation, focused in the direction of the electron's motion. Therefore, this effect is called "beaming". Synchrotron radiation possesses a characteristic and identifiable spectral shape, which is dependent on the emitting electron population.

The expression "non thermal radiation" is widely adopted in very-high-energy astrophysics referring to the spectral radiation of a given population of high-energy and very-high-energy particles. This emission is a 'continuum emission' with a different spectrum from the thermal *bremsstrahlung* (or blackbody) radiation.

When a charged particle moves in the presence of a magnetic field, it experiences a Lorentz force, which produces an acceleration whose direction is perpendicular to both the magnetic field line and the velocity of the particle (Figure 2.3). Consequently, the path followed by the particle is a helix. The radius of the circle described in the plane perpendicular to the magnetic field line is known as the cyclotron radius, and is also sometimes referred to as the Larmor radius, r_L. It is given by

$$r_L = \frac{mv_\perp}{|q|B} \tag{2.3}$$

where $|q|$ is the magnitude of the particle charge, m is its mass, B is the strength of the magnetic field, and $v_\perp$ is the component of the particle's velocity perpendicular to the magnetic field. If an electron moves through the magnetic field, this becomes

$$r_L = \frac{mv_\perp}{eB} \tag{2.4}$$

where e is the magnitude of the electron charge. In the following text, we partially refer to the treatment of Rybicki & Lightman (1980). We use the traditional VHE notation that uses Γ instead of γ for the bulk Lorentz factor. The relativistic angular velocity of rotation is

$$\omega_B = \frac{eB}{\Gamma mc}. \tag{2.5}$$

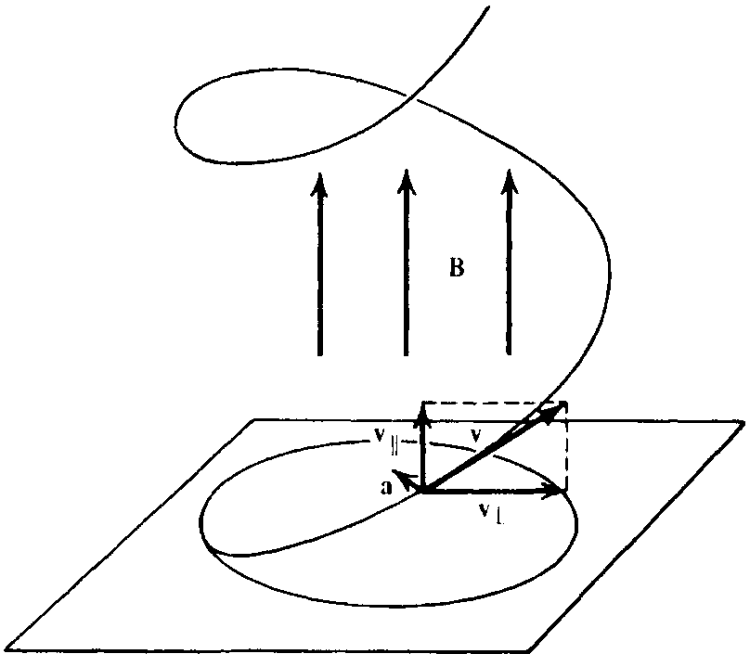

Figure 2.3: Motion of a charged particle through a magnetic field, B (Rybicki & Lightman, 1979). v is the speed of the particle. $\boldsymbol{v}$ has two components, $\boldsymbol{v}_{\parallel}$ and $\boldsymbol{v}_{\perp}$, parallel and perpendicular to the magnetic field, respectively. The pitch angle, θ, of the particle's path is given by $tan\ \theta = \boldsymbol{v}_{\perp}/\boldsymbol{v}_{\parallel}$, where θ is defined as the angle between $\boldsymbol{v}$ and $\boldsymbol{B}$

The acceleration a is, in practice, perpendicular to the velocity v, thus

$$a_\perp = \omega_B v_\perp \tag{2.6}$$

and the total emitted power is

$$P = \frac{2}{3} \cdot \frac{e^2 \Gamma^4}{c^3} \cdot a_\perp^2 = \frac{2}{3} r_0^2 c \, \beta_\perp^2 \, \Gamma^2 B^2 \tag{2.7}$$

where we need to average $\beta_\perp = v_\perp / c$ for isotropic velocity distributions. Then

$$\langle \beta_\perp^2 \rangle = \frac{\beta^2}{4\pi} \int sin^2\alpha \; d\Omega = \frac{2\beta^2}{3} \tag{2.8}$$

where α is the angle identified by the magnetic field and the particle velocity and $d\Omega$ is the subtended two-dimensional solid angle (in the three-dimensional space),

$$P = \frac{4}{9} r_0^2 c \beta^2 \Gamma^2 B^2 = \frac{4}{3} \sigma_T \, c \beta^2 \Gamma^2 U_B \tag{2.9}$$

where finally we substituted the Thomson cross-section, $\sigma_T = \frac{8}{3}\pi r_0^2$, and the magnetic field energy density, $U_B = B^2/8\pi$.

The synchrotron spectrum has a peak at linear frequency $\nu_{max} \propto B_\perp \Gamma^2$, where $\nu_{max} = \omega_{max}/2\pi$. $B_\perp$ and Γ are the magnetic field perpendicular to the direction of the motion and the bulk Lorentz factor, $\Gamma = (1 - \beta^2)^{-1/2}$, respectively. The spectrum emitted by a single electron averaged over the particle's orbit (Rybicki & Lightman, 1979) is

$$P(\omega) = P_\perp(\omega) + P_\parallel(\omega) = \frac{\sqrt{3}}{2\pi} \cdot \frac{e^3 B \; sin\theta}{mc^2} F\left(\frac{\omega}{\omega_c}\right) \tag{2.10}$$

where $P_\perp(\omega)$ and $P_\parallel(\omega)$ are the polarized emitted contributions of the synchrotron spectrum in the directions perpendicular and parallel to the magnetic

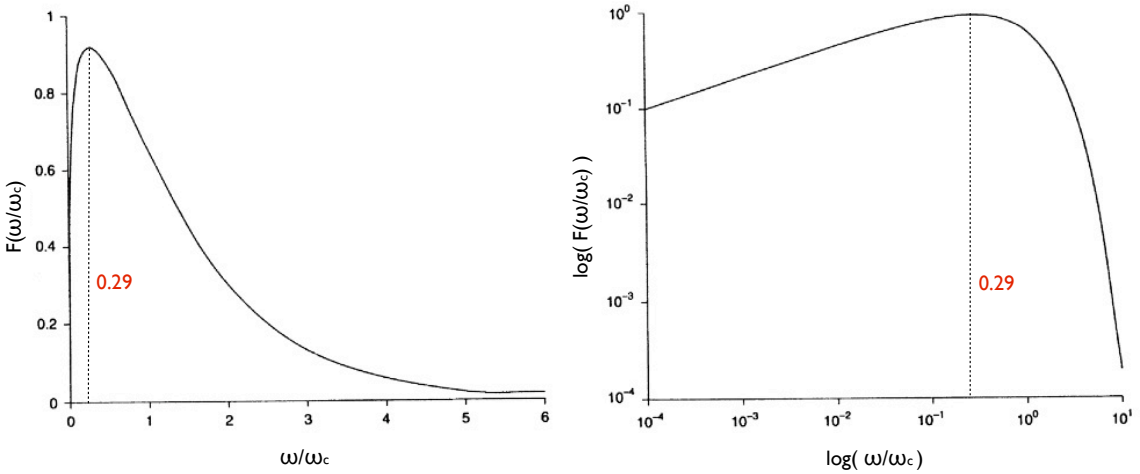

Figure 2.4: The spectrum of the synchrotron emission in terms of ω/ω_c (linear and logarithmic scales).

field,

$$\omega_c = \frac{3}{2}\frac{\Gamma^2 eBsin\alpha}{mc} \tag{2.11}$$

and

$$F\left(\frac{\omega}{\omega_c}\right) = \frac{\omega}{\omega_c}\int_{\omega/\omega_c}^{\infty} K_{5/3}(z)dz \ , \tag{2.12}$$

where ω_c is the critical angular frequency and $K_{5/3}(z)$ is one of the integral forms of the modified Bessel function of order 5/3. This spectral shape is shown in linear and logarithmic forms in terms of ω/ω_c in Figure 2.4. The peak of the emission spectrum occurs at $\omega_{max} = 0.29\ \omega_c$.

The spectrum can be approximated by a power law

$$P(\omega) \propto \omega^{-s}. \tag{2.13}$$

Analogously, its relation with a particle population of relativistic electrons is obtained by introducing the particle number density in any given energy bin

$(E, E + dE)$,

$$N(E) \propto E^{-p} \ , \quad E_1 < E < E_2 \ . \tag{2.14}$$

Under the assumption of a sufficiently wide energy interval $[E_1, E_2]$, this provides

$$P(\omega) \propto \omega^{-(p-1)/2} \ . \tag{2.15}$$

Then, in the hypothesis of a power-law particle energy population with index p, the index of the spectral emission is

$$s = \frac{p-1}{2} \ . \tag{2.16}$$

The total emitted radiation of a distribution of relativistic electrons isotropically directed in all directions is

$$\begin{aligned} P = \tfrac{1}{6\pi}\sigma_T c\beta^2\Gamma^2 B^2 \approx \tfrac{1}{6\pi}\sigma_T \ c \ B^2\Gamma^2 = \tfrac{0.05\cdot 6.65\times 10^{-25}\cdot 2.99\times 10^{10}}{6\pi}\cdot\Gamma^2 B^2 \ \ \text{erg/s} = \\ = 1.05\times 10^{-15}\cdot 6.24\times 10^{11}\cdot\Gamma^2 B^2 \ \ \text{eV/s} \\ = 6.55\times 10^{-4}\cdot\Gamma^2 B^2 \ \ \text{eV/s} \end{aligned} \tag{2.17}$$

The comoving cooling time for synchrotron emission, which is the time that an electron takes to lose its energy via synchrotron radiation cooling, is given by:

$$t_{cool} = \frac{E_e}{P} \tag{2.18}$$

where $E_e = \Gamma mc^2$ is the energy of one of the electrons. Synchrotron radiation emission is larger for electrons than for protons since the emitted energy is inversely proportional to the square of their masses.

- **Inverse Compton (IC) scattering**

  Inverse Compton (IC) scattering is the process that up-scatters low-energy photons to higher energies (Rybicki & Lightman, 1979). Compton scattering is an example of nonelastic scattering since $\epsilon_2 > \epsilon_1$, where ϵ_1 and ϵ_2 are the incident and scattered photon energies. However, this effect can be considered to be produced by an elastic collision between a photon and an electron. Then, if a photon is scattered by an electron,

$$\epsilon_2 = \frac{\epsilon_1}{1 + \frac{\epsilon_1}{mc^2}(1 - cos\,\zeta)} \tag{2.19}$$

  where ζ is the scattering angle, m is the electron mass and c is the speed of light. In terms of wavelengths

$$\lambda_2 = \lambda_c(1 - cos\ \zeta) + \lambda_1 \qquad \text{and} \qquad \lambda_c \equiv \frac{c}{\nu_c} = \frac{h}{mc} \tag{2.20}$$

  where λ_c is the Compton wavelength, which for an electron is 0.02426 Å. For longer wavelengths, $\lambda \gg \lambda_c$ (where $h\nu \ll mc^2$), IC scattering is almost elastic ($\epsilon_1 \simeq \epsilon_2$) and we can assume that there is no change in photon energy in the rest frame of the electron. Compton and IC scattering become less efficient toward higher energies. Using the differential cross-section Klein-Nishina formula (without relativistic corrections), we can compute the total cross-section:

$$\sigma = \sigma_T \cdot \frac{3}{4}\left[\frac{1+x}{x^3}\left[\frac{2x(1+x)}{1+2x} - ln(1+2x)\right] + \frac{1}{2x}ln(1+2x) - \frac{1+3x}{(1+2x)^2}\right] \tag{2.21}$$

  where $x = h\nu/mc^2$ and σ_T is the Thomson cross-section (Rybicki & Lightman, 1979). ν is the frequency of the incident photon and h is Planck's constant. However, we need to introduce a primed notation to transform the scattering

geometries from the rest frame to the observer's reference frame. From the Doppler shift formulae, we obtain

$$\epsilon_1' = \epsilon_1 \Gamma \, (1 - \beta \; cos \; \zeta) \qquad \text{and} \qquad \epsilon_2 = \epsilon_2' \Gamma \, (1 - \beta \; cos \; \zeta_2') \tag{2.22}$$

where ζ is the angle of the incident photon and ζ_2' is the angle of the scattered photon in the rest frame. β denotes v/c where v is the speed of the particle. Γ is the bulk Lorentz factor.

In the case of relativistic electrons, the total power emitted (or radiated) in the observer's frame is proportional to Γ^2. Then, the relativistic IC process enhances the photon energy by a factor of Γ^2 and, due to conservation of energy $\epsilon_1 < \Gamma mc^2 + \epsilon_2$, it cannot produce photons with energies larger than $\simeq \Gamma mc^2$.

The general derivation for up-scattering of isotropically distributed electrons is provied by Rybicki & Lightman (1979). In the observer's reference frame, the power emitted in an IC process (with the changes in energy of the photons being negligible in the electron rest frame, compared to the energy changes in the observer's frame), is given by

$$\frac{dE_{e_2}}{dt} = c \, \sigma_T \, \Gamma^2 \int (1 - \beta cos \; \zeta)^2 \epsilon \, v \, d\epsilon \tag{2.23}$$

where $\frac{dE_{e_2}}{dt}$ is the total power emitted by the electron in the observer's reference frame after the scattering. For an isotropic distribution of photons we have

$$\langle (1 - \beta cos \; \zeta)^2 \rangle = 1 + \frac{1}{3} \beta^2 \tag{2.24}$$

Thus

$$\frac{dE_{e_2}}{dt} = c \, \sigma_T \, \Gamma^2 (1 + \frac{1}{3} \beta^2) \int \epsilon \, v \, d\epsilon = c \, \sigma_T \, \Gamma^2 (1 + \frac{1}{3} \beta^2) \, U_{ph} \tag{2.25}$$

where $v\,d\epsilon$ is the density of photons having energy in the range $d\epsilon$ and $U_{ph} = \int \epsilon\, v\, d\epsilon$ is the photon energy density in the initial photon reference frame.

The rate of decrease of the photon energy is

$$\frac{dE_{e_2}}{dt} = -\sigma_T c U_{ph} \tag{2.26}$$

thus indicating the energy lost (or radiated) by E_{rad}. The net power lost by the electron is

$$P_{\rm IC} = \frac{dE_{rad}}{dt} = c\sigma_T U_{ph}\left[\Gamma^2(1+\frac{1}{3}\beta^2) - 1\right] \tag{2.27}$$

Since $\Gamma^2 - 1 = \Gamma^2\beta^2$, we obtain the IC power

$$P_{\rm IC} = \frac{4}{3}\sigma_T c \Gamma^2 \beta^2 U_{ph}. \tag{2.28}$$

The loss of energy of a population of relativistic electrons in a magnetic field due to synchrotron emission, $P_{\rm SYN}$, and the loss of energy due to the inverse Compton process, $P_{\rm IC}$, are related by the ratio between the magnetic field energy density, U_B, and the photon energy density U_{ph}:

$$\frac{P_{\rm SYN}}{P_{\rm IC}} = \frac{U_B}{U_{ph}} \tag{2.29}$$

The radiation which is enhanced toward higher energies by the IC process has been Compton up-scattered (or "comptonized"). It can be shown that the spectral index of the IC emitted radiation and the spectral index of the up-scattered photon family is

$$s = \frac{p-1}{2} \tag{2.30}$$

where p is the power-law index of the particle's population in a given interval of energies and s is the corresponding spectral index of the obtained photon distribution.

2.3.1 Interaction of γ-rays with Matter

In order to be detected, a photon must interact with matter. How γ-rays interact with matter depends on their energies. γ-rays interact by three major processes: photoelectric absorption, Compton scattering and, finally, pair-production (Figure 2.5). The probabilities of these processes depend on the γ-ray energy density and on the atomic number, Z, of the nucleus with which the γ-rays interact.

- **Photoelectric absorption**

  A γ-ray may be absorbed by a bound atomic electron. A part of its energy may be used to overcome the electron binding and, then, the remaining energy will be transferred as kinetic energy to the escaping electron.

  The photoelectric process is the most significant process of interaction for photons of relatively low energies (Figure 2.5). The dependence of photoelectric absorption probability per atom, τ, on photon energy, E_γ, and on Z can be approximated by

  $$\tau \propto \frac{Z^n}{{E_\gamma}^3} \tag{2.31}$$

  where the exponent n varies between 4 and 5 with γ-ray energy.

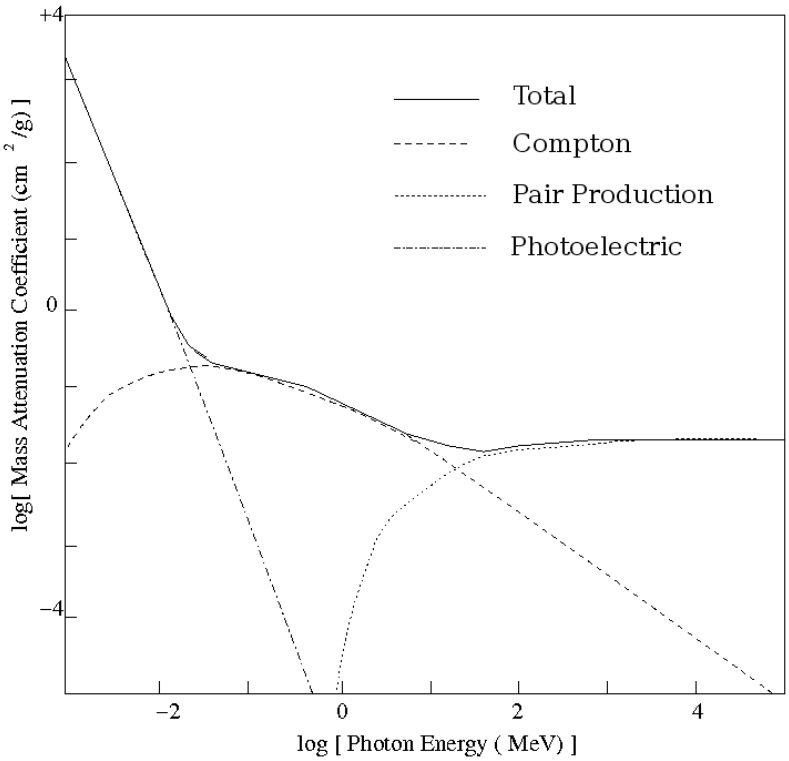

Figure 2.5: The three main interaction mechanisms that occur along the electromagnetic spectrum from a few keV to GeV energies: photoelectric absorption, Compton scattering and pair-production (Weekes, 2003).

- **Compton Scattering**

  Compton scattering occurs when a γ-ray of energy E_γ interacts with a free (or weakly bound) electron of energy E_e. The incident γ-ray loses some energy, which is imparted to the electron. With the remaining energy, another photon is emitted in a different direction, conserving the total momentum. The resulting change in wavelength is given by

$$\lambda_1 - \lambda_2 = \frac{h}{m\,c}(1 - cos\,\zeta). \tag{2.32}$$

  where λ_1 and λ_2 are the wavelengths of the incident and the scattered photon, h is Planck's constant, m is the electron mass and ζ is the angle between the incident-photon direction and scattered-photon direction.

- **Pair Production**

  The formation of an electron-positron pair is called the pair-production process. It occurs when the influence of a strong electromagnetic field originating in the nucleus is exerted on a γ-ray photon passing close enough. Pair-production becomes the dominant attenuation process between 10 MeV and 100 MeV as shown in Figure 2.5. The probability of a pair-production changes as a function of the square of Z - *i.e.*, the nucleus atomic number. At higher γ-ray energies, pair-production can also generate higher-energy leptons, such as the muon and tauon particles.

2.4 Types of VHE Sources

Recent developments in the field of VHE astrophysics have led to a dramatic increase in the number of detected sources that emit GeV-TeV γ-rays. VHE γ-ray studies have also provided important results regarding the origin of the cosmic rays.

A conclusive explanation of the origin of such cosmic rays is still elusive but, recently, the VERITAS Collaboration has provided an interesting contribution. In Acciari *et al.* (2009c), the VERITAS Collaboration suggests that cosmic ray production is directly linked to the star formation activity in the core of M82, where the density of cosmic rays is about 500 times the average galactic density. A similar result has been provided by Acero *et al.* (2009) for the starburst galaxy NGC253.

TeVCat[1] is an online catalog developed by Deirdre Horan and Scott Wakely (Horan and Wakely, 2008). It provides a list of the VHE sources detected above 50 GeV.

The source types can be classified into three main categories: galactic, extragalactic and unidentified sources (*e.g.* dark accelerators, primordial black holes).

2.4.1 Galactic Sources

Each galaxy is mainly composed of stars. By nuclear fusion, the hydrogen in the cores of stars is converted into helium. When the hydrogen depletes, the core becomes unstable and begins to fall in on itself under the effect of the gravitational forces.

[1] http://tevcat.uchicago.edu/

Supernova and Supernova Remnants

The creation of a supernova (Types I and II) is strictly dependent on the initial mass of a star (Figure 2.6).

A Type I supernova results from the explosion of a white dwarf star that has already ceased nuclear fusion and completed its life cycle. After it has accreted enough matter (*e.g.* from a nearby companion) to reach the Chandrasekhar limit (that, for a nonrotating star, is about 1.38 solar masses, $M_\odot$), the dwarf star starts collapsing under its own weight. Within a few seconds, significant portions of the star's matter ignite the nuclear fusion process. Such process releases a large amount of energy ($\sim 10^{44}$ J), which triggers the supernova explosion. The produced shockwave pushes the matter to velocities up to $0.03 - 0.06$ c, where c is the speed of light.

Type II supernovae originate from stars that already contain at least $9 - 10 M_\odot$ and no more than $40 - 50$ $M_\odot$. Hydrogen is also present in their spectra. Unlike the Sun, massive stars possess the mass needed to fuse elements with atomic mass greater than hydrogen and helium masses. In the core of the stars, the hydrogen is reprocessed to give helium and the outward pressure of the nuclear reactions maintains the hydrostatic equilibrium under the pressure of the gravitational forces. When the hydrogen is depleted, the core collapses again, causing both a rise of temperature and an increase of pressure, which provokes the ignition of helium. Then, a fusion cycle producing carbon is lit and the outward pressure begins to balance the gravitational collapse. This process repeats several times; each time the core collapses, a new ignition is lit. The entire process ends with the production of iron which fuel a new process of nuclear fusion. If the mass of the star is larger than the mass of the

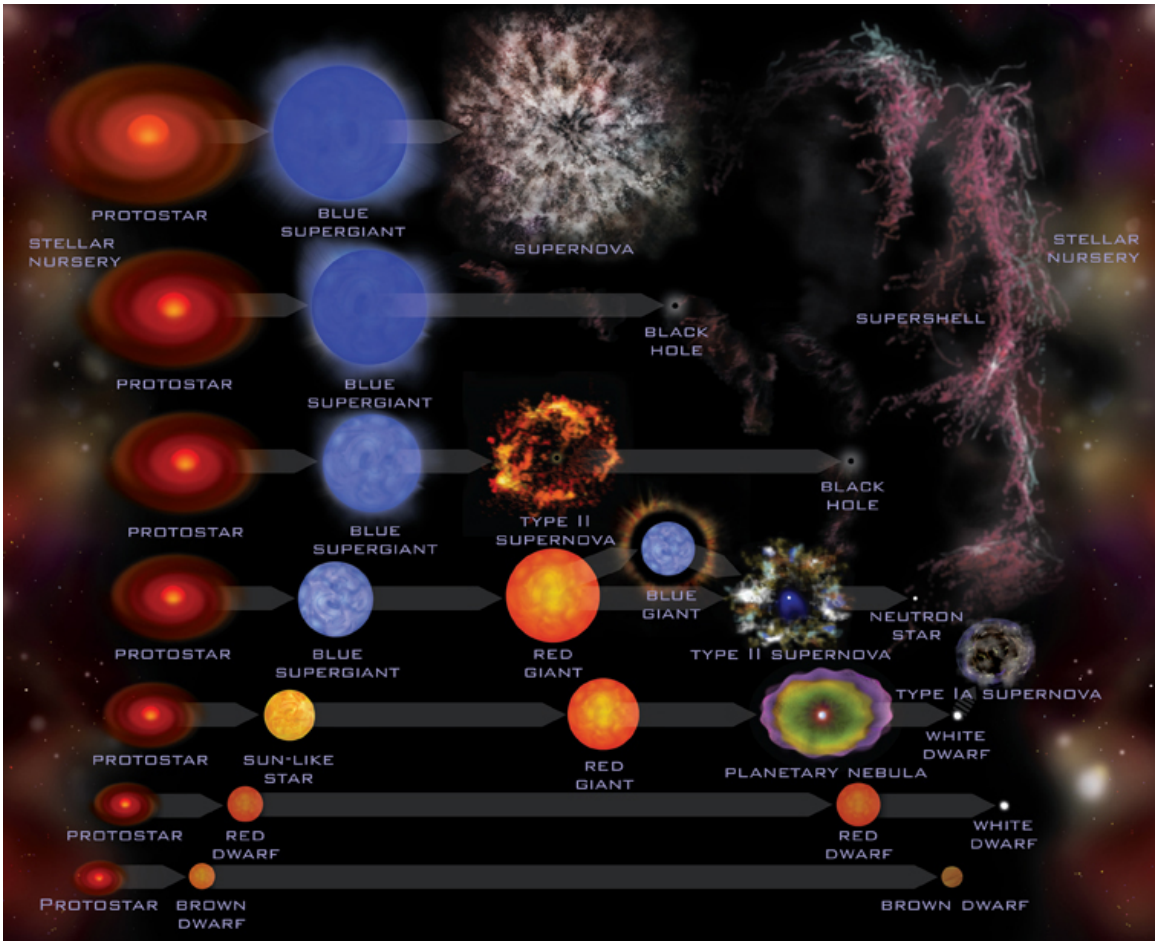

Figure 2.6: This figure gives a summary of the best current understanding of the evolution of stars (from Chandra X-Ray Observatory Poster, http : //chandra/harvard.edu).

Chandrasekhar limit, this provokes an implosion of the star and the collapse on itself with velocities reaching 0.23 c. As a result of such collapse, we obtain Pulsar Wind Nebulae (PWNe) and black holes.

Supernova remnants (SNR) are the result of stellar explosions. A supernova explosion is one of the most energetic events in the Universe; it expels much, or all, of the surrounding stellar material. When this material collides with the circumstellar or interstellar gas, it forms a shockwave that can heat the gas up to temperatures as high as 10^6 K forming a high-temperature plasma.

There are three general classes of SNR:

1. **Shell-type remnants**

   The Cygnus Loop is a shell-type supernova remnant (Figure 2.7). After the explosion, the supernova shockwave produces a ring-like shell of hot material (mainly gas).

2. **Crab-like remnants**

   Pulsar Wind Nebulae (PWNe) are Crab-like remnants. They sometimes possess a displacement that indicates an asymmetry in the explosion. After the explosion, the compact object receives a large velocity that pushes it away from the core. However, it is still unknown how the momentum is transferred to the PWN.

   The Crab Nebula is the most famous representative of this class of objects (see Figure 2.8). A beam of radiation is emitted along the direction of the pulsar magnetic axis. The beam is periodically aligned in the observer direction. The

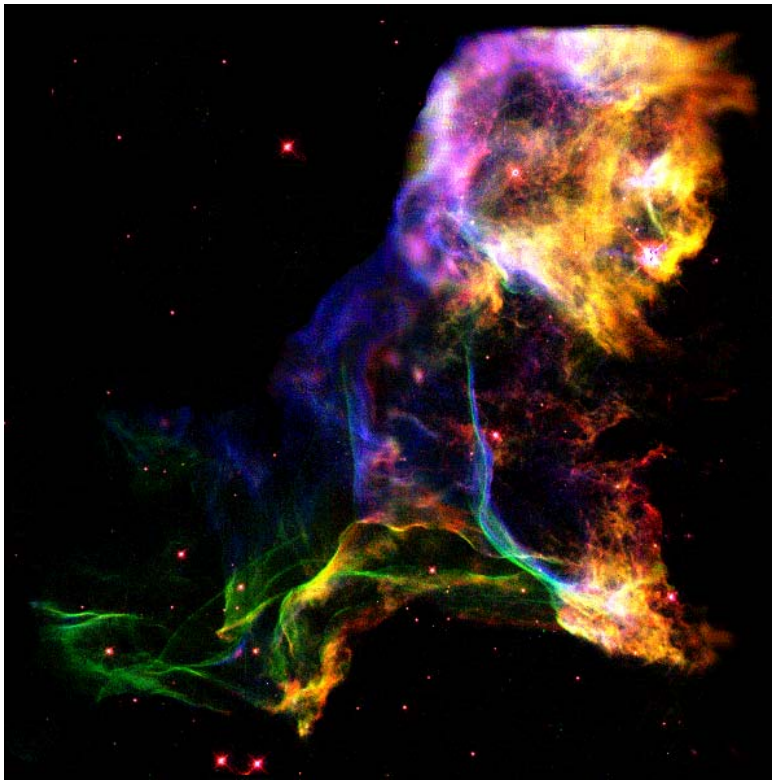

Figure 2.7: Cygnus Loop (from http://www.astro.rug.nl/).

Figure 2.8: The Crab Nebula. This image combines optical and X-ray (in red and blue, respectively) datasets from the Hubble Space Telescope and from the Chandra X-ray Observatory (Hester *et al.*, 2002).

direction of the electromagnetic beam is determined by the magnetic axis of the pulsar and the rotating magnetic field generates a concatenated electrical field. Electrons and protons move along the pulsar surface toward the regions around the magnetic poles where the beam is produced. They emit γ-rays traveling along the curved path of the magnetic field lines (Aliu *et al.*, 2011).

3. **Composite Remnants**

   The composite remnant class is comprised of remnants that can not be simply categorized as shell-type remnants or Crab-like remnants. We can divide them into two composite remnant subtypes:

- **Thermal composites** look like SNRs at radio wavelengths. At X-ray energies their emission is Crab-like, but presents absorption lines.
- **Plerionic composites** look Crab-like in both radio and X-ray wavebands, without presenting absorption lines in their central regions.

2.4.2 Unidentified Sources

A dark accelerator is an example of an unidentified Galactic source. It emits HE/VHE γ-ray photons but it does not possess an identified observable counterpart at lower energies. The first dark accelerator discovered was TeV J2032+2130, which is located in the Cygnus region (Aharonian *et al.*, 2002).

2.4.3 Extragalactic Sources

Most extragalactic objects that we observe at TeV energies are active galactic nuclei, AGN (Antonucci, 1993). Even the closest AGN observed at VHE are too far away to directly investigate their inner structure at present (see Table 2.1).

Over the past decade, several X-ray sky surveys have improved our understanding of the structure of these objects through a study of their continuum emission, which spans over several orders of magnitudes in the electromagnetic spectrum. AGN are very bright objects that present, in optical bands, luminosities of $4 - 10$ times larger than their host galaxies, and even more at ultraviolet wavelengths.

By investigating these objects at different wavelengths, astronomers have built a unified model of AGN (Figure 2.9), basing its structure on the presence of a super-massive black hole ($10^7 - 10^{10}\ M_\odot$) with an accretion disk. In the model, a dusty

TeV Extragalactic Sources

TevCat Name	Name	RA	Dec	Type	Observer	Date	Redshift
TeVJ2009-488	PKS 2005-489	20 09 29.3	-48 49 19	HBL	HESS	06.01.2005	z=0.071
TeVJ2359-306	H 2356-309	23 59 09	-30 37 22	HBL	HESS	04.01.2006	z=0.165
TeVJ1555+111	PG 1553+113	15 55 43.0	+11 11 24	HBL	HESS	03.01.2006	z=0.35
TeVJ2202+422	BL Lacertae	22 02 43.3	+42 16 40	LBL	Crimea	04.01.2001	z=0.069
TeVJ0222+430	3C66A	02 22 39.6	+43 02 08	IBL	Crimea	03.01.1998	z=0.444
TeVJ1136+701	Markarian 180	11 36 26.4	+70 09 27	HBL	MAGIC	09.01.2006	z=0.045
TeVJ0232+202	1ES 0229+20	02 32 48.4	+20 17 16	HBL	HESS	12.01.2006	z=0.14
TeVJ0550-322	PKS 0548-322	05 50 42.9	-32 16 34	HBL	HESS	07.01.2007	z=0.069
TeVJ0349-119	1ES 0347-121	03 49 23.2	-11 59 27.0	HBL	HESS	08.01.2007	z=0.188
TeVJ1015+494	1ES 1011+496	10 15 04.1	+49 26 01	HBL	MAGIC	09.01.2007	z=0.212
TeVJ0152+017	RGB J0152+017	01 52 33.5	+01 46 40.3	HBL	HESS	02.01.2008	z=0.08
TeVJ1221+282	W Comae	12 21 31.7	+28 13 59	IBL	VERITAS	08.01.2008	z=0.102
TeVJ0809+523	1ES 0806+524	08 09 49.2	+52 18 58	HBL	VERITAS	12.01.2008	z=0.138
TeVJ1256-057	3C279	12 56 11.1	-05 47 22	FSRQ	MAGIC	06.01.2008	z=0.5362
TeVJ0721+713	S5 0716+714	07 21 53.4	+71 20 36	LBL	MAGIC	04.01.2008	z=0.31
TeVJ0710+591	RGB J0710+591	07 10 30.1	+59 08 20.5	HBL	VERITAS	02.01.2009	z=0.125
TeVJ1104+382	Markarian 421	11 04 27.3	+38 12 32	HBL	Whipple	08.01.1992	z=0.031
TeVJ1653+397	Markarian 501	16 53 52.2	+39 45 36	HBL	Whipple	01.01.1996	z=0.034
TeVJ2347+517	1ES 2344+514	23 47 04.8	+51 42 18	HBL	Whipple	07.01.1998	z=0.044
TeVJ1428+426	H 1426+428	14 28 32.6	+42 40 21	HBL	Whipple	02.01.2002	z=0.129
TeVJ1959+651	1ES 1959+650	19 59 59.9	+65 08 55	HBL	Telescope Array	08.01.1999	z=0.048
TeVJ1230+123	M87	12 30 49.4	+12 23 28	FRI	HEGRA	05.01.2003	z=0.0044 -
TeVJ2158-302	PKS 2155-304	21 58 52.7	-30 13 18	HBL	Durham	06.01.1999	z=0.116
TeVJ1221+301	1ES 1218+304	12 21 21.9	+30 10 37	HBL	MAGIC	05.01.2006	z=0.182
TeVJ1103-234	1ES 1101-232	11 03 38	-23 29 31	HBL	HESS	04.01.2006	z=0.186
TeVJ2001+438	MAGIC J2001+435	20 01 13.5	+43 53 02.8	HBL	MAGIC	07.01.2010	-
TeVJ1503-582	HESS J1503-582	15 03 38	-58 13 45	DARK	HESS	12.01.2008	-
TeVJ1427+238	PKS 1424+240	14 27 00.39	+23 48 00.0	IBL	VERITAS	06.01.2009	-
TeVJ0319+187	RBS 0413	03 19 51.8	+18 45 34	HBL	VERITAS	10.01.2009	z=0.19
TeVJ0416+010	1ES 0414+009	04 16 52.41	+01 05 24.3	HBL	HESS	11.01.2009	z=0.287
TeVJ0507+676	1ES 0502+675	05 07 56.2	+67 37 24	HBL	VERITAS	11.01.2009	z=0.341
TeVJ1517-243	AP Lib	15 17 48.96	-24 23 06	LBL	HESS	07.01.2010	z=0.049
TeVJ0449-438	PKS 0447-439	04 49 24.7	-43 50 09	HBL	HESS	12.01.2009	z=0.2
TeVJ1512-091	PKS 1510-08	15 12 50.5	-09 06 00	FSRQ	HESS	03.01.2010	z=0.36
TeVJ1224+213	4C +21.35	12 24 54.4	+21 22 46	FSRQ	MAGIC	06.01.2010	z=0.432
TeVJ1443+120	1ES 1440+122	14 42 48.3	+12 00 40	IBL	VERITAS	08.01.2010	-

Table 2.1: TeV extragalactic source list of April 2011 from TeVCat (Horan & Wakely, 2008). This list contains high BL Lac (HBL), intermediate BL Lac (IBL), low BL Lac (LBL), dark matter (DARK), Fanaroff-Relay type I (FRI) and flat spectrum radio quasar (FSRQ) objects.

torus is also present, which surrounds the accretion disk, and blocks the emission from the side view. In addition, a broad-line region might be present but, unfortunately, reliable information is difficult to obtain since the broad-line region is spatially unresolved even in the nearest AGN (Terlevich *et al.*, 1992). Furthermore, extended clouds of gas orbiting the supermassive black hole produce atomic lines, due to absorption (Blandford and Konigl, 1979; Blandford and Rees, 1978). Finally, the acceleration of charged particles by electromagnetic fields inside the jets explains the emissions at higher frequencies.

At present, the radio emission coming from an AGN is believed to originate in plasma jets aligned with the rotation axis of the supermassive black holes. Theoretically, the variety of AGN types is largely a function of its viewing angle in relation to the jets (Figure 2.10). If the viewing angle is small, the emission is Doppler boosted from relativistic particles in the jet, and the object is termed a "blazar".

If the spectrum shows weak emission lines, the blazar is classified as a BL Lacertae object (Figure 2.11). The spectral energy distribution of the BL Lacs exhibits a typical structure with two humps (see Figure 2.12). Many galaxies are characterized by a large infrared luminosity, due to the presence of hidden active galactic nuclei and/or superstarbursts (Genzel *et al.*, 1998). Other AGN show a prominent emission in the ultraviolet part of the spectrum. The lower-energy peak in the spectral energy distribution is due to synchrotron emission, while the higher-energy peak is typically ascribed to IC scattering. Depending on the energy range within which the lower-energy peak occurs, BL Lacs are classified as low frequency BL Lacs or high frequency BL Lacs. A new category of intermediate-frequency BL Lacs (Swordy, 2008; Acciari

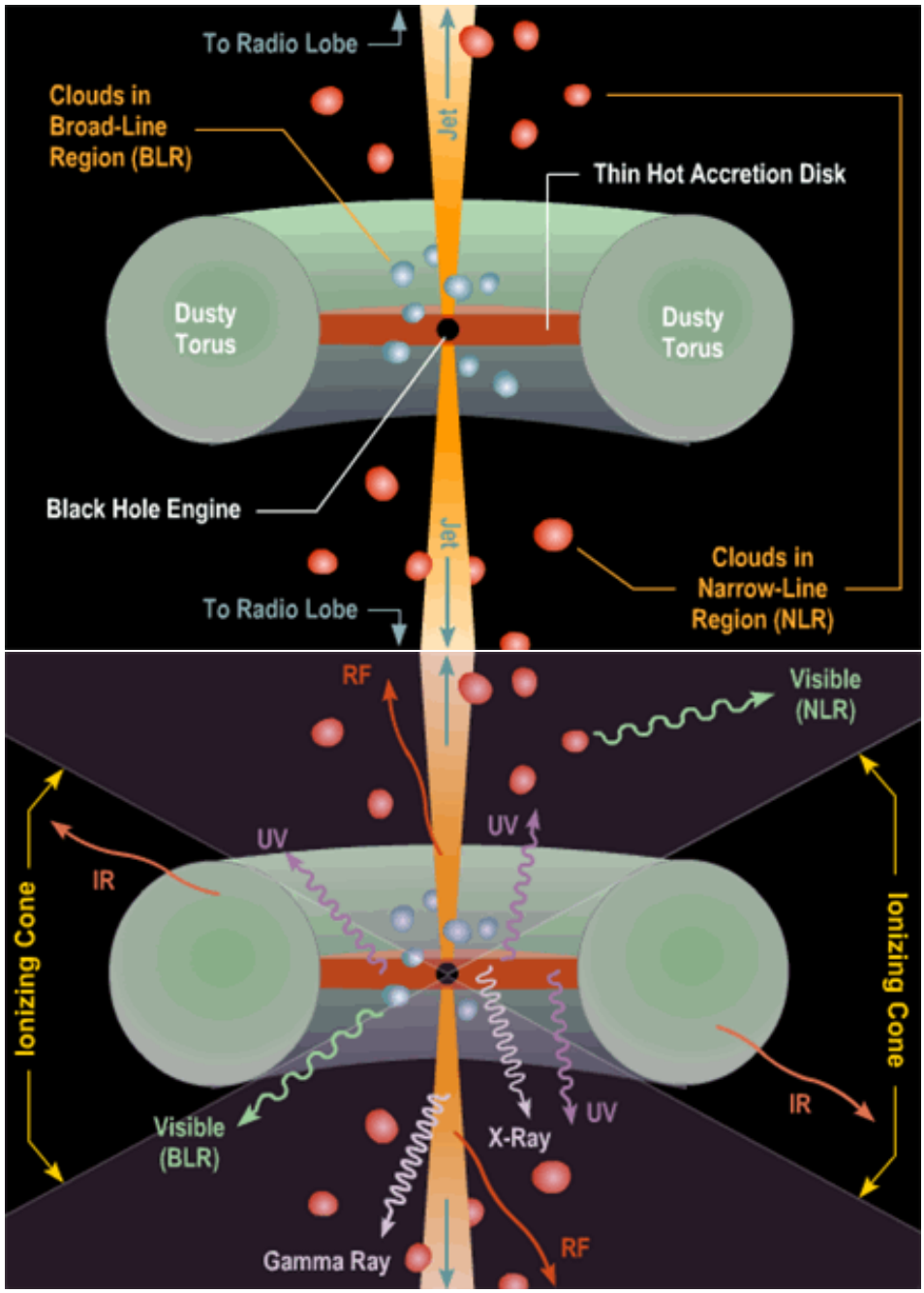

Figure 2.9: Unified AGN structure model **(a)** and multiwavelength emission model **(b)** from Moore, (2003).

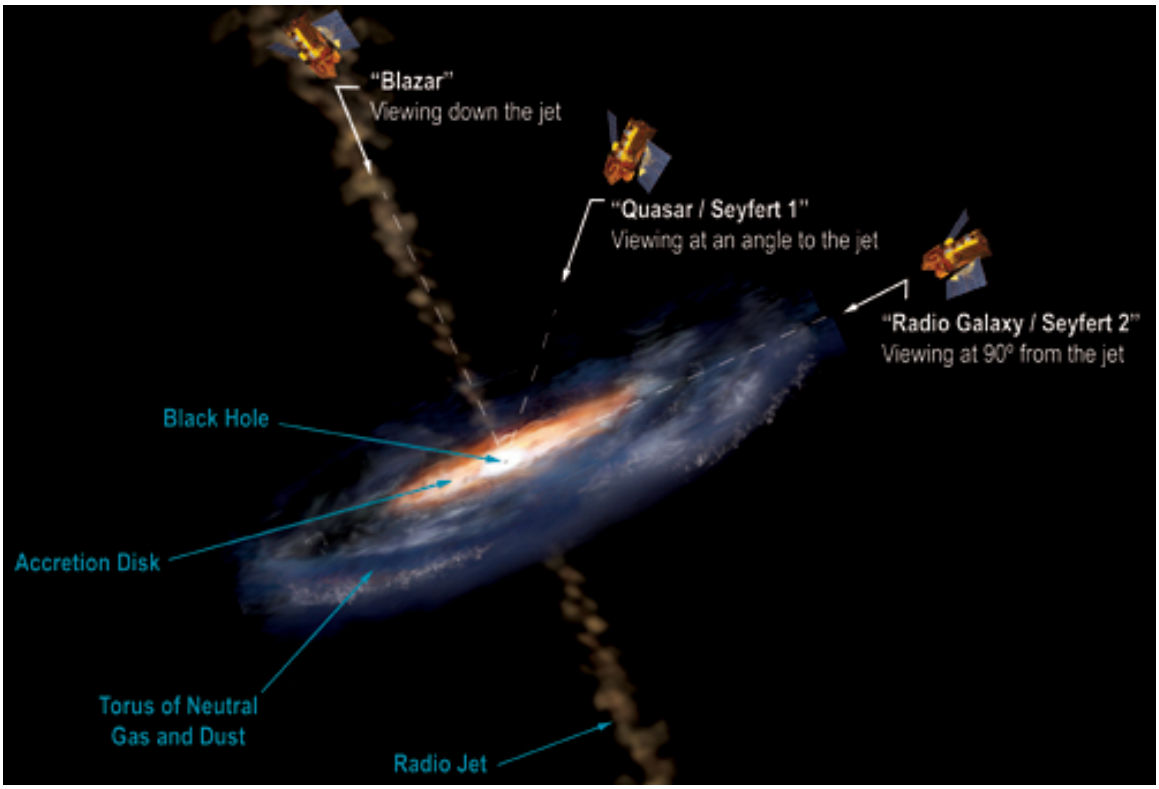

Figure 2.10: Classification of different type of galaxies dependent on the viewing angle. For smaller viewing angles, the observed emission is more intense, due to the Doppler boosting (from http://www.nasa.gov/centers/goddard).

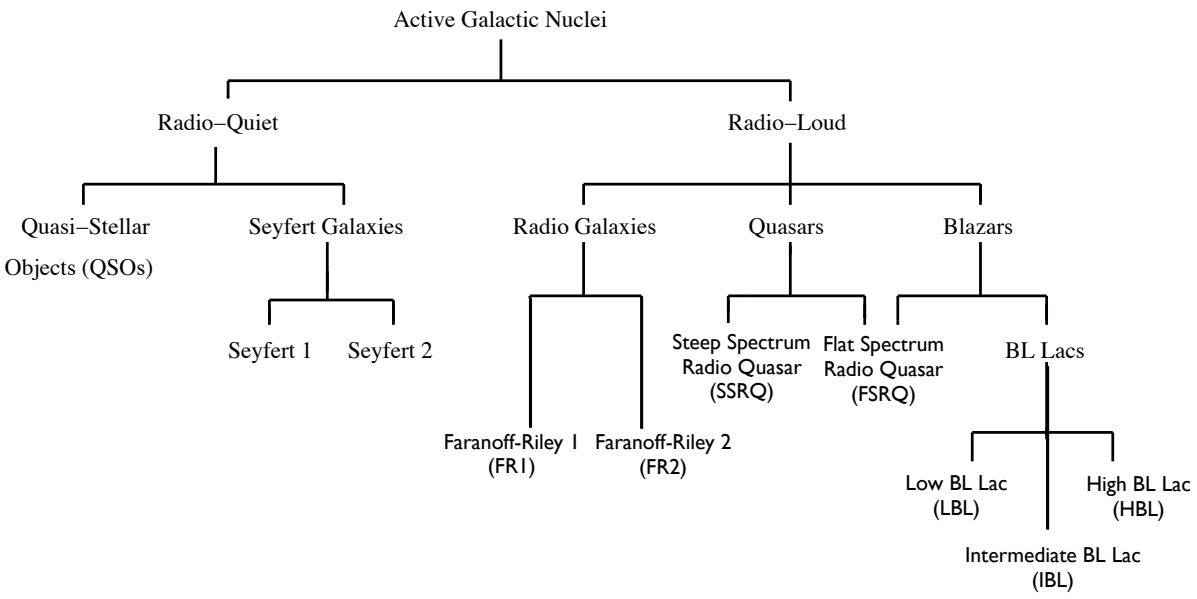

Figure 2.11: Classification of AGN types. Low BL Lacs (LBL) and High BL Lacs (HBL) are low frequency peaked and high frequency peaked BL Lacertae objects, respectively. A class of objects which is sometimes considered in between these two object types, intermediate frequency peaked BL Lacs (IBL), is also introduced in the classification (Toner, 2008).

et al., 2009a) has been identified between these two classes of BL Lacs.

2.5 Blazar's Relativistic Beaming

Relativistic effects enhance the observed blazar emission for small viewing angles along the jets. This process is universally termed relativistic beaming. The plasma that constitutes the jets is composed of electrons (or protons). Each particle in that population (or distribution) moves in a different direction, and the net speed of the whole particle distribution is the "bulk speed", which can be in the range of 0.95 c - 0.99 c, where c is the speed of light.

Considering the beaming geometry for a relativistic electron emitting synchrotron

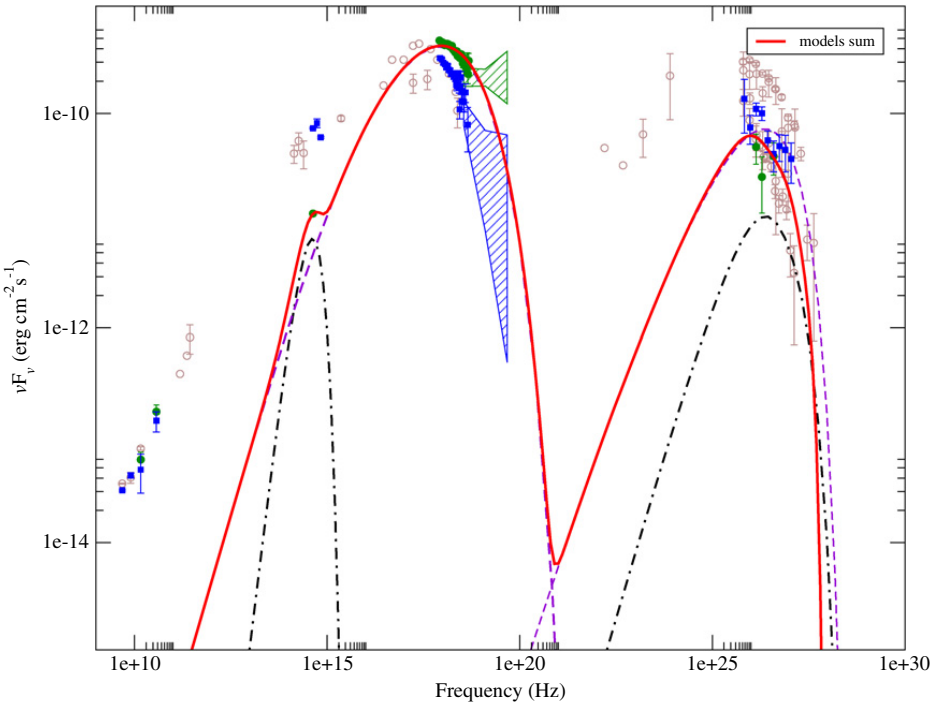

Figure 2.12: Spectral energy distribution of the High BL Lac object Markarian 421 (Horan *et al,* 2008).

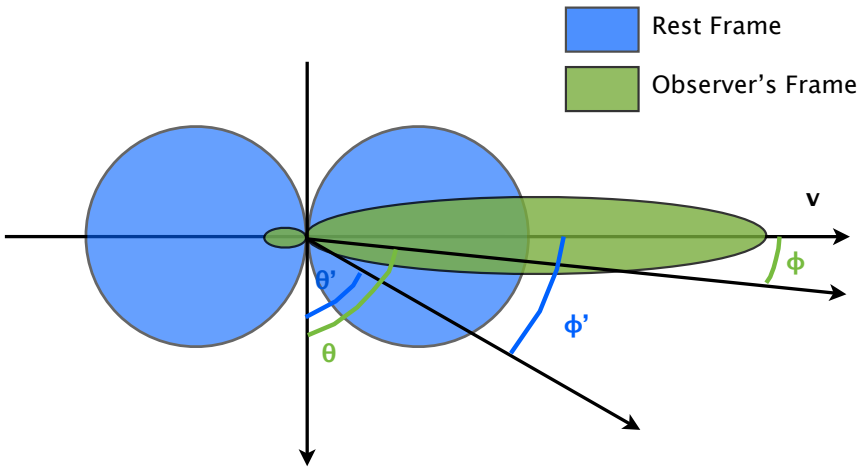

Figure 2.13: Beaming geometry for a relativistic electron emitting synchrotron radiation in the rest frame of reference of the particle (in blue). An electron moving in a magnetic field emits onto two lobes where θ' is the angle between the emission direction and the acceleration vector in the rest frame. In the observer's frame (in green), the radiation is focused into an angle $2\phi \approx 2/\Gamma$, where $\Gamma = 1/\sqrt{1 - v^2/c^2}$ and v is the speed of the accelerated particles.

radiation in the reference frame of the particle, an electron moving in a magnetic field emits into two lobes. (Figure 2.13). In the particle comoving reference frame, it is fairly realistic to assume that the angle $\phi' = \pm\pi/4$ is the angle at which the radiation intensity decreases to half its maximum value. The corresponding angle, ϕ, in the observer frame of reference is given by

$$|sin\phi| \approx |\phi| \approx 1/\Gamma \tag{2.33}$$

where $\Gamma = 1/\sqrt{1 - v^2/c^2}$ and v is the speed of the particle (see Figure 2.13). The radiation emitted within $-\pi/4 < \phi' < \pi/4$ is focused on the electron direction of motion within an angle $-1/\Gamma < \phi < 1/\Gamma$, which corresponds to a narrow emission cone in the forward direction and which is perpendicular to the acceleration provided

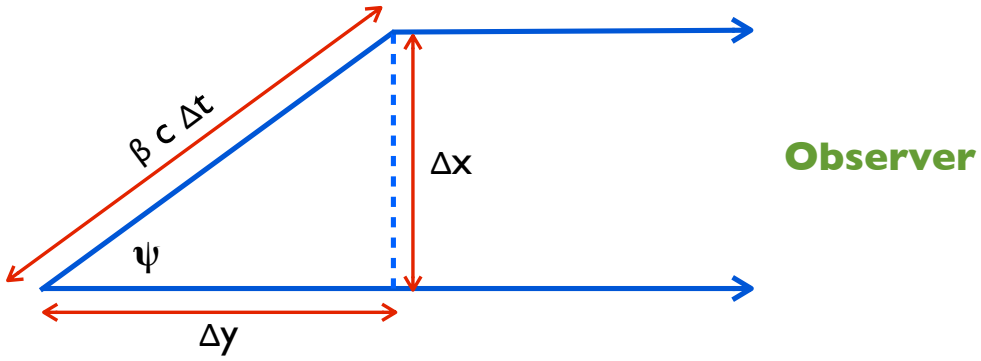

Figure 2.14: Geometry of the apparent velocity contribution in the line of sight of the observer.

by the magnetic field. Relativistic power enhancement occurs in the direction of motion by a factor Γ^2. This effect is associated with relativistic aberration, that provokes an enhancement of observed flux between the particle's reference frame and the observer's frame. Thereby, this increase of flux is observed every time the velocity vector of the electron is confined within $\phi = \pm 1/\Gamma$ of the observer's line of sight.

Also, the bulk of the hot plasma that constitutes the jet moves at the relativistic speed $\beta = v/c$ along the jet, with an angle ψ from the observer's line of sight (Figure 2.14).

The observed velocity is

$$\beta_{app} = \frac{\Delta x}{c\ \Delta t_{obs}} \tag{2.34}$$

where $\Delta x = \beta\, c\ \Delta t\, sin\psi$. Δx is the transverse distance traveled by the bulk of the hot plasma in a time Δt. Δt_{obs} is shorter than Δt, with $\Delta t_{obs} = \Delta t - \Delta y/c = \Delta t(1 - \beta\, cos\psi)$. Thus,

$$\beta_{app} = \frac{\beta\ sin\psi}{1 - \beta\ cos\psi} \tag{2.35}$$

For $\beta > 1/\sqrt{2}$, certain values of ψ will yield β_{app} greater than the unity, giving the appearance of superluminal motion.

Then, in the reference frame of the source, which moves at relativistic speed, we have

$$\Delta t' = \frac{\Delta t}{\Gamma} = \frac{\Delta t_{obs}}{\Gamma(1 - \beta cos\,\psi)} = \delta \Delta t_{obs}. \tag{2.36}$$

where δ is the Doppler factor. This yields

$$L_{app} = \delta^n L' \tag{2.37}$$

where L' is the true luminosity and n depends on the model of the jet: *e.g.* $n = 2+\alpha$, where α depends on the adopted blazar jet modeling (Urry & Padovani, 1995).

A final distortion effect is called "relativistic aberration" and affects angular measurements. Angles are dependent on the relative motion of the observer and the radiation is distorted into a cone along the source trajectory. The correction for such angles is proportional to δ^2, as follows

$$d\Omega' = \delta^2 d\Omega_{app}. \tag{2.38}$$

where $d\Omega'$ is the differential solid angle in the source's frame.

2.6 γ-ray Production Mechanisms in blazars

Production mechanisms that explain blazar spectral behaviors are still a matter of debate. Many production mechanisms have been introduced to explain particle injection and acceleration in the jets. There are two main types of model: leptonic models and hadronic models.

- **Synchrotron Self-Compton (SSC) and External Compton (EC)**

  In SSC leptonic models, the lower-energy peak in the spectral energy distribution is produced by the synchrotron emission of electrons. Its high-energy peak is due to the Comptonization (up-scattering) of the photon population. The photon population can either arise from synchrotron photons (SSC), or from photons from a source external to the jet, such as the accretion disk or the broad line region clouds (Dermer and Schlickeiser, 2002, for the EC model).

  The simplest form of an SSC model is a one-zone model (Sikora & Madejski, 2001), which assumes that, at any time, a single shock powers the emission along the jet, accelerating electrons/positrons which emit synchrotron radiation. In the SSC model, the synchrotron radiation and the Compton scattering are assumed to occur in the same region.

  The size of the region where the recorded radiation was originally emitted is given by

  $$R \leq \frac{\delta}{1+z}\, c\, t_{var} \tag{2.39}$$

  where t_{var} is the variability time, z is the redshift, R is the region radius and c is the speed of light. The Doppler factor, δ, is present in the formula because the observed time intervals are shorter than time intervals in the rest frame of the source.

  The electrons in a plasma emitting synchrotron radiation are expected to cool with a timescale determined by the energy of the electrons, which is inversely proportional to the rate at which their energy is radiated. The cooling time,

t'_{cool}, is, thus, related to the variability time of the source by

$$t'_{cool} \leq \delta \; t_{var} \; . \tag{2.40}$$

In addition to the SSC emissions, there are also IC processes (Krawczynski *et al.*, 2004) to account for. Most likely, both emission processes occur at the same time with different strengths and it is difficult to determine which one is the dominant process. The frequencies at which the synchrotron and IC peaks occur in the spectral energy distribution are

$$\nu_{\rm SYN} \sim \frac{4}{3} \cdot \frac{\delta \; n_L E_b^2}{(1+z)} \; , \qquad \nu_{\rm IC} \sim \frac{4}{3} E_b^2 \; \nu_{\rm SYN} \tag{2.41}$$

respectively, where $n_L = 2.8 \times 10^6 \, B$ Hz is the Larmor frequency and E_b is the synchrotron peak energy (or "break" energy) in units of mc^2 (Tavecchio *et al.*, 1998).

- **Hadronic**

  In the hadronic models, a highly relativistic outflow explains the continuum emission, producing hadronic interactions with ambient matter (Błażejowski *et al.*, 2005). The blazar's jets accelerate protons, which produce pions by interacting with matter and ambient photons.

  In hadronic models, an increase of neutrino emission is expected during VHE γ-ray flares. The detection and a possible correlation between VHE γ-rays and neutrinos would provide strong evidence for hadronic emission processes. However, it is difficult to explain the correlation between X-/γ-ray and VHE

γ-ray emissions observed from high frequency BL Lacs, *e.g.* Markarian 421 and Markarian 501, without reference to leptonic particle acceleration processes (Fossati *et al.*, 2008).

2.7 Markarian 421

At VHE, about 40 BL Lacs have been detected. The closest one is Markarian 421 with $z = 0.031$. Its closeness offers a unique opportunity and makes it one of the most observed TeV objects. Markarian 421 is located at RA $11h\ 04m\ 26s$ and Dec $+38^{\circ}$ $12'$ 47" (J2000 coordinates), and it is the brightest BL Lac object at TeV energies and in the UV sky (Maraschi *et al.*, 1999). It was the first source of extragalactic TeV γ-rays discovered when it was detected by the Whipple 10 m telescope in 1992 (Punch *et al.*, 1992) at a 6σ confidence level with $\sim 30\%$ of the Crab Nebula flux.

As a BL Lac object, Markarian 421 is a strong radio source characterized by the lack of sharp spectroscopic absorption lines in the infrared, optical and ultraviolet parts of the spectrum. This indicates that the source of its light is not starlight and it shows evidence of the presence of a very hot gas (Kino & Takahara, 2008). Markarian 421 has a continuum emission that can be adequately fitted by a simple power law. It is, therefore, clear that abundant "invisible" plasma content is present in the blazar jets (Kino & Takahara, 2008).

The spectrum of Markarian 421 has two broadband components (Sambruna *et al.*, 1996): the first extends from radio bands to soft X-rays, while the second extends up to TeV energies (see Figure 2.15).

Both SSC and EC models are widely used to explain the Markarian 421 spectrum.

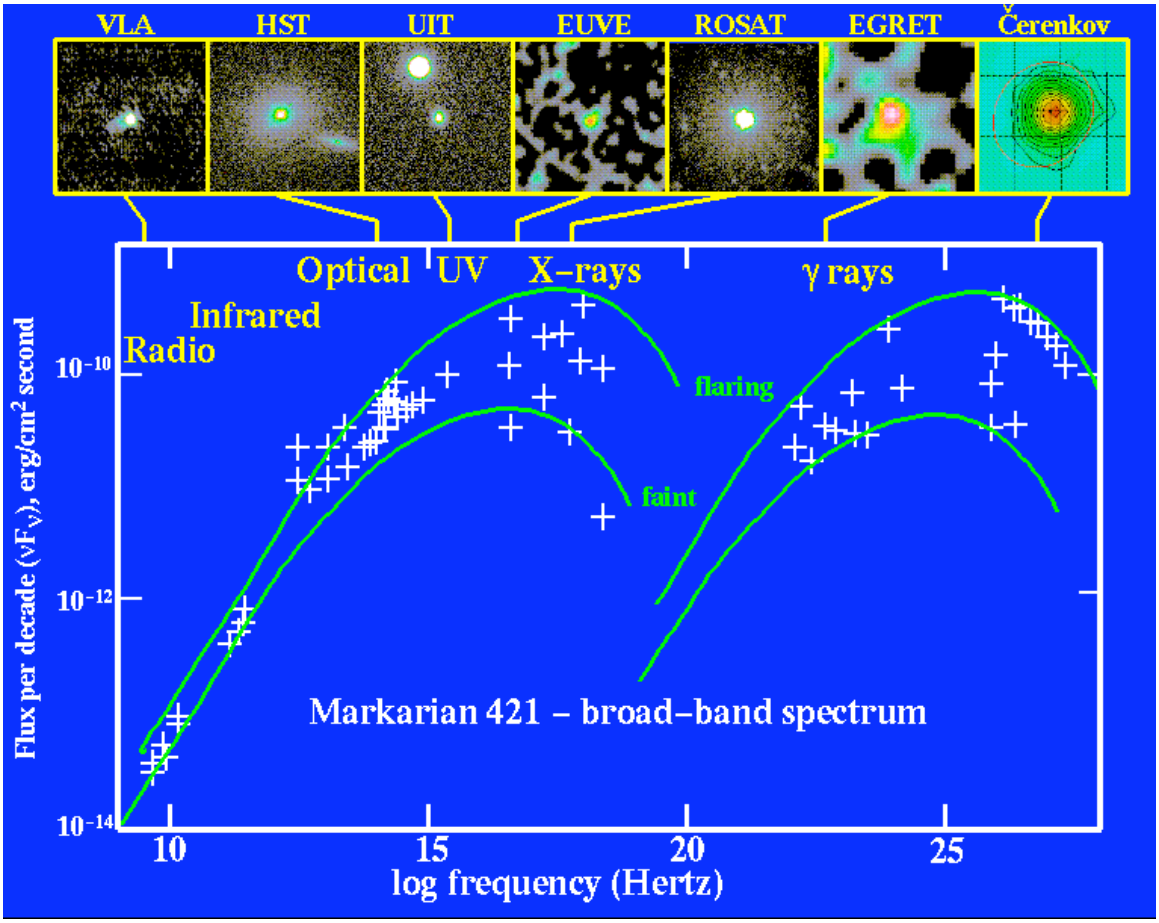

Figure 2.15: Multiwavelength spectral energy distribution of Markarian 421. Markarian 421 is one of the few objects that have been measured across a very wide wavelength range (from http://www.astr.ua.edu/keel/agn/mkn421.html).

At present, both the synchrotron-proton scenario − similarly to the one in the pion-photon production (Mücke *et al.*, 2003) − and the hybrid lepton-hadron emission model are partially favored. In fact, the two models would require only a moderate value of the diffuse photon field density in order to obtain to obtain a significant production of γ-rays in acceleration processes.

In the leptonic scenario, although the X-ray and TeV γ-ray fluxes should be correlated, it is not clear how well the correlation would hold for individual flares (Krawczynski *et al.*, 2004). Furthermore, separated X-ray and TeV flares have been observed (Rebillot *et al.*, 2006), and none of the proposed explanations seems to be conclusive.

Modeling of Markarian 421 data with SSC models revealed the first evidence for bulk jet Lorentz factors in the order of 50 (Krawczynski *et al.*, 2001) even though more recent works for other BL Lac objects provide larger values (Abdo *et al.*, 2011). Modeling of data shows that two-zone SSC models are more suitable than one-zone models for the description of spectral energy distribution behavior (Yang *et al.*, 2009), since the latter appear inadequate to accurately describe the observations (Błażejowski *et al.*, 2005).

The study of Markarian 421 plays a crucial role in the understanding of the AGN emission processes. Markarian 421 shows high variability in emission over timescales ranging from a few minutes to months (Acciari *et al.*, 2011) from radio to γ-ray wavelengths. The high variability of the emission indicates that the region of bright gas where the VHE radiation originates is small. In addition, the gas present in that region moves at very high speeds towards the Earth accelerated or decelerated

within the blazar jet (Levinson & Bromberg, 2007). The strong VHE radiation should originate at the centre of relativistic jet pointing at small angles from the observer line of sight (Nilsson *et al.*, 2007).

Some Markarian 421 emission processes might be further investigated by correlating the UV and TeV emission behaviors. Boettcher & Dermer (1995) have theoretically studied the case of the production of a $\gamma - \gamma$ absorption feature in the emission spectrum. This effect would produce an anti-correlation between the UV flux (increasing) and the TeV flux (lowering). More generally, in a traditional leptonic/SSC scenario, the existence of a UV versus TeV correlated emission could be caused by UV/X-ray synchrotron emissions leading and preceding emissions at higher energies such as TeV γ-ray emission (Chiaberge & Ghisellini, 1997).

There is strong evidence suggesting that X-ray and VHE TeV γ-ray activities are correlated when averaged over $\sim$ 1 week time intervals (Błażejowski *et al.*, 2005; Horan *et al.*, 2009). Furthermore, Horan *et al.* (2009) show a quadratic correlation trend between X-ray and γ-ray emission. However, a leptonic SSC model of the emission from the jet cannot completely explain such a correlation trend. To overcome these discrepancies, Katarzyński *et al.* (2001) have proposed some possible explanations. The most interesting of them assumes that the activity varies proportionally to the Doppler factor of an emitting source moving inside the jet that points in the observer's direction. This explanation would account for the observed rapid variability, which could be linked to jet instabilities (Fossati *et al.*, 2008).

Since 1988, a multiwavelength study between X-ray and UV bands has been carried out with the EXOSAT and IUE satellites (George *et al.*, 1988). More recently,

Tramacere *et al.* (2009) show that UV to X-ray emission from Markarian 421 may come from a population of electrons that is not referable to a simple power law. In Fossati *et al.* (2008), infrared and optical monitoring were performed using the Harvard-Smithsonian 48" telescope on Mt. Hopkins. No correlation was observed between γ-ray and optical data. Another attempt to investigate multiwavelength spectral characteristics was made in the work of Donnarumma *et al.* (2009). This paper work included a very wide set of measurements from optical to TeV energies performed during the enhanced Markarian 421 activity in the first half of June, 2008. Moreover, it did not provide any time-domain analysis between infrared/optical/ultraviolet emission with X-ray/γ-ray emission.

Chapter 3

Optical and Ultraviolet Data Analysis

A short and general introduction to the Ultra-Violet Optical Telescope (UVOT) hardware follows below. Then, we introduce a description of the standard Poole *et al.* (2008) UVOT data reduction pipeline and the results obtained processing the observations of Markarian 421 recorded during 2007-2008 monitoring season.

A subset of the custom optical and ultraviolet reduction pipeline and results will also be presented (Navajo, version 2.4.3, November 2009). Navajo (v2.4.3) adopts very conservative estimates for uncertainties. Our estimates are completely in agreement with those provided in a more recent and comprehensive study Breeveld *et al.* (2010).

3.1 Swift Satellite Mission

The Swift observatory (Gehrels *et al.*, 2004) is the first multiwavelength spacecraft observatory able to automatically re-orient itself (Figure 3.1). It was launched into a Low-Earth Orbit in November 2004 at 600 km above sea level with an orbital period

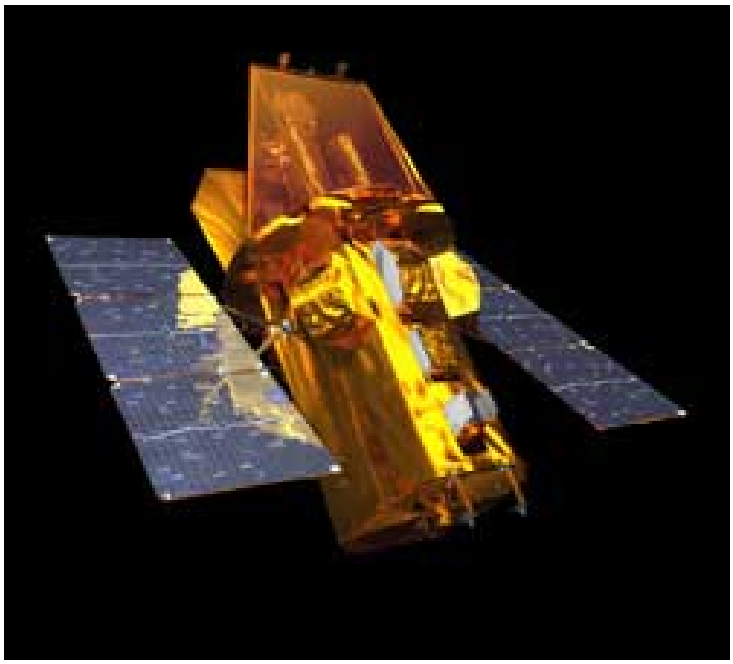

Figure 3.1: Swift Spacecraft (from the HEAsarc website).

of $\sim$90 minutes and an inclination of 22° (Table 3.1). Swift is controlled by the NASA Goddard Space Flight Center (Gehrels *et al.*, 2004), but the spacecraft is able to re-orient itself in autonomous slew mode in about $20 - 75$ seconds.
Although the primary aim of Swift satellite mission is to detect Gamma-Ray Bursts (GRBs), one of the secondary goals is to complete a first catalogue of known and unknown Active Galactic Nuclei (AGN) in our Local Universe. Over a nine-month period, Swift scanned the entire sky several times, finding more than 200 AGN.

The three observing instruments on board are:

- Burst Alert Telescope (BAT)

  BAT observes a large fraction of the sky (3 steradian) at any one time in the $15 - 150$ keV energy range. It can locate the position of incoming photons with an accuracy of 1 to 4 arcmin within 15 s.

Swift Spacecraft	
Organization	NASA
Launched	20 November 2004
Deorbited	no sooner than 2020
Mass	1500 Kg
Orbit height	600 Km
Orbit period	$\sim$ 90 min
Telescope style	coded mask (BAT),
	Wolter I (XRT),
	Ritchey-Chretien (UVOT)
Wavelength	γ-ray/X-ray/UV&Optical
Diameter	30 cm (UVOT)
Collecting area	5200 cm^2 (BAT)
Focal length	381 cm (UVOT)
Sensitivity	$B = 22.3$ mag (white light) in 1000 s (UVOT)
Pixel Scale	0.502 arcsec (UVOT)
Brightness Limit	$v = 7.4$ mag (UVOT)
Camera Speed	$\sim$ 11 ms (UVOT)

Table 3.1: Characteristics of the Swift spacecraft (Gehrels *et al.*, 2004).

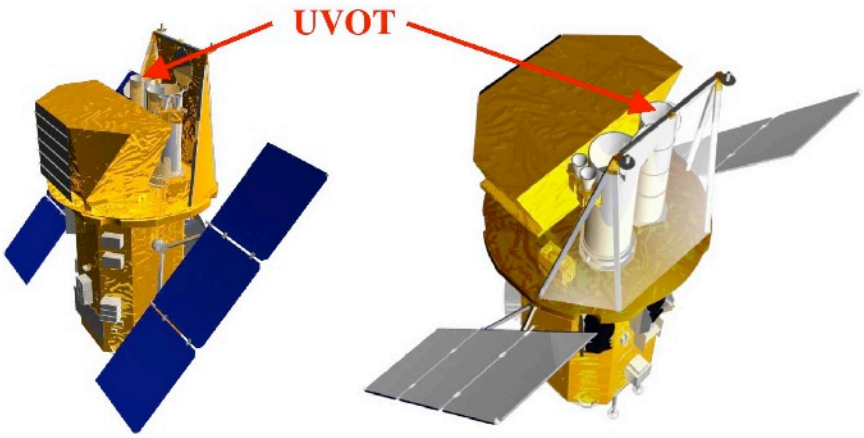

Figure 3.2: UVOT location on the Swift orbiting observatory (Roming *et al.*, 2005).

- X-Ray Telescope (XRT)

  XRT can be used to perform long-term monitoring (days and weeks) within the $0.2 - 10$ keV energy band. The data collected by XRT can also be used to provide a more precise location of X-ray sources and/or to obtain further multiwavelength information in order to constrain their redshifts. XRT is able to resolve sources within error circle locations of approximately 3.5 arcmin of radius.

- UltraViolet Optical Telescope (UVOT)

  UVOT (Gehrels *et al.*, 2004) provides simultaneous ultraviolet (UV) and optical coverage ($1700-6500$ Å, or $0.64-2.26$ eV) within a 17 arcsec $\times$ 17 arcsec field of view. The sensitivity of the UVOT telescope per filter is listed in Table 3.2. For a counting detector, the sensitivity equals the smallest number of photons that that detector can clearly measure. This corresponds to the minimum brightness of an astronomical object that the telescope can detect.

UVOT sensitivity		
Band	Filter	counts
Opt	v	143
	b	441
	u	217
UV	UVW1	199
	UVM2	53
	UVW2	87
Pan	white	1306

Table 3.2: UVOT sensitivity values estimated by simulating a star emission presenting a Vega-like spectrum with $v = 20$ mag.

Since it is sited above the atmosphere, which is opaque to ultraviolet light, UVOT provides significant contributions to multiwavelength studies. UVOT has photon-counting detectors that are capable of retrieving timing and the incoming direction of individual detected photons.

UVOT is a 30 cm Ritchey-Chrètien reflector that can detect objects of magnitude 24 in a 17-minute exposure. It is mounted on a telescope platform common to all instruments on the satellite. The UVOT team gained expertise in the instrument's design, testing, and performance while developing the Optical Monitor telescope (Kuin and Rosen, 2008) for the European Space Agency's X-ray Multi-Mirror Mission. Similar to the Optical Monitor telescope, the UVOT on-board telescope has two micro-channel plate intensified CCD detectors (Kawakami *et al.*, 1994; Roming *et al.*, 2005), although UVOT has an upgraded on-board preprocessing machine (Fordham *et al.*, 1992).

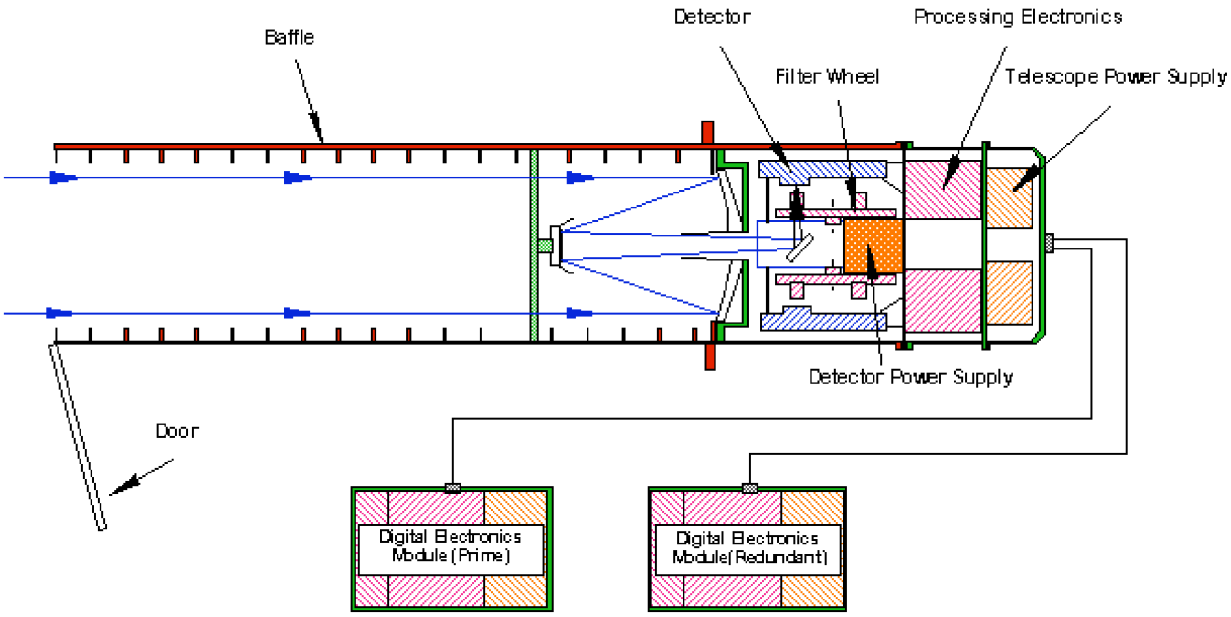

Figure 3.3: UVOT telescope hardware (Roming *et al.*, 2005).

UVOT is capable of detecting very low signal levels, unaffected by CCD read-out noise and cosmic ray events (Michel *et al.*, 1997). UVOT contains three optical and three ultraviolet filters (Table 3.3), a white-band filter, a magnifier and two low-resolution optical and ultraviolet graded-index prisms (Roming *et al.*, 2005, 2003). The UVOT telescope is able to record in three data modes. The first is the 'Image' mode that is largely adopted during monitoring; it adds the start and the stop times to the standard 2D sky map and discards the timing information on the individual detected photons, since they are directly summed on board the satellite. In the 'Event' mode, position and photon timing are recorded. The 'Image & Event' data mode records both information sets.

Swift/UVOT Filter Characteristics

Band	Filter	Central Wavelength Å	FWHM Å
Opt	v	5468	769
	b	4392	975
	u	3465	785
UV	UVW1	2600	693
	UVM2	2246	498
	UVW2	1928	657

Table 3.3: UVOT filter characteristics (Poole *et al.*, 2008). The central wavelength is the midpoint between the wavelengths at half maximum (FWHM).

3.2 Standard UVOT Data Reduction

There are three "data" levels that indicate the stage of the data-reduction process (Poole *et al.*, 2008). Level I is the "raw" data level. An analysis should start from Level I (or raw downloaded data) if there have been improvements in the calibration database since the original processing. Level II data are used in order to pursue photometrical computations analyzing UVOT images stored in sky coordinates (RA and Dec in J2000) together with the exposure map. As a result of the amplifying process, each incoming photon detected by the UVOT telescope is transformed into a splash of photons that hit the CCD detector over 3×3 pixels. A dedicated algorithm fits the spatial distribution of the re-emitted photons, determining its centre. This amplifying process produces a side effect called 8×8 pixel gain-variation pattern (Figure 3.4),

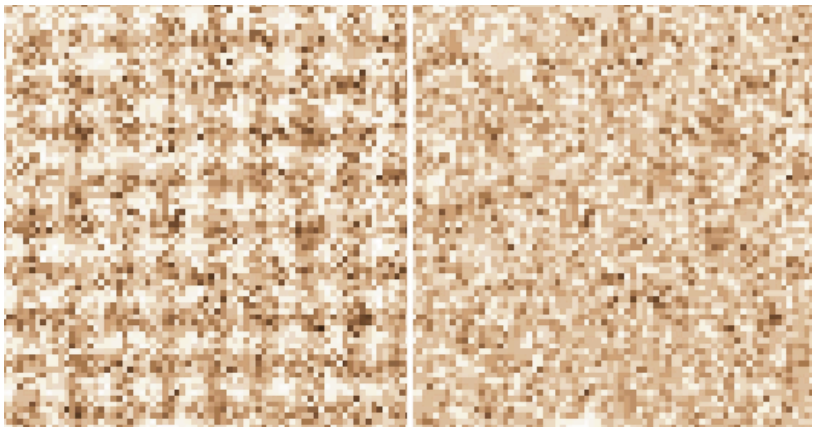

Figure 3.4: A portion of many images combined before and after modulo-8 pattern noise correction - left and right pictures, respectively (from the UVOT Software Manual at http://swift.gsfc.nasa.gov/docs/heasarc/caldb/swift/docs/uvot/index.html).

known as mod-8 noise. This is largely removed in Level II data. Photometry can be applied directly to the Level II dataset. Finally, Level III data provide preliminary photometrical estimates (that can be extracted and plotted).

3.2.1 Coincidence-Loss Correction

UVOT suffers from coincidence loss at high photon rates since UVOT is a photon-counting detector. Coincidence loss happens when two or more photons are detected from the same group of camera pixels within the same CCD read-out interval (Fordham *et al.*, 2000). The actual value of the coincidence correction depends on the detected count rate arising from the source and the background regions. Source and background regions are selected spatial regions whose photons are included in the photometric computation.

With a read-out time of $\sim$11 ms, the CCD camera begins to experience significant coincidence losses (Poole *et al.*, 2008) when the rate exceeds 10 count/s (corresponding

to 20.39 mag in the v optical band). The present coincidence-loss correction technique has not been tested for very high count rates above $\sim$ 90 count/s. Above such a threshold, the coincidence-loss correction becomes more uncertain.

The standard reduction pipeline is performed by running the UVOTSOURCE tool that is part of the HEAsoft software[1]. The UVOTSOURCE tool carries out a basic coincidence-loss compensation approach by introducing an empirical polynomial correction accounting for the differences between the observed and the theoretical count rates (Poole *et al.*, 2008). The theoretical corrected count rate for a point-like source is:

$$C_{theory} = \frac{-ln(1 - \alpha\, f_t\, C_{raw})}{\alpha\, f_t} \tag{3.1}$$

where C_{raw} is the observed count rate computed using the dead-time corrected time, f_t is the frame time and α is the dead-time correction factor. This correction assumes if photometry is computed for a fixed $\simeq$5 arcsec aperture. Assuming an homogeneous spread of the photon losses, Poole *et al.* (2008) introduce a polynomial correction to account for the full coincidence-loss correction (Figure 3.5).

In the case of a point-like source,

$$f(x) = 1 + a_1 \times x + a_2 \times x^2 + a_3 \times x^3 + a_4 \times x^4$$

with $a_1 = 0.066$, $a_2 = -0.091$, $a_3 = 0.029$ and $a_4 = 0.031$, where $x = f_t\, C_{raw}$ and $C_{corr} = f(x) \cdot C_{theory}$ is the full coincidence-corrected count rate (C_{corr} and C_{theory} are both in counts per second). The polynomial coefficients were determined by a

[1]The HEAsoft code is downloadable from the HEASARC website (http://heasarc.gsfc.nasa.gov/docs/software.html). It provides the tools to reduce and interpret astronomical data from different satellite missions. HEAsoft is written in an ensemble of different programming languages (Perl, C, Bourne Shell Scripting, *etc*). The Swift/UVOT code is part of the HEAsoft tools and is developed by the Swift Team.

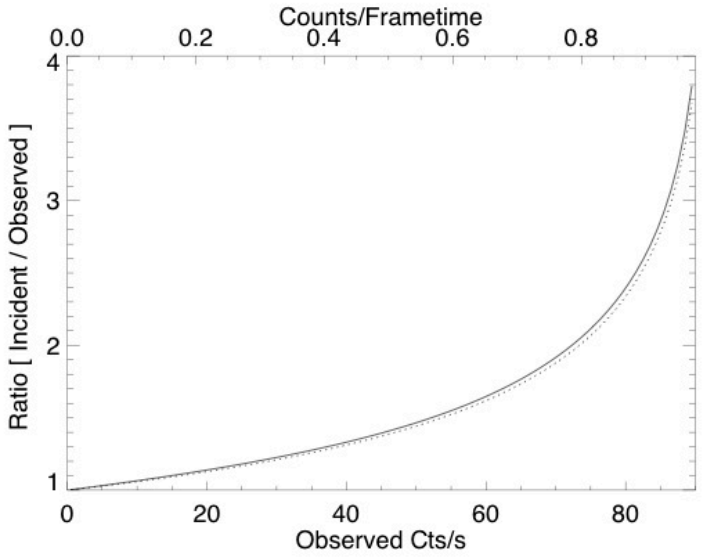

Figure 3.5: The dotted line shows the theoretical relation, while the solid line includes the "full" empirical polynomial adjustment to the theoretical relation (Poole *et al.*, 2008).

least-squares fit using the stars in the open cluster NGC 188 (Stetson *et al.*, 2004). The standard error of the incident count rate, is given by:

$$\sigma_{theory} = -\frac{1}{\alpha\, f_t}\; ln\left(1 \pm \frac{f_t\, \sigma_{raw}}{1 - f_t\, C_{raw}}\right) \tag{3.2}$$

where the standard error of the observed count rate is $\sigma_{raw} = [C_{raw}(1 - f_t\, C_{raw})]^{1/2}$ (Kuin and Rosen, 2008).

3.2.2 Position-Dependent Sensitivity

The variation in the sensitivity of the detector across the field of view has been investigated. In the literature, this effect is called large-scale sensitivity (LSS). The variation in LSS is measured in raw coordinates, or detector coordinates (Poole *et al.*, 2008). The UVOT development team has carried out a comprehensive study of the large scale sensitivity effect, producing 7 precise correction maps. (Figure 3.6).

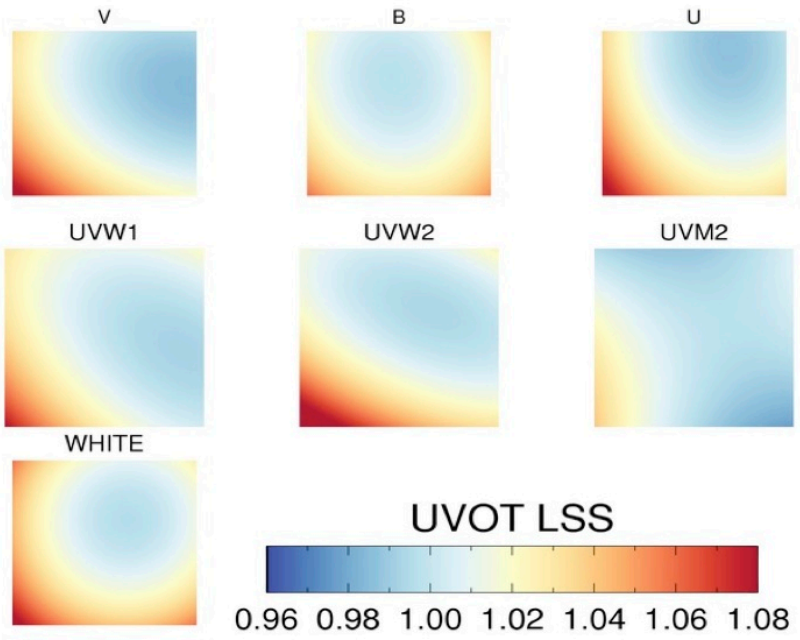

Figure 3.6: The large-scale sensitivity (LSS) maps released by the Swift Development Team of the seven optical and ultraviolet image filters (from http://swift.gsfc.nasa.gov/docs/heasarc/caldb/swift/docs/uvot/index.html).

3.2.3 Results of the Observational Programme

From September 2007 to the end of January 2008, the Swift/UVOT telescope was shut down. Between the beginning of February 2008 and June 2008, Swift/UVOT recorded more than a hundred observations of Markarian 421 spread over 37 separate days. This dataset contains the high-activity intervals detected in May and June 2008 from Markarian 421 (see Appendix A for a detailed list of observations) that have been recorded by many ground-based instruments and orbiting space telescopes. The high-activity state of Markarian 421 in May 2008 was also detected by VERITAS.

The UVOT instrument cycled through each of its three ultraviolet passbands (UVW1, UVM2 and UVW2, with central wavelengths of 2600 Å, 2246 Å and 1928 Å,

respectively). The total exposure time was circa 15 hours. A typical exposure duration (per filter) was circa 150 s per exposure, although it ranged between 50 s and 900 s. The data were recorded in Image mode, where the image was accumulated on board the Swift satellite while discarding the photon timing information within each single exposure in order to reduce the telemetry volume and the duration of transmission. The CCD spatial pixel size of the detector is approximately 0.5 arcsec $\times$ 0.5 arcsec that, generally, is binned in a 2×2 grid of adjacent pixels, giving an effective pixel size close to 1 arcsec $\times$ 1 arcsec.

We ran UVOTSOURCE using the following standard settings (see Table 3.4):

```
uvotsource "image=$Immagine" "outfile=outfile_$Immagine" \
"srcreg=$source_region" "bkgreg=$bkg_region" "sigma=3"
"apercorr=NONE" "lssfile=$lssfile_caldb" "zerofile=$zerofile_caldb" \
"coinfile=$coinfile_caldb" "psffile=$psffile_caldb" \
"syserr=YES" "frametime=$frametimesetting" "clobber=yes" "output=ALL"
```

We provided UVOTSOURCE with the Markarian 421 nominal position (RA: 166.11375° and Dec: 38.208889°) and adopted the photometric 5 arcsec aperture radius (Poole *et al.*, 2008). The background annulus region was also centered on the nominal source position with inner and outer radii of 20 and 30 arcsec, respectively. No quality checks are performed in selecting UVOT observations. UVOTSOURCE does not discard observations that show a large misalignment between the nominal and actual position of the source. UVOTSOURCE uses the calibration files from the standard calibration database released by the Swift/UVOT team.

UVOTSOURCE determines the total counts in a source region and then, using the

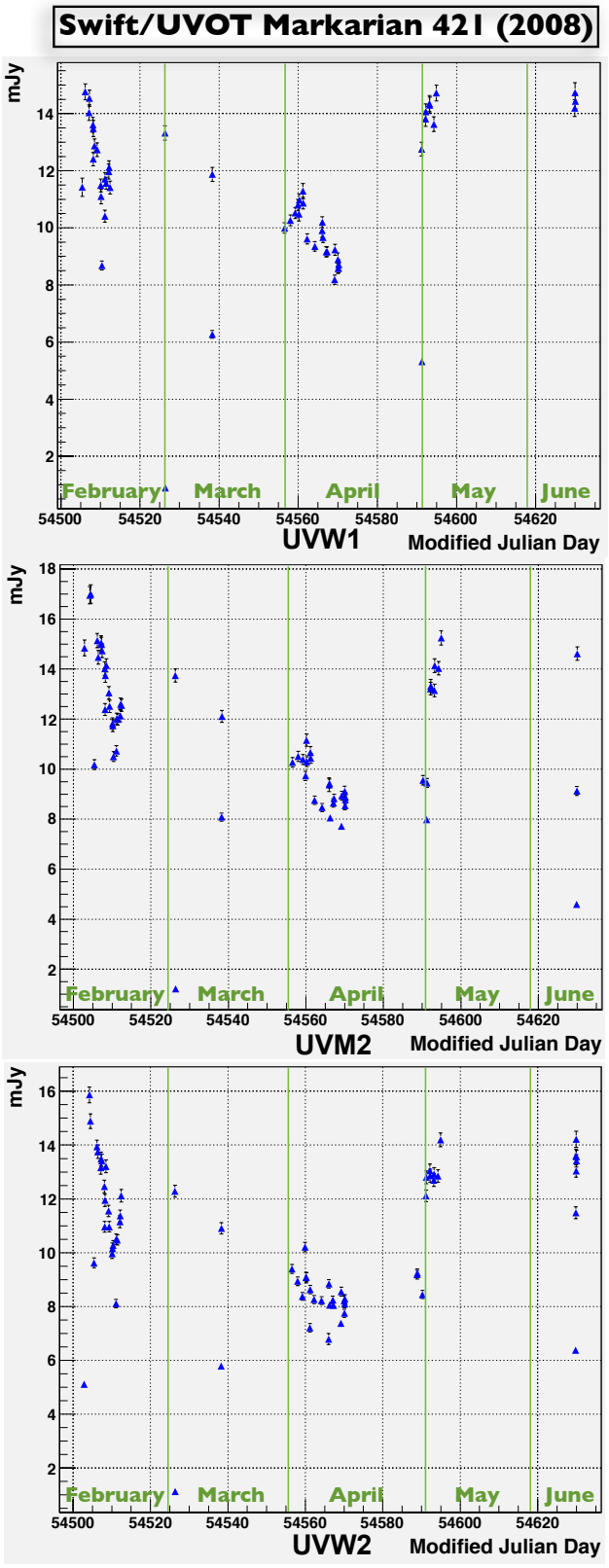

Figure 3.7: Standard analysis of the UVOT dataset. The plots show the lightcurves obtained using the three ultraviolet filters (UVW1, UVM2, UVW2).

UVOTSOURCE Parameters Setting	
image	Name of the UVOT SKY image (filename + extension).
outfile	Output FITS file to append results to.
srcreg	Name of an ASCII source region file.
bkgreg	Name of an ASCII background region file.
sigma	Level of detection significance over the mean background.
apercorr	Aperture correction calculation algorithm.
lssfile	Large-scale sensitivity correction file from the calibration database.
zerofile	Zero points file from the calibration database.
coinfile	Coincidence-loss correction file from the calibration database.
psffile	Point spread function file from the calibration data base.
syserr	Adds systematic errors in the photometric calibration.
frametime	The frame time, in seconds, for the exposure.
clobber	It controls whether to overwrite pre-existing output files.
output	Output sections: ALL indicates that all sections are to be output.

Table 3.4: Swift/UVOT manual settings description of the UVOTSOURCE parameters.

effective exposure time, calculates a source region count rate that includes superimposed background. A count rate is determined, similarly, for the background region. Then the background count rate is subtracted from the source-region count rate to obtain the source excess rate. Further details of the standard reduction pipeline are given in Poole *et al.* (2008).

Figure 3.7 shows the Markarian 421 lightcurves computed by the standard analysis. Due to their close frequency bands, the trends of the three ultraviolet bands (UVW1, UVM2, UVW2) are fairly similar. However, the computed lightcurve values seem to experience a sort of unnatural short-term fluctuation; therefore, we suspect

that some of the results might be not genuine. As a result, we have developed our own analysis pipeline, which incorporates more stringent quality checks.

3.3 Navajo Analysis

Since the purpose of the UVOT detector is to look at faint or very faint objects (Poole *et al.*, 2008), the official UVOT public software − which recently has been improved − provides very reliable results in a wide range of situations.

For some astronomical sources, the standard UVOT analysis pipeline requires further adjustments and finer settings. In our case, the Markarian 421 field of view has very bright sources. Therefore, UVOT records the incoming flux from these objects, which, unfortunately, causes also a wide range of superimposed noise (a noise mainly consisting of instrumental scattered light). Markarian 421 UVOT observations typically present different types of alterations, including saturations, inhomogeneous "smeared" scattered-light patterns, and random fluctuations.

As an improvement to the standard analysis, we have developed the Navajo data reduction pipeline. While still using the calibration database released from the Swift team, it provides a more reliable computation of UVOT photometry. Furthermore, Navajo automatically downloads datasets in the specified time interval. It compares the positions and magnitudes of objects in the field of view with those in specific catalogues (*e.g.* dwarf stars, TeVCat, USNOB1). It applies post photometric and cosmological corrections (*e.g.*, reddening, host galaxy spectral emission, redshift), and it produces a full automation of the reduction pipeline, which adopts dedicated sets of analysis parameters for different sources. Wherever possible, we have attempted

to extend the public reduction pipeline, or else we have investigated some secondary aspects (Li *et al.*, 2006) in order to locate a consistent subset of parameters that might increase the reliability of the results.

3.3.1 PSF Temperature Dependent Variation

During Swift's quasi circular low-Earth orbit, the PSF of UVOT changes slightly. In the final section of their work, Poole *et al.* (2008) suggests that the PSF may change along with spacecraft temperature variations. This may lead to a bias in the photometric computations, which should be affected even more by the adoption of small aperture radii (*e.g.* up to $2-3$ arcsec).

In each case, we have analyzed data from reference stars (*e.g.* WD1657+343) and we have carried out photometry using a 5 arcsec radius aperture, since this is the same aperture radius we have adopted for the Markarian 421 dataset analysis. Here we report only on a part of that study. Then, we tested the rates obtained with the recorded telemetry values of three different temperature sensors (identified as "TEMP" in the data files). The lack of information on the design of the satellite subsystems made it difficult to ascertain where the temperature sensors were located on the spacecraft. We assumed that such sensors are located in the internal workings of the satellite.

Adopting a 5 arcsec aperture, the analysis of the WD1657+343 dataset did not return any evidence of significant correlation. No cross-correlation is evident between ultraviolet band rates and temperature variation along the satellite orbit.

Furthermore, the Markarian 421 dataset used in this study only included data in

the UV bands. We conclude that, at most, the ultraviolet observations could be very weakly affected by temperature along the orbit of the Swift spacecraft when using a 5 arcsec radius aperture.

3.3.2 Quality Checks

UVOT is a photon-counting detector in which each image is obtained by appropriately summing detected photon events. In the UVOT image mode, the on-board software sums all of the events and discards the temporal information of the photons (Poole *et al.*, 2008). The procedure used attempts to automatically account for telescope slewing. Generally, this task is performed well, but the presence of external light contamination (coming from outside the source and background regions) makes it problematic, thereby returning incorrect data image observations (see Figure 3.8).

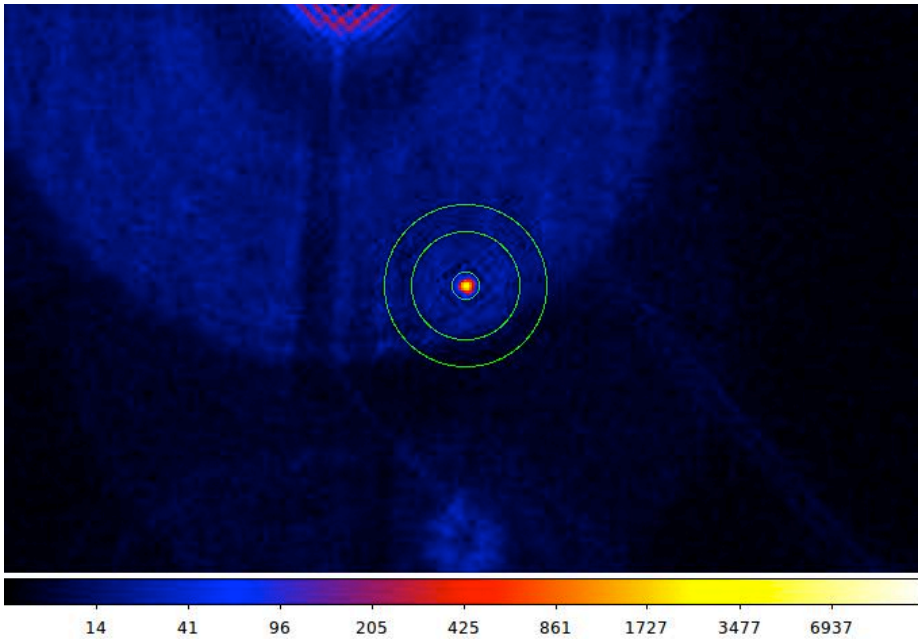

Figure 3.8: Example of FOV contamination in the case of Markarian 421.

We attempted to classify the main contributors to the image contamination. These are outlined as follows:

- Some images present evidence of smeared objects instead of point-like objects due to incorrect telescope pointing computation, associated with satellite slewing (Figure 3.9a), which the on-board software failed to account for.

- In addition to this, and as a result of the same slewing issue, some objects appear "doubled" (see Figure 3.9b).

- Moreover, it appears that in the presence of pixel saturation, the camera switches off a region of pixels resulting in squared added shadow patterns (see added patterns in Figure 3.9c).

Inspecting the images, we discard those images that display contamination on the observed object (*e.g.* in our case Markarian 421), allowing those that do not show any contamination to be analyzed. However, images that present moderate contaminations on the other bright objects in the field of view are accepted.

Generally, Navajo attempts to identify these problematical images. However, we have found it necessary to introduce an automatic procedure that inspects all the images. About 3% of the observations were discarded after inspecting the Markarian 421 2007-2008 dataset.

3.3.3 Misalignment Compensation

Basic astrometric corrections are applied to the UVOT Level II data by the standard pipeline. They consist of simple geometrical shifts and rotations applied to the

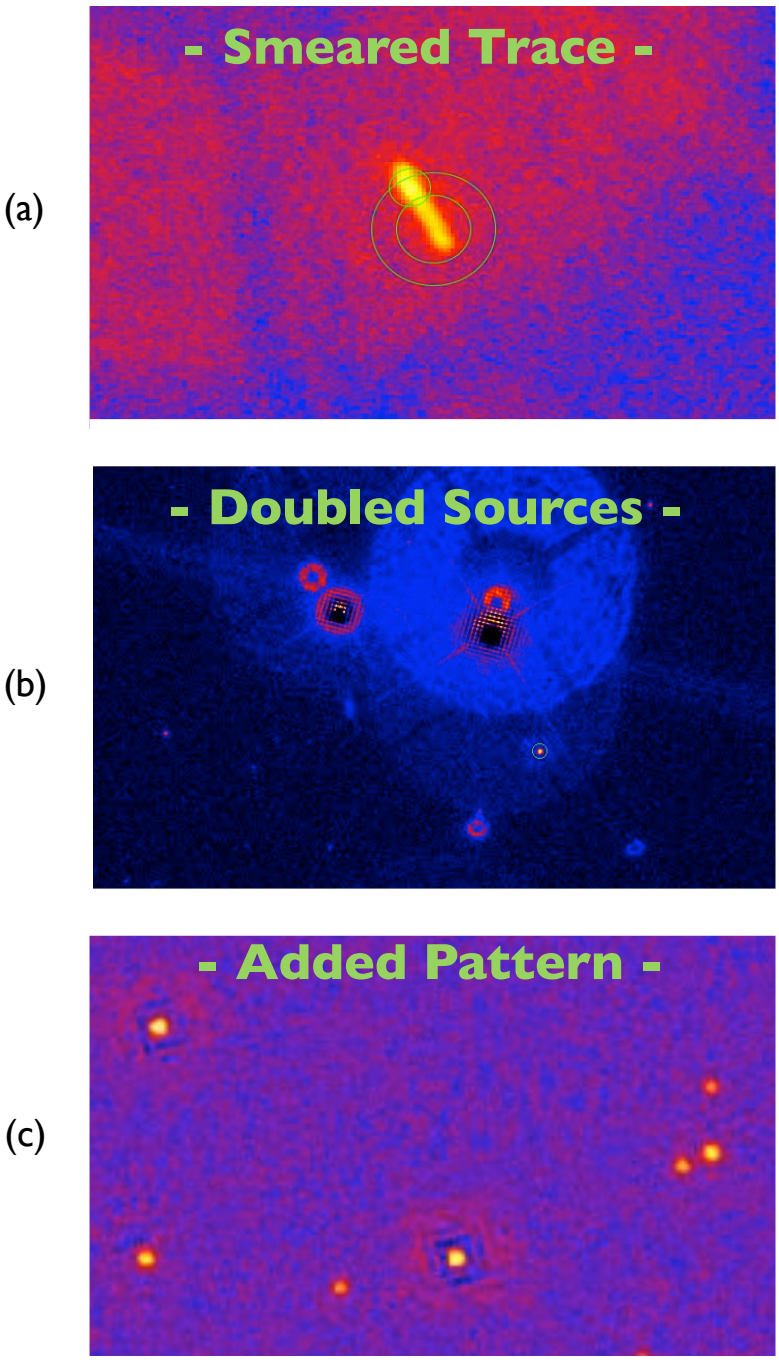

Figure 3.9: Examples of quality-check classification Markarian 421 dataset contaminated observations. (a) Some images present evidence of smeared objects, (b) others present objects that appear doubled. (c) In presence of bright stars, we obtain squared added shadow patterns.

raw data by some of the pipeline's routines. The evaluation of star displacements from known positions is done by a procedure that identifies astronomical objects and retrieves their relative displacements by "triangulating". The measurements obtained by triangulation of the relative positions of bright objects in the FOV are then compared with those stored in a given database (*e.g.* USNO type catalog). This comparison allows for precise astrometric correction of the objects in the UVOT field of view. Depending on the adopted algorithm minimization settings, the residual displacement between the position of a source and its nominal (or expected) position may be less than 1 arcsec (Poole *et al.*, 2008). When some bright sources are present in the UVOT field of view, the standard astrometric correction technique fails in triangulating the stars' positions and the misalignment between expected and actual source positions still remains significant (Figure 3.10). Failing of the astrometric correction is in part due to the presence of the added squared shadow patterns around bright stars in the FOV. A secondary cause could be the appearance of some artifact due to optics (see Figure 3.8).

We have adopted an improved approach to astrometric misalignment correction, consisting of a spatial fitting procedure. Assuming a geometric point-like source emission, in a relatively wide region close to the putative source position (*e.g.* generally 15 arcsec radius), we have searched for the maximum of the source of emitted radiation by fitting a Gaussian. In the presence of any high superimposed background noise, saturation and/or smearing, this approach returns more reliable results than the approach implemented using only the standard pipeline.

Here we compare the results obtained by the standard UVOT pipeline and the

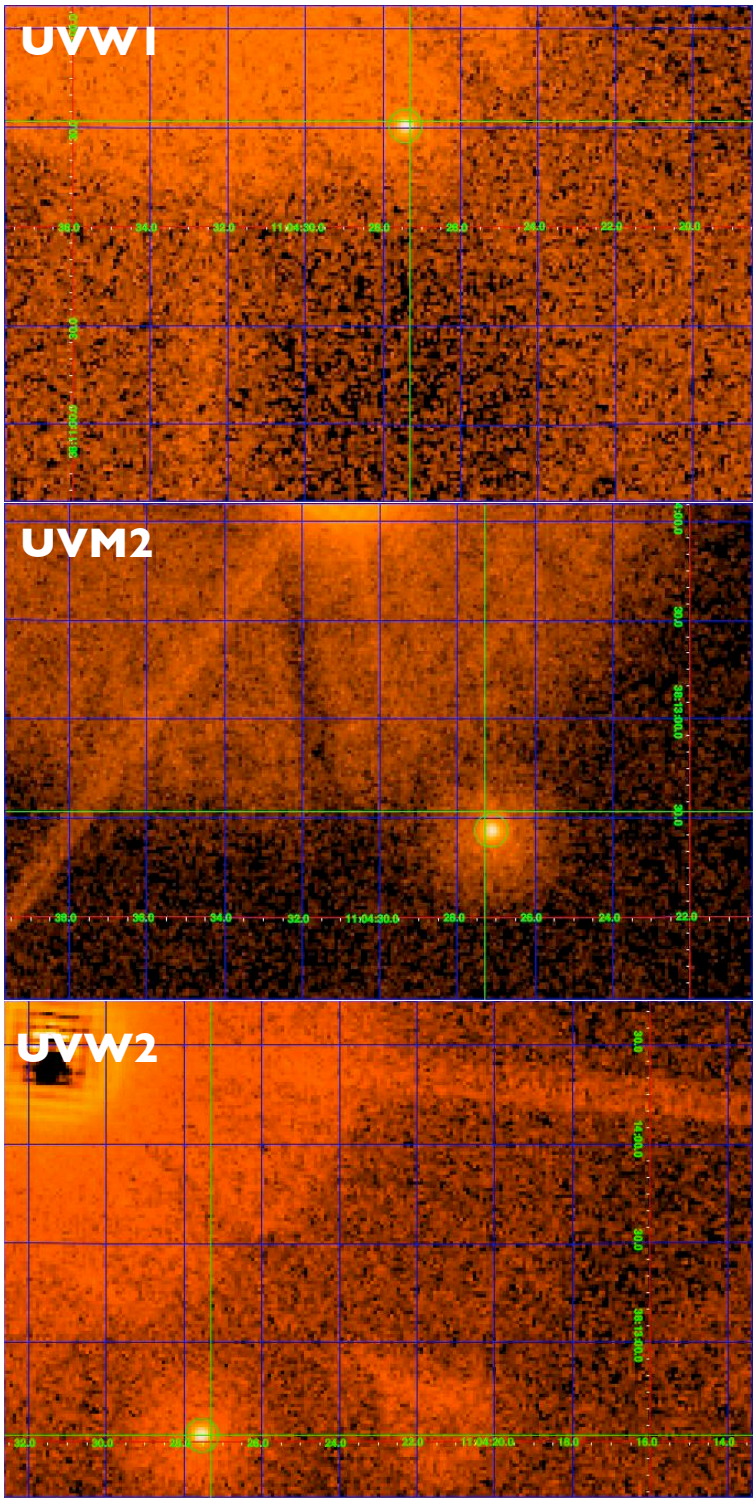

Figure 3.10: Three examples of pointing misalignment of UVW1, UVM2 and UVW2 filters. The green cross is the expected nominal source position and the green circle (5 arcsec radius) is the actual position.

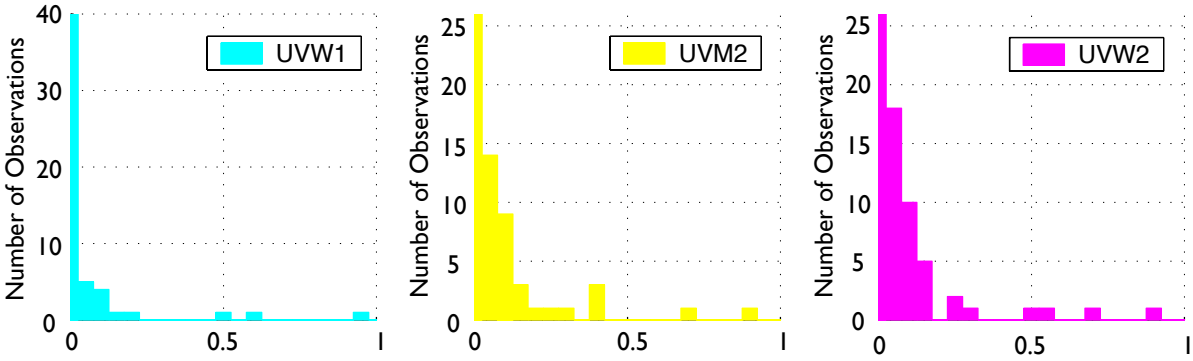

Figure 3.11: Histograms of the deviation factor between the flux returned by the Swift/UVOT public tool and the Navajo pipeline.

Navajo pipeline. First, we ran the Markarian 421 dataset analysis using the standard pipeline (UVOTSOURCE), followed by the Navajo pipeline which computes the corrected source and background region files. Figure 3.11 shows the deviation factor between the flux obtained with the public tool and the Navajo pipeline:

$$\frac{F_{\rm Navajo} - F_{\rm Standard}}{F_{\rm Navajo}} = 1 - \frac{F_{\rm Standard}}{F_{\rm Navajo}} \tag{3.3}$$

where $F_{\rm Navajo}$ and $F_{\rm Standard}$ are the fluxes computed by Navajo and the standard pipeline, respectively. Nearly 30% of the computed UVW1 rates show deviations of 0.10 or greater. In the case of UVM2 and UVW2, 30% of the observed rates experience deviations greater than 0.30. Therefore, the level of deviation observed in UVW1 is less than that seen in the other two bands.

At times, a very large misalignment existed between the expected and the actual position of Markarian 421. In our dataset, this misalignment strongly affected the count rate computation of more than 5% of the observations, of which $< 70\%$ of the incoming photons from the source region are properly accounted for (Figure 3.12). Thus, it is evident that the astrometric compensations introduced by Navajo help

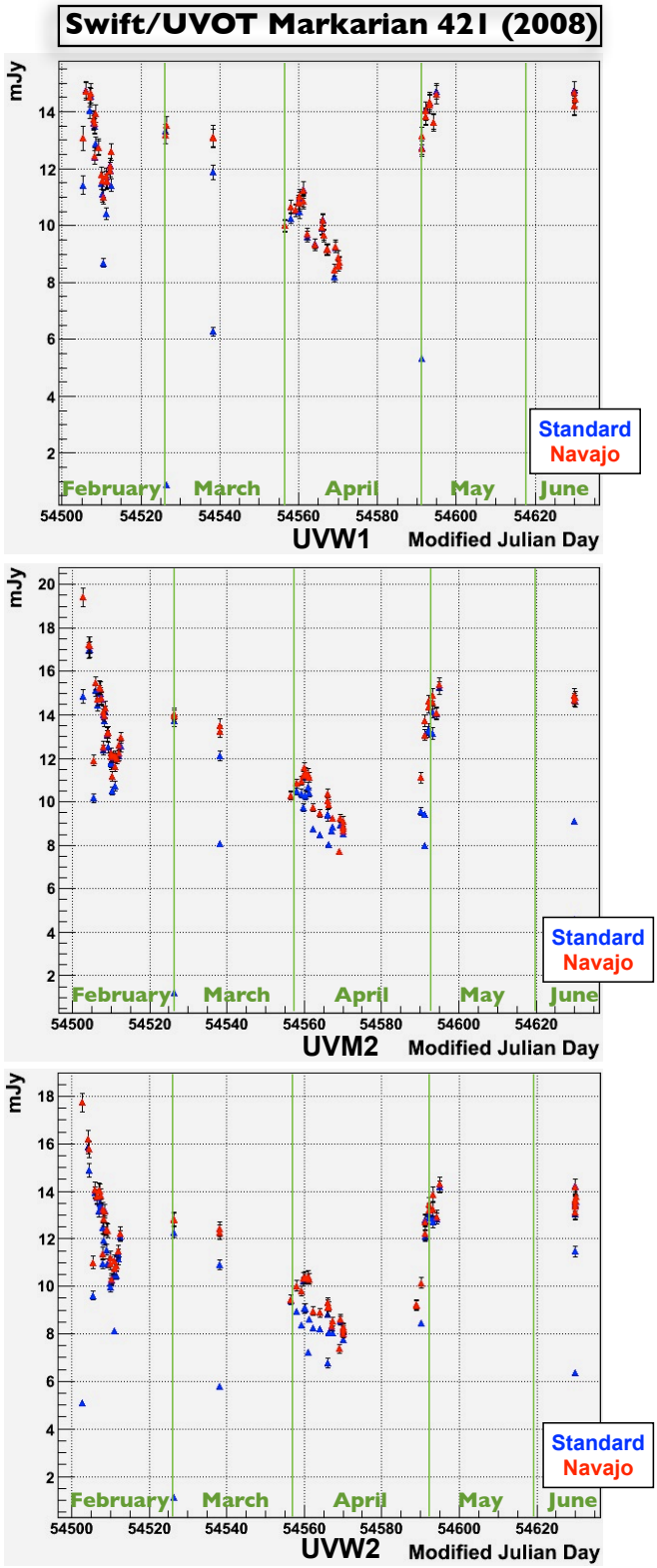

Figure 3.12: The plots return a comparison of the three ultraviolet filters (UVW1, UVM2, UVW2). In blue we have results obtained using the uncorrected astrometric misalignment (obtained with standard settings using the public software) and in red the results obtained applying Navajo with the misalignment correction.

to produce more reliable results than the astrometric corrections introduced by the public pipeline.

3.3.4 Reddening and Redshift Corrections

We must compensate for the effects of propagation of the radiation through the Galactic space, which is filled with dust and gas. This gas mainly consists of hydrogen and helium (in their neutral or ionized states). Dust interferes with a large amount of astronomical measurements in two ways: extinction and reddening (Mathis, 1990). It absorbs and scatters optical light and it emits FIR (Far InfraRed) radiation between 100 and 250 μm. Scattering by the dust and absorption/re-emission by gas lead to the rise in spectral extinction. Also, since dust grains scatter blue light more strongly than red light, the scattered radiation intensity changes non linearly along the electromagnetic spectrum, leading to the "reddening" of the UVOT images.

In order to compute the Galactic spectral extinction, we must obtain the Galactic reddening factor E_{B-V}. The reddening factor is related to the difference in extinction in the B and V bands, *i.e.*

$$E_{B-V} = A_B - A_V \tag{3.4}$$

where the extinction A is measured in magnitudes. It is related to the amount of Galactic dust that the light passes through along its path toward the observer (Finkbeiner *et al.*, 1999). The reddening factor is obtained from a look-up table provided by Schlegel *et al.* (1998) and illustrated in Figure 3.13. In the Markarian 421 direction, the retrieved Galactic smoothed reddening factor is 0.015 mag. In normalizing the dust column density, we expect a 10% statistical uncertainty on the

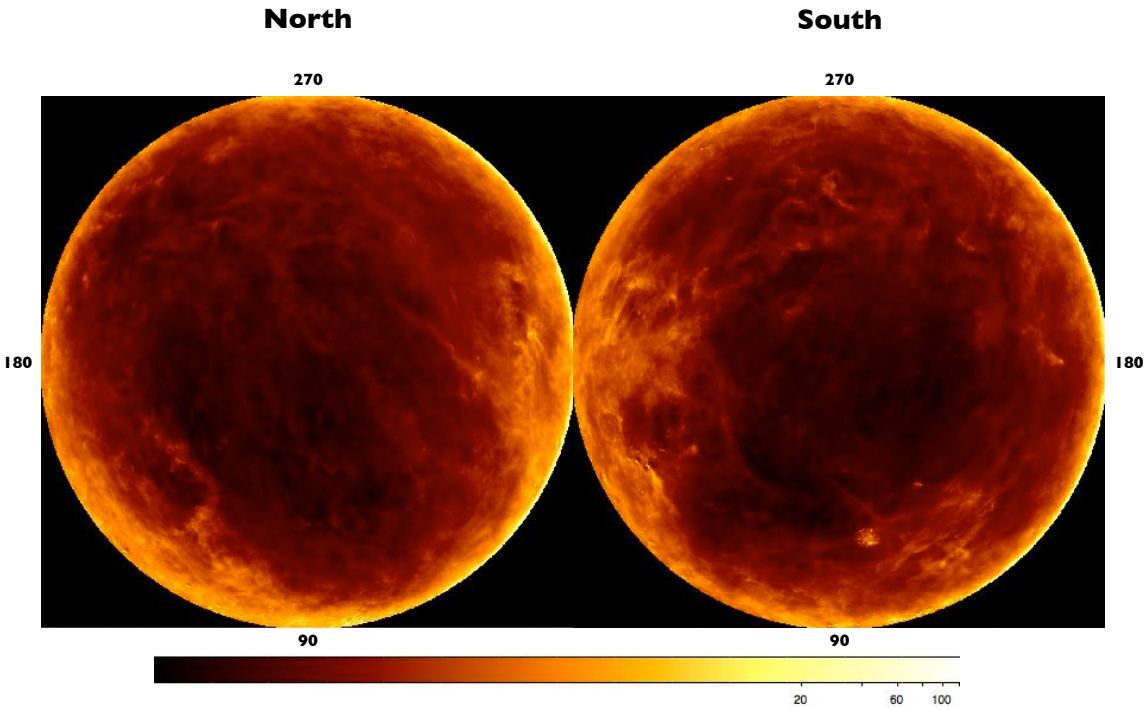

Figure 3.13: Reddening factors for the full sky in Galactic coordinates (Schlegel *et al.*, 1998).

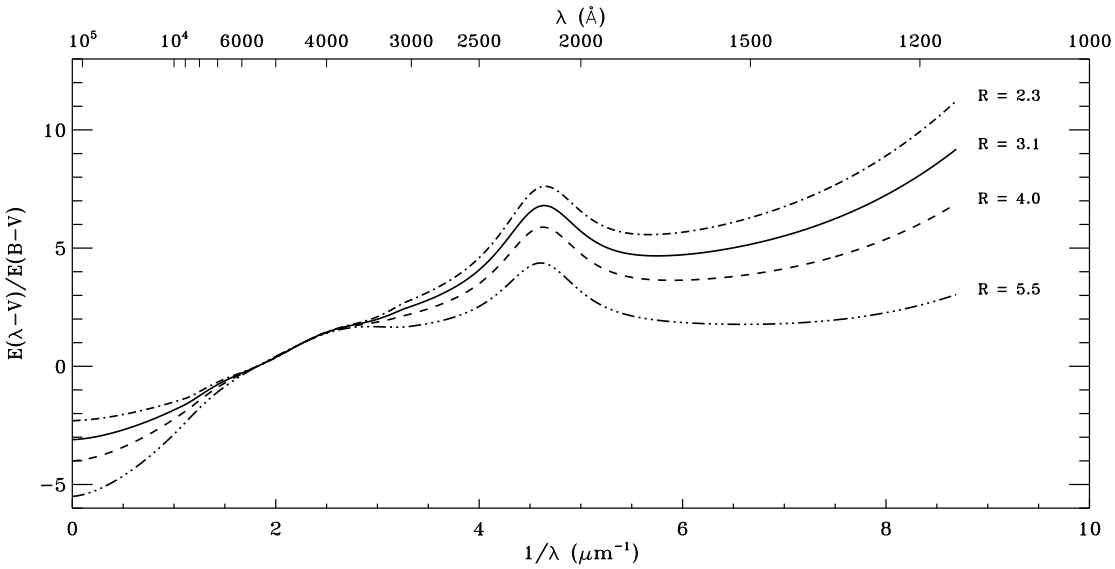

Figure 3.14: FIR through UV extinction curves expressed as a 1-parameter family that varies linearly with R_V^{-1} (Fitzpatrick, 1999). That extinction curves are plotted for a few representative values of R_V.

reddening estimate for low Galactic latitude objects (Schlegel *et al.*, 1998); this is probably an overestimation considering that our observed object, Markarian 412, is a high Galactic latitude object for which, the reddening uncertainty, is expected to be reduced.

We define R_V as the extinction coefficient in the V band expressed as a fraction of the reddening factor. In each direction, the R_V ratio seems to be linearly well correlated with the dust grain size. The extinction coefficient is, thus, related to the average size of dust grains by comparing the extinction in the V and B bands:

$$R_V = \frac{A_V}{E_{B-V}} \tag{3.5}$$

An averaged value commonly used in the Milky Way is $R_V = 3.1$ (Schlegel *et al.*, 1998) and, in the Markarian 421 direction, this gives $A_V = 0.0465$ mag.

Finally, using the extinction model in Figure 3.14 (Fitzpatrick and Massa, 1999;

Spectral Extinction	
Filter	A_λ
A_{W1}	0.098 mag
A_{M2}	0.143 mag
A_{W2}	0.136 mag

Table 3.5: Spectral extinction of the UVOT ultraviolet bands in the direction of Markarian 421.

Fitzpatrick, 1999), we determine the extinction values A_λ for the UVOT ultraviolet bands (Table 3.5), since:

$$E_{\lambda-V} = A_\lambda - A_V \tag{3.6}$$

Next, we carried out the redshift correction for each band of the UVOT detector, by shifting the effective wavelength from the observed wavelength to the emitted one in the source reference frame. The results of the analysis of the Markarian 421 dataset are redshift corrected for $z = 0.031$.

The observed photons at frequency ν are emitted by the source at frequency $\nu' = \nu(1+z)$ (where the 'primed' notation indicates the source rest frame). Also, the redshift affects the flux density in two of its aspects: the photon energies and the observed photon rates, which are redshifted. Both reduce the flux density by a factor $(1+z)^2$. However, the bandwidth is stretched by a factor $(1+z)$. Thus, the flux density is only enhanced by one power of the $(1+z)$ factor. Therefore, for any UVOT band, we can compute:

$$F' = (z+1) \cdot F \quad \text{and} \quad F'_{err} = (z+1) \cdot F_{err} \tag{3.7}$$

where F and F_{err} are the observed flux and flux uncertainty, respectively.

3.4 Further Results with Navajo

The Swift Ultraviolet/Optical Telescope dataset comprises Markarian 421 observations performed during the time interval between September 1, 2007 and June 30, 2011 (MJD 54495 to 54640). The results of the dataset analysis already contributed to a multiwavelength study (Acciari *et al.*, 2011).

During this observational campaign, the UVOT lightcurves of Markarian 421 showed three more intensive periods of observation, corresponding to very active states, leaving large observing temporal gaps (Figure 3.15). Mainly, this is due to the fact that, traditionally, multiwavelength campaigns are mostly triggered when the observed object becomes particularly bright.

Although the observations forming the UVW1, UVM2 and UVW2 lightcurves were not exactly simultaneous, similarities between UVOT lightcurves are clearly evident. Primary and secondary analyses were carried out using the UVOTSOURCE standard tool and the Navajo UVOT pipeline (Acciari *et al.*, 2011, Navajo v2.4.3 January 2009). Both analyses used the calibration database released[2] on February 2010. Photometry was computed by using a 5 arcsec source region centred on the source position and photometric corrections were applied following Poole *et al.* (2008) and Li *et al.* (2006). The Markarian 421 dataset only included data in the UV bands. Adopting a relatively large photometric radius aperture of 5 arcsec, ultraviolet fluxes are, in practice, not affected by temperature changes along the orbit of the Swift spacecraft. Astronomical

[2]http://heasarc.gsfc.nasa.gov/docs/heasarc/caldb

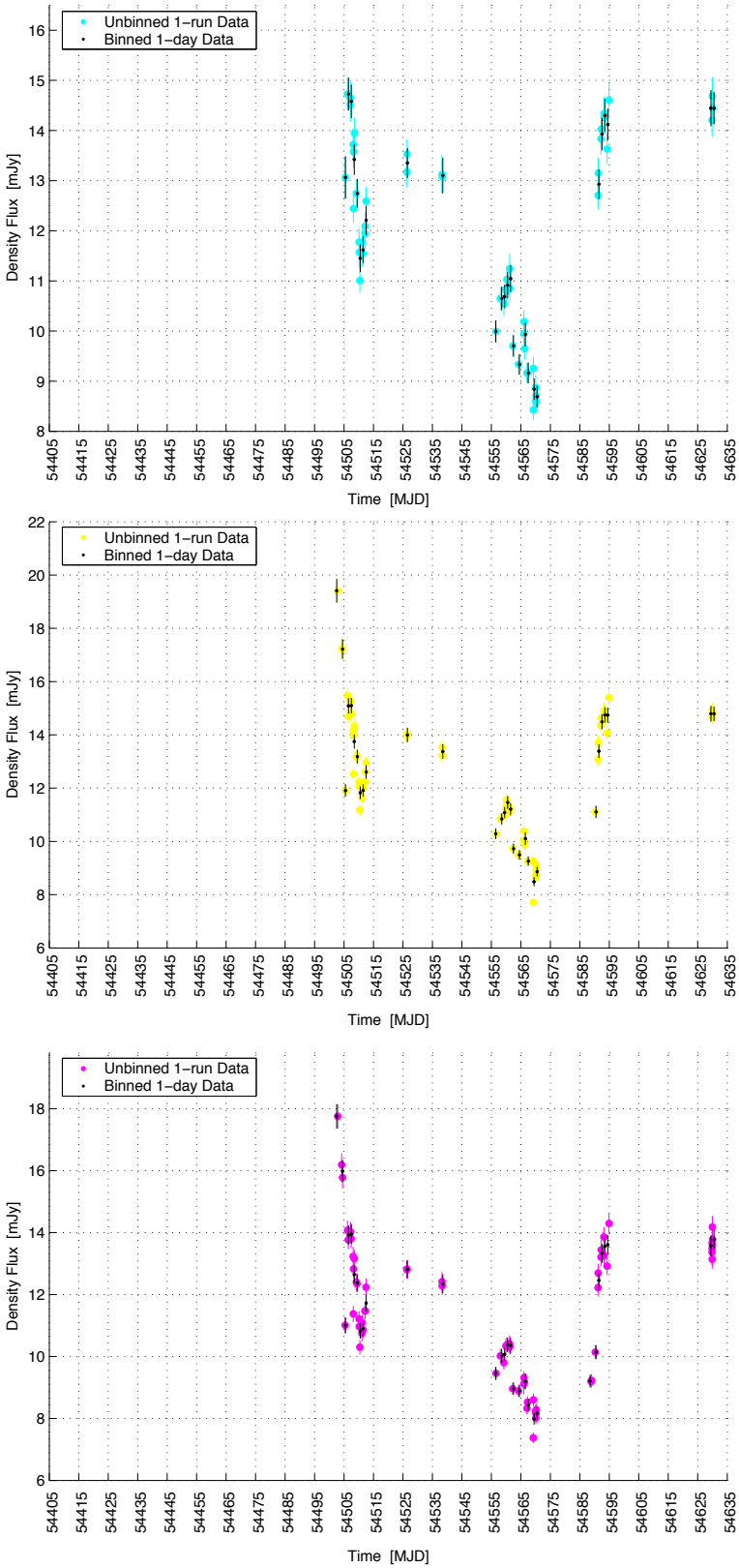

Figure 3.15: Unbinned and 1-day binned lightcurves of UVW1, UVM2 and UVW2 ultraviolet bands during the 2007-08 monitoring campaign reduced by using Navajo.

misalignment was accounted for, as described in Section 3.3.3.

Some caveats have to be mentioned. There is the presence of bright sources in the field of view which could cause significant coincidence losses, leading to an additional underestimation of the Markarian 421 blazar flux. In a more general context, weak sources on top of a high background emission would bring a larger uncertainty on the estimate of systematics due to the poor signal-to-noise ratio. An additional systematic uncertainty of 10% was added to the absolute UVOT fluxes to account for these uncertainties considering that Markarian 421 is a relatively strong source. More recently, Breeveld *et al.* (2010) showed that, in the case of a strong source placed on top of a strong background emission (as in the case of Markarian 421), the computed photometric count rate experiences an increase of the coincidence loss, which is $< 3\%$ of the estimated flux per pixel.

Results are, then, redshift corrected ($z = 0.031$) in amplitude and frequency. For Markarian 421, the E_{B-V} factor is 0.015 ± 0.002 mag. In order to obtain this value, a subprogram of Navajo has computed the weighted average of the four E_{B-V} values closest to the source position. These values were extracted from the extinction map provided by Schlegel *et al.* (1998). Then, we obtained the spectral extinction values shown in Table 3.5 with a custom algorithm implementing Opt/UV corrections (Fitzpatrick, 1999). The quantification of UV intergalactic absorption is still a matter of debate and, therefore, we made no correction. However, the relatively small redshift of Markarian 421 suggests that such a contribution would have a low value in any case.

In the present investigation, a correction for radiation arising from the host galaxy

has not been applied, but we have provided a very conservative estimate of the associated systematic error (Acciari *et al.*, 2011). The estimate of the host-galaxy contribution of Nilsson *et al.* (2003) is for the R band. We have also obtained the corresponding components for the V , B and U bands from Fukugita *et al.* (1995). The findings of Arimoto (1996) were then used to estimate the metallicity of the Markarian 421 giant elliptical host galaxy and, therefore, to constrain its contribution to the UV bands to be less than 5% (Han et al. 2007). Here, we assume that the presence of the flux excess in the far UV spectrum (or upturn) of elliptical galaxies might partially arise for an old population of stars hot helium-burning in absence of hydrogen-rich envelopes.

PEGASE-HR Input Settings	
Galaxy Age:	12.8 Gyr
Galaxy Shape:	Giant Early Type
Star Mass (min-max):	0.08 - 120
Initial Mass Function:	Rana-Basu
Fraction of Binary Systems:	0.05
Initial Metallicity (mass fraction):	0.03
Star Formation Rate:	$(M_{gas})^{p_1}/p_2$
Age of Galactic Winds:	2 Gyr
Nebular Emission:	Yes

Table 3.6: PEGASE-HR input parameters for Markarian 421.

In addition, we have further constrained and verified the estimate of these systematics that can be associated with host-galaxy emission. We have computed the

PEGASE-HR Results	
V-R	0.640 mag
B-V	1.031 mag
U-B	0.767 mag
UVW1-U	0.799 mag
UVM2-UVW1	0.540 mag
UVW2-UVM2	-0.253 mag

Table 3.7: PEGASE-HR host-galaxy correction factors for Markarian 421.

host-galaxy contribution of Markarian 421 using the PEGASE-HR code (Le Borgne *et al.*, 2004). We modified this software, enabling it to compute host-galaxy contributions for the UVOT ultraviolet bands. In our modeling, we assumed the parameters in Table 3.6. We obtained the correction factors in Table 3.7. The host galaxy contribution was computed using the 6.2 mJy correction in the R band from Nilsson *et al.* (2007), and then dereddened for 0.05 mag (no K-correction applied). Thus, we obtained a value of $R = 14.20$ mag.

The results in Table 3.7 are very similar with those provided by Fukugita *et al.* (1995) - $(V - R) = 0.61$ mag and $(B - V) = 0.96$ mag for 13 Gyr old giant elliptical galaxy. This is remarkable given that the two estimation methods are independent.

Next, we obtained an estimate of the radiation emitted by the Markarian 421 host galaxy in the ultraviolet bands: $\mathrm{UVW1_{HG}} = 17.44$ mag, $\mathrm{UVM2_{HG}} = 17.98$ mag and $\mathrm{UVW2_{HG}} = 17.72$ mag. During the 2007-2008 season, Markarian 421 was in a very-high-activity state having its minimum of emission around 13 mag for all ultraviolet bands. Then, we conclude that the upper limit of the host galaxy emission ratio for

UVW1, UVM2 and UVW2 bands is less than 2% of the total incoming measured flux.

These UVOT results do not include zodiacal light correction but, since Markarian 421 is far from the solar system dust rings, this would be negligible. In any case, the signal-to-background subtraction approach to the calculation of the source count rate helps to contain the zodiacal light contribution (as first-order approximation). Also, Markarian 421 evaluations do not need any particular compensation for the Galactic diffuse light, since the source is far from the Galactic plane.

In conclusion, we have designed a data reduction software particularly targeted to the study of strong sources like Markarian 421. As a result, we have provided more reliable results through the introduction of a series of double checks and validation processes in regard to the methods and assumptions already implemented in standard analyses. Moreover, we have introduced further postphotometric data refinements. The work we have done in this specific context has contributed to improve the overall pipeline robustness (Acciari *et al.*, 2011).

Chapter 4

Very Energetic Radiation Imaging Telescope Array System

VHE γ-rays are emitted by very powerful astrophysical objects. One can observe low-energy γ-rays by using relatively small detectors installed on orbiting observatories. Since the flux of γ-rays decreases with energy (generally according to a power-law trend), satellite experiments are not suitable for observing VHE γ-rays, since their sensitive area is too small compared to the γ-ray flux above a certain energy. Until recently, there was a gap in coverage of detectors between $\sim$ 10 GeV - approximately the maximum photon energy effectively detectable by satellites like EGRET (Energetic Gamma-Ray Experiment Telescope) - and $\sim$ 300 GeV (the minimum photon energy detectable by ground-based γ-ray telescopes until recently). With the progress in technology, the new generation of γ-ray orbiting detectors on satellites (*e.g.* Swift, AGILE and Fermi) has discovered hundreds of new high-energy (MeV-GeV) sources, although the number of identified objects is substantially smaller above 100 GeV.

The VHE γ-rays and cosmic rays entering the atmosphere produce showers of charged particles that in turn produce Cherenkov light which needs to be accurately recorded in order to compute the energy and the arrival direction of the originating particle. Thus, using imaging atmospheric Cherenkov telescope (IACT) arrays, the observation of γ-rays is indirect.

4.1 γ-ray induced and Hadron-Induced Showers

An extensive air shower (EAS) is initiated by a primary particle coming in at the top of the atmosphere and interacting with a nucleus in an air molecule. For $E_\gamma > 10$ MeV, pair production is the dominant process for γ-ray interactions. Pair-production produces an e^- and an e^+ and is induced by a primary γ-ray passing close to a nucleus (Figures 4.1 and 4.2). In passing close to atmospheric nuclei, the

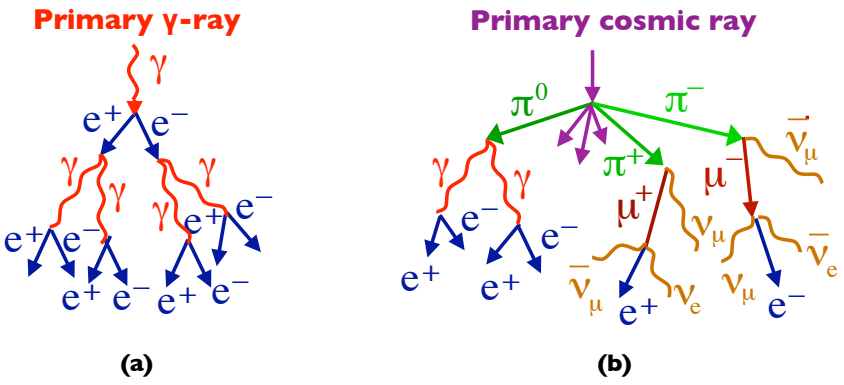

Figure 4.1: **(a)** Schematic diagram of the structure of a γ-ray induced EAS and **(b)** a hadron-induced EAS - adapted from Horan (2001).

electron and positron produced by the VHE γ-ray will suffer *bremsstrahlung*, where the pair-produced electron will emit γ-ray photons when accelerated (or decelerated) by Coulomb interactions. This effect is increasingly important at higher energies.

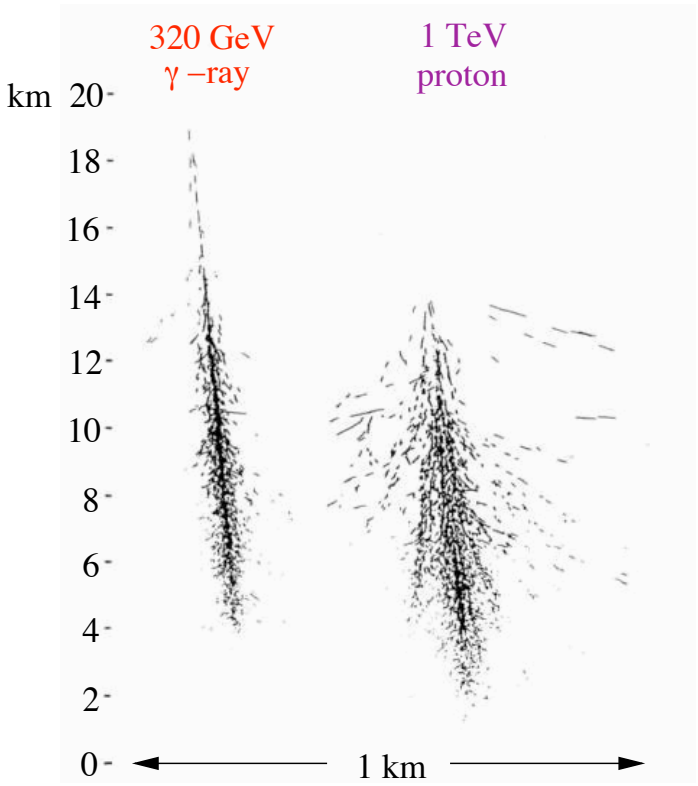

Figure 4.2: Simulation of the tracks of two EASs which produce similar amounts of Cherenkov light. The shower on the left was initiated by a 320 GeV γ-ray and the shower on the right was initiated by a 1 TeV proton. Although the proton that initiated one of the two showers possesses a higher energy, the γ-ray initiates a thinner cone and more "collimated" track (Hillas, 1996).

Each of the secondary γ-rays can produce an electron-positron pair, in turn, leading to an EAS that may consist of thousands of particles (Figure 4.2).

The number of particles in the shower grows until the e^- and e^+ energy losses, due to ionization of the medium become, quantitatively, more important than the losses due to radiation processes. The cascading effect vanishes when the secondary particles are no longer energetic enough to radiate or pair produce.

Cosmic rays also produce EASs (Figures 4.1 and 4.2). These particles, most of which are protons, cause nuclear disintegration at the top of the atmosphere with the emission of further particles, which in turn produce disintegrations. In these nuclear collisions involving primary cosmic rays, or their fragments, we can observe mesons, including pions. Neutral pions decay to photons: $\pi^0 \rightarrow \gamma + \gamma$, with a mean lifetime of $\tau = 8.4 \times 10^{-17}$ s in the particle reference frame. Meanwhile, the charged pions decay to muons and neutrinos:

$$\pi^+ \rightarrow \mu^+ + \nu_\mu \quad , \quad \pi^- \rightarrow \mu^- + \overline{\nu}_\mu \quad , \quad \tau = 2.5 \times 10^{-8}\text{s} \tag{4.1}$$

The muons subsequently decay as follows

$$\mu^+ \rightarrow e^+ + \nu_e + \bar{\nu}_\mu \quad , \quad \mu^- \rightarrow e^- + \bar{\nu}_e + \nu_\mu \quad , \quad \tau = 2.2 \times 10^{-6}\text{s} \tag{4.2}$$

The decay of the π^0 into two high-energy γ-rays initiates what is called the 'electromagnetic component' of the shower.

4.2 Cherenkov Light

While the majority of EASs do not make it to ground level, Cherenkov radiation, produced by the interaction of charged particles in the EAS with the atmosphere,

reaches the ground. This type of interaction involves a charged particle moving faster than the speed of light in that medium, *i.e.*, $v > c/n$, where n is the refractive index of the medium and v and c are the speed of light in the medium and in a vacuum, respectively. When the charged particle passes through the dielectric atmospheric medium, the molecules that compose the dielectric become polarized. These dipoles relax once the particle has moved past (Figure 4.3), emitting Cherenkov light.

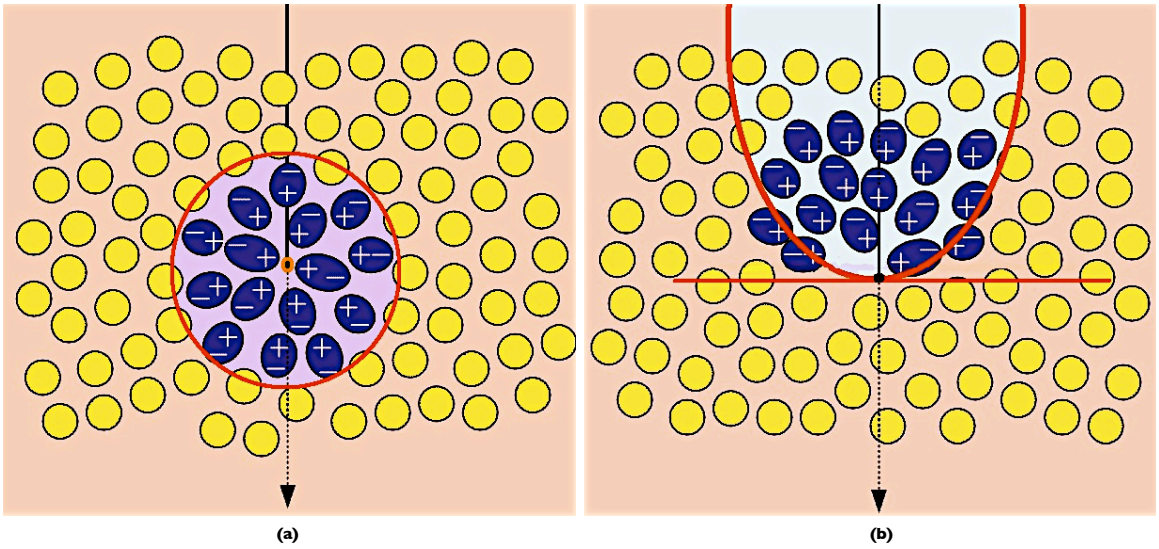

Figure 4.3: If the particle moves slower or at the speed of light in the medium, polarization is symmetric in relation to the direction of motion **(a)** and the dipoles interfere destructively. The Cherenkov radiation appears when the charged particle possesses a speed greater than the speed of light in the medium **(b)**.

In general, the Cherenkov radiation (especially the emission angle) can be explained by the Huygens construction. A charged particle passing close to a molecule of the dielectric medium polarizes its molecules, thus inducing a dipole state. Once the particle has passed, this polarized state relaxes, causing each dipole to emit a small electromagnetic pulse. For slow moving particles, polarization is perfectly symmetrical, resulting in zero net electric field at large distances (and thus no radiation).

However, when the particle is moving at $v > c/n$, the state still has axial symmetry about the direction of motion, but no longer possess "longitudinal" symmetry along the direction of motion. The dipole field established in the dielectric can only be collapsed with the emission of electromagnetic pulses that interfere coherently, producing a pulse of Cherenkov radiation.

In a time Δt, the particle has moved along the propagation direction at a distance $\nu\Delta t$ (Figure 4.4), where ν is the speed of the particle in the medium. At very-high-energies above 100 GeV, a significant portion of the particle energy is released by radiative processes. The particle has been quasi continuously emitting light along the traveled path in that time interval. Simple trigonometry determines the angle of the emission θ to be:

$$\theta = cos^{-1}\frac{c\Delta t/n}{\nu\Delta t} = cos^{-1}\frac{c}{\nu n} \tag{4.3}$$

or

$$\theta = cos^{-1}\frac{1}{n\beta} \tag{4.4}$$

where n is the refractive index or the medium, which is dependent on the wavelength, and $\beta = v/c$.

The angle θ has a maximum for $\beta = 1$:

$$\theta_{max} = cos^{-1}\frac{1}{n} \tag{4.5}$$

The minimum velocity a particle in a medium needs to produce Cherenkov light corresponds to $\beta_{min} = 1/n$. The corresponding threshold energy is given as follows:

$$E_{min} = \frac{m_0 c^2}{\sqrt{1-\beta_{min}^2}}. \tag{4.6}$$

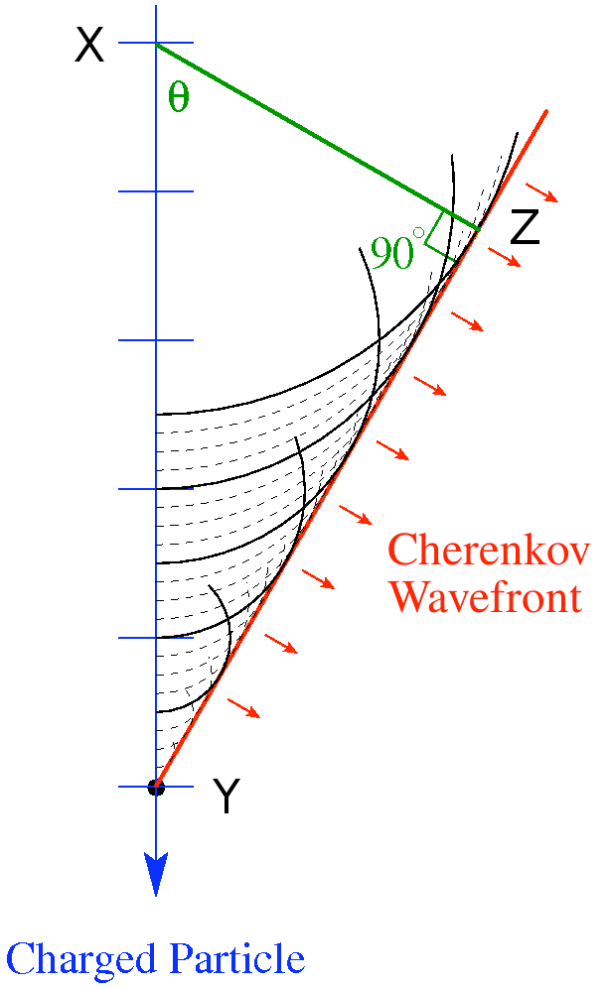

Figure 4.4: Formation of coherent Cherenkov radiation. The charged particle travels from X to Y in the same time the radiation emitted at X by the atoms of the material travels from X to Z. The Cherenkov angle θ is also shown in the figure (Horan, 2001).

where m_0 is the mass of the particle. At an altitude close to the shower maximum - located around 8 km above sea level with a refractive index of $n \simeq 1.00011$- the maximum Cherenkov emission angle, θ_{max}, is $\sim 0.86°$. At that altitude, the Cherenkov light production thresholds are $E_{min,e} = 34$ MeV, $E_{min,muon} = 7$ GeV and $E_{min,p} = 63$ GeV for electrons, muons and protons, respectively.

The lateral distribution of Cherenkov light (Figure 4.5) from γ-ray showers is determined by the Cherenkov emission angle θ, by the energy of the incoming particle, and by multiple Coulomb scattering of the charged component of the shower along the atmospheric path.

Most of the Cherenkov light from a shower is produced close to shower maximum, at altitudes between 7 km and 10 km. Cherenkov photons produced at that altitude tend to arrive in a light "pool" between 100 and 120 m from the projection of the centre of the EAS on the ground at sea level. For example, at an altitude of 1268 m (where the VERITAS array is located), we will receive Cherenkov showers with light pools of about 120 m in radius (Figure 4.5).

The number of Cherenkov photons emitted by a particle with atomic number Z per unit path length and per unit energy interval (You *et al.*, 1984) is equal to

$$\frac{d^2N}{dxd\lambda} = \frac{2\pi\alpha Z^2}{\lambda^2}\left(1 - \frac{1}{\beta^2 n^2(\lambda)}\right) \tag{4.7}$$

where $\alpha = \frac{e^2}{2\epsilon hc} = \frac{1}{137.036}$ is the fine structure constant and λ is the wavelength of the emitted photons. The larger part of Cherenkov radiation is emitted in the UV range, while another part is in the visible blue range, since $\frac{d^2N}{dxd\lambda} \propto \frac{1}{\lambda^2}$ (Figure 4.6). It is possible to estimate the number of photons in the Cherenkov light pool. For the case of an electron moving along a track of length l, within a wavelength range between

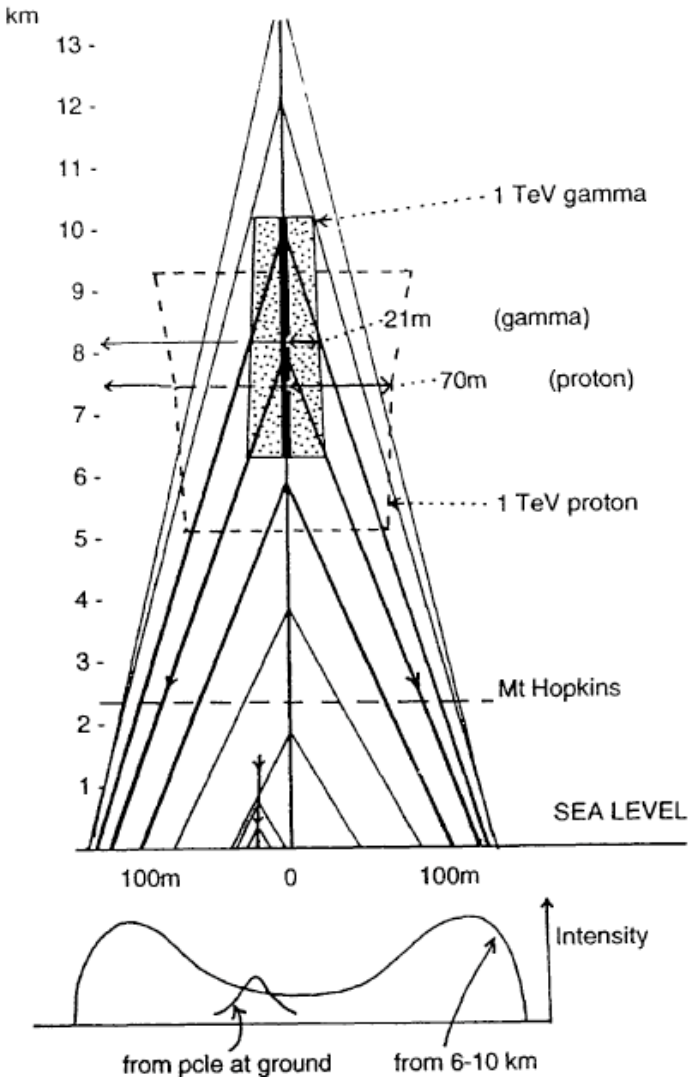

Figure 4.5: Typical lateral distribution of Cherenkov light at the ground. As the shower develops, the Cherenkov angle increases, due to an increasing atmospheric density. The shaded box indicates the main region of the emission of Cherenkov light in γ-ray showers: 25% of light is emitted above the top of the box and 25% of light below the bottom. The dashed-line box indicates the corresponding main region of emission in proton showers of the same energy. Cherenkov light is emitted at the angles shown from ultra-fast particles traveling along the vertical axis, resulting in a peak of intensity on the ground just beyond 100 m from the projection of the shower axis on the ground (Hillas, 1996).

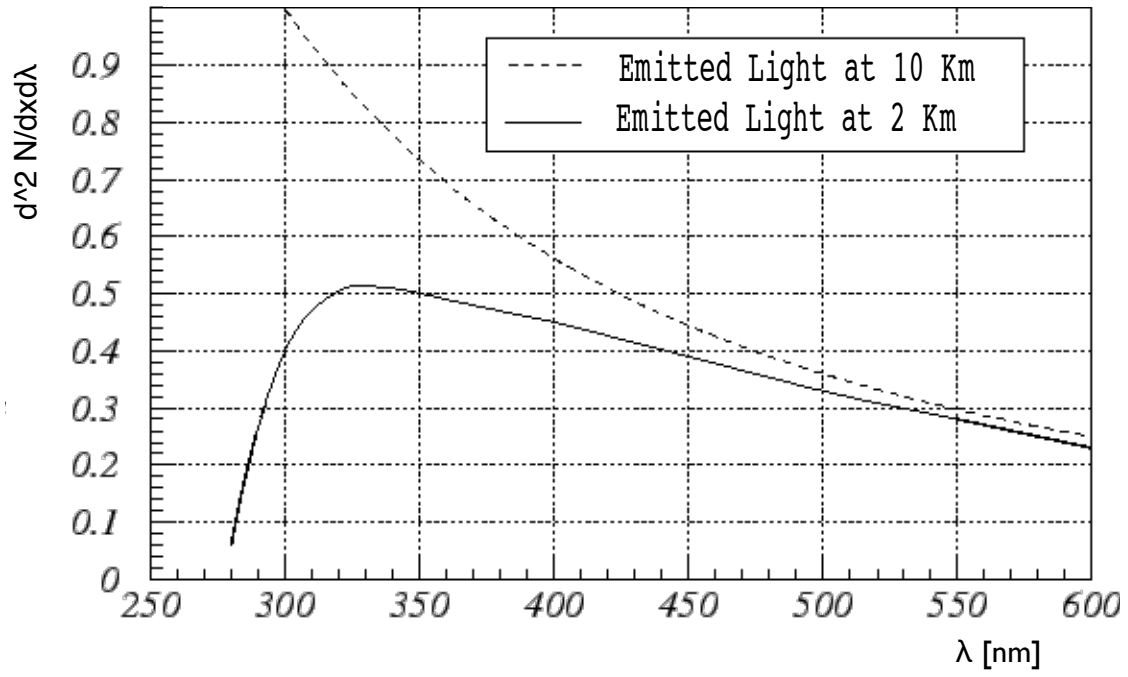

Figure 4.6: Differential Cherenkov photon spectrum. The computations include absorption by ozone and Rayleigh and Mie scattering (Barrio, 1998).

λ_1 and λ_2, we will have:

$$N = 2\pi\alpha Z^2 l \cdot \left(\frac{1}{\lambda_2} - \frac{1}{\lambda_1}\cdot\right)\left(1 - \frac{1}{\beta^2 n^2(\lambda)}\right) \tag{4.8}$$

where $n(\lambda)$ is the refractive index of the medium, which is a function of the photon wavelength, λ.

4.3 The VERITAS Array Telescope

Until recently, the energy regime between $30-100$ GeV has been a poorly explored domain for astrophysical observations. Recent developments though, including the successful launch of the Fermi satellite and the ground-based detection of pulsed emission from the Crab pulsar below 100 GeV (Albert *et al.*, 2008), have highlighted the potential of this spectral region for γ-ray observatories. VERITAS is a major

Figure 4.7: Four-telescope panorama at the FLWO by VERITAS Collaboration. This was the telescope configuration at the time the data used in this work were recorded (from http://veritas.sao.arizona.edu).

ground-based observatory covering the energy range of $0.05 - 50$ TeV (with its best sensitivity from $0.1-10$ TeV). It consists of an array of four 12-m imaging atmospheric Cherenkov telescopes (IACT) for γ-ray astronomy and it is located at the base camp of

the Fred Lawrence Whipple Observatory (FLWO) in southern Arizona at an altitude of 1268 m (Figure 4.7). The four γ-ray telescopes comprising VERITAS act together to greatly increase background rejection in the data. At the time the dataset used in this work was recorded, the telescope layout was as shown in Figure 4.8. More recently, in order to improve sensitivity, the telescope labeled as 'Tel. 1' has been moved. VERITAS was designed as a successor to the Whipple 10 m telescope, located

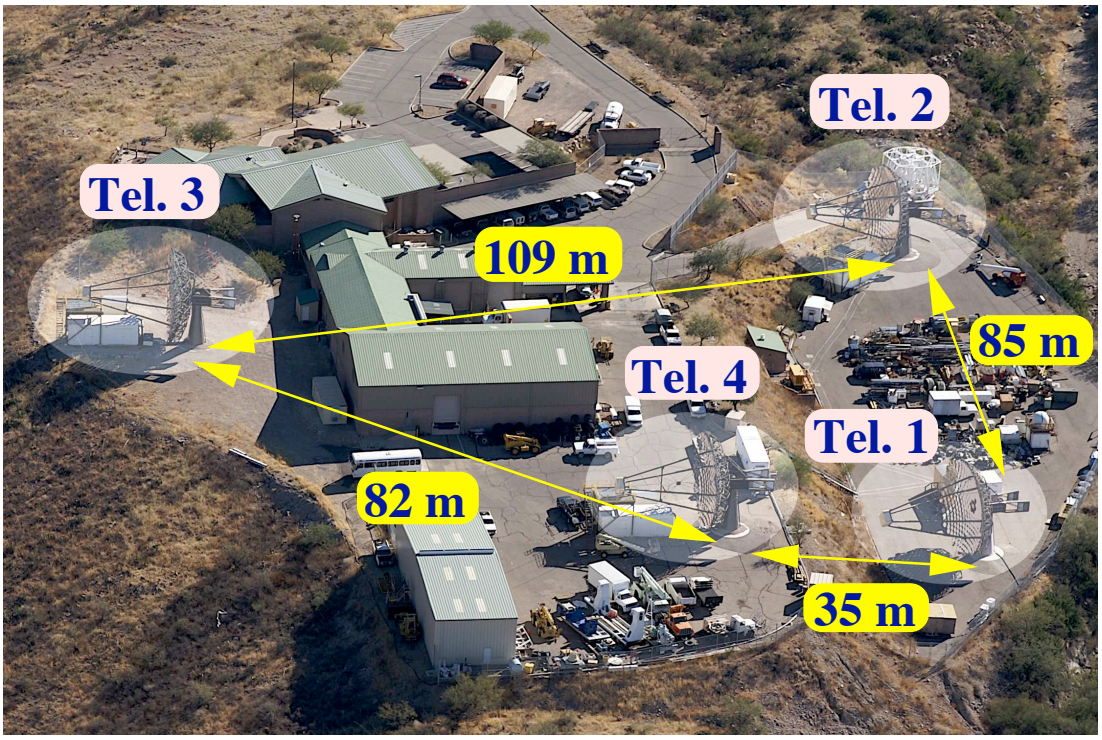

Figure 4.8: View of the VERITAS telescope layout at the FLWO basecamp showing the numbering of telescopes and their separations at the time when the dataset was recorded. More recently, in order to improve sensitivity, the telescope labeled as 'Tel. 1' has been moved.

on Mount Hopkins. VERITAS has a flux sensitivity factor 10 times better than the previous IACT generation (Weekes *et al.*, 2002).

VERITAS combines a wide energy range with good energy resolution ($\Delta E/E =$

$15 - 20\%$) and good angular resolution ($\approx 0.03^\circ$ at 1 TeV). The high sensitivity of VERITAS allows the detection of sources with a flux of 1% of the Crab Nebula in under 50 hours of observations at 70° elevation.

4.3.1 Optics

Each VERITAS telescope has a Davies-Cotton design (Davies and Cotton, 1957; White, 2005) and includes a spherical tubular steel optical support structure with an opening diameter of 12 m. Each telescope has an altitude-over-azimuth mount. Custom software controls the motion of the telescopes. Maximum slew speed is $1^\circ/\mathrm{s}$ (Holder *et al.*, 2006) and tracking errors are 0.01° maximum. A photomultiplier tube camera is housed in a box ("focus box") held at the telescope's focal plane by four steel arms.

The $D = 12$ m reflector diameter provides a greater collector surface area than the Whipple 10 m γ-ray telescope (Kildea *et al.*, 2007). A further improvement is that the f focal length number was chosen to be $f/1.0$, *i.e.*, the focal point is at $F = 12$ m, against $f/0.7$ for the Whipple 10m (Figure 4.9). Simulations showed that a larger ratio reduces the aberration due to the light reflected by mirrors that are off-axis (Krennrich *et al.*, 2000; Weekes *et al.*, 2000; Lessard, 1999). The Davies-Cotton design is not isochronous. Due to the way the facets are placed, a planar wavefront impinging perpendicularly on the telescope has a time spread of approximatively 4 ns when received at the focal point.

Each of the four VERITAS telescopes is tiled with 345 hexagonal mirrors that bring the reflector area to ~ 110 m^2. The facet side-to-side dimension is 61 cm (with

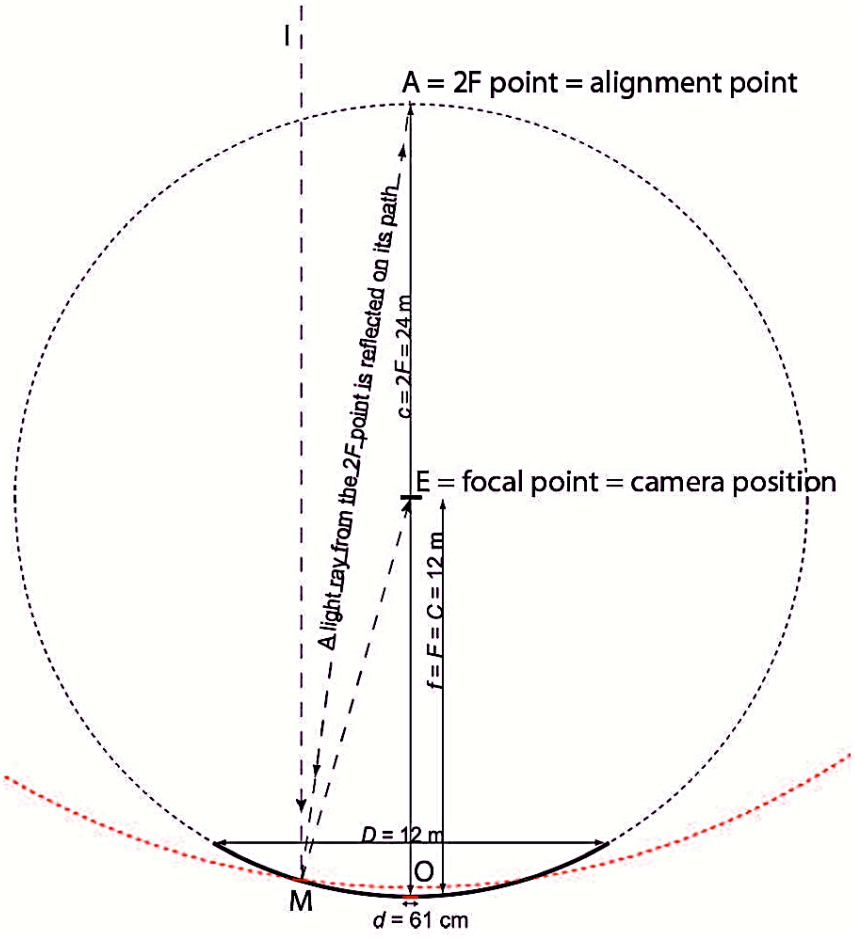

Figure 4.9: Davies-Cotton telescope design. The spherical mirror facets mounted on the 12 m spherical reflector are hexagonal, measure 61 cm across, and have a radius of curvature of 24 m. A light ray coming from point I (representing light coming from infinity), and parallel to the optic axis, is reflected by facet M to the focal point E where the camera is positioned. A light ray coming from point A, at twice the focal distance on the optic axis, bounces back on itself after reflection at point M. The same is true for the facet at point O, or at any other point on the dish. Note that the triangle AEM is isosceles, with two sides equal to the focal distance, and that the point A is not the centre of curvature of the facet located at point M (Valcarcel, 2008).

a corresponding area of 0.322 m^2) and 11.5 mm thick at the edges but less thick toward the centre. Each facet has a 24 m radius of curvature (Roache *et al.*, 2007).

4.3.2 Coating of Mirrors

The mirrors facets are coated at FLWO, where a layer of aluminum (of thickness 180 nm) is deposited on the surfaces of their front sides. The coating allows the mirrors to achieve a reflectivity greater than 85% over the UV/Optical spectrum ($280 - 450$ nm). In particular, it is kept $\geq 90\%$ at 320 nm, which corresponds to the point on the spectrum where the Cherenkov light is mostly emitted (see Figure 4.6). The aluminum layer is also anodized to make the coat more resistant to degradation in the extreme environmental conditions of the Arizona desert. The time-dependent degradation of the mirror's reflectivity is currently under investigation. Preliminary results seem to indicate a 10-20% reduction in ultraviolet reflectivity per year, which is an acceptable rate. Furthermore, there is an on-going programme of re-coating mirror facets.

4.3.3 Mirrors and Bias Alignment Technique

In order to perform the optical alignment of the mirrors of each VERITAS telescope, we orientated each telescope in the direction of an alignment point, located at a distance of 24 m (see Figure 4.9). At the alignment point, we placed a laser that could be directed towards any of the facets of the reflector. The returning beam was used to estimate the amount of compensation needed for each facet to reorientate the beam toward the alignment point. This was the mirror alignment methodology

used at the time of the data recording (Toner et al., 2007). Each telescope undergoes changes in structural deformation that modify its optical characteristics as it moves in elevation. Since the alignment process is performed at 0° elevation, the point spread function would degrade quite significantly during observations at different elevations. The "bias alignment" procedure was introduced to account for telescope structural deformation at different elevation angles (Toner et al., 2007). In practice, by introducing a well chosen misalignment of the facets during the alignment at 0° of elevation, the facets assume the most effective orientation at around 65° of elevation. The relative motion of the mirrors between 0° and 65° of elevation is measured by placing laser pointers on the mirror facets and orientating them to produce spots of light on a screen placed at the focal point. A CCD camera is, then, used to take two images: one at 0° and the other at 65°. The displacement of the spots in the two images provides the amount by which each facet has moved. Then, each facet is misaligned by minus that amount at 0° elevation. This is called "bias alignement". After bias alignment, the full width half maximum of the point spread function is $< 0.075°$ between 55° and 85° elevation, with a minimum at 65° (Figure 4.10). This point spread function is about half the pixel size of the photomultiplier tube camera located in the focus box.

4.3.4 Camera and Light Cones

Cherenkov photons from EASs are collected by cameras consisting of arrays of photomultiplier tubes in the focal planes of the telescopes, which convert the light images into amplified electrical pulses. Each camera is housed in a protective box

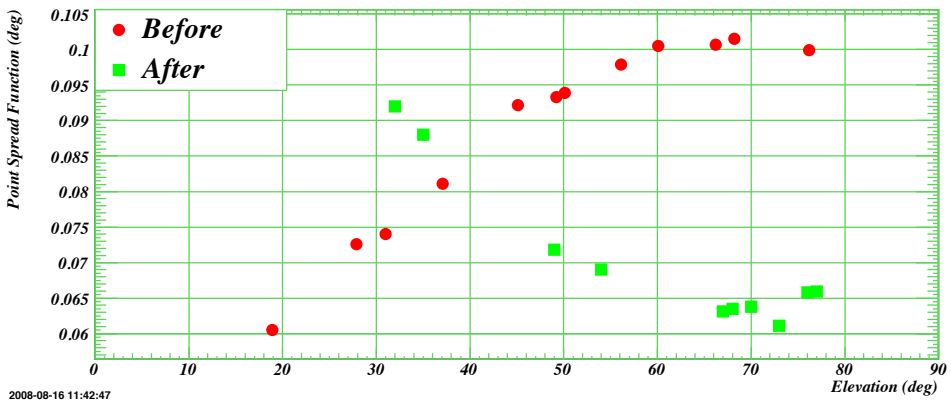

Figure 4.10: The plot shows the improvement at higher elevations of the point spread function of 'Tel. 1'. The circles and the squares refer to measurements taken before and after the bias alignment (from Toner *et al.*, 2007).

with a shutter at the focal point and consists of an array of 499 PMTs (Photonis XP2970/02, 29 mm diameter, quantum efficiency of $18 - 22\%$). The size of each PMT in the camera corresponds to 0.15° bringing the entire camera field of view to 3.5°.

A preamplifier is added to each PMT to boost the output pulse by a factor of 6.6. Particular care was taken in reducing the preamplifier noise. This gives a low level of noise after transmission through 45 m of cable that feeds the amplified signals to the triggering and data acquisition electronics.

Bright stars in the field of view (or bright light from human activity near the observatory) could possibly damage the camera PMTs. To automatically turn off pixels at risk of being damaged, each preamplifier contains an additional dedicated output that allows the anode current to be monitored. The current-monitoring system has a switch for automatic or manual suppression of individual channels that present high currents. Moreover, during observation, the preamplifiers might overheat the

camera electronics resulting in failures. Therefore, temperature and humidity sensors have been installed in the camera box. Observers can turn off the camera system if there is any risk of damage to the camera.

During night time, there is still diffuse light from the sky. We refer to this radiation as night-sky background and it limits our observation sensitivity. It is mainly generated by human settlements. Fortunately, the night-sky background is lower at the bluer ultraviolet frequencies, within which Cherenkov radiation falls. Thus, photomultiplier tubes with peak sensitivity in the blue region can detect the Cherenkov light from EASs over the night-sky background light (Nagai *et al.*, 2007).

The photomultiplier tubes (or "pixels") forming the camera have circular faces (Figure 4.11). This means that their close-packed tiling is not optimum for light collection as many gaps exist between the circular sections. To increase the collection efficiency, light hexagonal concentrators (lightcones) have been introduced and coated with aluminum layers. The lightcones also reduce the night-sky background light reaching the detector. In numerical simulations, and in field tests, it was verified that the hybrid Winston cone exhibited the most effective results (Krennrich *et al.*, 2007). This hybrid configuration allows the lightcones to achieve a reflectivity comparable with that of the mirrors, >85% above 260 nm. Furthermore, the hexagonal tiling increases the camera collection efficiency from 55% to 75% (Figure 4.11). Lightcones are recoated at least every two years and cleaned monthly with CO_2 snow (Roache *et al.*, 2007) since cleaning removes the dust deposited by the wind. The dust accumulation is not uniform, introducing $\sim$ 5% of uncertainty in the camera collection efficiency.

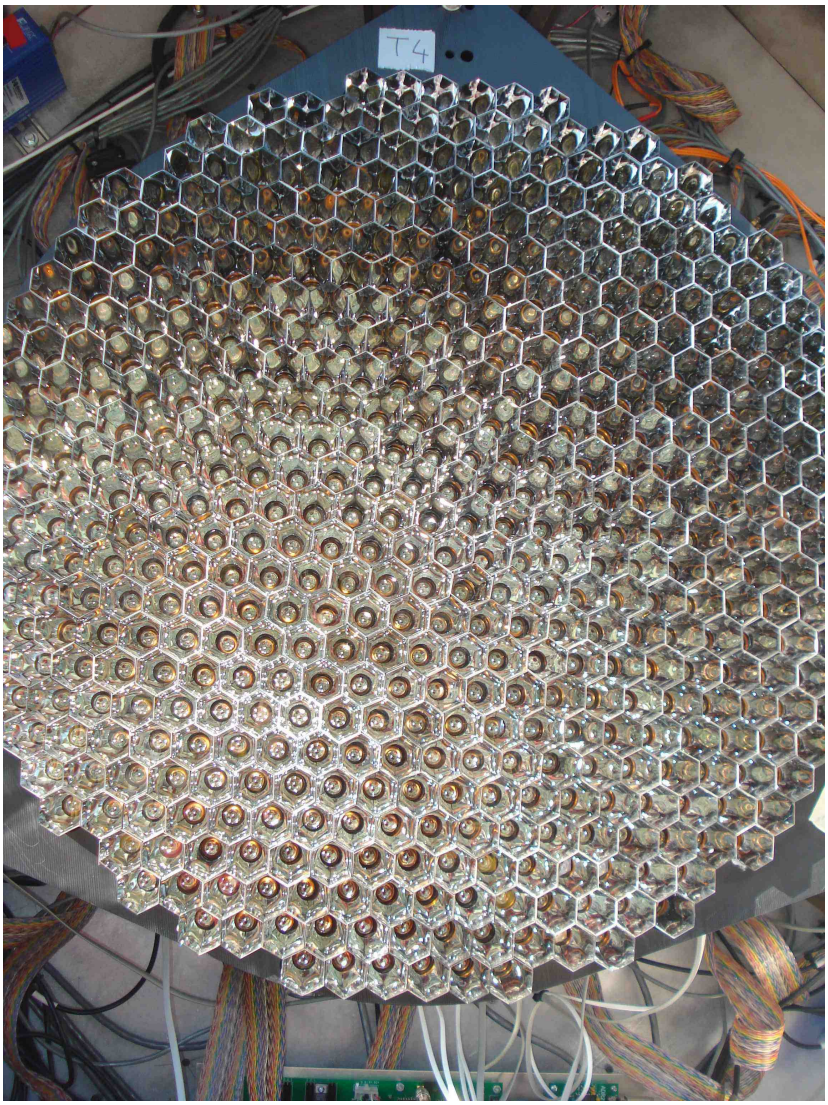

Figure 4.11: The PMT camera with the lightcones that provide a higher photon collection efficiency.

4.3.5 Trigger Selection

The VERITAS array employs a system of three trigger levels (Figure 4.12) to exclude the background cosmic ray events:

- An initial trigger, which acts at the single pixel level (first-level trigger).
- A pattern trigger, which acts on the relative timing and distribution of pixel-level triggers within a single telescope camera (second-level trigger).
- An array-level trigger, which requires simultaneous observation of an air-shower event in multiple telescopes (third-level trigger).

The first-level trigger consists of constant fraction discriminators (CFD) processing the analogue photomultiplier-tube signals. The CFDs contain a programmable 6 ns delay to compensate for different photomultiplier tube transit times and cable lengths for different pixels. When photons hit a photomultiplier tube, the PMT produces an output pulse that is proportional to the intensity of the incoming light. If the PMT output exceeds the threshold, the first-level trigger is passed. However, the exact time of the pulse reaching the triggering threshold suffers jitter and many pulses starting at the same time (but having different amplitudes) cross the first-level trigger threshold at different times (Vassiliev *et al.*, 2003). Setting the CFD threshold as low as possible allows the detection of low-energy events, but, as the CFD threshold is lowered, the rate of first-level triggers grows because of night-sky background fluctuations. The CFD is set at the point where the night-sky background fluctuations stop dominating the trigger rate. The CFD threshold is set to 50 mV, which corresponds to $4 - 5$

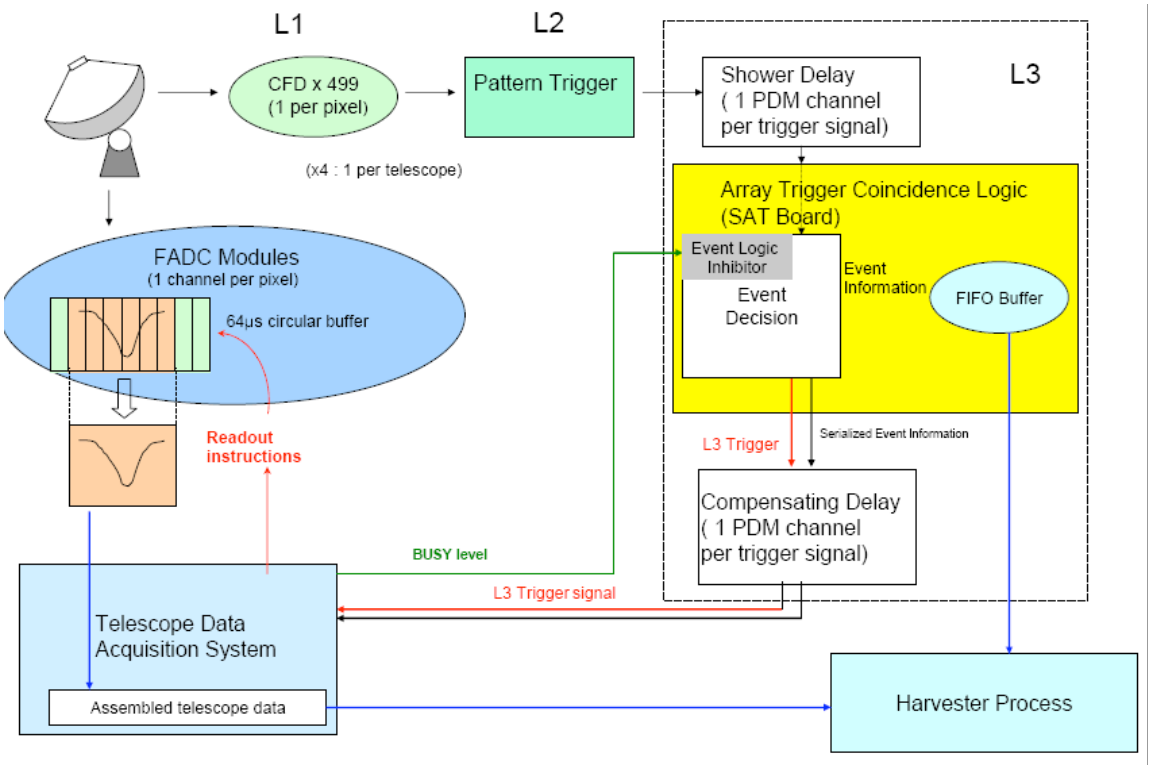

Figure 4.12: A schematic diagram illustrating the VERITAS trigger levels (Weinstein, 2007)

photoelectrons (Weinstein, 2007). This allows observations to be taken over a wide range of conditions of the night-sky background.

The purpose of the second-level trigger is to examine the spatial and temporal distribution of the first-level signals from a camera in order to identify patterns that may be produced by γ-ray induced showers. This "pattern trigger" looks for images that may represent real γ-ray and cosmic ray induced signals rather than simply random noise. The usual requirement is that three adjacent pixels fire within a timing window which corresponds approximately to the time spread of the Cherenkov light front arriving on the detector, with allowance for electronic jitter. By setting this time window as narrow as possible, a large proportion of false triggers is avoided, allowing one to reduce the energy threshold.

The profile of the Cherenkov shower is such that the wavefront does not reach each telescope at exactly the same time. The data acquisition system records events in response to the third-level trigger (Weinstein, 2007) and part of its role is to compensate for the delay on signals from the different cameras. For the four-telescope data, the third-level trigger was set to require at least three telescopes to record an event within a 100 ns coincidence window. This value of time window was conservatively chosen so as to allow for different widths and curvatures in the Cherenkov light fronts (and for some electronic jitter). However, a study shows that the rates remain stable if the window is narrowed to around 25 ns (Weinstein, 2007). In the future, the coincidence window will be reduced close to this value so as to lower the rate of accidental triggers.

All types of VHE showers are recorded. The patterns produced by cosmic ray showers due to cosmic rays can be recognized because they usually produce images that look different from the images that γ-rays produce. Thus, the patterns can be discriminated during the offline analysis from those produced by γ-rays. However, a subset of cosmic rays can produce images in a single telescope camera similar to those produced by γ-rays. The ability to discriminate between these two possibilities improves if these showers are viewed from different locations. By combining multiple reconstructed images, obtained from different telescope cameras, it is possible to further constrain the shower profile.

4.3.6 Data Acquisition

A PMT provides an analogue electrical pulse for all light falling on it. The Flash Analogue to Digital Converters (FADCs) in the data acquisition system are responsible for digitizing these analogue pulses. The FADC boards continuously record data until they receive a signal that an event has occurred. The data acquisition pauses until the relevant data are read out, then continues digitizing data until the next event. The signal from each photomultiplier tube is digitized in 2 ns bins and stored with a total look-back memory of 32 μs. After the memory is full, the system begins to rewrite it from the beginning, overwriting the recorded data. Additionally, the data acquisition system includes features to handle the read out of special trigger types (Cogan, 2006).

FADCs also switch between high and low-gain signal paths. If a pulse comes through the FADC exceeding the dynamic range of the high-gain path, the signal

from the low-gain path is digitized (*e.g.*, for large signals, when the digitization would saturate at the maximum value of 255 digital counts, the board actually switches to a lower gain path, reducing the input gain by a factor of 6, which allows digitization of larger pulses). FADCs provide a very high sampling frequency for digitizing the photomultiplier tube pulses (the length of the Cherenkov pulses is of the order of a few nanoseconds). In this way, one can select a more appropriate integration window, and therefore have better control of the signal to noise ratio.

When the third-level trigger sends a signal to the acquisition system, it begins to record an event (Hays, 2007). For each telescope, there are four Virtual Machine Environment (VME) crates that hold the FADC boards plus one that holds a clock trigger module and a Global Positioning System (GPS) clock that will provide a correct time tag for the data. Upon receipt of the trigger signal, the VME acquisition module asks the FADC boards to extract a 48 ns (24 samples) segment that contains the pulses which caused the system to trigger. The VME system stores the information it reads into 8 MB buffers that are transferred onto a computer running "event builder" software. The event builder, thus, receives fragments of events from each telescope camera. Adding timing information obtained from a GPS auxiliary device, the event builder assembles the data to form a telescope event file and writes them into a single array file that follows a format called the VERITAS Bank Format (VBF).

Chapter 5

TeV Analysis Techniques with VEGAS

The purpose of the analysis technique is to identify γ-ray initiated events and estimate the energy of the primary γ-rays above the atmosphere. This is not a simple task and it needs dedicated software for its completion. We have carried out our data reduction using VEGAS (VEritas Gamma-ray Analysis Suite), described in Daniel (2008) and Cogan (2008). Since each extensive air shower is different and results from a series of random processes, the VEGAS package involves simulations of Cherenkov showers originating from γ-rays and particles. After the calibration of each telescope in the VERITAS array, this software is able to separate contributions due to hadrons (99.9% of the events) from those due to γ-rays. Then, applying the proper selection, it estimates the energy of the γ-rays at the top of the atmosphere that produced the showers.

VEGAS performs the complete reduction of data in several steps, or "stages".

Stage 1 of the analysis is responsible for collecting all hardware-dependent quantities (*e.g.* source position, image-camera status, timing of the recorded events, *etc.*) from the on-line database. *Stage 2* applies the necessary corrections evaluated from a calibration run (called a laser run): a subprogramme calculates both the relative gain of each pixel and the relative timing corrections to be applied to the data.

Although VEGAS was designed as a pipeline with six different stages, later *Stage 3* was combined with *Stage 4*: this new portion of software was then renamed *Stage 4.2* as illustrated in Figure 5.1.

Stage 4.2 of VEGAS reconstructs the Cherenkov shower parameters and performs a stereo reconstruction. After calculating Hillas parameters (Hillas, 1985), the code computes a more convenient set of equivalent parameters to distinguish more efficiently between γ-ray and hadron-initiated showers.

Depending on the source being observed, a dedicated set of "quality cuts" is obtained and applied to the dataset, typically prior to the application of the main set of cuts based on single-telescope image parameters by *Stage 5*. The purpose of such cuts is to exclude events which can not be properly reconstructed due to truncation or due to them lying too close to the optic axis of one telescope. *Stage 5* also selects the γ-ray induced showers. Finally, *Stage 6* lists the results and produces energy spectra and sky maps.

5.1 Observation Mode

In the case of VERITAS, stereoscopic observations are available because multiple telescopes view the same portion of the sky at the same time. The source position and

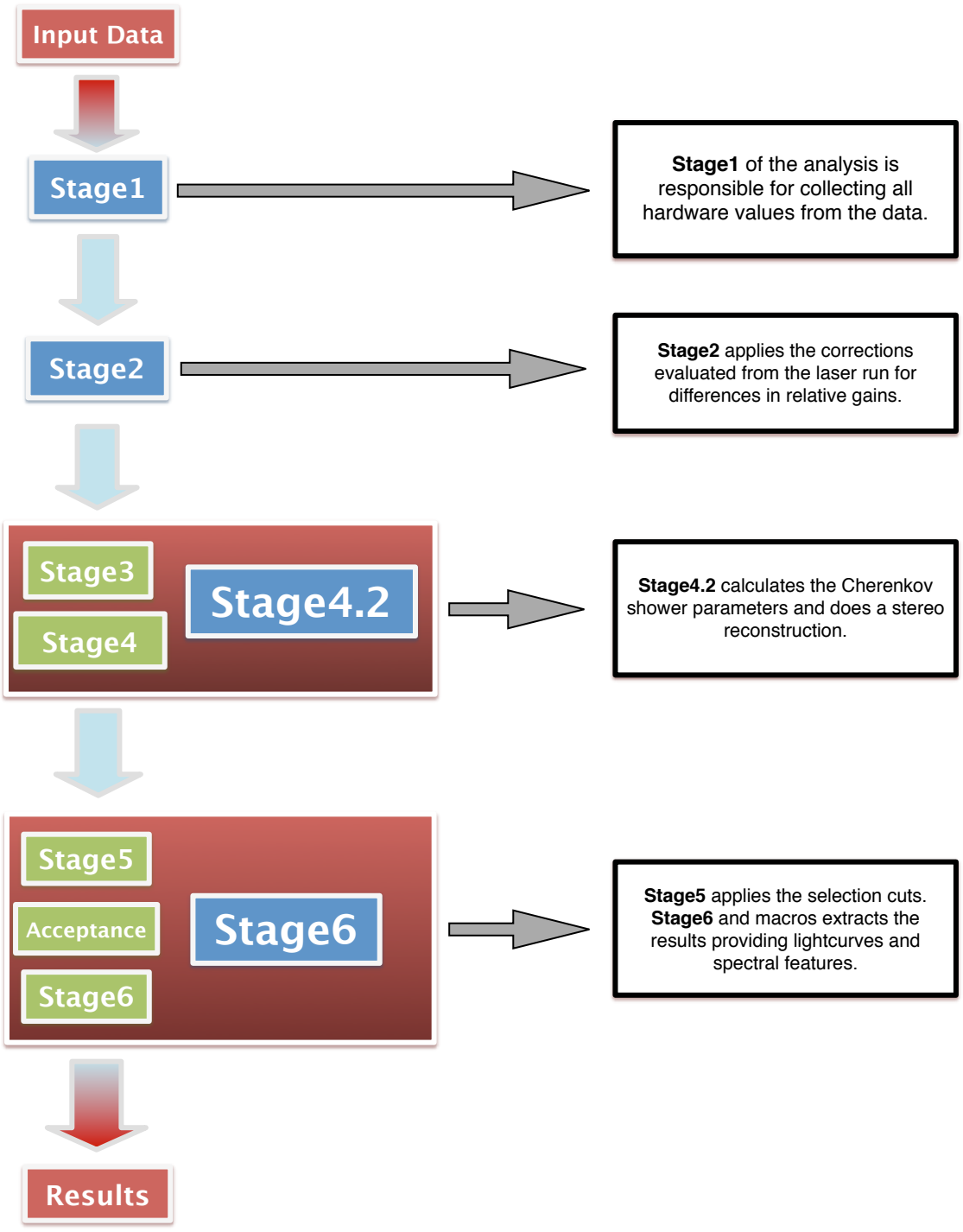

Figure 5.1: Block diagram of the VEGAS software designed as a pipeline with four main steps.

the shower core can be determined with a very precise accuracy. When the telescopes are pointed with the central pixels located at an offset distance in declination or right ascension from the nominal source position, the observing mode is called *wobble* mode. The background event rate is estimated from sky regions in the field of view at the same offset distance from the centre as the target. This process offers the possibility of continuous monitoring of a target without having to interrupt the observation of the source. Due to inhomogeneities caused, for example, by single broken pixels in the camera, it is necessary to introduce a particular observation strategy. The rotation of the target around the camera centre reduces the inhomogeneities and further decreases the need for corrections. When possible, the same number of runs are recorded with the target located at the same offset distance from the centre of the field of view, alternately to the North (N), South (S), East (E) and West (W) directions in the equatorial coordinate system. The optimum offset distance of the source/target location from the centre of the field of view is determined by using simulations of the detector response. However, it is possible that the background measurement might not be statistically independent from the signal of a strong source (Bretz, 2005).

5.2 FADC Charge Integration Window

The charge statistical information (referred to as Qstats by VEGAS) includes the mean and the variance of the charge in each channel when there is no Cherenkov pulse present, but the PMT and related hardware are switched on. The charge statistics can be computed for a series of timing integration window lengths, with length expressed

here in units of number of samples. Each sample has a duration of 2 ns. Note that charge statistics change during a run, mainly because of rotating star fields, the telescope elevation and the weather.

The measurements of the pulse height and shape are highly dependent on the FADC window sampling. Based on the experience of data analysis, in order to maximize the signal to noise ratio in the case of the low-gain read-out mode, a timing integration window length of 12 samples (or 24 ns) is needed, whereas a high-gain read-out mode needs an integration window length of 7 samples (or 14 ns). Analyses of data confirm that the shower pulses are well contained by these timing integration window lengths.

At present, VEGAS calculates a mean trace arrival time for each camera and then defines the FADC integration window. Based on our dataset, we set the timing integration window at 7 samples. The timing integration window width of 12 samples would be needed if a larger number of lower-energy events (< 300 GeV) were present in our dataset.

Relative-timing corrections are necessary for a correct positioning of the timing-integration window for each channel. The arrival time of the photoelectron pulse generated by a given PMT channel, referred to as T_{zero}, is defined as the time at which the edge of the digitized pulse FADC trace reaches half of its maximum value (Figure 5.2). The arrival time of each FADC trace is different. It is dependent on cable length, HV and any electronic delays on the FADC boards. Relative timing between channels is returned by the T_{offset} calculation. For a given channel, this is the average difference between a specific channel's arrival time and the average arrival

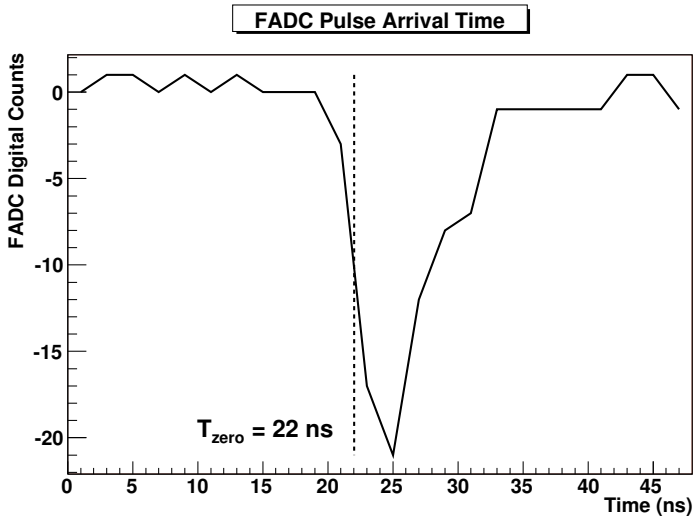

Figure 5.2: This FADC trace has 24 samples, corresponding to 48 ns duration. The arrival time of a single FADC trace, referred to as T_{zero}, is defined as the time on the leading edge at which the trace reaches half of its maximum value after subtraction of the pedestal baseline (Cogan, 2006).

time of the event. The arrival time of the event, T_{event}, is simply the average of the T_{zero} arrival times of all the channels in that event (see Figure 5.3) and is given by

$$T_{event} = \frac{1}{n}\sum_{i=1}^{n} T_{zero}$$

where n is the number of channels. The time difference ΔT between the i^{th} channel and that event arrival time is:

$$\Delta T_i = T_{zero_i} - T_{event}$$

T_{offset} can be obtained by computing the average measured arrival time of each channel for m events[1] (Cogan, 2006). For a large number of events, m, the average relative

[1]Separate T_{offset} calculations are made for the high-gain and low-gain channels

arrival time for a single channel i is given by

$$T_{offset_i} = \frac{1}{m}\sum_{j=1}^{m} \Delta T_{i_j}$$

where ΔT_{i_j} is the time difference of the i^{th} channel in the j^{th} event.

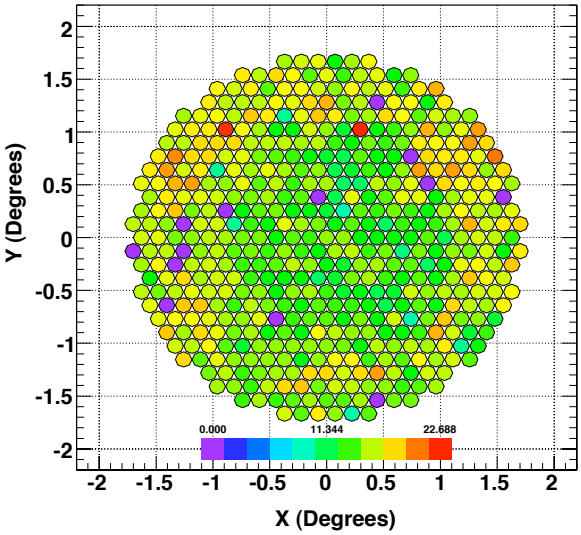

Figure 5.3: Example of the measured T_{zero} arrival times per channel.

5.3 Calculation of Pedestals

Pedestal triggers are artificial triggers introduced to inject events not associated with showers. The pedestal is the output value of a FADC when there is no Cherenkov light input. This base value is adjustable and is usually set at around 16 digital counts. Then, small negative fluctuations ascribable to the night-sky background do not result in negative values that the FADCs cannot properly handle. In order to correctly account for the FADC charge together with its statistical significance associated with

the night-sky background, both the pedestal and the variance (referred to as the "pedvar") must be computed.

In order to generate reliable statistics for the pedestal measurement, a high pedestal event rate is desirable, but this increases deadtime. Independently for each PMT camera, we subtract the mean pedestal value from each FADC recorded value and, then, we divide the result by pedvar. Channel records are identified as not reliable (labeled "bad") when the difference between each single FADC value and the variance computed over all the recorded FADC values is too large.

The pedestal distribution for a single channel can be calculated for multiple FADC timing integration window sizes. Allowing circular read-out, a FADC trace always provides sufficient samples to accommodate a multiple of the integration window length. For example, the FADC buffers can handle cases in which the integration window size is not a divisor of 24 samples (that is the length of the FADC buffer) but, generally, the last window will be not statistically independent from the first. The measure of mean and variance of pedestals is determined for each channel every three minutes of the data run. This interval is long enough to accumulate sufficient statistics to give a reliable measure of mean and variance but also short enough to be sensitive to changes in the level of night-sky background.

In the presence of a large night-sky background contamination, the charge distribution is much wider (Figure 5.4). For an observation field such as the Crab Nebula, the night-sky background is significantly greater than that of the observation field of the extragalactic source Markarian 421, resulting in a wider pedestal distribution.

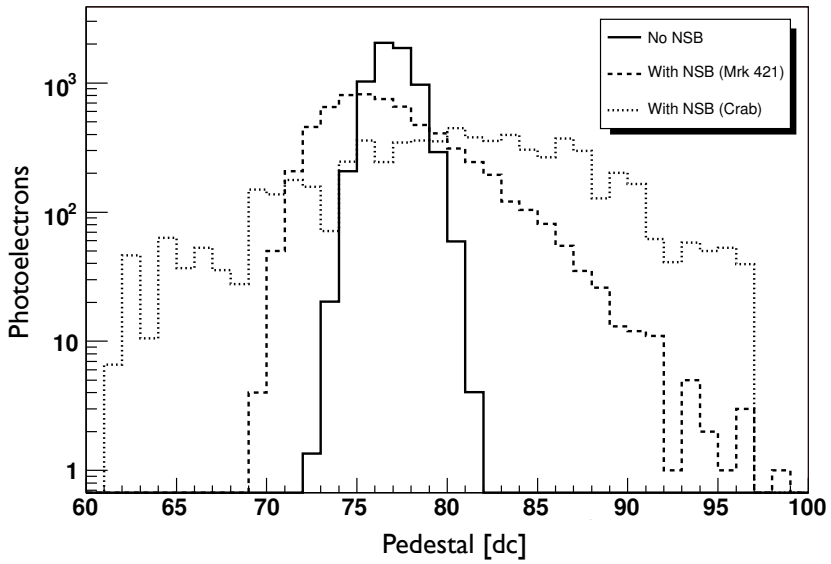

Figure 5.4: Example of pedestal distributions. Due to its nature, night-sky background is not described by a "peaking" distribution and, hence, it does not have a symmetry axis. In the case of Markarian 421, we have less broadening of the pedestal distribution than the Crab pedestal distribution since the fluctuation of the night-sky background is smaller in the FOV of Markarian 421 (Cogan, 2006).

5.3.1 Calculation of Pedestals

In addition to being triggered by Cherenkov light from extensive air showers, an IACT may be triggered by events due to fluctuations in the night-sky background. We could use those fluctuations in the night-sky background to roughly test inhomogeneities across the PMT camera FOV. A more precise approach is pursued by recording, at the beginning of each night, a few minutes of uniform intensity UV laser shot run, which is referred to as a "laser run". VERITAS uses a nitrogen laser system with a wavelength of $\lambda = 337$ nm and a pulse length of 4 ns. The beam is directed into a dye, which fluoresces at 400 nm. The laser beam is sent through neutral density filters in sequential wheels which vary the transmission of the beam between 0.02% and 100% (Hanna, 2008). The beam is, then, divided among ten optical fibres, four of which are routed to optical diffusers located on the optical axes of the telescopes at 4 metres from the PMTs to uniformly illuminate the cameras. The recorded data are used to measure the relative timing between PMT pixels and, more importantly, to compute the relative gains of pixels since each pixel returns a different response to the same amount of simultaneous light illumination. After this gain calibration is applied, a dedicated algorithm is used to exclude pixels in the image with a signal due to night-sky background noise and malfunctioning pixels.

This process is known as "image cleaning". It consists of a two-step method which mainly depends on each single PMT pulse and on a measure of the noise in each pixel (pedvar). The pulse recorded in the FADC traces is integrated and compared to the pedvar value. The pixel is classified as a "picture" pixel if the integrated pulse is, at least, 5 times the pedvar value. Any pixel bordering a picture pixel having an

amount of charge greater than 2.5 times the pedvar is subsequently classified as a "boundary" pixel. Finally, the image cleaning algorithm identifies and discards the picture pixels that have no adjacent boundary pixels. Thus, only data from picture pixels with close boundary pixels are kept.

5.4 Shower Reconstruction

5.4.1 Hillas Parameters

On a single telescope basis, the parameterization of any cascade event is performed by *Stage 4.2*. Cosmic ray induced air showers produce neutral pions that decay to give γ-rays, which in turn produce electromagnetic cascades with emission of Cherenkov light. However, Cherenkov light produced by hadronic showers is distributed over a larger lateral distribution than in the case of showers of γ-ray initiated events. Consequently, γ-ray induced EASs present a very compact elliptical shape projection on the camera image, whereas cosmic ray induced air showers have quasi circular sections. Such morphological aspects make it possible to statistically categorize the showers in relation to their original initiating particle.

After the image cleaning process, the recorded camera images are parameterized by calculating first and second statistical moments of the light distribution using events in the camera plane coordinates. The original Hillas parameterisation approach introduces six parameters (Hillas, 1985) obtained by fitting an ellipse to the images (see Figure 5.5):

- ***distance***: angular distance between the centre of the field of view and the

image centroid (degrees).

- ***width***: transverse angular extent of the fitted ellipse (degrees, the semi-minor axis length).

- ***length***: longitudinal angular extent of the fitted ellipse (degrees, the semi-major axis length).

- ***miss***: perpendicular angular distance between the image axis and the centre of the field of view (degrees).

- ***azwidth***: transverse angular extent of the fitted ellipse, but in respect to an axis that passes through the image centroid and through the centre of the field of view (degrees).

- ***fracN***: percentage of the signal contained in the N highest pixels.

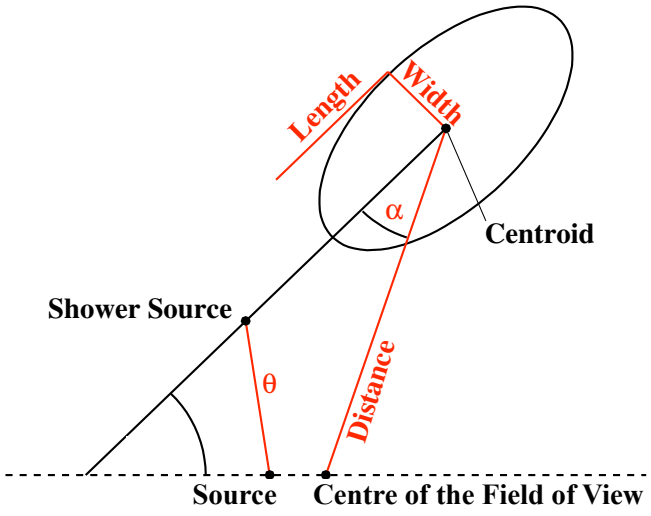

Figure 5.5: The diagram shows 2D Hillas parameters (Hillas, 1985) and subsequently defined parameters (adapted from Cogan, 2006).

Subsequently, some further parameters related to the shape of the camera reconstructed image were also introduced (Lessard *et al.*, 2001):

- $\boldsymbol{x_c}$, $\boldsymbol{y_c}$: coordinates of the centroid of the image, weighted by the signal recorded in the image pixels (degrees).
- $\boldsymbol{\alpha}$: angle between the major axis of the fitted ellipse and the axis that passes through the image centroid and the centre of the field of view (degrees).
- ***size***: sum, in digital counts, of the signals in the image pixels.
- ***asymmetry***: skewness of the signal distribution along the major axis.
- $\boldsymbol{\theta}$: angular distance between the reconstructed shower origin in the field of view and the putative source position.

5.4.2 Shower Reconstruction using Hillas Parameters

Having an array of γ-ray telescopes such as VERITAS, one can combine the measurements of the Hillas parameters and derive a new set of improved parameters that better represent the shower characteristics. Also, the stereoscopic views of the showers make it possible to deduce shower trajectories in the atmosphere with greater accuracy. *Stage 4.2* in VEGAS analysis performs the calculation of the shower trajectories and parameters.

Before proceeding to shower reconstruction, each telescope image is tested for "quality" selection criteria. *Stage 4.2* does not discriminate between γ-rays and cosmic rays but removes events that could give erroneous reconstruction of shower parameters due to images presenting unclear shapes. For example, events could be too

12 samples	
N_{tubes}	> 5
$size$	> 500 d.c.
$distance$	$< 1.43°$

Table 5.1: Quality-cut parameters for low-gain channels with the timing integration window length set to 12 samples. N_{tubes} is the minimum number of triggered tubes required for accepted events.

small on the camera plane or images could be detected with relatively large impact distances and, thus, be truncated at the edge of the camera. The set of quality cuts is summarized in Table 5.1. A better angular resolution allows one to increase the resolution of the location of the shower origins and, consequently, obtain a more detailed map of the observed portion of the sky with a more accurate reconstruction of the source position. It also improves morphological studies of any extended source. During the period covered by our dataset, VERITAS could reconstruct the shower axis to an angular accuracy (or angular resolution) of 0.05° (Cogan, 2008).

VEGAS implements several techniques of shower reconstruction. In the analysis presented in this thesis, we used the default method (or "Method 3"). This method computes and intersects each pair of major axes of the fitted ellipses in the camera plane (Figure 5.6). It determines the axis and the impact distance of the Cherenkov showers using the intersection points (Hofmann *et al.*, 1999). The difference between the putative position of the source in the sky and the reconstructed arrival direction of the showers is defined as θ.

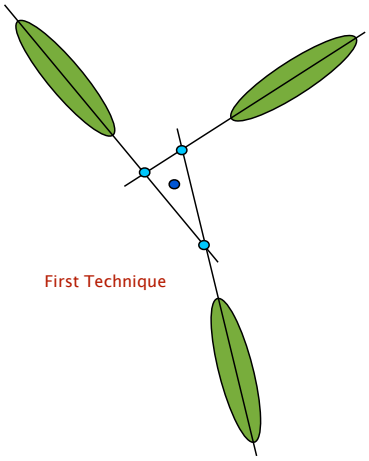

Figure 5.6: Projection of a Cherenkov shower in a 2D plane. This algorithm computes and intersects each pair of major axes of the fitted ellipses in the camera plane, determining the arrival direction of the recorded Cherenkov-shower events.

5.5 Selection Cuts

After reconstructing the trajectory of the primary particle, it is necessary to extract the information required in order to determine whether the primary particle is a γ-ray or not. Discrimination is based on how the morphology of the showers changes between different initiating particles, since there are differences in the development of the two types of showers as they propagate through the atmosphere. For example, the opening angle in a hadron-initiated shower is wider than the opening angle in a γ-ray induced shower. Moreover, the effect of the interaction of the geomagnetic field with the hadronic EAS provides a further difference between γ-initiated and hadron-initiated showers (Commichau *et al.*, 2008).

The Hillas parameters and the other subsequently defined parameters provide categorizing information regarding the shape of the observed showers. Thus, they can be combined to obtain new parameters that are directly comparable with those

obtained by simulation and fruitful in distinguishing between γ-initiated showers and hadronic showers (Daum *et al.*, 1997). VEGAS introduces the Mean Scaled Width (MSW) and the Mean Scaled Length (MSL) in order to help distinguish between the different classes of images (Valcarcel, 2008):

$$MSW := \frac{1}{N_n} \sum_{n=1}^{N_n} \frac{W_n}{W_{sim}(z_n, d_n, E_n)} \tag{5.1}$$

$$MSL := \frac{1}{N_n} \sum_{n=1}^{N_n} \frac{L_n}{L_{sim}(z_n, d_n, E_n)} \tag{5.2}$$

L_n and W_n are the values of the length and width parameters, respectively, that are measured in camera n. N_n is the number of triggered telescopes. L_n and W_n are compared to $L_{sim}(z_n, d_n, E_n)$ and $W_{sim}(z_n, d_n, E_n)$, which are the predictions for the values of the parameter under investigation based on the zenith angle z_n, the impact distance, d_n, of the shower from telescope n − meaning the distance to the shower core − and the energy, E_n, of the shower (Valcarcel, 2008).

The values L_{sim} and W_{sim} are obtained from simulations. Monte Carlo simulations are very important for VERITAS and VEGAS development, detector design and data analysis (Maier, 2008), especially in order to build look-up tables used to estimate the shower parameters, the energy of the primary particles, and the detector effective area.

The use of MSW and MSL combined parameters is pursued in *Stage 5* of the VEGAS pipeline, which is a proper "cutting" stage, where images that do not resemble γ-ray induced showers are rejected. The adopted optimized cut values are obtained via Monte Carlo shower simulation.

Most of the Cherenkov-shower events from the sky are hadron-initiated showers. Using looser ranges of parameter values in image cuts includes a larger fraction of the

incoming γ-ray initiated showers, but also passes an even larger fraction of hadron events. Tighter cuts would exclude most of the hadron events, but also exclude a larger fraction of real γ-ray events. The optimum parameter values, used in an image cut, are a trade-off between the larger number of the non γ-ray events incorrectly classified as γ-ray events and retained, and the number of real γ-ray events that are not recognized as such and, consequently, discarded.

To measure the performance of a given detector (or a system of multiple detectors acting together), we introduce the following sensitivity value, $\sigma/\sqrt{h}$, where σ is the significance, defined as $E_{Source}/\sqrt{E_{Background}}$. E_{Source} and $E_{Background}$ are the numbers of events per unit of area around the source and the defined background regions, respectively. h is the observation time in hours. The cut values are chosen to optimize the significance.

The ranges of the parameter values used in the image cuts affect the sensitivity and they are optimized separately for each observed object at the beginning of each observing season (assuming, in the majority of cases, a point-like source). There are slight variations in the ranges of individual cut parameters, which are re-optimised year by year to accommodate changes to the telescope configuration, hardware, performance and offline analysis software. The optimization of the cut parameters is different in the case of high gains and low gains (Table 5.2). Cosmic ray background rejection efficiency is up to 99.999%, with retention of more than 50% of the γ-ray events (de la Calle Perez, 2006).

The set of cuts that we used in our analysis was developed to classify any event that triggered at least two telescopes in the same timing window, excluding those events

12 samples, no Tel. 1 and Tel. 4 events					
% Crab	Ring Size	MSW low	MSW high	MSL low	MSL high
	[deg]				
100%	0.157	0.05	1.21	0.05	1.42

Table 5.2: Set of cuts used for Markarian 421 data analysis with timing integration window length of 12 samples and excluding events triggering only Tel. 1 and Tel. 4. The ring size parameter is the radius (expressed in degrees) of the source region encircling the putative position of the observed source.

that only triggered the two closest telescopes (Tel. 1 and Tel. 4) . At low energy ($\leq$ 300 GeV), the shape cuts MSW and MSL are not very effective in discriminating between γ-ray events and cosmic ray events, since the angular resolution of the detector begins to degrade (Celik, 2008). Indeed, lower-energy showers with faint Cherenkov light emissions are more difficult to detect than higher-energy ones that result in brighter emissions.

5.6 Signal and Background Estimation

Once the γ-like images have been selected, an analysis is carried out to determine the statistical significance of any excess from the direction of the assumed source. This analysis is carried out by *Stage 6* of VEGAS. Not all of the observed γ-ray like events within the field of view are accepted, only those within a certain angular distance of the assumed source position. The angular distance between the reconstructed arrival direction and the putative source location is indicated by θ in Figure 5.5.

5.6.1 Reflected Regions Background Model

In our data reduction, we adopted the reflected regions background model approach (Aharonian *et al.*, 2006). This algorithm estimates the number of background cosmic ray events in the source (or "ON") region that are classified as γ-like events. It does this by looking at the number of γ-like events falling in n_{OFF} background (or "OFF") regions that are each the same size as the source region and are located at the same distance from the centre of the field of view as the source region is located (Figure 5.7a). As an alternative, the VEGAS software also implements the ring background model algorithm (Aharonian *et al.*, 2006) in which the background is estimated using an annular region around the nominal position of the source (Figure 5.7b).

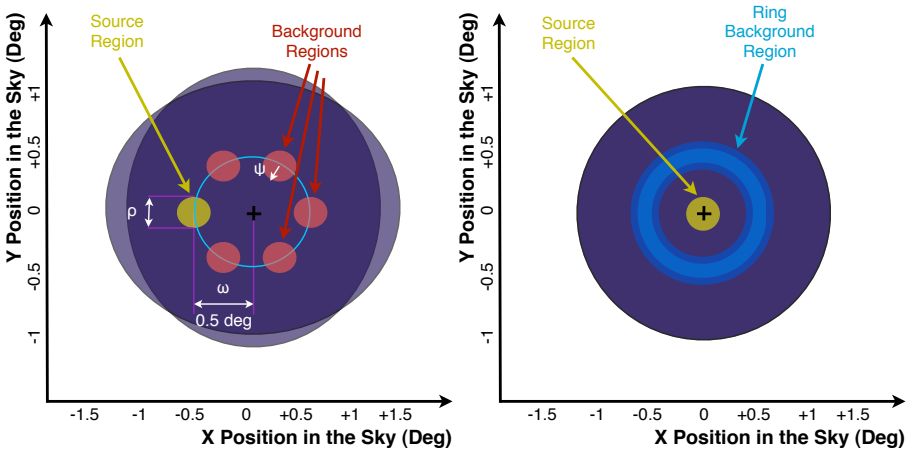

Figure 5.7: **(a)** The centre of the field of view is surrounded by a circle of radius ω (the wobble offset) and n_{OFF} background regions located around that circle. Given the angular diameter of the regions $\rho = 2\psi$, it is possible to fit $N = floor(2\pi/\rho)$ regions, one of which is the source region, around the pointed location. **(b)** Background events are estimated by looking at the number of γ-like events falling in an annular region around the source region. In this case, the background and the source regions have different acceptances. The different shadings between light purple and dark purple are due to the summation of runs with different north, south, east, west wobble offset orientations breaking the circular symmetry.

The reflected regions background model technique may suffer weakly from systematic effects due to radial inhomogeneities in the acceptance behavior. The acceptance at any point across the FOV is defined as the probability of detecting γ-ray or hadron showers from that direction. The acceptance is highest at the centre of the field of view and lower toward the camera's edges. Acceptance also accounts for the variation in sensitivity across the field of view as a function of zenith angle and initial energy of the primary particle (Berge *et al.*, 2007). In the acceptance-modeling process, all events which are categorized by selection criteria as γ-like or as hadron-like events are used to make a bi-dimensional acceptance map with camera coordinates. That map is radially symmetric if, in the modeling, we ignore zenith angle dependencies. A more precise modeling of the acceptance would introduce a small non-radial correction term across the field of view to account for small variations due to the Earth's magnetic field. In order to minimize the systematic effects due to zenith-dependent acceptance variations, we cycled the wobble position through north, south, east and west orientations of the source location on successive runs (Figure 5.7a). Therefore, the acceptance distribution is smoothed to filter out irregularities. Then, the acceptance map is normalized for the acceptance value measured at the camera centre.

5.6.2 Significance

Once we have determined N_{ON}, the number of γ-like events in the region centred on the putative position of the source, we have to estimate $\hat{N}_{BKG}$, the number of the events that were produced by the hadronic background. $\hat{N}_{BKG}$ is obtained by averaging the numbers of γ-like events in the n_{OFF} background regions. The background

estimate is

$$\hat{N}_{BKG} = k \cdot N_{OFF} \tag{5.3}$$

where the parameter k is a normalisation factor, which accounts for solid-angle, exposure-time and zenith-angle. N_{OFF} is the total number of γ-like events falling in the OFF regions.

Since the n_{OFF} background regions are each the same size as the source region and are all at the same distance from the centre of the field of view as the source region, $k = 1/n_{OFF}$ and

$$\hat{N}_{BKG} = \frac{1}{n_{OFF}} \sum_{i=1}^{n_{OFF}} N_{OFF,i} \tag{5.4}$$

where $N_{OFF,i}$ is the number of the γ-like events in the i-th OFF region.

Then, we estimate the final number of real γ-ray events, N_{Source}, with

$$N_{Source} = N_{ON} - \hat{N}_{BKG}. \tag{5.5}$$

Since source and background counts are the results of two independent measurements, $\hat{\sigma}_{N_{Source}}$, the estimate of the standard deviation of N_{Source}, is given by

$$\hat{\sigma}_{N_{Source}} = \sqrt{N_{ON} + k\ \hat{N}_{BKG}} \tag{5.6}$$

The significance, S, is defined as the number of the standard deviations that separate N_{Source} from an expectation of zero signal. Thus

$$S = \frac{N_{Source}}{\hat{\sigma}_{N_{Source}}} = \frac{N_{ON} - \hat{N}_{BKG}}{\sqrt{N_{ON} + k\ \hat{N}_{BKG}}} \tag{5.7}$$

Assuming uncorrelated contributions,

$$\delta S = \sqrt{1 + S^2 \left(\frac{\delta\hat{\sigma}_{N_{Source}}}{\hat{\sigma}_{N_{Source}}} \right)^2} \tag{5.8}$$

where δS is the significance uncertainty and $\delta\hat{\sigma}_{N_{Source}}$ is the corresponding uncertainty on the standard deviation estimate (Valcarcel, 2008; Linnemann, 2003).

5.6.3 Differential and Integral Flux

There is a high probability of detecting a Cherenkov shower when it falls within ~ 100 m radius from the centre of the imaging atmospheric Cherenkov telescope array. When a Cherenkov shower falls in a "transition" region extending a little outside that radius, there is a lower probability that the shower will be detected. The detector effective collection area (or "effective area") is the parameter of the detector's model that compensates for the rate loss of event detections in the transition region.

The effective area at each zenith angle is computed via the simulation of γ-ray events falling randomly in a circle of area A_0 in the plane perpendicular to the optic axis at the centre of the array. A_0 has a radius of 500 m that is chosen empirically since very few showers would trigger the array at such a distance. While VERITAS can detect shower cascades generated at larger distances, generally they are accompanied by large uncertainties in shower reconstruction and, thus, they are discarded. This also reduces the computational demands in building the look-up tables used for the γ-ray energy reconstruction. The effective area of the array for the energy range E_j to $E_j + \Delta E_j$, is given by

$$A_{\mathrm{Eff}}(E_j, E_j + \Delta E_j) = A_0 \frac{N_{Sim,cut}(E_j, E_j + \Delta E_j)}{N_{Sim}(E_j, E_j + \Delta E_j)} \tag{5.9}$$

where $N_{Sim,cut}(E_j, E_j + \Delta E_j)$ and $N_{Sim}(E_j, E_j + \Delta E_j)$ are, respectively, the number of simulated events that pass the cuts and the number of simulated showers in a given energy bin E_j and $E_j + \Delta E_j$ (Mohanty *et al.*, 1998).

For each detected event that is reconstructed and passes the event-selection criteria, a collection area is calculated. The events are counted in discrete energy bins labelled by j, each covering the interval $(E_j, E_j + \Delta E_j)$. Then, in the same energy range, the differential flux dF_j/dE (Aharonian *et al.*, 2004) is given by

$$\frac{dF_j}{dE} = \frac{1}{T} \cdot \frac{N_{Source}(E_j, E_j + \Delta E_j)}{\Delta E_j \cdot A_{\rm Eff}(E_j, E_j + \Delta E_j)} \tag{5.10}$$

where T is the observation duration and $N_{Source}(E_j, E_j + \Delta E_j)$ is the number of γ-ray events with energy between E_j and $E_j + \Delta E_j$. The differential flux uncertainty is

$$\delta\left(\frac{dF_j}{dE}\right) = \frac{1}{T} \cdot \frac{\delta N_{Source}(E_j, E_j + \Delta E_j)}{\Delta E_j \cdot A_{\rm Eff}(E_j, E_j + \Delta E_j)} \tag{5.11}$$

where δN_{Source} is the uncertainty on the number of the γ-ray events arising from the source region. We assume that uncertainties in quantities other than N_{Source} are negligible.

Finally, we introduce the integral flux, since it is often useful in comparing different source emission models and results from different instruments. It has been a standard practice to assume a simple power law for the source spectrum (Mohanty *et al.*, 1998):

$$F(E)dE = F_0 \; E^{-\Gamma} dE \tag{5.12}$$

where $F(E)dE$ is the number of γ-rays per unit area per unit time within the infinitesimal energy interval $(E, E + dE)$, F_0 is the flux constant and Γ the spectral index. Then, the integral flux, which is integrated over the energy range above the threshold energy of the array.

$$F_{Int} = F_0 \int E^{-\Gamma} dE = \frac{1}{1-\Gamma} F_0 \; E^{1-\Gamma} \tag{5.13}$$

5.7 VERITAS Dataset Results

Since the discovery of its TeV emission (Punch *et al.*, 1992), Markarian 421 has been continuously monitored by a number of ground-based imaging atmospheric Cherenkov telescopes. Over this monitoring period, Markarian 421 has shown moderate (Abdo *et al.*, 2011), high and very-high γ-ray emission activity states (Krennrich *et al.*, 2002; Aleksić *et al.*, 2010) and some rapid flares on timescales from a few days to a few tens of seconds (Pichel & Rovero, 2008; Gaidos *et al.*, 1996; Zweerink *et al.*, 1997; Fossati *et al.*, 2008; Donnarumma *et al.*, 2009). Its relatively high emission level in most cases allows for the reconstruction of the γ-ray energy spectrum.

In the present work, we focus on a VERITAS Markarian 421 database recorded during the September 2007 to June 2008 (MJD 54344-54618) observing season. In total, 249 observation runs were attempted on Markarian 421 during that season. All data were taken in wobble tracking mode using 0.5° offsets. 29 of these runs were unusable because of problems related to the data acquisition system and observer errors. Further data diagnostic checks were performed after the application of *Stage 1* of the analysis of the remaining runs. In particular, the stereoscopic trigger event rate was verified to be stable and above 150 Hz, which indicates that the acquisition system worked properly. We rejected only 20 runs out of a set of 32 runs that were terminated early by observers and had durations ranging from 5 to less than 15 min. A further 52 runs were rejected because they were recorded during poor weather conditions. 148 good runs, with a total livetime of about 2600 min ($\sim$43 h), remained after all these quality checks. A detailed listing of the data runs and corresponding laser runs used can be found in Appendix A. The dataset was analyzed applying the VERITAS cut parameters set out in this chapter (Section 5.5, Table 5.2).

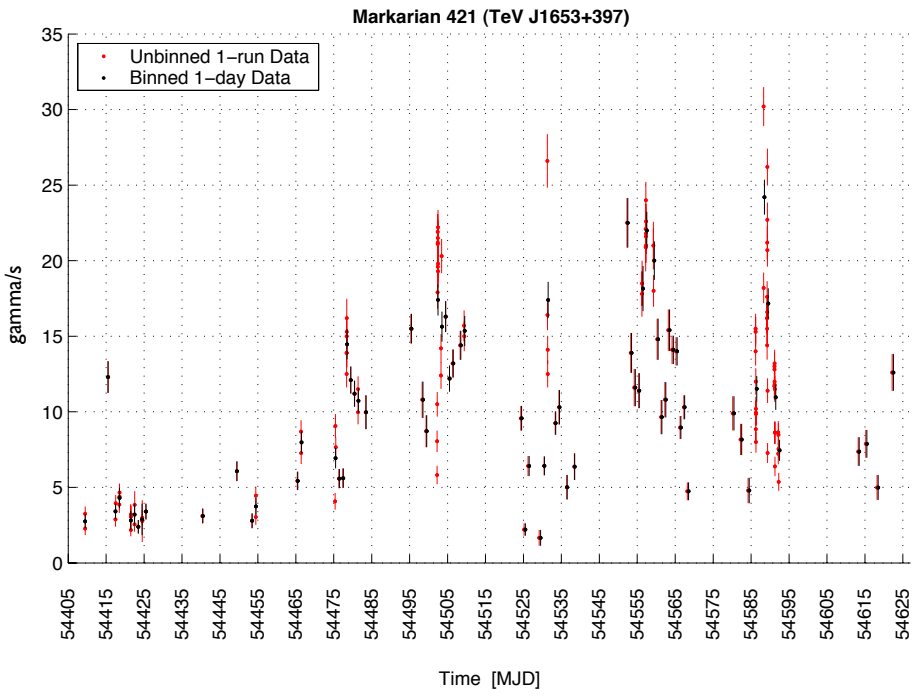

Figure 5.8: Markarian 421 excess rates (γ-rays per second) recorded by VEGAS from September 2007 to June 2008 (MJD 54344-54618).

VEGAS software is able to identify stars in the field of view by searching a star catalogue. By default, the VEGAS code excludes events arising from circular regions with 0.3° radius centred on the stars present in the FOV (49 Ursae Majoris at RA 165.210°, Dec 39.212° and 47 Ursae Majoris at RA 164.162°, Dec 40.698°).

The events passing VERITAS cuts are used to obtain the excess-rate behavior (see Figure 5.8) and to produce a two-dimensional sky map according to their arrival direction (see Figure 5.9), with corrections made for variation in the acceptance across the field of view.

Figure 5.10 illustrates the so called θ^2 plot for Markarian 421 during the 2007-2008 observing season. The θ^2 plot is a mono-dimensional representation of the events contained in the two-dimensional sky map (Figure 5.9). It is computed by integrating

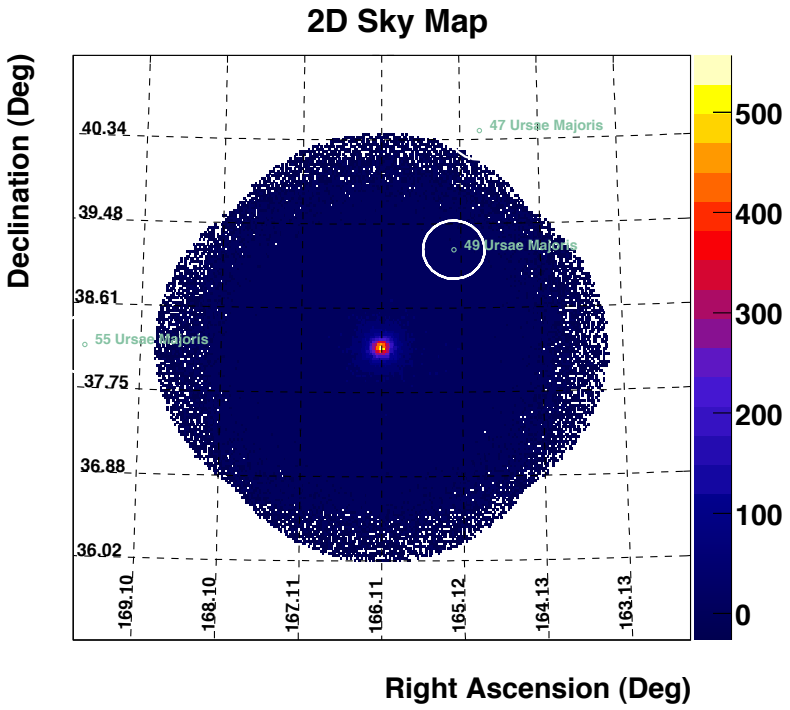

Figure 5.9: The arrival directions of the reconstructed γ-ray-like showers are binned in square bins of width 0.025°. Markarian 421 is located at the centre of the field of view.

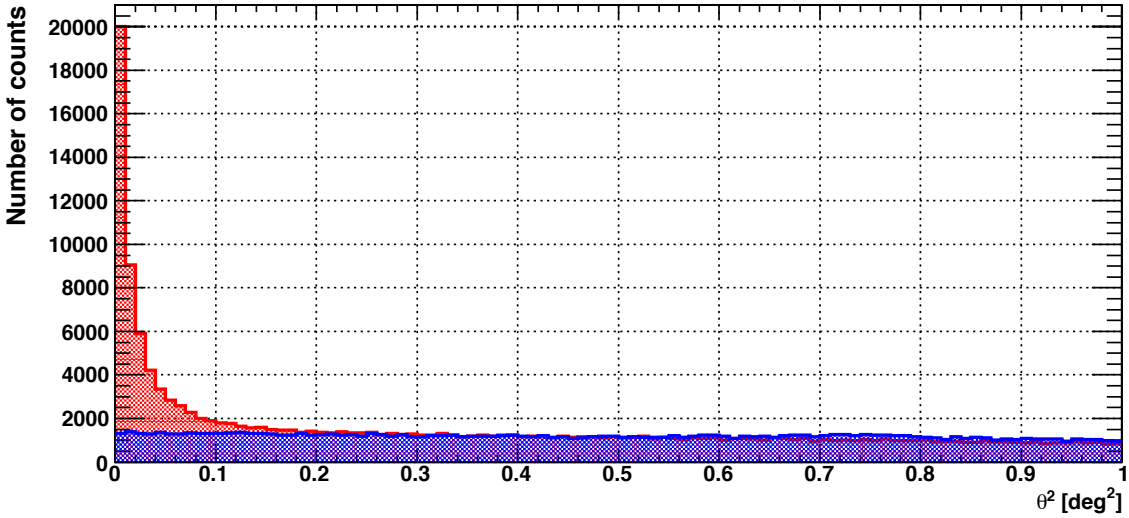

Figure 5.10: θ^2 plot for Markarian 421 during 2007-08 observing season. In red we have the number of the source counts and in blue the background estimate. The background estimate is obtained averaging the numbers of events falling in the same bins in OFF regions.

the event number in a series of annular regions centred on the source position with increasing inner and outer radii. In red we have the number of the source counts and in blue the background estimate. The narrow peak at small values of θ^2 indicates an excess of showers arriving from the direction of the source position. N_{ON}, the number of γ-like events from the source, is estimated by integrating the number of the events inside a circular region of radius 0.157° centred on the source position ($N_{ON} = 27006$ events). The same operation is carried out on the background regions and then normalized to obtain $\hat{N}_{BKG}$, an estimate of the background in the source region ($\hat{N}_{BKG} = 3539$, see Formulas 5.5, 5.3 and 5.4).

To assess if a given number of γ-ray excess events is unlikely to have arisen by chance, we computed its statistical significance level using Formulas 5.7 and 5.8. The significance of the number of excess events from Markarian 421 over the complete

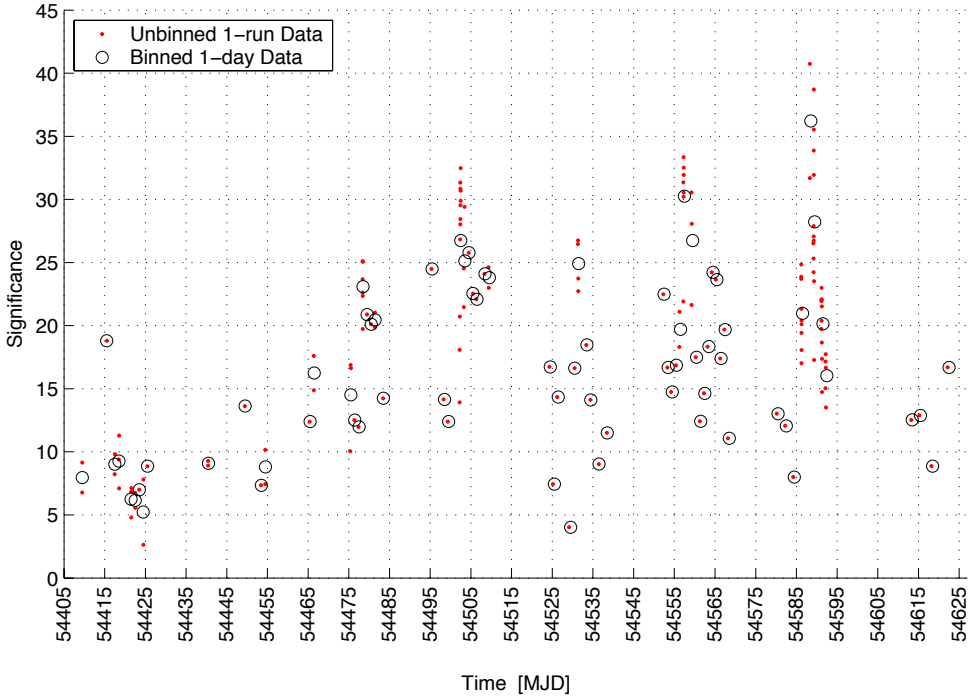

Figure 5.11: Markarian 421 significance of excess number of events plotted on run-by-run and daily bases.

dataset is around 223σ. Significances on a run-by-run and on a daily basis are shown in Figure 5.11. In most of the cases, due to its high level of γ-ray emission at TeV energy, Markarian 421 provides a high number of event detections, easily allowing the reconstruction of the energy spectrum of the γ-ray emission.

A time-dependent integral flux was then computed from the number of excess events (see Formulas 5.10, 5.11, 5.12 and 5.13). The integral fluxes have been calculated for the entire spectrum above 300 GeV (Figure 5.12). The periodic gaps in the dataset are due to no observations being taken during bright-moon phases. The Markarian 421 differential energy spectrum computed with the VERITAS dataset between October 2007 and June 2008, above 300 GeV, is shown in Figure 5.13. The best power-law fit yielded an index of $\Gamma = 2.35 \pm 0.01$ with a reduced χ^2 minimization

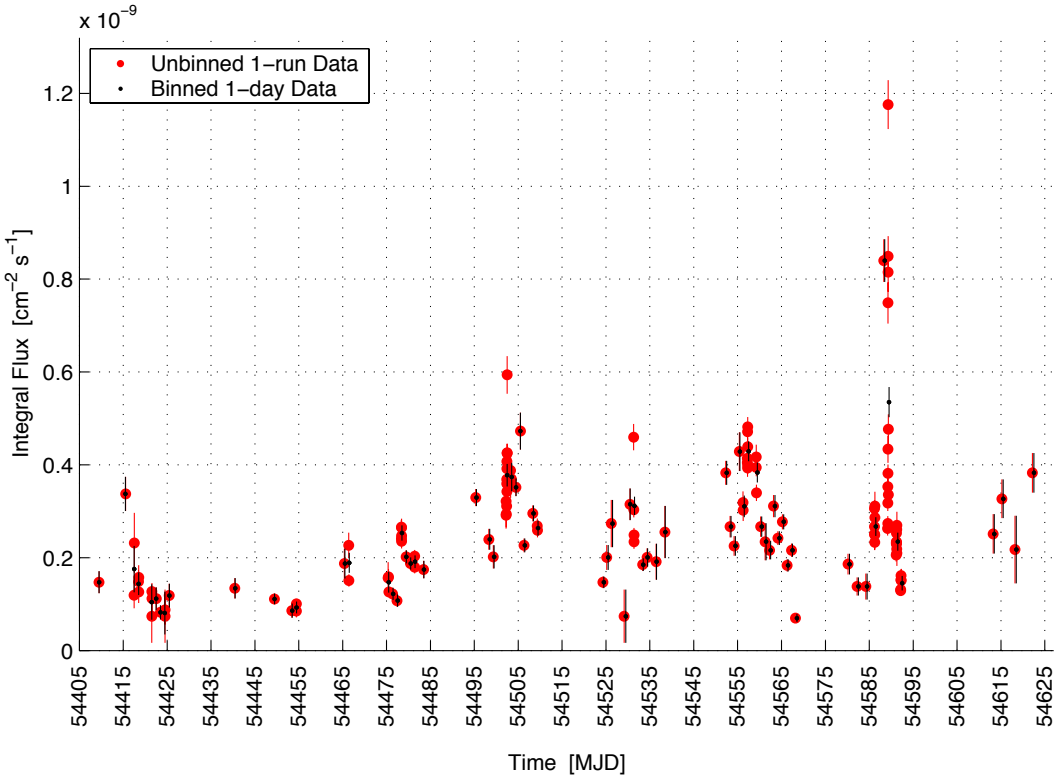

Figure 5.12: The Markarian 421 run-by-run integral flux lightcurve and the daily averaged (binned) lightcurve recorded by VERITAS during the 2007-08 season.

of 32.1. However, the power law plus exponential cutoff fits even better, giving an index of $\Gamma = 2.08 \pm 0.03$ with a cutoff energy at 4.43 ± 0.40 TeV (reduced χ^2 of 2.2).

In May and in June 2008, the dataset showed two temporal intervals with high levels of emission. During high flares of May 2^{nd} and 3^{rd} 2008 (MJD $54588 - 54589$), we obtained for the power law, and for power law plus an exponential cutoff, spectral indices of $\Gamma = 2.23 \pm 0.06$ and $\Gamma = 1.73 \pm 0.26$ with exponential cutoff at 3.73 ± 1.78 TeV, respectively. For June 6^{th} (MJD 54623) flare, we obtained $\Gamma = 2.35 \pm 0.17$ and $\Gamma = 2.05 \pm 0.55$ with the cutoff at 5.24 ± 0.95 TeV for the power law and the power law plus exponential cutoff fittings, respectively.

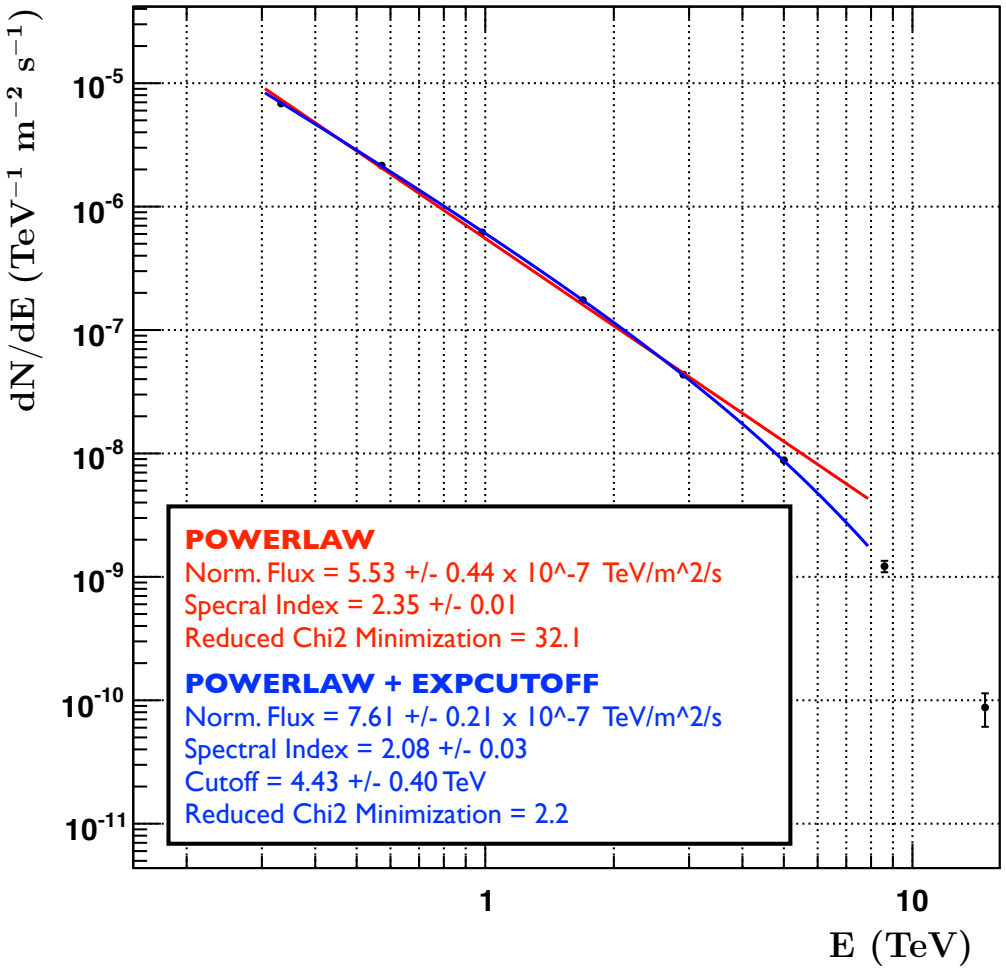

Figure 5.13: The emission spectrum of Markarian 421 observed by VERITAS during the 2007-2008 season.

The largest known TeV flare from Markarian 421, which occurred around 2^{nd} and 3^{rd} May, 2008 (MJD $54588 - 54589$), reached a peak count rate of nearly 10 Crab. There, the characteristic timescales of flux variability decreased to less than a hour since the flare was well contained within a time interval of 5 hours (Acciari *et al.*, 2011) and the power law fit in the spectrum for a very-high state was $\Gamma = 1.87 \pm 0.17$ with an exponential cut off of 2.74 ± 0.60 TeV. Our results statistically agree with those of Acciari *et al.* (2011), but there is a slightly bigger uncertainty. This is ascribable to the use of different analysis software and different releases of the lookup tables. Other historical strong flares were recorded in 1996 and 2001 - see Zweerink *et al.* (1997) and Donnarumma *et al.* (2009), respectively. During the flare of June 6^{th}, 2008, Donnarumma *et al.* (2009) obtained a power law photon index fit of $\Gamma = 2.78 \pm 0.09$, computed using VERITAS, HESS, and MAGIC joint observations. The small offset between our results and the Donnarumma *et al.* (2009) results is ascribable to the selection of different datasets of observations.

A further comparison with the analysis of data recorded on March 2001 by the Whipple Collaboration (Krennrich *et al.*, 2002) shows the Markarian 421 TeV power-law spectrum shifted from $\Gamma \simeq 2.72 \pm 0.11$ (low-activity state) to $\Gamma \simeq 1.89 \pm 0.11$ (high-activity state).

For sudden high flux variations, our results show evidence for correlation between TeV flux increases and TeV spectral hardening (see Figure 5.14). By using a power law plus exponential cutoff to model the TeV spectrum, we obtained a correlation index of 0.86 ± 0.42 over the whole TeV spectrum (see Figure 5.14).

We should point out that the majority of the TeV studies on Markarian 421 do not describe its low and very-low activity states well - with some outstanding exceptions

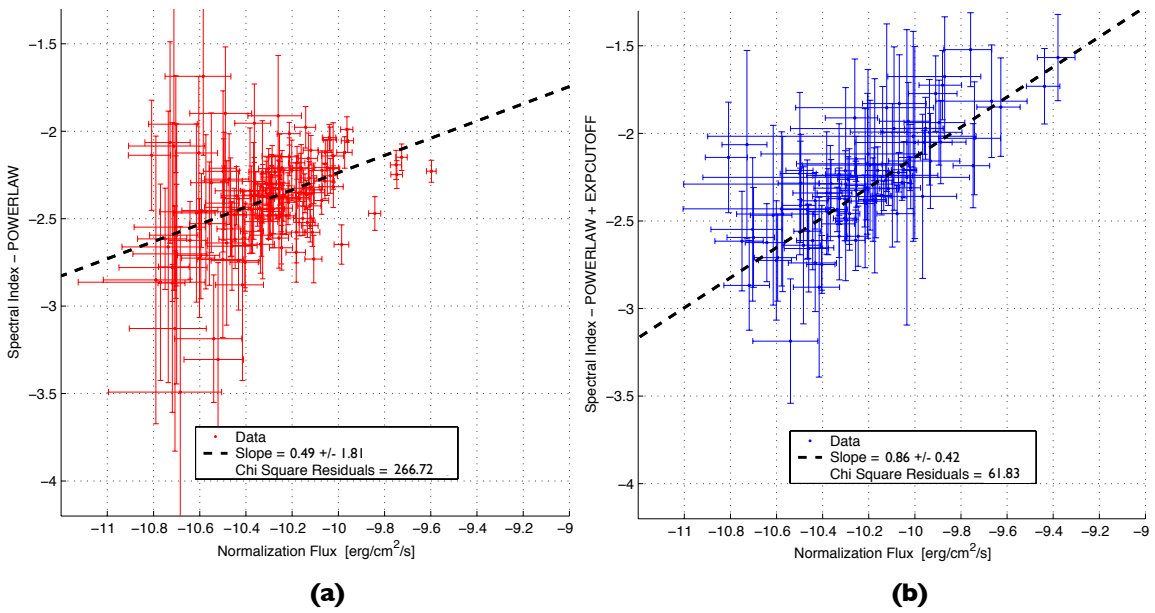

Figure 5.14: Scatter plots between the Markarian 421 spectral indexes and normalization flux factors **(a)** in the case of the spectral power law fitting and **(b)** the power law plus exponential cutoff fitting.

(Acciari *et al.*, 2011; Abdo *et al.*, 2011). The main reason is that, traditionally, several observing campaigns were triggered by an enhanced flux level of X-rays and γ-rays and hence many of the studies on Markarian 421 are biased towards high and very-high activity states. In these studies, it is likely that a reduced number of more powerful processes dominates, providing the largest fraction of emitted radiation and hiding more moderate contributions produced by secondary emission processes. In fact, from 5^{th} August, 2008, to 12^{th} March, 2010, Abdo *et al.* (2011) carried out the most extensive multiwavelength campaign (MWL) on Markarian 421. That campaign did not suffer from a "high-activity bias" and its results can be considered in a more general context. During this period, Markarian 421 showed an average flux of about half that of the Crab Nebula, and displayed mild flux variations of a factor of two.

Above 300 GeV, the resulting spectrum was fitted with a single log-parabola

$$F(E) = K \left(\frac{E}{0.3 \text{ TeV}} \right)^{\Gamma + \beta \log(\frac{E}{0.3 \text{ TeV}})} \tag{5.14}$$

where $K = 6.50 \pm 0.13 \times 10^{-10}$ ph/cm^2/s/erg, $\beta = 0.33 \pm 0.06$ and $\Gamma = 2.48 \pm 0.03$ with $\chi^2/NDF = 11/6$. The comparison with the fits of simple power law functions returned larger fitting uncertainties, which clearly confirmed the presence of a curvature in the spectral energy distribution (SED). Thus, beside a strong emission, a portion of the recorded signal power is provided by secondary, yet not well investigated, blazar emission mechanisms that contribute their own characteristic spectral features.

Chapter 6

Variability Analysis and Correlation

High BL Lacertae object Markarian 421 was the second VHE source that was detected (Punch *et al.*, 1992). Following this discovery, the astrophysical community has continually documented its emissions and variability (Macomb *et al.*, 1995; Takahashi *et al.*, 1996). Several multiwavelength campaigns investigated Markarian 421 variability on short timescales − from a few seconds to hours, see Zweerink *et al.* (1997); Błażejowski *et al.* (2005); Donnarumma *et al.* (2009) − and on longer timescales − from a day to weeks and years; see Acciari *et al.* (2011); Abdo *et al.* (2011).

Historically, X-ray emission is known to be the most variable portion of the blazar spectrum and it shows very unpredictable trends and a large variability (Zhang *et al.*, 2005). However, during the 2007-2008 observing season, Markarian 421 exhibited a larger TeV variability than X-ray variability (Pichel & Rovero, 2008; Aleksić *et al.*, 2010; Acciari *et al.*, 2011). As a result of such large variability and unpredictable lightcurve behavior, blazars were treated as random nonstationary processes.

6.1 Blazar Activity

Blazar emission studies investigate the spectral energy distribution (SED) (Finke *et al.*, 2008) and/or carry out the time-domain analysis of the emission (Zhang *et al.*, 2005). In principle, by combining these approaches, it is possible to obtain a considerable amount of information in order to identify the blazar emission mechanisms. However, in many cases, it is only possible to apply one of these two approaches.

The VHE and UV data discussed in this thesis form part of a larger multiwavelength study, which includes SED analysis and modeling (Acciari *et al.*, 2011). Although for the same observational period very detailed spectral studies of Markarian 421 have been provided at different wavelengths − see Pittori *et al.* (2008); Reyes (2008); Donnarumma *et al.* (2009); Acciari *et al.* (2009b); D'Ammando *et al.* (2009) − a complete time analysis of these data has not yet been published.

The VERITAS 2007-2008 dataset had a relatively regular observation scheduling. The majority of the UVOT dataset is distributed in three dense observation periods consisting of a total of just 40 days. The division of TeV data roughly corresponds to lunar dark periods. Although, in principle, we should not expect a simultaneous variation between TeV and UV bands (due to their frequency separation and different emission processes), it would be desirable to have the observations uniformly spread over time. Since UVOT and VERITAS observations are generally not simultaneous, we have identified some common intervals in time to make a comparison possible between these two different datasets. We have listed the start-time and the end-time for each individual subinterval in Tables 6.1 and 6.2. The hardest constraint in selecting such time intervals was how to match the TeV observations with the

UVOT observation schedule, which is largely unevenly sampled. In general UVOT observations were not simultaneous to VERITAS observations (see Figure 6.1).

Within each time slot we identified, the source presents a particular activity state. Generally, different activity states correspond to different combinations of dominant emission mechanisms (or modes[1]) that produce a particular lightcurve trend (or behavior). The "Activity" column in Table 6.1 reports the average activity levels which describes the source emission behavior. Such description is achieved by introducing one letter representing the dominant trend that is the biggest in terms of measured signal power. In Table 6.2, the same column reports composite average activity levels which more precisely describe the even more complex blazar emission behavior at TeV energies. There, for each time interval, the first letter represents the dominant trend and the second stands for the secondary one.

Looking at Figure 6.1, we see that the UVOT data have similar variations in the different channels, likely due to the relatively small frequency separation of ultraviolet bands. Consequently, as a first order approximation, we argue that the observed UV emission in different bands is produced by the same combination of underlying blazar processes.

[1]Types of systems are classified in terms of their independent physical parameters that are called modes. They are, in fact, the degrees of freedom (or dimensions) of the system. Systems are, then, modeled by identifying dominant and secondary modes that correspond to dominant and secondary emission mechanisms.

UVOT Period Subdivision Dataset

Period	Subinterval	Date	MJD Start-End	Days	Activity	Filter	Obs.	Obs. 1-Day
						UVW1	55	29
Season		1^{st} Nov 2007 - 18 Jun 2008	54405 - 54635	230	M	UVM2	60	30
						UVW2	66	31
0	-	1^{st} Nov 2007 - 30 Jan 2008	54405 - 54495	18	-	-	-	
						UVW1	-	-
	A	30 Jan 2008 - 4 Feb 2008	54495 - 54500	5	-	UVM2	-	-
						UVW2	-	-
						UVW1	18	8
1	B	4 Feb 2008 - 17 Feb 2008	54500 - 54513	13	H	UVM2	24	10
						UVW2	24	10
						UVW1	-	-
	C	17 Feb 2008 - 24 Feb 2008	54513 - 54520	7	-	UVM2	-	-
						UVW2	-	-
						UVW1	2	1
	A	24 Feb 2008 - 4 Mar 2008	54520 - 54529	9	M	UVM2	2	1
						UVW2	2	1
						UVW1	-	-
2	B	4 Mar 2008 - 9 Mar 2008	54529 - 54534	5	-	UVM2	-	-
						UVW2	-	-
						UVW1	2	1
	C	9 Mar 2008 - 20 Mar 2008	54534 - 54545	11	M	UVM2	2	1
						UVW2	2	1
						UVW1	-	-
	A	20 Mar 2008 - 31 Mar 2008	54545 - 54556	11	-	UVM2	-	-
						UVW2	-	-
						UVW1	8	5
3	B	31 Mar 2008 - 6 April 2008	54556 - 54562	6	M	UVM2	8	5
						UVW2	7	5
						UVW1	13	6
	C	6 April 2008 - 19 April 2008	54562 - 54575	13	L	UVM2	12	6
						UVW2	13	6
						UVW1	8	4
4	-	19 April 2008 - 14 May 2008	54575 - 54600	25	M	UVM2	9	5
						UVW2	11	6
						UVW1	3	2
5	-	14 May 2008 - 18 Jun 2008	54600 - 54635	35	M	UVM2	3	2
						UVW2	7	2

Table 6.1: The H in the "Activity" column stands for High, M for Medium and L for Low (*e.g.* L stands for low activity of the source during the relevant time interval). The column labeled "Obs." indicates the number of observations made during the selected time interval, whereas "Obs. 1-day" indicates the number of observations binned by adopting a 1-day bin width in the corresponding selected time interval.

VERITAS Period Subdivision Dataset

Period	Subinterval	Date	MJD Start-End	Days	Activity	Obs.	Obs. 1-Day
Season		1^{st} Nov 2007 - 18 Jun 2008	54405 - 54635	230	M H HH	141	67
	A	1^{st} Nov 2007 - 1^{st} Dec 2007	54405 - 54435	30	LM	17	9
	B	1^{st} Dec 2007 - 26 Dec 2007	54435 - 54460	25	LL	6	4
0	C	26 Dec 2007 - 5 Jan 2008	54460 - 54470	10	LM	3	2
	D	5 Jan 2008 - 12 Jan 2008	54470 - 54477	7	LM	4	2
	E	12 Jan 2008 - 30 Jan 2008	54477 - 54495	18	LM	12	6
	A	30 Jan 2008 - 4 Feb 2008	54495 - 54500	5	LH	3	3
1	B	4 Feb 2008 - 17 Feb 2008	54500 - 54513	13	MM	21	7
	C	17 Feb 2008 - 24 Feb 2008	54513 - 54520	7	-	-	-
	A	24 Feb 2008 - 4 Mar 2008	54520 - 54529	9	ML	3	3
2	B	4 Mar 2008 - 9 Mar 2008	54529 - 54534	5	MM	7	4
	C	9 Mar 2008 - 20 Mar 2008	54534 - 54545	11	ML	3	3
	A	20 Mar 2008 - 31 Mar 2008	54545 - 54556	11	MM	4	4
3	B	31 Mar 2008 - 6 April 2008	54556 - 54562	6	MH	14	5
	C	6 April 2008 - 19 April 2008	54562 - 54575	13	ML	7	7
4	-	19 April 2008 - 14 May 2008	54575 - 54600	25	HH	39	8
5	-	14 May 2008 - 18 Jun 2008	54600 - 54635	35	MM	4	4

Table 6.2: The H in the "Activity" column stands for High, M for Medium and L for Low (*e.g.* L stands for low activity of the source during the relevant time interval). The first letter in the 'Activity' column indicates the primary dominant trend and the second indicates the secondary trend fluctuations superimposed on the primary trend. The column labeled "Obs." indicates the number of observations made during the selected time interval, whereas "Obs. 1-day" indicates the number of observations binned by adopting a 1-day bin width in the corresponding selected time interval.

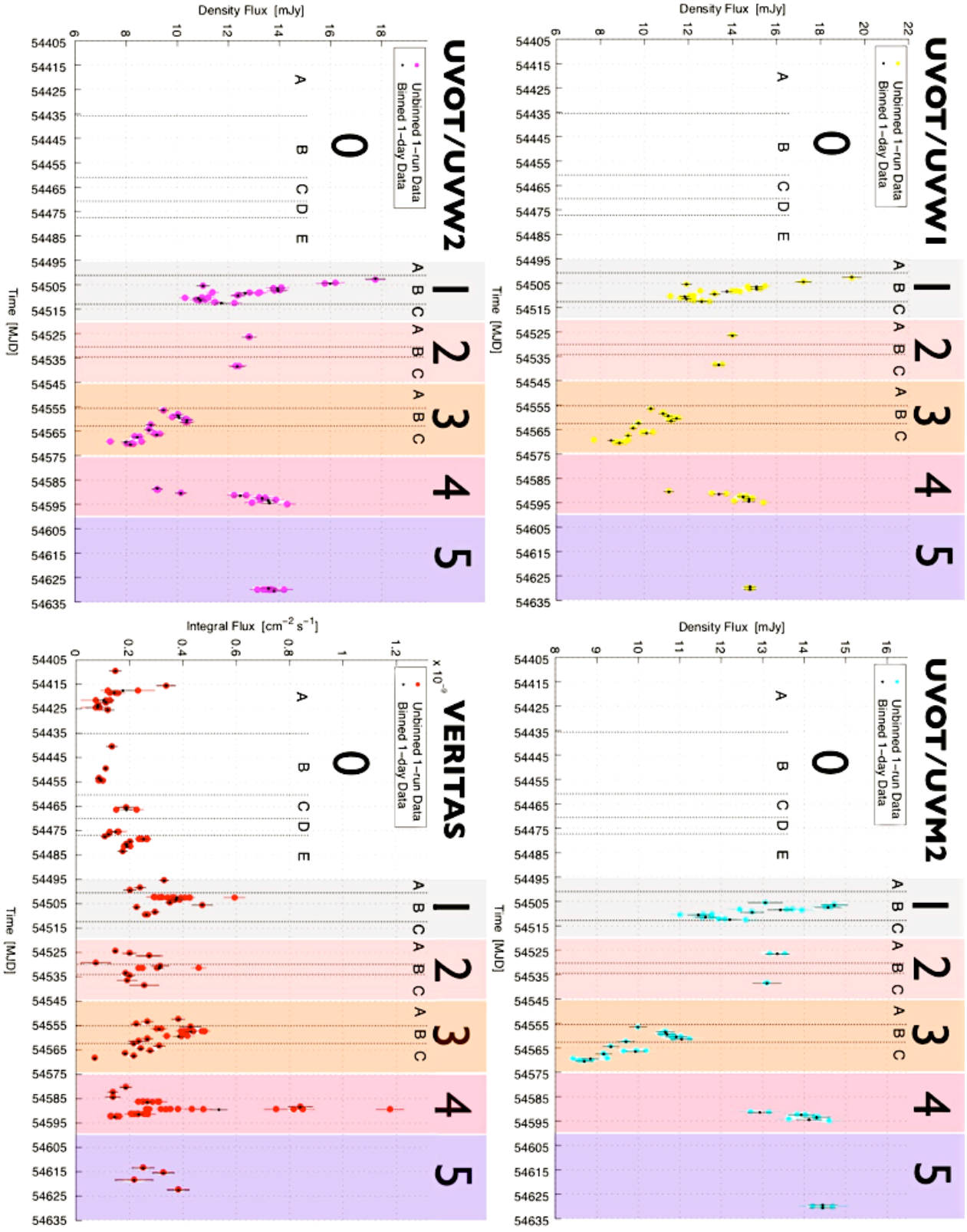

Figure 6.1: UVOT and VERITAS lightcurves with the indication of the time interval that we selected.

6.2 The Statistical Nature of the Blazar Emission

Generally, the analysis of lightcurves at any wavelength provides physical insight into the emission processes. In the case of blazar objects, the signals that have been recorded at GeV-TeV energies are the result of several reprocessings by different production mechanisms. Due to the nondeterministic[2] nature of the blazar emission, we must assume that one or more of these processes is, therefore, nondeterministic. Consequently, we can treat any blazar lightcurve as the result of nondeterministic processes. However, partially, the unpredictable behavior might originate from an incorrect methodology in time-analysis modeling, which typically assumes no prior knowledge of the whole blazar system. Thus, previous studies do not include any *a priori* assumption when performing the time-domain analysis. However, even when dealing with nondeterministic systems, it is possible to separate them into two output components: one that is statistically predictable (or random) and one that is unpredictable (or irregular). The component of the signal that is nondeterministic is the portion of the signal with noise-like characteristics[3].

The investigation of nondeterministic random behaviors might provide excellent physical characteristics of the physics and evolution of the blazar processes, since it relates, for example, information on the blazar's structure, emission mechanisms and jet characteristics. Both short-term and long-term predictability can be investi-

[2]Formally, we describe deterministic signals via analytical functions. Nondeterministic signals are either random or irregular. Random signals can be described by using probabilistic analytical sets of functions.

[3]Commonly, in the case of blazar HE and VHE observations, astronomers refer to the nondeterministic random fluctuations as 'signal' (with noise-like characteristics), whereas experts in signal identification and processing refer to it as 'noise' (Press, 1978).

gated in order to obtain information. Although some types of noise show a very poor nondeterministic predictable behavior (*e.g.*, white noise), other types exhibit unpredictability to a lesser extent. The time-domain behavior of nonwhite noise becomes statistically predictable for short-term evolutions, but also gradually unpredictable over longer timescales. By introducing a correct analysis approach, the nondeterministic random component of the recorded signal would provide significant insights into the blazar's system (particularly on very long timescales), where the "noisy" portion of the signal appears to have long-term memory of the past blazar behavior (or blazar system evolution) (Press, 1978), and where each type of noise is typically related to a given class of originating processes[4].

Currently, we have a limited knowledge of the interactions of the underlying processes governing a blazar's emission. The mean and the variance of any recorded lightcurve are not constant. Thus, at least one significant component of the blazar output signal clearly characterizes the blazar system also as a nonstationary process (likely nonlinear), in which the parameters are, as a result, time-varying[5].

Each lightcurve is one single "realisation" of an ensemble generated by nonstationary emission processes. As result, one may conclude that two lightcurves, which

[4]For example, raw time series data of the number of sunspots have been measured for some time. This monitoring clearly shows the 11 and 22 year period of the sunspot cycle. One might expect that a periodic feature due to these medium term cycles should be present in the results of a frequency-domain analysis. Actually, on long periods, the frequency-domain analysis does not return such a result, possibly because the underlying processes do not possess a high-phase coherence for long periods (although the related processes maintain good phase coherence over short periods). However, more interestingly, the solar spectrum emission density approaches a well defined power law spectral index, demonstrating that the combination of processes at work has a "memory" of its evolution in time (Press, 1978).

[5]This is related to the blazar emission. Instrumental uncertainty on the measurement of the signal is a distinct issue.

have different statistical moments (such as mean and variance), might be different realisations of the same nonstationary process (Vaughan *et al.*, 2003). In the context of a multiwavelength campaign, we can equivalently handle simultaneous realisations from different energy bands or multiple segments of a given longer realisation. However, the nonstationary-like nature of the blazar system clearly justifies the larger volume of data initially required in order to extract unambiguous information about the blazar emission mechanisms and structures.

6.3 Noise-like variability

Red noise, also called Brownian noise or "random walk noise", indicates a peculiar power density spectrum behavior which decreases with increasing frequency – $P(\nu) \propto \nu^{-2}$ where $P(\nu)$ is the power at frequency ν. The red noise power is mostly concentrated at low frequencies, but does not include a constant component at zero frequency. Red noise describes a heavily filtered low-pass type of noise. Some other types of noise are described by even steeper power law slope indexes, such as the flicker walk noise. This shows a $P(\nu) \propto \nu^{-3}$ variation and, although there is no general consensus, some refer to it as "black" noise (Kihara *et al.*, 2002). Moreover, the term "red" noise is often used in conjunction with white noise (ν^0) and pink flicker noise (ν^{-1}) (Press, 1978). By definition, a red noise-like signal can be obtained through integration of white noise (in the time-domain). It is nonstationary, although it is the result of the integration of the stationary white noise. Its spectrum converges by integrating from a given frequency to infinity since the amount of power at high frequencies is finite. The direct consequence is that it is always defined as an averaged

value, integrating from any given point to infinity (Press, 1978). However, the red-noise theoretical spectrum diverges if integrated toward zero frequency. Therefore, looking over longer timescales, the random walk function moves away from its initial value and, thus, there is no well-defined mean over long timescales.

The analysis of blazar lightcurves revealed the presence of red noise that characterized the lightcurves with large variations on longer timescales (lower energies), likely produced by the underlying emission processes (Abdo, 2010). The typical power spectral density of the emission associated with red noise (between $10^{-5} - 10^{-3}$ Hz) is well described by a power-law of $P(\nu) \propto \nu^{-\alpha}$, where α is ~ 2 (Kataoka *et al.*, 2001; Zhang *et al.*, 1999, 2002).

Thus, random walk noise is nonstationary, since it has no constant mean and no constant variance and the origin of it in the blazar's lightcurves is not yet known. Unfortunately, there are not any studies indicating if such noise is only superimposed on different signal components of the blazar's emission, or whether it is convolved with them. Intuitively, relying on the Press (1978) study, we are rather in favour of the latter hypothesis.

6.4 Modeling and Computing

In recent years, several space-based satellite missions and Earth-based collaborations have provided a large amount of blazar observations covering the whole electromagnetic spectrum. Moreover, the presence of many observatories spread over the world has offered a major opportunity to probe more details by increasing the resolution of the monitored sources in time, even in spectral bands not previously covered

by space-based observatories.

This has allowed precise time investigations of blazar behaviors between different spectral bands, but only a few of these investigations have met even with partial success. In particular, Fossati *et al.* (2008) have made cross-correlation analyses between TeV and X-ray datasets providing the evidence of an energy-dependent time-delay in the Markarian 421 emission. Although we expect the presence of such energy-dependent cross-correlations to be visible, in many practical situations, if a time lag exists, it is particularly difficult to detect. When looking at other findings (Acciari *et al.*, 2009d), we should assume that, in general cases, a "modulation" of the blazar's emission might be present in some spectral bands, together with a given time delay. Such signal modulation might strongly contribute to hiding the presence of possible correlations, which then turn out to be undetectable through traditional analytical approaches.

The characteristic and variability timescale estimated by introducing time-domain analysis provides a very significant contribution to the understanding of the physics underpinning blazar behavior. In this context, traditional approaches such as statistical variability estimates and correlation analysis have been, more recently, utilized alongside newer approaches, such as structure function analysis. The intrinsic weaknesses of the time-series analysis in the presence of time gaps should be reduced through the introduction of mathematical and modeling refinements.

We produced a software suite composed of several analysis libraries that introduce refinements to existing time analysis approaches. The statistical variability estimate was improved through the introduction of methods that, accounting for the nonho-

mogeneous observation scheduling, compute the spectral index of unevenly sampled time series (see Section 6.5).

Traditional correlation analysis seems to be one of the weaker segments in the time-domain investigation. When any frequency- or time-domain feature modulates the behavior of a signal, the correlation drastically decreases. In any case, the superimposing of a modulation on the signal leads to a softer correlation detection. In our case, the correlation analysis is refined by introducing a technique initially developed in econometrics. By detrending, or removing, the constant and linear trends of a given time series, our code allows the user to correlate nonstationary time series that would not be correctly accounted for by using the traditional approach, which suits only stationary time series (see Section 6.6).

Finally, in our code, we extended the ability of the structure function analysis to discern the range of timescales that contribute to variations, by introducing a parameterization of its characteristic timescales and by computing the corresponding uncertainty via a Monte-Carlo simulation[6] (see Section 6.10).

Unlike traditional time-analysis packages that are not directly extendable to nonlinear time analysis through the use of unevenly sampled time series, the analysis libraries implemented in our software suite provide such a possibility. We carried out our time data analyses, shown later in this chapter, by using this software suite. A schematic representation of one of the suite subpackages developed to implement the detrending technique as part of the correlation analysis is shown in Figure 6.2.

[6]The GSL libraries (Galassi, 2009) provide additional support for modeling random effects and for Monte-Carlo simulations.

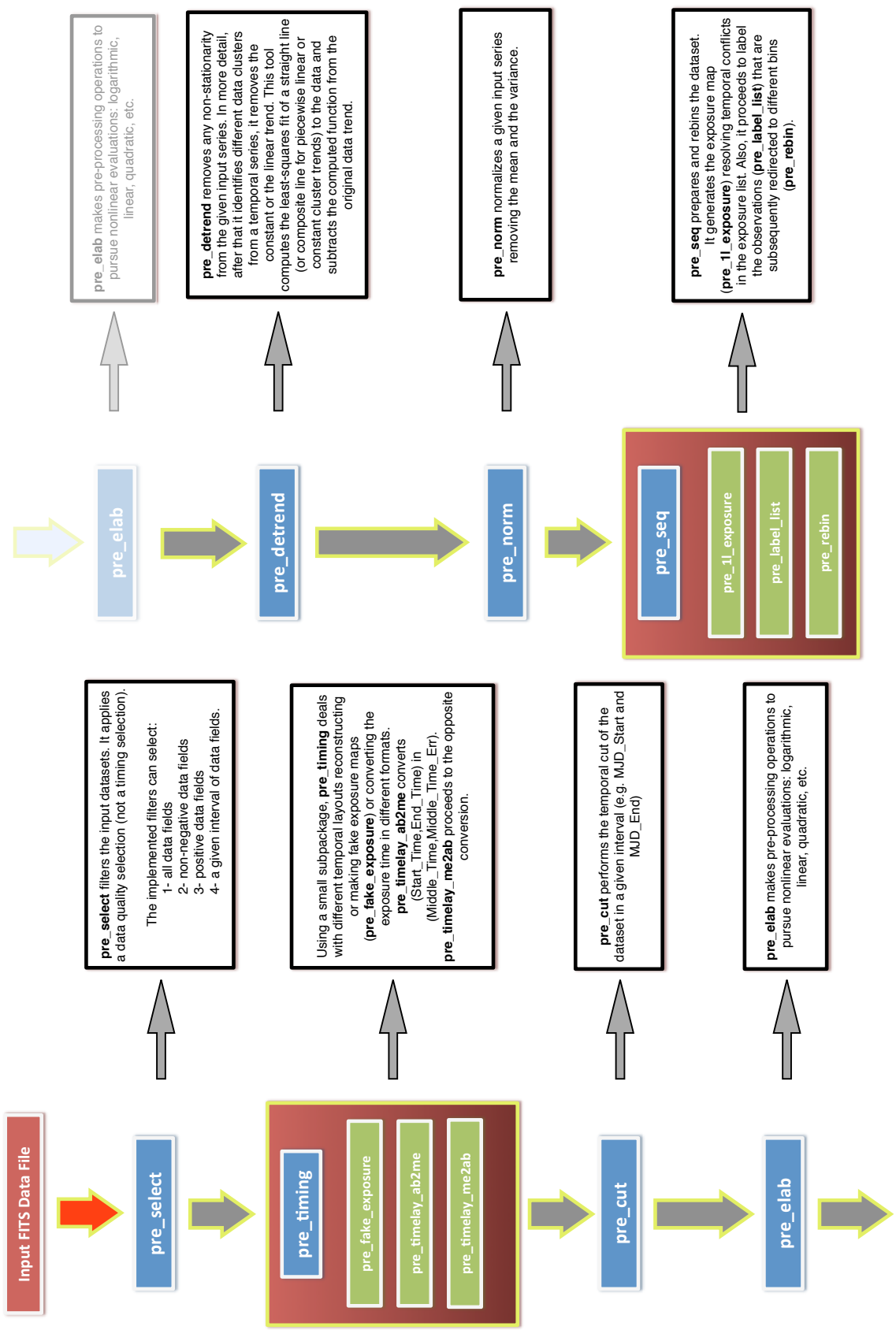

Figure 6.2: This drawing shows a simplified schematic view of the adopted data quality and time-filtering pipeline for detrending.

6.5 Variability Analysis

In order to search for variability in a number of lightcurves (or short segments of longer lightcurves), one could test whether their variances differ significantly. Variance estimates, in fact, can be seen as a direct measure of the source activity. The measure of this correlation allows quantification, in a statistical sense, of whether an underlying combination of emission processes can be responsible for a given trend in the dataset and whether there is also a presence of any type of noise (*e.g.*, red noise). Furthermore, if the measured variance evolves with time, it can be also interpreted as a measure of the "nonstationarity".

The practical aspects of measuring the variability amplitude in random unevenly sampled lightcurves typical of AGNs have been explored in Vaughan *et al.* (2003). That paper is focused on the statistical properties of the quantities commonly used to estimate the variability amplitude in given sequences, such the variance σ^2, and the fractional root mean squared variability amplitude, F_{var}.

They are defined as:

$$F_{var} = \frac{\sigma_{\rm XS}}{f} = \frac{\sqrt{\sigma^2 - f_{err}^2}}{f} \tag{6.1}$$

where $\sigma_{\rm XS}$ is the excess variance. Each flux measurement f_i has a measurement error $f_{err,i}$. f is the arithmetic mean of the N fluxes

$$f = \frac{1}{N}\sum_{i=1}^{N} f_i \tag{6.2}$$

and σ^2 is the variance

$$\sigma^2 = \frac{1}{N-1}\sum_{i=1}^{N}(f_i - f)^2 \tag{6.3}$$

and f_{err}^2 is the mean measurement error squared:

$$f_{err}^2 = \frac{1}{N}\sum_{i=1}^{N} f_{err,i}^2 \tag{6.4}$$

The uncertainty in F_{var} is given by

$$\Delta F_{var} = \sqrt{\frac{1}{2N}\left(\frac{f_{err}^2}{F_{var} f^2}\right)^2 + \left(\frac{1}{f}\sqrt{\frac{f_{err}^2}{N}}\right)^2} \tag{6.5}$$

The fractional root mean squared variability F_{var} is a dimensionless variability amplitude computed on a normalized distribution. It is used to compare the variability of sources of different luminosities (Vaughan *et al.*, 2003). In the event that the mean square measurement error exceeds the variance of the time series, the square root term becomes imaginary. Thus, the value of F_{var} is not defined if the variability is lower than the instrument can reasonably discern.

A further parameter is needed to estimate rapid lightcurve variations. Zhang *et al.* (2005) introduce the point-to-point fractional root mean squared variability amplitude, F_{pp}, in order to probe the short timescale variability by measuring the variations between adjacent points in the lightcurve,

$$F_{pp} = \frac{1}{f}\sqrt{\frac{1}{2(N-1)}\sum_{i=1}^{N-1}(f_{i+1} - f_i)^2 - f_{err}^2} \tag{6.6}$$

It is adopted to characterize the short term variability of the time series (Edelson *et al.*, 2002). The uncertainty for F_{pp} is given by

$$\Delta F_{pp} = \sqrt{\frac{1}{2N}\left(\frac{f_{err}^2}{F_{pp} f^2}\right)^2 + \left(\frac{1}{f}\sqrt{\frac{f_{err}^2}{N}}\right)^2}\,. \tag{6.7}$$

With very unevenly sampled or small, datasets the value of F_{pp} may be unrealistically high. Also F_{pp} becomes imaginary when the measurement uncertainties are greater than the variance fluctuation (Edelson *et al.*, 2002).

In the presence of extensive and repeated observations, the statistical properties of power spectral density (PSD) can be extracted directly by using a discrete Fourier transform (DFT) but the limited duration of the observations and their inhomogeneous observational scheduling represent a strong limitation on the reliability of the results[7]. Thus, we can introduce the ratio $F_{\rm VR} = F_{var}/F_{pp}$, which provides similar information to the power spectral density slope (Vaughan, 2005). It is a measure of the long timescale variance relative to the variance at a short timescale and, thus, it shows a type of information that is directly related to the slope index of a power law approximating the power spectral density behavior.

Since F_{pp} is a typical measure of the variation between successive measures, $F_{\rm VR}$ is the ratio of the long and short term variance estimates and it is obtained by dividing F_{var} into the mean spectral component of the time series, F_{pp}. This allows a given $F_{\rm VR}$ to be directly compared with other $F_{\rm VR}$ indexes, which can be computed on different time series of data generated by the same process[8], or by a different one.

6.5.1 Markarian 421 Variability Analysis Results

The Markarian 421 UVOT ultraviolet lightcurves show some gaps caused by orbit periodicities of the Swift satellite and by the inhomogeneous observation scheduling. Unfortunately, these gaps are fairly extended in time.

[7]There are some caveats to be mentioned in adopting a discrete Fourier approach for the computation of the PSD. We should consider that uneven (nonuniform) time series require the implementation of nonuniform DFT (NDFT) algorithm but, unfortunately, the reliability of this discrete-time transform is not guaranteed in our case in which it is not possible to clearly assess whether the observation scheduling (sampling rate) satisfies the Perseval's theorem requirements.

[8]Roughly, the computation of $F_{\rm VR}$ can be compared to finding the inverse of the derivation operation of a curve via the "prediction" of its slope (that is returned as an averaged as opposed to "instantaneous" prediction returned by an operation of differrentiation).

UVOT Period Dataset

Period	Date	MJD Start-End	Days	Filter	Obs.	F_{mean} mJy	F_{max} mJy	$F_{\rm NR}$	$F_{var} \pm \Delta F_{var}$ %	$F_{pp} \pm \Delta F_{pp}$ %	$F_{\rm VR} \pm \Delta F_{\rm VR}$
				UVW1	55	11.9	14.7	1.2	16.4 ± 0.3	4.8 ± 0.3	3.4 ± 0.3
Season	1^{st} Nov 2007 - 18 Jun 2008	54405 - 54635	230	UVM2	60	12.6	19.4	1.5	19.0 ± 0.3	6.5 ± 0.3	3.0 ± 0.2
				UVW2	66	11.6	17.8	1.5	19.2 ± 0.3	5.9 ± 0.3	3.2 ± 0.2
0	1^{st} Nov 2007 - 30 Jan 2008	54405 - 54495	90	-	-	-	-	-	-	-	-
				UVW1	18	12.7	14.7	1.2	9.1 ± 0.6	3.6 ± 0.6	2.6 ± 0.6
1	30 Jan 2008 - 24 Feb 2008	54495 - 54520	25	UVM2	24	13.8	19.4	1.4	14.8 ± 0.4	7.7 ± 0.4	1.9 ± 0.2
				UVW2	24	12.7	17.7	1.4	14.8 ± 0.5	7.4 ± 0.5	2.0 ± 0.2
				UVW1	4	13.2	13.5	1.0	i	i	i
2	24 Feb 2008 - 20 Mar 2008	54520 - 54545	25	UVM2	4	13.7	14.0	1.1	2±1	i	i
				UVW2	4	12.6	12.8	1.0	i	i	i
				UVW1	21	9.8	11.2	1.1	8.9 ± 0.5	2.6 ± 0.6	3 ± 1
3	20 Mar 2008 - 19 Apr 2008	54545 - 54575	30	UVM2	20	10.0	11.6	1.2	10.7 ± 0.5	4.3 ± 0.5	2.5 ± 0.4
				UVW2	20	9.1	10.4	1.1	9.7 ± 0.5	3.8 ± 0.6	2.5 ± 0.5
				UVW1	8	13.8	14.6	1.1	4.00±0.9	1±1	2±2
4	19 Apr 2008 - 14 May 2008	54575 - 54600	25	UVM2	11	14.0	15.4	1.1	8.9±0.7	4.3±0.7	2.1±0.5
				UVW2	9	12.2	14.3	1.2	14.8±0.7	4.7±0.7	3.1±0.6
				UVW1	3	14.4	14.7	1.0	i	i	i
5	14 May 2008 - 18 Jun 2008	54600 - 54635	35	UVM2	3	14.8	14.9	1.0	i	i	i
				UVW2	7	13.6	14.2	1.0	i	1±1	i

Table 6.3: Variability results for UVOT bands for the whole season and separately for all the observation periods. The 'i' stands for imaginary number. $F_{\rm NR}$ is computed simply by dividing F_{max} by F_{mean}. The column labeled "Obs." indicates the number of observations made during the selected time interval.

UVOT Period Subinterval Dataset

Period	Subinterval	Date	MJD Start-End	Days	Filter	Obs.	F_{mean}	F_{max}	$F_{\rm NR}$	$F_{var} \pm \Delta F_{var}$	$F_{pp} \pm \Delta F_{pp}$	$F_{\rm VR} \pm \Delta F_{\rm VR}$
							mJy	mJy		%	%	
					UVW1	-	-	-	-	-	-	-
	A	30 Jan 2008 - 4 Feb 2008	54495 - 54500	5	UVM2	-	-	-	-	-	-	-
					UVW2	-	-	-	-	-	-	-
					UVW1	18	12.7	14.7	1.2	9.1±0.6	3.6±0.6	2.5±0.6
1	B	4 Feb 2008 - 17 Feb 2008	54500 - 54513	13	UVM2	24	13.8	19.4	1.4	14.8±0.4	7.7±0.4	1.9±0.2
					UVW2	24	12.8	17.7	1.4	14.8±0.5	7.4±0.5	2±2
					UVW1	-	-	-	-	-	-	-
	C	17 Feb 2008 - 24 Feb 2008	54513 - 54520	7	UVM2	-	-	-	-	-	-	-
					UVW2	-	-	-	-	-	-	-
					UVW1	2	13.10	13.13	1.00	i	i	-
	A	24 Feb 2008 - 4 Mar 2008	54520 - 54529	9	UVM2	2	14.00	14.04	1.00	i	i	-
					UVW2	2	12.81	12.83	1.00	i	i	-
					UVW1	-	-	-	-	-	-	-
2	B	4 Mar 2008 - 9 Mar 2008	54529 - 54534	5	UVM2	-	-	-	-	-	-	-
					UVW2	-	-	-	-	-	-	-
					UVW1	2	13.35	13.53	1.01	i	i	-
	C	9 Mar 2008 - 20 Mar 2008	54534 - 54545	11	UVM2	2	13.38	13.53	1.01	i	i	-
					UVW2	2	12.35	12.42	1.01	i	i	-
					UVW1	-	-	-	-	-	-	-
	A	20 Mar 2008 - 31 Mar 2008	54545 - 54556	11	UVM2	-	-	-	-	-	-	-
					UVW2	-	-	-	-	-	-	-
					UVW1	8	10.7	11.2	1.0	2.5±0.9	i	i
3	B	31 Mar 2008 - 5 Apr 2008	54556 - 54562	6	UVM2	8	11.1	11.6	1.0	2.9±0.8	i	i
					UVW2	7	10.1	10.4	1.0	3±1	0.3±0.5	10±2
					UVW1	13	9.2	10.2	1.1	5.6±0.7	2.6±0.8	2.1±0.9
	C	6 Mar 2008 - 19 Apr 2008	54562 - 54575	13	UVM2	12	9.3	10.4	1.1	7.4±0.6	5.3±0.6	1.4±0.3
					UVW2	13	8.5	9.3	1.1	6.0±0.7	4.0±0.7	1.5±0.4

Table 6.4: Variability results of the UVOT dataset for 'Periods 1', 'Period 2' and 'Period 3' with their corresponding subintervals. The 'i' stands for imaginary number. $F_{\rm NR}$ is computed simply by dividing F_{max} by F_{mean}. The column labeled "Obs." indicates the number of observations made during the selected time interval.

A complete set of the UVOT variability results for the 2007-2008 dataset is shown in Tables 6.3 and 6.4. During this campaign ($54005 < \mathrm{MJD} < 54635$), UVOT UVW1, UVM2 and UVW2 lightcurves show evidence of moderate variability trends. Averaging over the whole season (Equation 6.1), F_{var} quantifies for each UV band the variability of the signal as 16.4%, 19.0%, 19.2% in the UVW1, UVM2 and UVW2 bands, respectively. The F_{pp} values that we computed (Equation 6.6) are 4.8%, 6.5%, 5.9%, respectively. Comparing F_{var} (low frequencies) with F_{pp} (high frequencies), we concluded that Markarian 421 emission presents larger variabilities on longer timescales. The F_{VR} ratios of the three ultraviolet UVOT bands are 3.4 ± 0.3, 3.0 ± 0.2 and 3.2 ± 0.2, respectively (Tables 6.3).

VERITAS flux variations have been computed for all the time intervals in Tables 6.5 and 6.6. The ratio between the maximum and the averaged fluxes, F_{NR}, is 4.3, F_{var} is $58 \pm 1\%$ and the point-to-point variability F_{pp} is $30 \pm 1\%$ for the whole season. Thus, we obtain $F_{\mathrm{VR}} = 1.9 \pm 0.1$.

Not being close to zero, the $F_{\mathrm{VR,UVOT}}$ and $F_{\mathrm{VR,VERITAS}}$ values reveal the presence of some type of nonwhite noise superimposed and/or convolved with the recorded UVOT and VERITAS lightcurves. In fact, as expected for blazars, it seems that Markarian 421 possesses a red-noise power spectrum.

Although the fractional root mean square variability amplitude, F_{var}, is fairly robust to uneven sampling, the point-to-point variability amplitude, F_{pp}, strongly depends on the observation scheduling, which might prevent the F_{VR} ratio converging toward the statistical expected value. To constrain more precisely and quantify the relation between F_{VR} and the PSD index α for our datasets, we carried out further

VERITAS Period Dataset

Period	Date	MJD Start-End	Days	Obs.	F_{mean} erg/cm^2/s	F_{max} erg/cm^2/s	$F_{\rm NR}$	$F_{var} \pm \Delta F_{var}$ %	$F_{pp} \pm \Delta F_{pp}$ %	$F_{\rm VR} \pm \Delta F_{\rm VR}$
Season	1^{st} Nov 2007 - 18 Jun 2008	54405 - 54635	230	141	2.71×10^{-10}	1.18×10^{-9}	4.3	58 ± 1	30 ± 1	1.9 ± 0.1
0	1^{st} Nov 2007 - 30 Jan 2008	54405 - 54495	90	42	1.50×10^{-10}	3.37×10^{-10}	2.2	44 ± 4	27 ± 4	1.6 ± 0.4
1	30 Jan 2008 - 24 Feb 2008	54495 - 54520	65	24	3.46×10^{-10}	5.94×10^{-10}	1.7	23 ± 2	16 ± 2	1.4 ± 0.3
2	24 Feb 2008 - 20 Mar 2008	54520 - 54545	25	13	2.38×10^{-10}	4.60×10^{-10}	1.9	35 ± 5	29 ± 6	1.2 ± 0.4
3	20 Mar 2008 - 19 Apr 2008	54545 - 54575	30	25	3.24×10^{-10}	4.82×10^{-10}	1.5	30 ± 2	15 ± 2	2.0 ± 0.4
4	19 Apr 2008 - 14 May 2008	54575 - 54600	25	39	3.32×10^{-10}	1.18×10^{-9}	3.5	70 ± 2	40 ± 2	1.7 ± 0.1
5	14 May 2008 - 18 Jun 2008	54600 - 54635	35	4	2.9×10^{-10}	3.83×10^{-10}	1.3	11 ± 20	19± 15	0.6 ± 0.2

Table 6.5: Variability results for VERITAS for the whole season and for the 6 identified observational periods. $F_{\rm NR}$ is computed simply by dividing F_{max} by F_{mean}. The column labeled "Obs." indicates the number of observations made during the selected time interval.

VERITAS Period Subinterval Dataset

Period	Interval	Date	MJD Start-End	Days	Obs.	F_{mean} erg/cm^2/s	F_{max} erg/cm^2/s	$F_{\rm NR}$	$F_{var} \pm \Delta F_{var}$ %	$F_{pp} \pm \Delta F_{pp}$ %	$F_{\rm VR} \pm \Delta F_{\rm VR}$
	A	1^{st} Nov 2007 - 1^{st} Dec 2007	54405 - 54435	30	17	1.21×10^{-10}	3.37×10^{-10}	2.8	52±10	44±10	1.2±0.5
	B	1^{st} Dec 2007 - 26 Dec 2008	54435 - 54460	25	6	8.65×10^{-11}	1.34×10^{-10}	1.5	46±11	59±11	0.8±0.3
0	C	26 Dec 2007 - 5 Jan 2008	54460 - 54470	10	3	1.88×10^{-10}	2.27×10^{-10}	1.2	10±2	14±1	0.7±0.2
	D	5 Jan 2008 - 12 Jan 2008	54470 - 54477	7	4	1.41×10^{-10}	1.59×10^{-10}	1.1	i	i	i
	E	12 Jan 2007 - 30 Jan 2008	54477 - 54495	18	12	2.14×10^{-10}	2.66×10^{-10}	1.2	20±3	12±3	1.8±0.7
	A	30 Jan 2008 - 4 Feb 2008	54495 - 54500	5	3	2.57×10^{-10}	3.30×10^{-10}	1.3	23±7	15±7	1.5±0.1
1	B	4 Feb 2008 - 17 Feb 2008	54500 - 54513	13	21	3.58×10^{-10}	5.94×10^{-10}	1.7	21±2	16±2	1.3±0.3
	C	17 Feb 2008 - 24 Feb 2008	54413 - 54520	7	-	-	-	-	-	-	-
	A	24 Feb 2008 - 4 Mar 2008	54520 - 54545	9	3	2.07×10^{-10}	2.73×10^{-10}	1.3	22±15	5±4	4.9±0.4
2	B	4 Mar 2008 - 9 Mar 2008	54520 - 54545	5	7	2.60×10^{-10}	4.60×10^{-10}	1.8	44±6	34±6	1.3±0.4
	C	9 Mar 2008 - 20 Mar 2008	54520 - 54545	11	3	2.16×10^{-10}	2.55×10^{-10}	1.2	i	i	i
	A	20 Mar 2008 - 31 Mar 2008	54545 - 54575	11	4	3.26×10^{-10}	4.28×10^{-10}	1.3	27±6	27±6	1.0±0.4
3	B	31 Mar 2008 - 6 Apr 2008	54545 - 54575	6	14	3.77×10^{-10}	4.82×10^{-10}	1.3	18±2	7±3	2.6±0.1
	C	6 Mar 2008 - 19 Apr 2008	54545 - 54575	13	7	2.17×10^{-10}	3.11×10^{-10}	1.4	34±4	27±4	1.3±0.3

Table 6.6: Variability results for VERITAS for 'Period 0', 'Period 1', 'Period 2' and 'Period 3' with their corresponding subintervals. The 'i' stands for imaginary number. $F_{\rm NR}$ is computed simply by dividing F_{max} by F_{mean}. The column labeled "Obs." indicates the number of observations made during the selected time interval.

analysis as follows. For each UVOT and VERITAS lightcurve, we generated 300 simulated lightcurves. Each of them was modeled after the corresponding UVOT or VERITAS lightcurve, possessing the same statistical moments of the corresponding lightcurve but with PSD index α ranging between -3 and $+3$. In Figure 6.3, there is an example of time- and frequency-domain visualization of white, pink and red noise obtained by using one simulated lightcurve and by imposing a different PSD slope for each kind of noise. The required spectral slope is imposed on a given lightcurve by generating the appropriate frequency-domain series, with power-law spectral magnitudes and randomised phases (Little *et al.*, 2007) and subsequently by applying the inverse Fourier transform. Finally, the obtained series is then convolved (or binned) with the observation timetable of the original lightcurve. Thus, we analyzed the variability of any produced simulated lightcurve by computing F_{mean}, F_{max}, $F_{\rm NR}$, F_{var}, F_{pp} and $F_{\rm VR}$. Figure 6.4 shows an example of variability values and their uncertainty (blue lines, continuous and dashed, respectively) for a VERITAS dataset. In Figure 6.4a, the F_{var} (blue line) cuts the simulated values for about $\alpha > 1.5$. The simulated lightcurves have the same statistical moments as the original lightcurve and they are produced by using different spectral indexes α. Red dots represent the F_{var} computed by binning the simulated lightcurves with the real observation scheduling. Black dots return the F_{var} values obtained by using simulated lightcurves evenly sampled rather than according to the observation scheduling. Figure 6.4b returns the information related to the point-to-point variability amplitude F_{pp}. Finally, Figure 6.5 illustrates the relation between the $F_{\rm VR}$ and the PSD index α values in the case of the UVOT and VERITAS datasets.

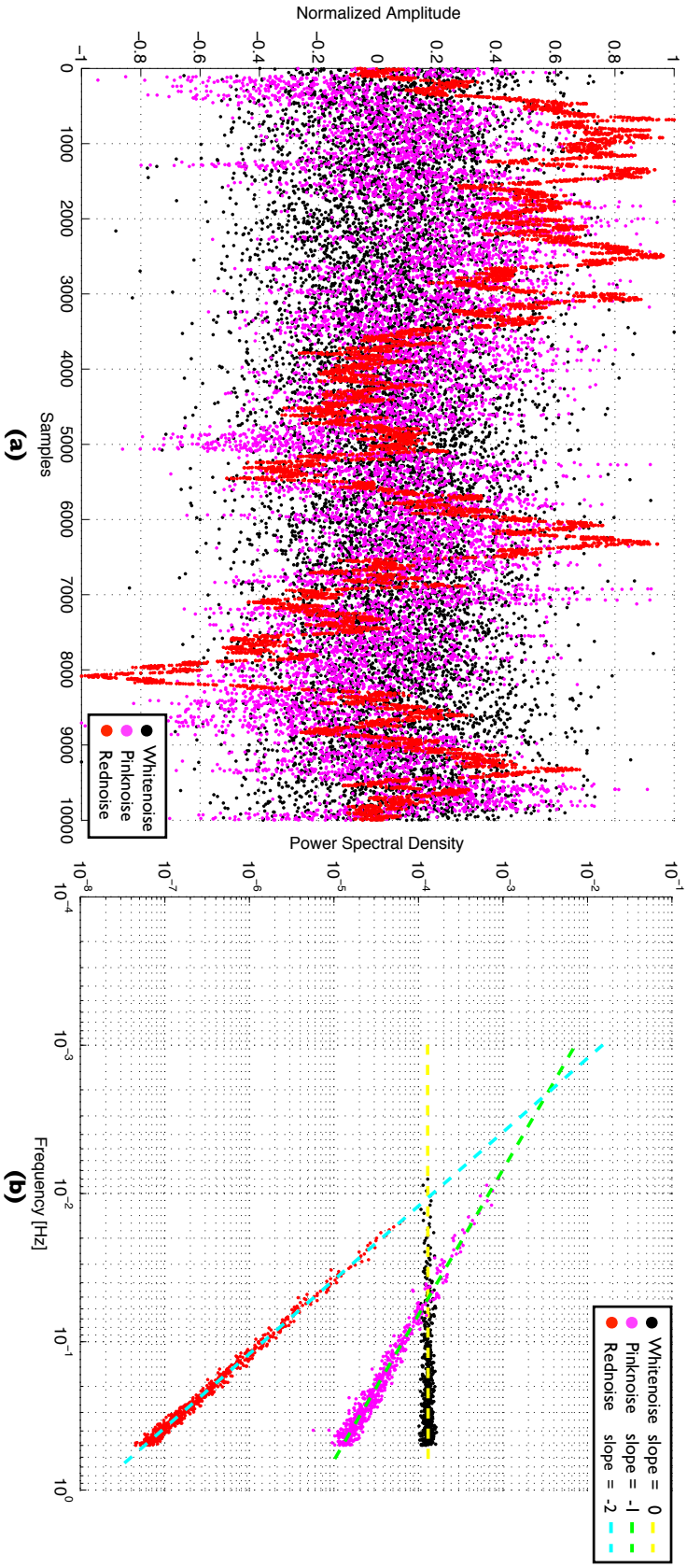

Figure 6.3: **(a)** Examples of white, pink and red noise time series. **(b)** PSD plots of the corresponding frequency-domain slope indexes.

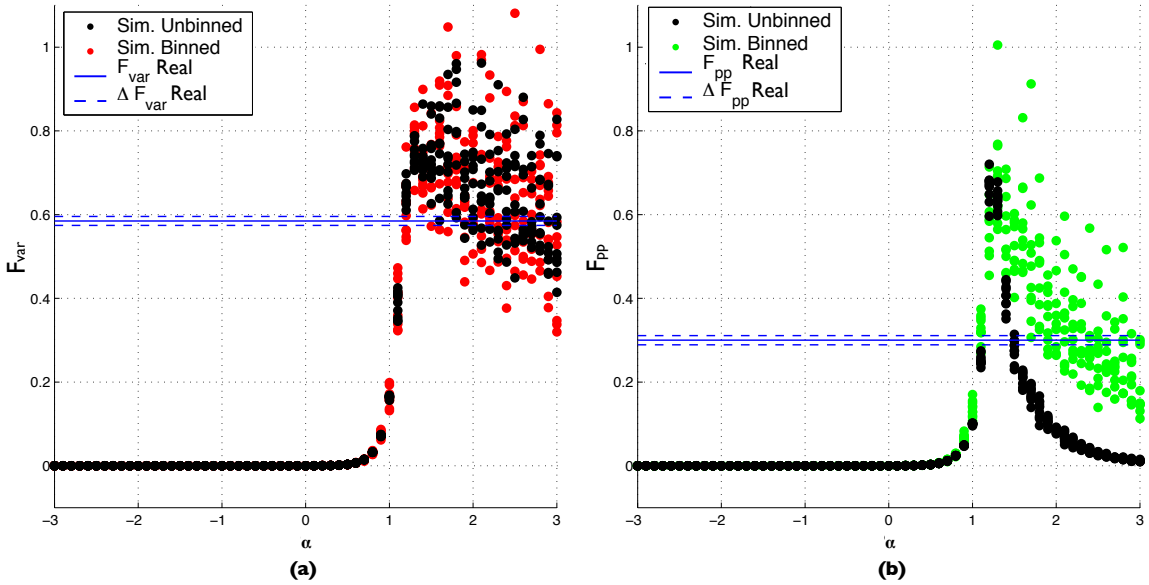

Figure 6.4: **(a)** VERITAS F_{var} and **(b)** VERITAS F_{pp} values computed from real and simulated lightcurves (binned and unbinned).

Introducing this simulation approach, we provide a particular statistical characterization of the $F_{\rm VR}$ versus α relation. Thereby, we independently confirm that power spectral densities of the TeV blazar object Markarian 421 are effectively described by a power law $P(\nu) \propto \nu^{-\alpha}$ (Zhang *et al.*, 2006) , where $P(\nu)$ is the power at frequency ν with α between 2 and 3 in the case of UVOT dataset results and between 1.5 and 3 for the VERITAS dataset results. This analysis confirms that variability decreases toward shorter timescales. Thus, we conclude that VHE emission possesses, at least, a partial red-noise-like nature that is expected to contribute less significantly at VHE than in the UVOT band. Also, the simulations confirm and validate the results provided by the $F_{\rm VR}$ estimator that is relatively robust to uneven scheduling of the observations. Unfortunately, our datasets have large and irregular time gaps. With longer and more homogeneous datasets, we would be able to further reduce

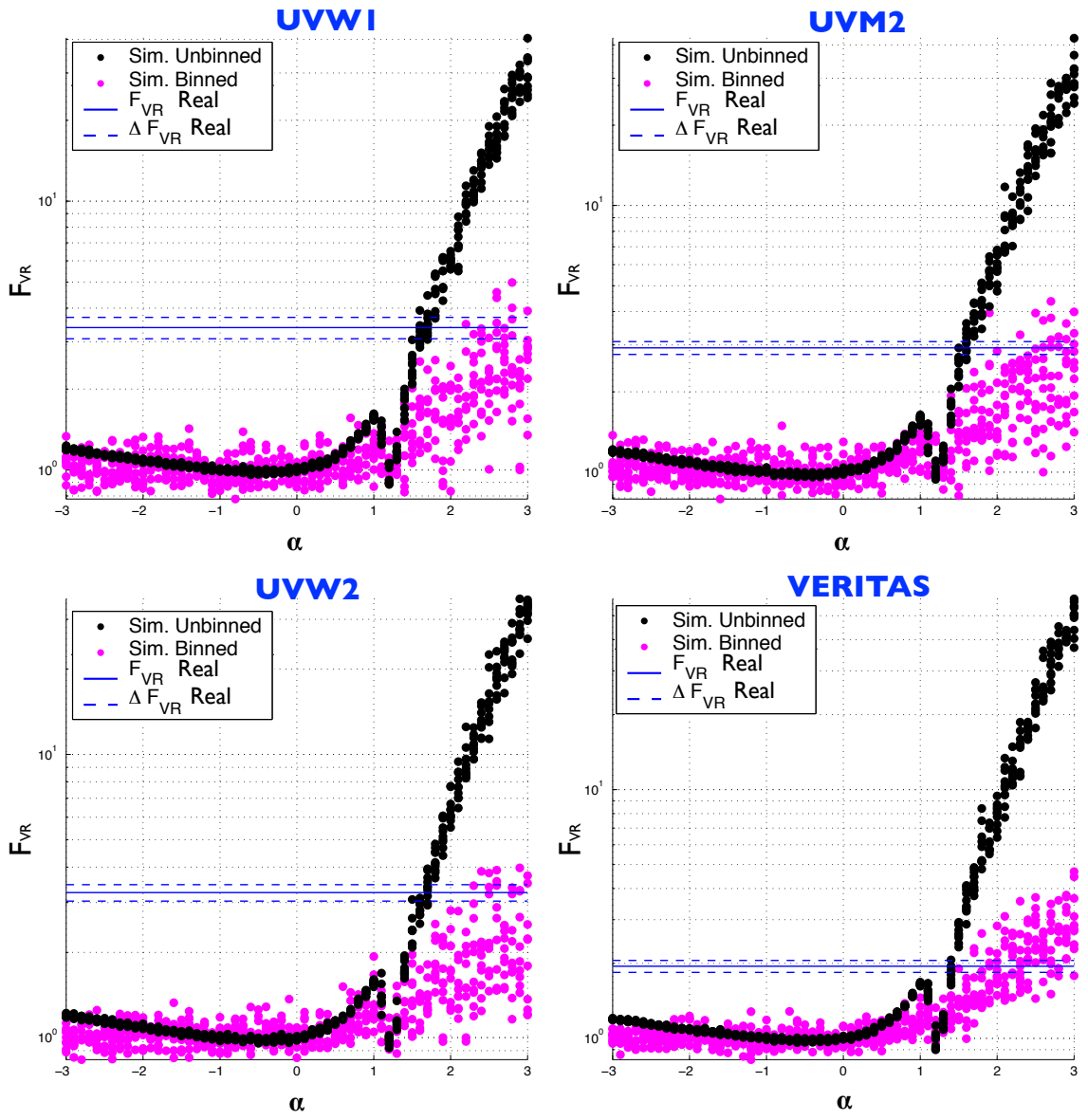

Figure 6.5: The blue lines indicate the $F_{\rm VR}$ values computed from the UVOT and the VERITAS real lightcurves. The black dots represent $F_{\rm VR}$ values computed by using the simulated lightcuves imposing a given spectral trend α between -3 and $+3$ (unbinned). Magenta dots are obtained by convolving (or binning) the VERITAS observation scheduling with the unbinned $F_{\rm VR}$ values.

the estimate uncertainty of the spectral index intervals and to trace time-dependent changes of the spectral index, if present (Figure 6.5).

Interestingly, the VHE variability seems correlated at 2σ confidence level[9] with enhancement of the flux (see Tables 6.5 and 6.6). During our campaign, two moderate flares were detected at very high energies, and a third flare (2-3 May, 2008) reached a flux of more than 10 Crab in a few minutes (Acciari *et al.*, 2011; Pichel & Rovero, 2008). We observed that during 'Period 4', which shows the highest TeV flux level of the season ($F_{max} = 1.18 \times 10^{-9}$ erg/cm^2/s and $F_{mean} = 3.32 \times 10^{-10}$ erg/cm^2/s), the VERITAS F_{var} and F_{pp} flux variabilities (70% an 40%, respectively) were larger than those computed in the relatively quiescent and moderately flaring 'Period 1' (where $F_{var} = 23\%$ and $F_{pp} = 16\%$, respectively). The maximum γ-ray flux in 'Period 4' was five times the averaged seasonal level ($F_{max} = 1.18 \times 10^{-9}$ erg/cm^2/s and $F_{mean} = 2.71 \times 10^{-10}$ erg/cm^2/s).

6.6 Correlation Analysis

Correlation analysis is one of the most used and powerful tools within time-domain analysis. However, a continuous correlation function approach can return misleading results (Gaskell & Peterson, 1987) if applied to unevenly sampled astronomical measurements with large time gaps (Welsh, 1999). The presence of extended gaps in our dataset led us to adopt the discrete correlation function (DCF) in the form introduced by Edelson *et al.* (1995).

[9]We achieve this result by propagating the flux and the variability uncertainties, respectively.

6.6.1 Discrete Correlation Function

The DCF is, essentially, a mathematical approach introduced to deal with practical cases (Edelson & Krolik, 1988). Like other time and frequency-domain analyses, the DCF returns useful statistical interpretations on the nature of the observed processes. White & Peterson (1994) and Welsh (1999) point out that the Edelson & Krolik (1988) approach to the discrete correlation function can suffer from incorrect weighting of the correlation factors, leading to an ambiguous interpretation of the DCF results. Therefore, we computed the discrete correlation function adopting the linear discrete correlation formulation from Edelson *et al.* (1995).

To investigate the correlation of two signals $a(t)$ and $b(t)$, the introduced formulation of the DCF is

$$UDCF_{ij} = \frac{(a_i - \bar{a})(b_j - \bar{b})}{\sigma_a \sigma_b} \tag{6.8}$$

where $UDCF$ is the "unbinned DCF", a_i and b_j are samples of signals $a(t)$ and $b(t)$. $\bar{a}$ and $\bar{b}$ are the average values of signals $a(t)$ and $b(t)$. σ_a and σ_b are the standard deviations of $a(t)$ and $b(t)$. The $UDCF_{ij}$ factors are binned into bins of width $\Delta\tau$ and time lag τ,

$$\tau - \Delta\tau/2 < \Delta\tau_{ij} \leq \tau + \Delta\tau/2 \tag{6.9}$$

where $\Delta\tau_{ij} = \tau(b_j) - \tau(a_i)$ and the DCF at time lag τ is

$$\rho(\tau) = \frac{1}{M} \sum UDCF_{ij} \tag{6.10}$$

with M the number of pairs computed for each given lag. Furthermore, it is possible to define a standard error for the DCF (Edelson & Krolik, 1988) in the case in which

the $UDCF_{ij}$ values within a single bin are uncorrelated. The standard error is:

$$\delta\rho(\tau) = \frac{1}{M-1}\left(\sum\left[UDCF_{ij} - \rho(\tau)\right]^2\right)^{1/2}. \tag{6.11}$$

It is advisable to exclude $\rho(\tau)$ with $M \leq 5$ in order to obtain reliable statistical results.

6.6.2 Uncertainties in Measurements

We implemented simulations which provide a reliable treatment of the measurement uncertainties by computing the uncertainty in each bin by using the real time series, instead of assuming an *a priori* uncertainty distribution. A general analytical treatment which accounts for these uncertainties is still unknown and it is an open issue in the modern statistical literature.

Equation 6.11 only estimates the DCF standard error. However, we should sum in quadrature with it a further component due to the propagation in the correlation operation of the lightcurve uncertainties. We estimate the correlation uncertainties from the computation of time-series uncertainty via simulations. This is achieved by adding a random contribution to every sample of the two real time series (a_i and b_j) to be correlated. The random contributions are $\leq aerr_i$ and $\leq berr_j$ where $aerr_i$ and $berr_j$ are the i-th and j-th time-series measurement uncertainties of the $a(t)$ and $b(t)$ time series.

The obtained time series to be correlated are, then

$$a'_i = a_i + y_n(aerr_i), \qquad b'_j = b_j + y_n(berr_j) \tag{6.12}$$

where a_i and b_j are the i-th and the j-th samples of the original signals, respectively,

and $y_n(aerr_i)$ and $y_n(berr_j)$ are the random contributions. These have been computed by selecting uniform random values in the range $-aerr_i < y_n(aerr_i) < aerr_i$ and $-berr_j < y_n(berr_j) < berr_j$.

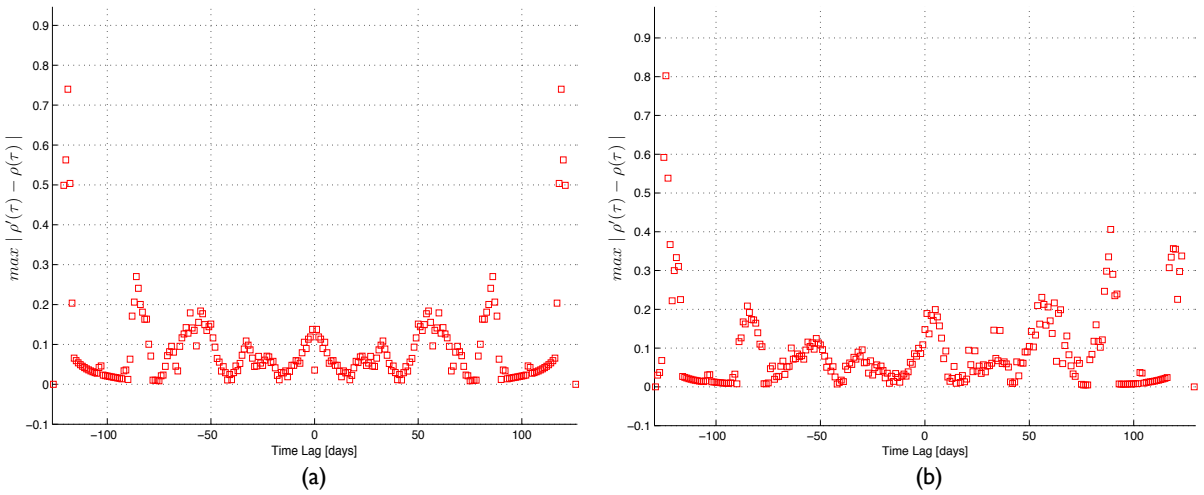

Figure 6.6: **(a)** UVW1 vs. UVW1 autocorrelation uncertainty analysis and **(b)** UVW1 vs. UVM2 cross-correlation uncertainty analysis. The computed DCF uncertainties range between 0 and 1.

We then generate $N = 1{,}000$ of a'_i and b'_j sequences for every pair of real lightcurves to be correlated. Afterwards, we correlate these sequences obtaining the $\rho'(\tau)$ correlation factors. We compare them to the correlation factors $\rho(\tau)$ obtained by correlating the original sequences. Then, we regard the maximum deviation, $\mid \rho'(\tau) - \rho(\tau) \mid$, of the simulated correlation factor $\rho'(\tau)$ from the real correlation factor $\rho(\tau)$ as the correlation factor uncertainty for time lag τ (Figure 6.6). The identification of such maximum values will allow us to account for the real lightcurve uncertainty component in the correlation operation.

6.6.3 Simulated Correlation Threshold

In order to assess the significance of results from discrete cross-correlation and autocorrelation analyses, we compare the obtained results with a "statistical threshold" (Figure 6.7). For each of the two sequences to be correlated, we generate 5,000 random sequences with the same mean, variance and time binning as the original ones. We obtain the thresholds correlating either of the real sequences with the simulated ones. For each pair of lightcurves to be analysed, we obtain a "cloud" of uncertainty that is made by two different distributions of results. In Figure 6.7, the yellow dots correspond to the correlation factors obtained by correlating simulated lightcurves with the first of the original lightcurves to be correlated. The second uncertainty distribution of results is represented by the blue dots obtained by correlating another set of simulated lightcurves with the second of the lightcurve pairs to be correlated.

Then, for each given time lag, the chance probability to obtain correlation factors from real data falling outside the range of the simulated stochastic threshold is less than 1 in 10,000.

6.7 Markarian 421 Correlation Results

Using the three UVOT lightcurves and the VERITAS lightcurve (see Figure 6.1), we carried out the cross-correlation analysis and autocorrelation analysis following the approach of Edelson & Krolik (1988).

VERITAS and UVOT autocorrelation analyses show very low correlation factors at any nonzero time lag, except the autocorrelation peak at zero lag (Figure 6.8).

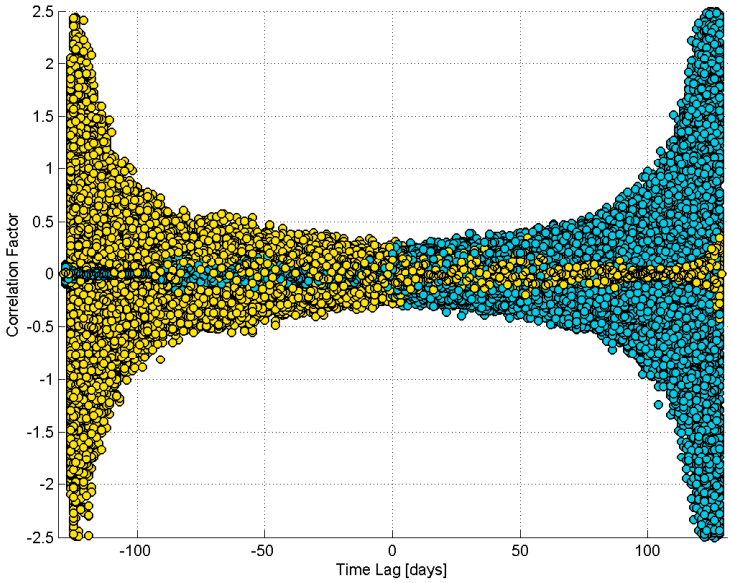

Figure 6.7: Example of the simulated correlation threshold (yellow and cyan clouds) generated from two different uncorrelated lightcurves with different number of samples.

By comparing the autocorrelation analysis results of the VERITAS dataset with the simulated autocorrelation threshold (yellow and blue clouds of dots), it is possible to conclude that there are no significant autocorrelation factors for nonzero time lags.

The autocorrelations of the UVW1, UVM2 and UVW2 lightcurves have similar behaviors. This is mainly ascribable to the closeness in frequency of the UVOT bands.

UVM2 and UVW2 linear autocorrelations do not contain any significant autocorrelation feature, except at zero lag. However, UVW1 exhibits a peculiar behavior: for large time lags, the DCF produces two temporally extended 12-day wide humps (Figure 6.8). The hump clearly peaks at -86 and -76 (76 and 86) days with autocorrelation factors of 0.66 ± 0.03 and 0.57 ± 0.03 (see Figure 6.8). These peaks are also partially visible in the UVM2 and UVW2 autocorrelation analyses. Since there is no evidence of any periodicity from the observation scheduling, the presence of such

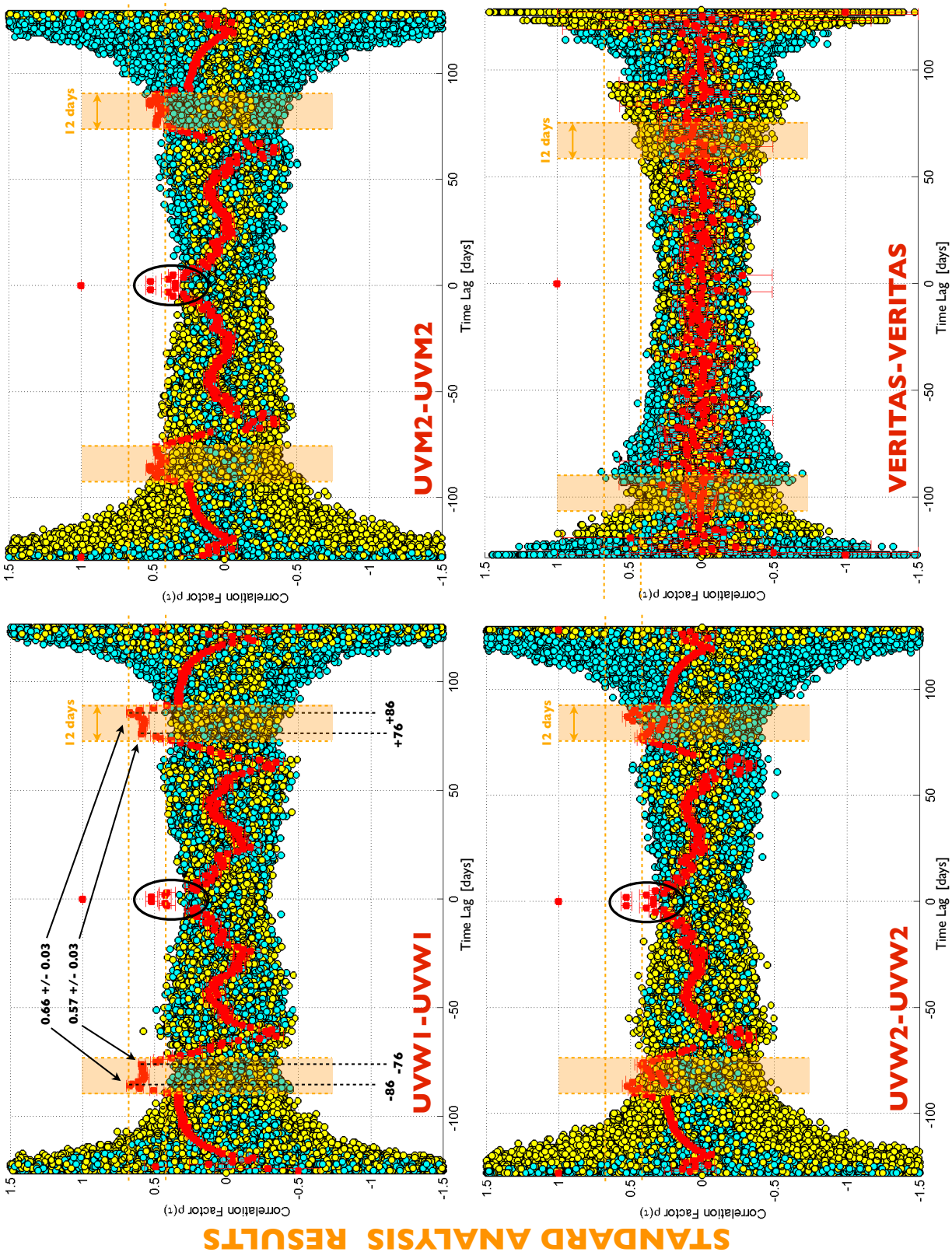

Figure 6.8: Autocorrelation analyses of the UVOT and VERITAS (red dots). The simulated correlation threshold (yellow and blue dots) describes the chance probability of 1 in 10,000.

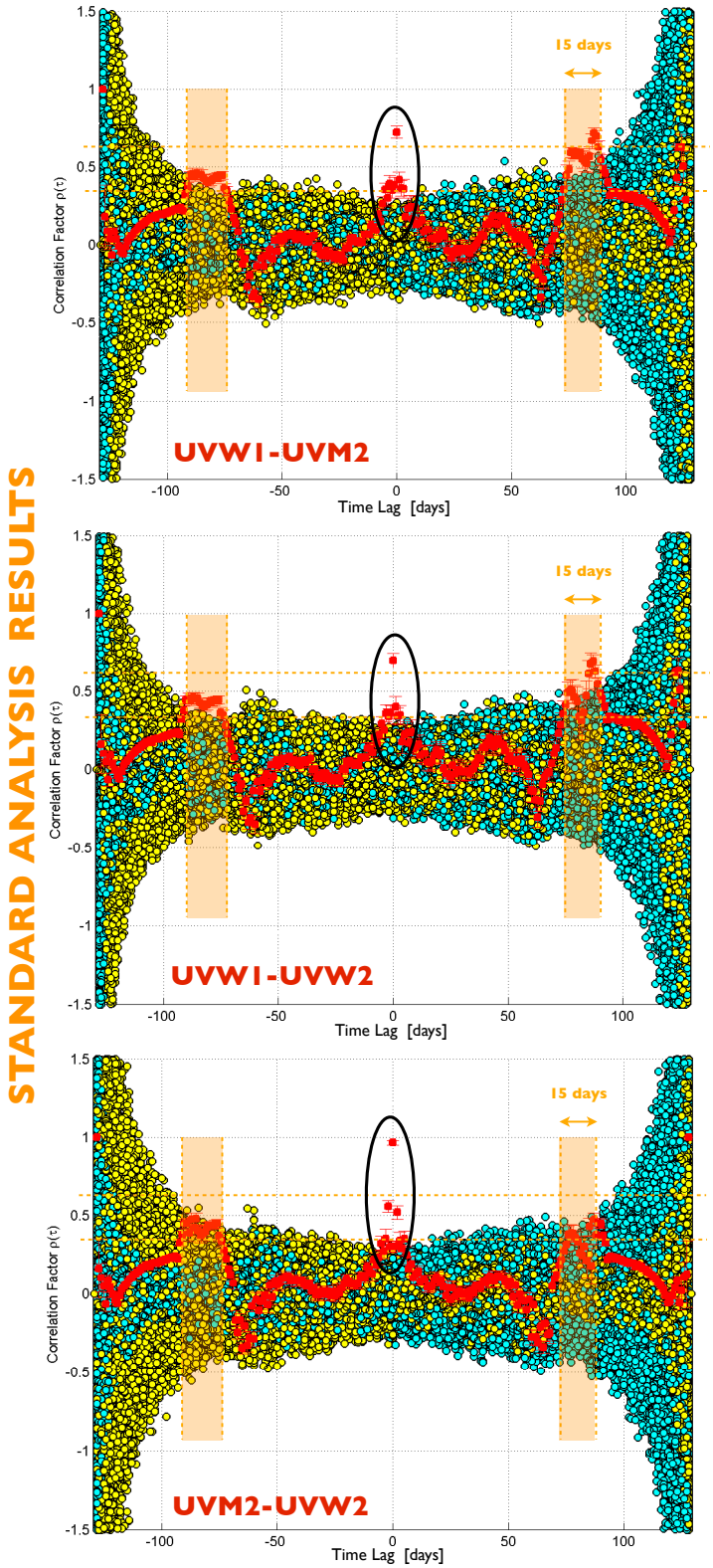

Figure 6.9: Cross-correlation analyses between the UVOT lightcurves (red dots). The simulated correlation threshold (yellow and blue dots) describes the chance probability of 1 in 10,000. For positive lags, the first-named lightcurve lags the second one.

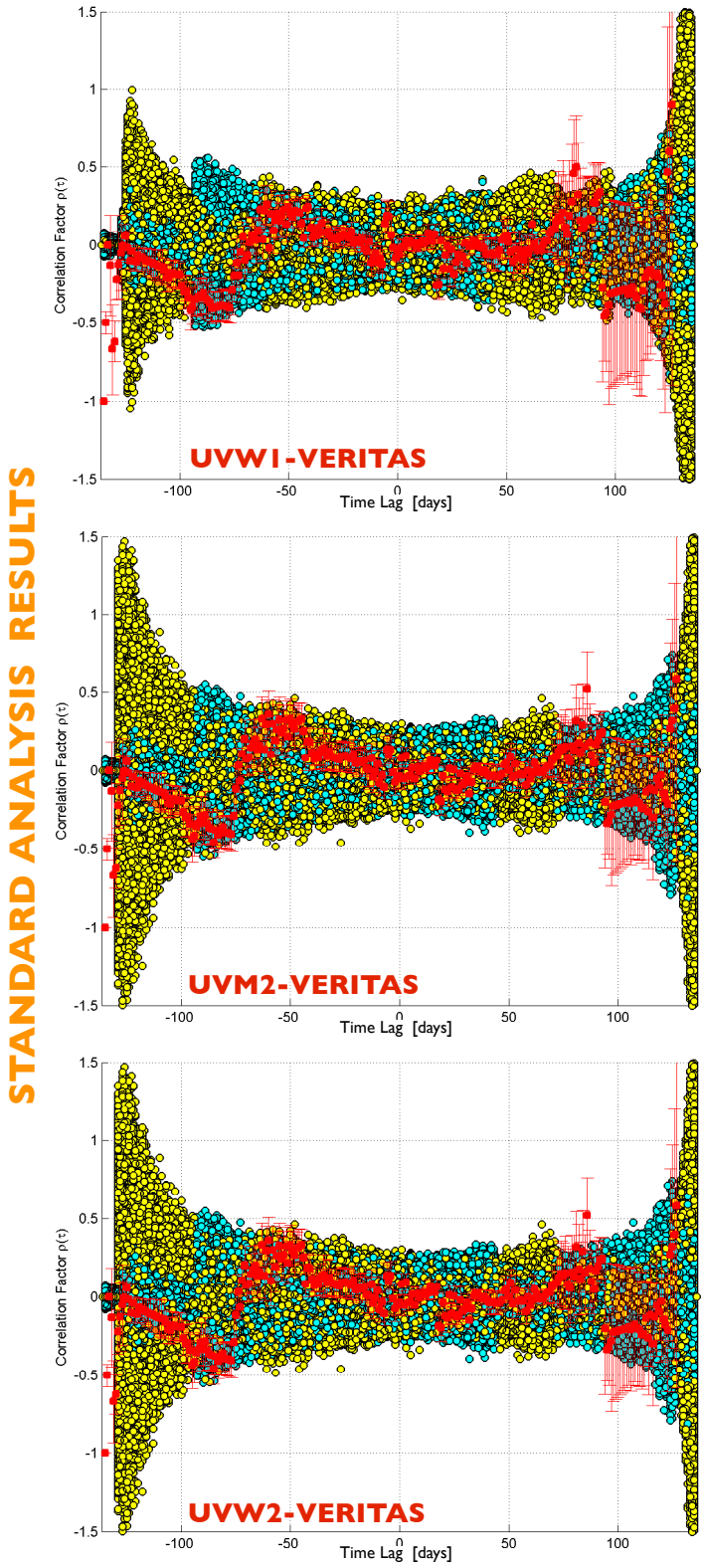

Figure 6.10: Cross-correlation analyses between UVOT lightcurves and VERITAS lightcurve (red dots). The simulated correlation threshold (yellow and blue dots) describe the chance probability of 1 in 10,000. For positive lags, the first-named lightcurve lags the second one.

characteristics would seem to arise from Markarian 421 emission at ultraviolet frequencies. Due to their close energy bands, the UVOT lightcurves are not independent and are expected to be well cross-correlated at zero lag (Figure 6.9). Although moderate UVW1-UVM2 and UVW1-UVW2 zero lag cross-correlation values are present (0.73 ± 0.04 and 0.70 ± 0.04, respectively), the UVM2-UVW2 zero lag correlation factor is very significant and close to unity with $\rho_{\mathrm{UVM2-UVW2}} = 0.96 \pm 0.03$.

Cross-correlation values between the UVOT lightcurves and the VERITAS integral flux lightcurve are not significant at any lag (Figure 6.10). Indeed, the absence of the cross-correlation detection between UVOT and VERITAS sequences is not surprising. In fact, the traditional linear cross-correlation analysis, for sequences assumed stationary, is largely inappropriate to deal with nonstationary behaviors.

6.8 Stationary Approximation

The traditional treatment of correlation - *e.g.* Edelson & Krolik (1988) - only yields reliable results when using stationary sequences. Since the blazar's emission is generated by random nonstationary processes, the results obtained by simply correlating the recorded lightcurves are no longer reliable. Correlation analyses of nonstationary sequences require extra care. For example, two random nonstationary sequences generated by two independent processes should be completely uncorrelated but often this is not the case. The presence of false correlation detection between random independent nonstationary sequences was investigated by Granger and Newbold (2001). They showed that, in some independent sequences produced by nonstationary processes, the cross-correlation and autocorrelation do not appear to converge in

terms of probability toward the expected null values, although the original processes are clearly independent and therefore uncorrelated. Furthermore, looking at any two series of regression residuals, Phillips (1986) showed that the larger the time-series samples, the greater the chance of experiencing spurious correlations.

In order to investigate hidden correlation aspects and to correct spurious correlations between nonstationary sequences, we introduced methods to produce "stationary approximations" of nonstationary sequences produced by nonstationary blazar systems. Technically, these approximations are called "wide-stationary" approximations (Vaughan *et al.*, 2003; Welsh, 1999).

To "stationarize" a given sequence produced by a nonstationary process, a rescaled range statistical analysis (also called "detrending") was first introduced by Hurst (Hurst, 1951) and re-introduced by Arianos and Carbone (2009) to remove nonstationary trends of random sequences. The subtraction of a constant is the most used approach to detrending, although, generally, it does not remove the majority of spurious features and does not significantly help to show hidden features. A linear transformation due to the subtraction of a constant and a linear trend is also used. However, to deal with highly unevenly-sampled time series data with large time gaps, a "clustered constant and linear detrending" provides a more precise stationarization of the temporal sequences. The clusterization is applied by dividing each lightcurve into a few subintervals. Then, in turn, one can detrend each cluster of data by subtracting both the constant and the linear trend computed in each of those intervals (Figure 6.11). Finally, the detrended sequence is rescaled to unity variance.

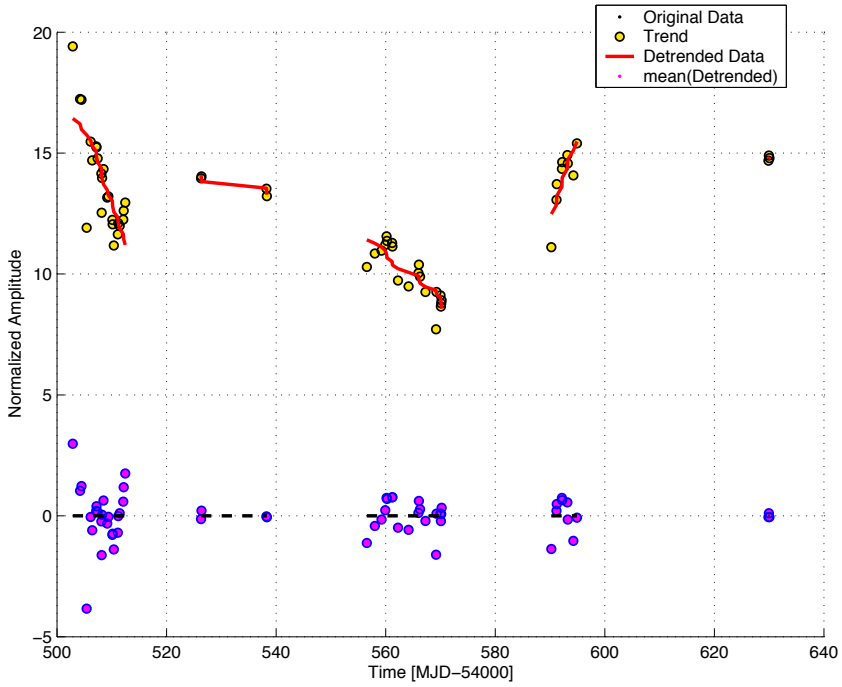

Figure 6.11: Example of a constant plus linear detrending of UVW1 ultraviolet band.

6.9 Results from Stationary Approximation

In order to detect the eventual presence of correlation between the UVOT and VERITAS datasets in stationarized time series, we ran a new correlation analysis applying detrending. For each lightcurve, we computed 1) a constant trend and 2) a constant and a linear trend, to subtract from each of the time intervals outlined in Tables 6.1 and 6.2. Then, in turn, we removed the computed trends from the original lightcurves to convert the nonstationary dataset into a (wide-)stationary dataset. We adopted the one-day bin size since smaller bin sizes would require more intra-day observations, whereas bigger bin sizes would largely reduce the resolution of the correlation analysis.

The cross-correlation analyses between each of the three ultraviolet lightcurves

(UVW1, UVM2, UVW2) and the VERITAS integral flux lightcurve, detrended for a constant value, show evidence of the presence for moderate cross-correlation factors. In each case, the UVOT lightcurve seems to lag the VERITAS lightcurve around +82 days ($\rho_{+82} = 0.60 \pm 0.20$). Detrending the time series for a linear plus constant factor, the DCF analyses first provide an anticorrelation peak around +84 days with $\rho_{+84} = -0.50 \pm 0.20$ and, second, a correlation peak around +86 days providing, in magnitude, similar correlation factors of $\rho_{+86} = +0.50 \pm 0.20$ (Figure 6.12).

Here we provide an interpretation of these latter results. Whereas the cross-correlation analysis of constant detrended lightcurves provide a promising correlation factor around +82 days of time lag, we have to discard this since it is too close to the correlation/anticorrelation peak pair found in the subsequent analysis where the time series was detrended for a linear trend plus a constant factor. The stationarization process obtained by detrending of sequences removes "power" from the original signal and, consequently, a portion of the information. Thus, the signal-to-noise ratio begins to decrease because lower orders of detrending (removing lower frequency contents) subtract larger amounts of real information related to the signal and, proportionally, smaller portions of noise (since noise is still present at higher frequency). Thus, due to the lower fraction of power as a result of the signal at larger time lags, the correlation analysis begins primarily to return the information related to the noise variance. Evidence of this is the very fast correlation/anticorrelation peak pairs produced at +86 and +84 days of time lag. The blazar physical system hardly shows such a fast change. This fast change can be more easily explained if we assume that those correlation/anticorrelation values might be due to noise which, due to its own nature,

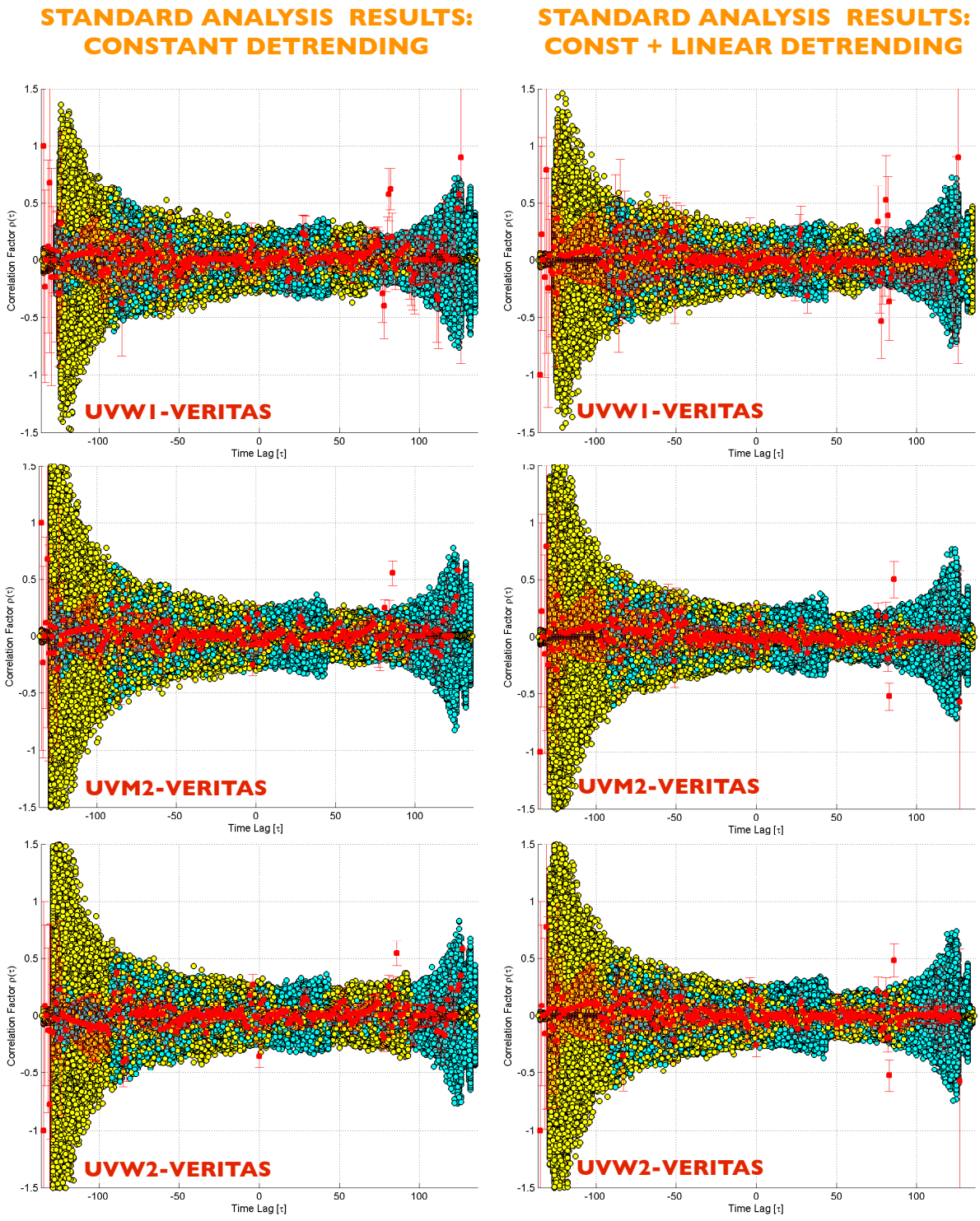

Figure 6.12: Cross-correlations between the constant and constant plus linear detrended UVW1, UVM2, UVW2 UVOT lightcurves and each of the integral flux VERITAS lightcurve (red dots). The simulated correlation threshold (yellow and blue dots) describes the chance probability of 1 in 10,000. For positive lags, the first-named lightcurve lags the second one.

provides sudden changes.

6.10 Structure Function Variability Analysis

Characteristic timescales are significant parameters that, in our case, provide information about the variability "speed" of the processes that may be driving blazar emissions from time to time. However, in general cases, it is difficult to produce a reliable estimate of characteristic timescales due to time series characteristics (for example, nonstationarity or uneven sampling). One of the most remarkable aspects of structure function analysis is its ability to correctly discern such a range of timescales that may contribute to variations in a given dataset.

6.10.1 Structure Function Calculation

Initially, structure function analysis was introduced by Kolmogorov (around 1940) and then reintroduced for astronomical use by Simonetti *et al.* (1985). It returns similar information to the PSD computed via Fourier approaches and obtained only by using evenly sampled, or uniform, time series. However, structure functions deal with unevenly sampled time series (Hughes *et al.*, 1992; Zhang *et al.*, 2002). Since extended gaps and unevenly sampled observations exist in the VERITAS and the UVOT datasets, the structure function approach, therefore, seems to be one of the most reliable techniques to get feasible estimates of lightcurve variabilities (Paltani, 1999; Kataoka *et al.*, 2001).

For a finite zero-mean sequence of measurements $s(t)$ sampled at times t_i where $i = 1, 2, 3, 4, ..., n_{sample}$, where n_{sample} is the number of samples, we can compute the

first order structure function as follows:

$$D(\tau) = \frac{1}{N(\tau)} \sum_{i=1}^{N(\tau)} [s(t_i + \tau) - s(t_i)]^2, \tag{6.13}$$

where, τ is the time separation (or time lag) of the $N(\tau)$ pairs of points separated by times between $\tau - \Delta\tau/2$ and $\tau + \Delta\tau/2$ where $\Delta\tau$ is the bin width.

However, this formulation does not allow us to clearly assess the other important properties of the structure functions. Thereby, we provide an appropriate reformulation. If $D(\tau)$ is the structure function of the signal $s(t)$ with mean 0, and variance 1, we have

$$D(\tau) = E[(s(t) - s(t+\tau))^2] = E[s(t)^2] + E[s(t+\tau)^2] - 2E[s(t)s(t+\tau)] \tag{6.14}$$

where $E[...]$ is the average operator and τ is the time lag. Under wide-stationary process assumptions:

$$D(\tau) = \sigma^2 + \sigma^2 - 2\sigma^2\rho(\tau) = 2\sigma^2 [1 - \rho(\tau)] \tag{6.15}$$

where $\rho(\tau)$ is the autocorrelation coefficient between $s(t)$ and $s(t+\tau)$, and σ^2 is the variance of the time series (Lainela & Valtaoja, 1993; Zhang *et al.*, 2002). In practice, the first order structure function removes only the linear component of the signal (Simonetti *et al.*, 1985).

The typical trend of the first-order structure function in Figure 6.13 was calculated via Equation 6.15. The first plateau is due to σ_n^2, that is the variance of the noise. The higher plateau consists of the variance of the real signal after removing the variance of the noise, here σ_y^2 (Simonetti *et al.*, 1985, see Equations A13 and A14). The link between the two plateaus is termed the slope. Assuming that the random error is

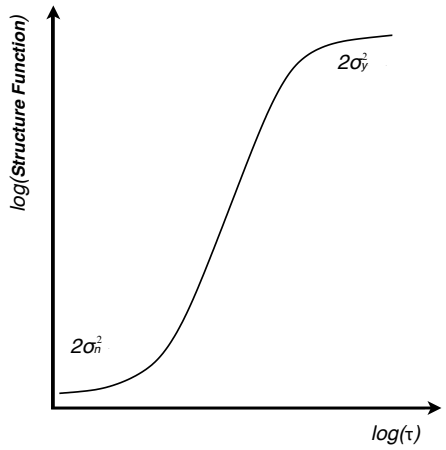

Figure 6.13: Plot of an ideal structure function. The first plateau is due to σ_n^2, which is the noise variance. The higher plateau consists of the signal variance, here σ_y^2. The link between the two plateaus is termed the "slope".

produced by a white noise distribution, we have:

$$D(\tau) = D_y(\tau) + 2\sigma_n^2 \tag{6.16}$$

where σ_n^2 is the noise variance and $D_y(\tau)$ is the structure function which is computed on a theoretical signal (in the absence of superimposed white noise). The uncertainty in the structure function is given by

$$\delta D(\tau) \approx \sqrt{\frac{8\sigma_n^2}{N(\tau)} D(\tau)} \tag{6.17}$$

as obtained in Simonetti *et al.* (1985).

The presence of deviations from the theoretical trend along the plateaus, and indeed along the slope, is common. These deviations can be caused by a number of flares, or by insufficient data sampling. More likely, they can be related to the nonstationary behavior of the time series. If the lightcurves to be analyzed are affected by uneven sampling, the related structure functions return a type of "break"[10] (Hughes

[10]In the most general sense, we use the term "break" for any irregularity that might deviate from

et al., 1992), showing more evident breaks with larger gaps of observations. Possible change from a linear trend along the central part of the slope between the $2\sigma_n^2$ of the noise plateau and the $2\sigma_y^2$ signal plateau might be due to the presence of variability changes in the input series. This alteration could also be due to a sudden appearance of nonstationarity. More generally, it could depend on the presence of special features in the original signal such as periodicities which would greatly affect the behavior of the second plateau at the same time.

6.10.2 The Characteristic Timescales

The minimum characteristic timescale, τ_{min}, is estimated via the point where the computed structure function emerges from the noise variance plateau with a sudden step and, typically, begins its steepening on the slope segment of the structure function (see Figure 6.13). Similarly, the maximum timescale, τ_{max}, is the corresponding point where the slope flattens on the signal variance value, which corresponds to the higher plateau.

There is a straightforward relationship between τ_{min} and τ_{max} and the characteristic frequencies of the power spectral density function made on a limited portion of the spectrum. For any limited frequency interval, the presence of the cutoff frequency ν_{max} and the break frequency ν_{min}, limiting the frequency band, would ensure the convergence of the excess variance, leading to a reliable frequency-domain transformation (Zhang *et al.*, 2002). Then,

$$\nu_{min} = \frac{1}{\tau_{max}} \quad \text{and} \quad \nu_{max} = \frac{1}{\tau_{min}} \ . \tag{6.18}$$

---

the theoretical structure function trend.

which corresponds to the introduced structure function characteristic timescales.

If a given lightcurve possesses a spectral index of $\alpha = 2$ in the frequency domain ($P(\nu) \propto \nu^{-\alpha}$), which corresponds to a red-noise trend, the index of its structure function slope segment connecting the two plateaus would be linear and equal to $\beta_{SF} = 1$ (Paltani & Courvoisier, 1997; Rutman, 1978; Simonetti *et al.*, 1985), and the range between ν_{min} and ν_{max} can be accurately fitted by a power-law. In the limit of long enough observing time $T \to \infty$ and small enough sampling time $\Delta t \to 0$ (Zhang *et al.*, 2002):

$$\alpha = \beta_{SF} + 1\,. \tag{6.19}$$

Structure functions computed by using real time series, generally, do not resemble the expected theoretical trend shown in Figure 6.13. This can strongly bias the estimation of the τ_{max} characteristic timescale. The presence of such alterations is mainly ascribable to the presence of large dataset gaps and uneven sampling rates. Nonstationary behavior of the recorded lightcurves can also play an important role in shaping the structure function. Although the presence of periodicities is unlikely, in this latter case, the structure function might be modulated and this may contribute to partially shifting the characteristic timescales from the real position.

The structure function analysis carried out in the present work has been implemented via a portion of subroutines that are part of a more complete software suite already used in Fossati *et al.* (2008). Further details regarding that suite are provided by Toner (2008).

The code generates a large number of simulated lightcurves ($N = 1{,}000$) for each $\tau_{ratio} = \tau_{rise}/\tau_{fall}$ value in a given range, where τ_{rise} and τ_{fall} are the assumed rise

Number of Up and Down Transitions

	1σ	2σ	3σ	4σ	5σ
VERITAS Integral Flux	26.45	14.33	7.71	5.51	5.51
VERITAS Rate	29.75	24.24	17.63	11.02	8.82
UVW1	87.14	62.25	49.80	12.45	12.45
UVM2	92.10	61.40	40.93	30.70	10.23
UVW2	67.64	45.09	22.55	22.55	7.52

Table 6.7: Estimated number of "up and down" transitions (per day) with the corresponding uncertainty measurements for the VERITAS and UVOT lightcurves.

and fall characteristic timescales of flares, respectively. Each lightcurve is produced by generating a number of flares[11] at random times. Furthermore, from each group of lightcurves with a specific τ_{ratio} we compute a corresponding group of structure functions. Each group of N structure functions is then averaged to obtain an averaged structure function. Finally, the best τ_{ratio} is obtained by identifying the average simulated structure function that best fits the structure function for the real lightcurve.

The number of up and down transitions registered in real lightcurves depends on the amount of the lightcurve measurement uncertainty with a specific confidence level. If the uncertainty level increases, the number of flares that we register becomes lower. Having looked at the estimates in Table 6.7, we counted the number of flares corresponding to the 1σ confidence level. For comparison, in Table 6.7 we also show the estimation of the up and down transitions of the VERITAS rate lightcurve.

[11]The number of up and down transitions measured in real datasets is used to determine the number of flares to insert randomly in the simulated lightcurves. The flares are modeled as a sum of triangular shapes by choosing the length of their inclined segments proportional to the assigned rise and fall times (Fossati *et al.*, 2008).

Subsequently, it can be noted that the numbers of up and down transitions of the VERITAS integral flux lightcurve and the VERITAS rate lightcurve are fairly similar at 1σ, while they differ drastically for other confidence levels. This is an important aspect to clarify, since it would be expected that these two VERITAS lightcurves possess a similar amount of transitions, although their position in the rate lightcurve would appear enhanced/reduced in the integral flux lightcurve, in accordance with the corresponding energy content of the recorded events. Also, setting a 1σ threshold makes the estimates of the number of the flares consistent for UVW1, UVM2 and UVW2 bands. For larger thresholds, the number of flares begins to diverge toward different solutions for the three ultraviolet bands. This is not desirable since the spectral closeness of these UVOT bands suggests there should be a common value.

In our analysis, the simulated lightcurves are modeled by using a set of 60 τ_{rise}/τ_{fall} ratios between 1/5 and 5. The structure functions computed from each simulated lightcurve were averaged and, then, compared with the structure function derived from the real lightcurve. Iterating this process for a number of different values of characteristic timescales (*e.g.* $\tau_{rise} = 0.01 - 10$), we obtain the average simulated structure function that best fits the real structure functions. To compare the structure functions obtained from the real and the simulated lightcurves, we also implemented the "comparison" method, or rather a modified t_{Test}, between the means of two correlated samples:

$$t_{Test} = \frac{\sum_{i=1}^{N}(SF_i - \overline{SF_i})^2}{N_i} \tag{6.20}$$

where SF_i is the computed structure function using the original lightcurve, $\overline{SF_i}$ is the structure function averaged and computed using the simulated lightcurves and N_i is

the number of bins used in the structure function. The t_{Test} acts as an asymptotically unbiased estimator, where a large number of trials are needed in order to converge to the correct value. That estimator chooses the simulated average structure function that most closely matches the structure function made with the real lightcurve.

A t_{Test}-fit plot (Figure 6.14) is produced for different pairs of τ_{rise} and τ_{fall} values adopted to model the corresponding group of simulated lightcurves.

6.11 Structure Function Analysis Results

For each structure function analysis, we found the values of the τ_{rise}/τ_{fall} ratio and the τ_{rise} values that return the minimum fitting t_{Test} value (see Figure 6.14). Then, we compute the τ_{fall} value (Figure 6.15). Finally, from the plot of the structure function, we obtain the τ_{max} and τ_{min}. Additionally, we obtained slopes and uncertainties for any analyzed structure function. Structure function analyses and related plots are provided in Figure 6.16, and the results are summarized in Table 6.8.

The three UVOT measurement datasets show relatively good sampling in small periods, with some extended gaps of observation at longer time lags. The structure function analysis of the UVW1, UVM2 and UVW2 bands (Figure 6.16) minimizes for $\tau_{ratio} = \tau_{rise}/\tau_{fall} = 0.86$.

The UVOT τ_{ratio} uncertainty is computed via simulation. We have generated a set of 10 random lightcurves convolved with the same distribution in time as the original UVOT lightcurves. Each generated lightcurve possesses a PSD slope index of -2 (red noise trend), and the same number and values of mean, variance and number of up

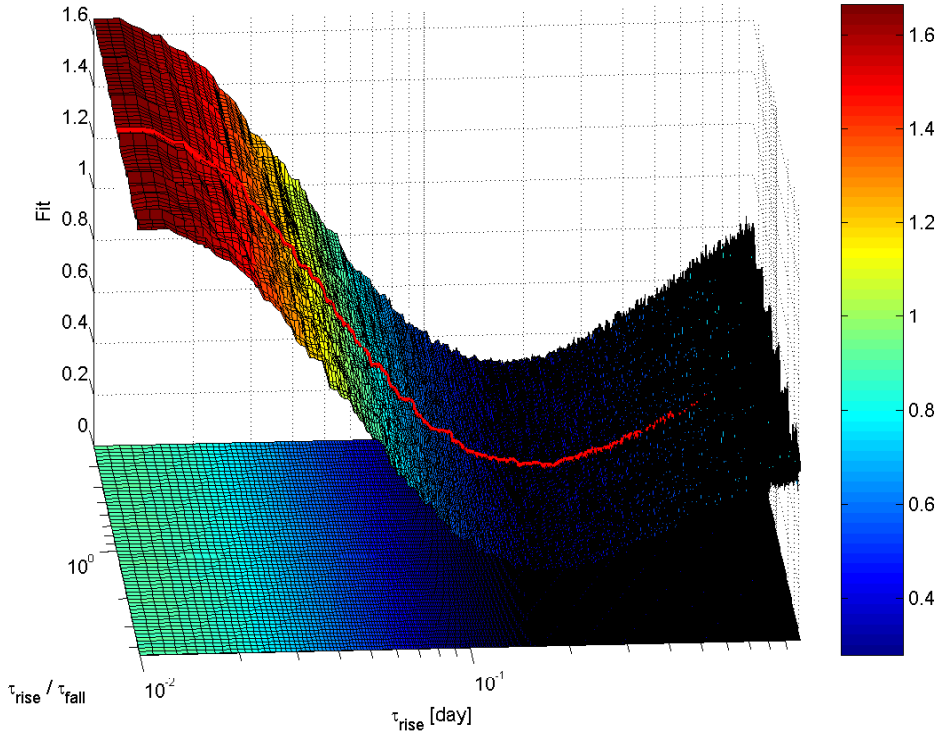

Figure 6.14: t_{Test} minimization fit between structure functions obtained from real and simulated lightcurves varying for different τ_{rise} and characteristic τ_{rise}/τ_{fall} ratio. The algorithm chose the curve having the minimum fit value (red line) to select the characteristic ratio and the characteristic rise time.

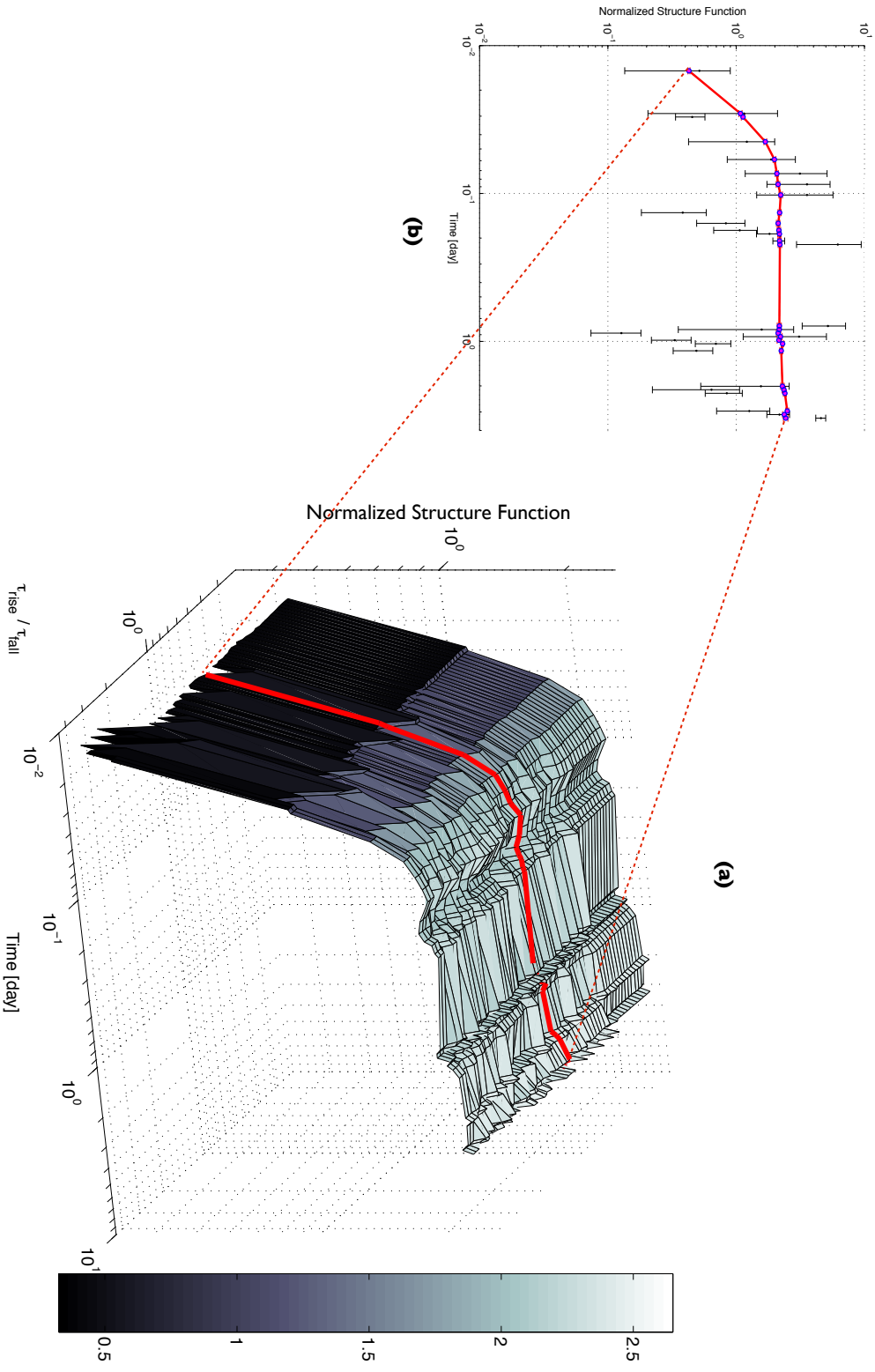

Figure 6.15: **(a)** Structure functions obtained from simulated lightcurves varying for different τ_{rise} and characteristic τ_{rise}/τ_{fall} ratios. **(b)** Fitting between the selected structure function and the real structure function.

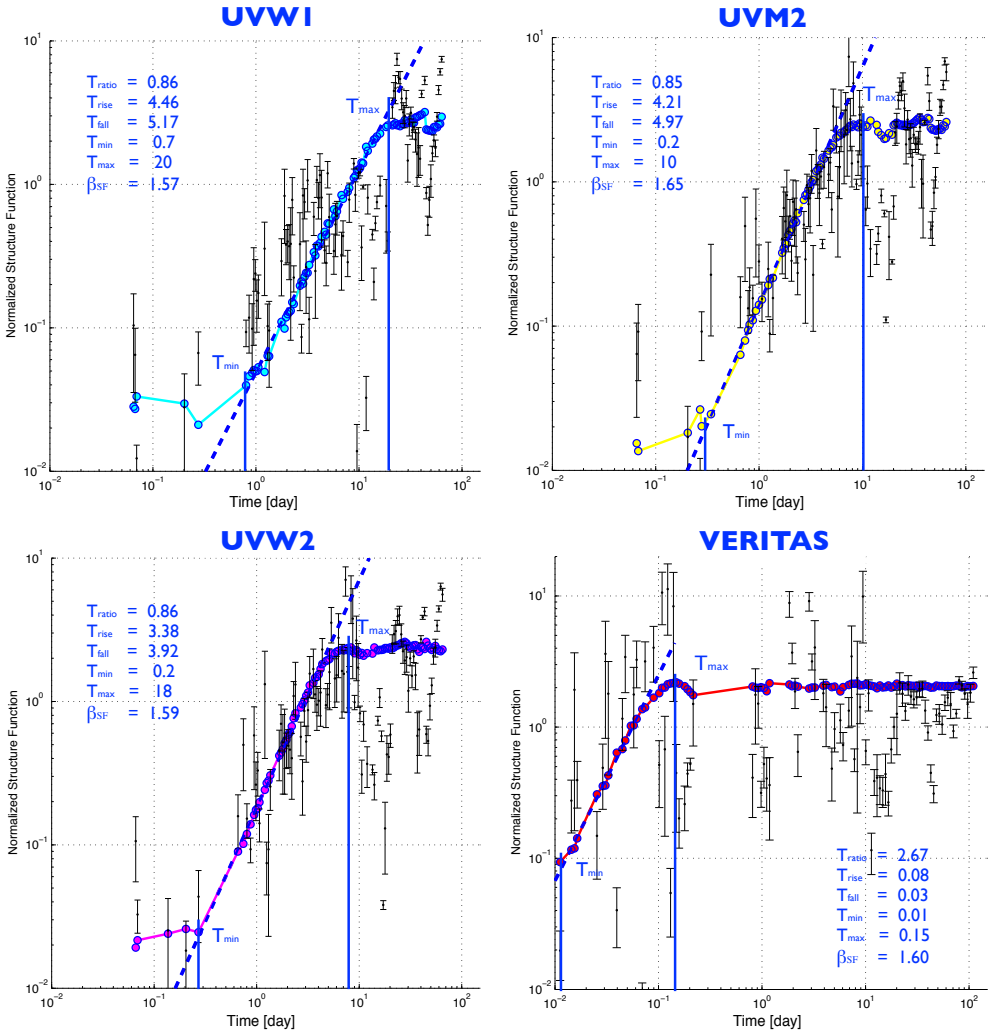

Figure 6.16: The plots of the structure functions were computed by using the whole season dataset. Points with black errorbars in each plot are the structure functions computed with the real lightcurves. The continuous lines are the structure functions computed for the simulated lightcurves with a rise/fall time that minimizes the statistical test, whereas the dotted blue lines indicates the "slope" segment fitting.

Datasets Characteristic Timescales and Slopes

	VERITAS	UVW1	UVM2	UVW2
τ_{ratio}	2.67	0.86	0.85	0.86
τ_{rise}	0.08	4.46	4.21	3.38
τ_{fall}	0.03	5.17	4.97	3.92
τ_{min}	0.01	0.7	0.2	0.3
τ_{max}	0.15	20	10	18
β_{SF}	1.6	1.57	1.65	1.59

Table 6.8: Characteristic timescale results (in days) of the UVW1, UVM2, UVW2 and VERITAS energy bands. The table also returns the β_{SF} structure function slope values directly related to the estimation of power spectral density slopes, $\widehat{\alpha}$, with the following relation: $\widehat{\alpha} = \beta_{SF} + 1$ (Zhang *et al.*, 2002).

and down transitions presented by the UVW1 lightcurve. We have then computed the structure functions, parameterizing for τ_{rise}/τ_{fall} as in the case of the original datasets. Computing the standard deviation of the best τ_{ratio} values obtained by evaluating the UVW1 simulated lightcurves, we have obtained the $\delta\tau_{ratio,\mathrm{UVW1}} = \pm 0.3$. Since all the UVOT lightcurves present very similar behavior, observing scheduling and spectral bands, the results obtained in the case of UVW1 are applicable also in the case of UVM2 and UVW2 datasets. The timescales τ_{rise} of UVW1, UVM2 and UVW2 are 4.46, 4.21 and 3.38 days, whereas the timescales τ_{fall} are 5.17, 4.97 and 3.92 days, respectively. All the structure functions experience some deviations from a theoretical trend but, however, they are closely approximated by the reconstructed structure functions.

VERITAS structure function characteristic timescales show a larger value for $\tau_{ratio,\mathrm{VERITAS}} = 2.7 \pm 0.7$. The uncertainty on the timescale ratio is computed with

the same approach adopted for the UVOT dataset. The associated VERITAS rise and fall timescales are $\tau_{rise} = 0.08$ days and $\tau_{fall} = 0.03$ days.

The slope value β_{SF} is directly related to the estimate of the power spectral density, $\widehat{\alpha}$, by the following relation: $\widehat{\alpha} = \beta_{SF} + 1$ (Zhang *et al.*, 2002). For the VERITAS and UVOT datasets we estimate[12] $\beta_{SF} = 1.6 \pm 0.1$.

The structure function slopes obtained by using the UVOT dataset might be compatible with the analysis reported by the EUVE mission in the extreme UV spectral range ($70 - 760$ Å). Takahashi *et al.* (2000) analyze the observational dataset recorded during 1998 in which $\beta_{SF} = 1.2$ but, unfortunately, they do not quote the uncertainty on this estimate.

Through fitting the measured ultraviolet structure functions into those generated from simulated lightcurves, we derived the rise-timescale and fall-timescale to be approximately $4 - 5$ days for the ultraviolet bands. The ultraviolet result is in agreement with previous results that have set the characteristic timescales for optical lightcurves between 10 and 20 days (Horan *et al.*, 2009):

$$\tau_{opt} = \sqrt{\frac{\omega_{UV}}{\omega_{opt}}} \cdot t_{obs,UV} \approx \sqrt{\frac{10^{16}}{10^{15}}} \cdot 5 \simeq 16 \; days. \tag{6.21}$$

For consistency with Horan *et al.* (2009), in this last calculation we assumed a characteristic timescale ratio equal to unity.

[12]The slope uncertainty is estimated by the same simulation process that produces the $\Delta\tau_{ratio}$ uncertainties for both the reduced VERITAS and UVOT datasets.

Chapter 7

Conclusions

7.1 Summary

This work investigated the multiwavelength behavior of Markarian 421 using ultraviolet UVOT/Swift and TeV VERITAS observations.

In Chapter 2, we provided a review of the fundamentals in VHE astrophysics. Chapter 3 was dedicated to reducing the UVOT UVW1, UVM2 and UVW2 ultraviolet data using a custom-built pipeline (Navajo, version 2.4.3, November 2009) that extended the public standard pipeline with the introduction of a series of corrections (*e.g.*, astrometry, reddening, redshift) and quality checks. A lightcurve for each UVOT band was produced (Figure 3.15).

In Chapter 4, we introduced the principles of atmospheric Cherenkov imaging telescope operation and the specific design of the VERITAS array. In Chapter 5, we reduced a VERITAS dataset using the VEGAS analysis software producing the lightcurve of the integral fluxes on a run-by-run basis (see Figure 5.12). A further

investigation was pursued by fitting a power law and a power law plus exponential cutoff to the spectrum of the VERITAS datasets (Figure 5.13).

In Chapter 6, we carried out a detailed analysis of the temporal features present in UVOT and VERITAS lightcurves for the entire monitoring season and, separately, for several selected time subintervals (see Figure 6.1). This analysis included a variability study with particular emphasis on the identification of noise-like characteristics of the signal produced by blazar processes. We carried out the cross-correlation and auto-correlation analyses of the UVOT and the VERITAS lightcurves. Finally, with the structure function analysis, we determined the ranges of some characteristic timescales that contribute to the temporal variability of UVOT and VERITAS lightcurves.

7.2 Discussion and Conclusion

Due to its high level of γ-ray emission at TeV energies, Markarian 421 provides a high number of event detections. The number of the excess counts has been used to compute a time-dependent integral flux (see Section 5.7). The integral fluxes have been calculated for the entire spectrum above 300 GeV (Figure 5.12). The Markarian 421 UVOT lightcurves have three intensive periods of observation corresponding to very active emission states, with large observing temporal gaps between them (Figure 6.1). In contrast to this, the VERITAS lightcurve has a more homogeneous time observation scheduling.

- **TeV flux increase accompanied with power spectral hardening**

  For sudden high flux variations, our results show evidence for correlation between TeV flux increases and TeV power spectral hardening (Figure 5.14). By using a power law plus exponential cutoff to model the TeV spectrum, the overall power spectral index increases from about -3 to -1.5 (see Figure 5.14) with a simultaneous flux enhancement of one order of magnitude. We obtained a correlation index of 0.86 ± 0.42 over the whole TeV spectrum. Interestingly, Acciari *et al.* (2011) also provided a good fit for this correlated behavior between flux and spectrum by fitting a log-parabola.

  The correlation between the spectral hardening and the flux increase might be simply explained by an increase of the magnetic field. Alternatively, we can conjecture that the correlation might arise from the hardening of the electron population that drives the synchrotron emission.

- **TeV correlation between variability and increased flux**

  The TeV variability seems to be correlated at 2σ confidence level with enhancement of the TeV flux (see Tables 6.5 and 6.6). During our campaign, two moderate flares were detected at very high energies, and a third flare (2-3 May, 2008) reached a flux of more than 10 Crab in a few minutes (Acciari *et al.*, 2011). We observe that during 'Period 4' (19^{th} of April 2008 - 14^{th} of May 2008) which shows the highest TeV flux level in our dataset ($F_{max,4} = 1.18 \times 10^{-9}$ erg/cm^2/s and $F_{mean,4} = 3.32 \times 10^{-10}$ erg/cm^2/s), the VERITAS F_{var} and F_{pp} flux variabilities ($F_{var,4} = 70\%$ and $F_{pp,4} = 40\%$, respectively) are larger than those

computed in the relatively quiescent and moderately flaring 'Period 1' (with $F_{max,1} = 5.94 \times 10^{-10}$ erg/cm^2/s and $F_{mean,1} = 3.46 \times 10^{-10}$ erg/cm^2/s where $F_{var,1} = 23\%$ and $F_{pp,1} = 16\%$, respectively).

- **No evidence for time-domain correlation**

  The correlation analysis applied to the stationary approximation of UVOT and VERITAS lightcurves is still not conclusive. Cross-correlating each of the three UVOT ultraviolet lightcurves (UVW1, UVM2, UVW2) and the VERITAS integral flux lightcurve detrended for a constant value would seem to show the presence of moderate cross-correlation factors. In each case, the UVOT lightcurve seems to lag behind the VERITAS lightcurve by around +82 days ($\rho_{+82} = 0.60 \pm 0.20$). At large time lags, detrending the time series for a linear plus constant factor, DCF analyses provide a first anticorrelation peak around +84 days with $\rho_{+84} = -0.50 \pm 0.20$ and a second correlation peak around +86 days yielding, in modulus, similar correlation factor values around $\rho_{+86} = +0.50 \pm 0.20$ (Figure 6.12).

  However, we argue that these correlation results are not significant, since the stationarized sequences are obtained applying detrending which, removing power from the original signal, deletes a portion of the signal information. Thus, the signal-to-noise ratio drastically begins to decrease (see Section 6.9). Lower orders of detrending (removing lower frequency contents) subtract, proportionally, a larger amount of the deterministic signal information and a smaller portion of nondeterministic signal with noise-like characteristics. Thereby, we can con-

clude that the very fast correlation/anticorrelation peak pair produced at +86 and +84 days of time lag might be produced, in this case, only by chance since blazars hardly show such sudden changes.

- **Characteristic rise and fall time ratio**

  The structure function is a very convenient approach to determining the range of timescales that contribute to the temporal variability of a given lightcurve (Hughes *et al.*, 1992; Zhang *et al.*, 2002). At TeV energies, we obtain a $\tau_{ratio,\mathrm{VERITAS}}$ factor that is equal to 2.7 ± 0.7, which is the ratio of the rise and fall timescales (Table 6.8). This value is remarkably close to that obtained in Abramowski *et al.* (2011) for the M87 emission, since $\tau^{M87}_{rise,\mathrm{VHE}}/\tau^{M87}_{fall,\mathrm{VHE}} \sim 2.7$. We experience a distinctly different value at UV bands ($\tau_{ratio,\mathrm{UVOT}} = 0.9 \pm 0.3$).

- **Noise-like variability**

  The computational method adopted can be used for discrete gapped datasets where it is not possible to obtain a power spectral density by Fourier methods (see Section 6.5.1).

  Introducing this simulation approach, we provided a statistical characterization of the F_{VR} versus α relation for the particular dataset to be computed. This approach confirms that the power spectral densities of the TeV blazar object Markarian 421 is effectively described by a power law $P(\nu) \propto \nu^{-\alpha}$ with $\alpha_{\mathrm{UVOT}} = 2 - 3$ and $\alpha_{\mathrm{VERITAS}} = 1.5 - 3$.

  We note the red/black noise presence between the two plateaus (see Figure 6.16) on the Markarian 421 emissions at TeV and UV wavelengths. Similar values

were previously noticed by Kataoka (1999), Kataoka *et al.* (2001) and Abdo (2010). By introducing dedicated technique refinements, we constrained the related uncertainty of its estimation to less then 4%. Since the slope value β_{SF} of the structure function is related to the PSD slope as $\widehat{\alpha} = \beta_{SF} + 1$ (Zhang *et al.*, 2002), we obtained $\widehat{\alpha} = 2.6 \pm 0.1$ for both VERITAS and UVOT datasets (Table 6.8).

The observed jet emission can be modeled as the response of different interconnected systems relating different acceleration mechanisms. By virtue of the Brownian path followed by the re-heating particles in magnetized clouds, the second-order Fermi acceleration process is a random-walk (or red-noise) process. This acceleration process already possesses a prominent importance in blazar jet emission and its variation might explain the changes in the blazar jet emission. In Kataoka (1999) and Kataoka *et al.* (2001), it was shown that several blazars presented a variation in their PSD power-law slope indexes in different time intervals of observations (*e.g.*, Markarian 421 presented variability changes of $P(\nu) \simeq 2.2$, 2.4 and 2.6 during a monitoring campaign in 1996-1997. Our work shows that the measured variability (quantified by the computation of the PSD power-law slope index) should be identical through many decades of energy and, possibly, indicate a dominant or a less significant contribution of the second-order Fermi mechanism to the jet emission.

- **Blazar noise and system stability**

  Since the PSD index $\hat{\alpha}$ is 2.6 ± 0.1, the overall blazar system might possess an even fractional nature (Mandelbrot & van Ness, 1968), revealing a mixed-

like blazar structure made by interconnected systems that, naturally, provide a detected signal with different types of noise[1].

Interestingly, the appreciable presence of red noise helps in outlining some qualitative conclusions regarding the blazar system. One of the possible origins of the red noise fluctuations has been associated with the accretion disk emissions of blazars at X-ray energies (Azarnia *et al.*, 2005). However, the fluctuations of a fully chaotic system should exhibit $\alpha = 1$, instead of $\alpha \geq 2$. Thus, it seems that the blazar system is, at least, partially integrable since it was found that regular integrable[2] systems present a red noise behavior (Molina *et al.*, 2010).

An integrable system guarantees the ability of that system to produce analytical explicit solutions. The existence of such analytical solutions ensure the existence of dynamical stability point(s) or region(s) of the entire blazar (interconnected) system.

Furthermore, although even non fully chaotic systems can reach sometimes a sort of "restricted" statistical stability (Grebogi *et al.*, 1983; Brown and Rulkov, 1997; Sadgrove *et al.*, 2008), regular integrable systems guarantee the existence of the stability for any initial condition[3]. Thereby, we might argue that the evolution of the blazar system toward stability should be reflected on the blazar structure. The stability of the blazar system reflects on its structure and its

[1]A further similar reprocessing might, also, take place along the path of the radiation toward the observer.

[2]A system is integrable, or Hamiltonian, if it is possible to analytically integrate its equations.

[3]For example, in the case of the three-body system under gravity attraction, the existence of a stable configuration for any of its initial conditions is not sure because of its system's nonintegrability.

evolution. Generally, in nature, stable systems have evolved over longer periods of time than unstable ones. Thus, we might tentatively infer that blazars are very old objects. This might suggest why blazars are hosted by very old early-type elliptical galaxies. However, further investigations are required.

Providing an estimate of the source variability behavior and a classification of the blazar flares at different wavelengths, time-domain studies can significantly contribute in constraining and identifying the blazar emission mechanisms. In this context, the study of the blazar system and its stability can help to discover peculiar aspects of the blazar evolution and, thus, on the blazar structure. Simple leptonic homogeneous one-zone SSC models cannot explain most of the SED features of Markarian 421 during a moderate/high activity emission state or, indeed, during a very low-activity state (Abdo *et al.*, 2011). Ultimate answers to the fundamental questions of the blazar structure still have to provided. The precise locations of the VHE γ-ray emitting zones still remain unclear. Some scenarios try to locate them between the jets and the broad-line regions producing γ-rays through Comptonization of UV photons (Watanabe *et al.*, 2009). However, in our case, this mechanism is not applicable since Markarian 421 has no broad-line region. Others locate the VHE emission zones at larger distances, for example interacting with the cosmic microwave background (Böttcher *et al.*, 2008). We note that showing a very short-time variability behavior and the presence of an asymmetry between the rise and fall flare segments in the VERITAS lightcurve, the VHE emission mechanism of Markarian 421 requires (still in a leptonic scenario) $t_{inj} \sim t_{lc} \equiv R/c$ (Chiaberge & Ghisellini, 1999), where t_{inj} is the electron injection time and t_{lc} is the light crossing time of photons produced in

the spherical region (via Comptonization of ambient photons) with radius R. Furthermore, $\tau_{ratio,\mathrm{VERITAS}} = 2.7 \pm 0.7$ being larger than unity suggests a slow rise of the emission providing $t_{cool} \gg t_{lc}$, where t_{cool} is the synchrotron and SSC cooling time ($t_{cool}^{-1} = t_{syn}^{-1} + t_{SSC}^{-1}$). We note that, in presence of asymmetric flares at VHE (without emission plateaus between the rise and fall segments), the injection time is constrained toward low or moderate values - see (Chiaberge & Ghisellini, 1999) - reaching at most $t_{inj} \leq t_{lc}$. In this case $t'(I'_{max}) \simeq t_{rise}\,\delta \simeq 1.5\ t_{lc}$, where $t'(I'_{max})$ indicates the time interval between the beginning of the injection and the maximum intensity of the emission in the frame reference of the emitter. Assuming a typical Doppler factor $\delta = 50$ for Markarian 421, we obtain an estimate of the typical reprocessing spherical region of radius $R(\delta = 50) = 7 \times 10^{15}$ cm.

7.3 The future of γ-ray Astronomy

7.3.1 VERITAS Upgrade

The VERITAS Collaboration has already worked to improve the sensitivity of the array telescopes. The current pre-upgrade sensitivity is such that a point-like source emitting 1% Crab-flux above the 100 GeV is detected at 5σ confidence level after only 25 hours of observation (Kieda, 2011). The Collaboration is working to obtain a further enhancement of the array sensitivity through upgrades that, mainly, will allow for better rejection of background events.

In 2010, the VERITAS collaboration started the upgrading of the cameras by adopting new 33% quantum efficiency PMTs (Hamamatsu R10560). These PMTs have $\sim$ 3 mm smaller diameter than the currently adopted Photonis XP2970. The

installation on all four telescope cameras was carried out during the Summer of 2012.

Further efforts have already been aimed at replacing the second-level trigger with a higher-speed FPGA computing-based pattern trigger system. The upgrade of the inter-telescope networking Kieda (2011) will allow the implementation of new triggering systems that will allow the reduction of cosmic ray background providing an increase in sensitivity and lowering the detection energy threshold to 65 GeV.

7.3.2 Cherenkov Telescope Array

The Cherenkov Telescope Array (CTA) is the proposed next generation ground-based Very High Energy (VHE) γ-ray instrument. More than a hundred institutes from 27 countries (CTA Consortium, 2010) are engaged in its development. The

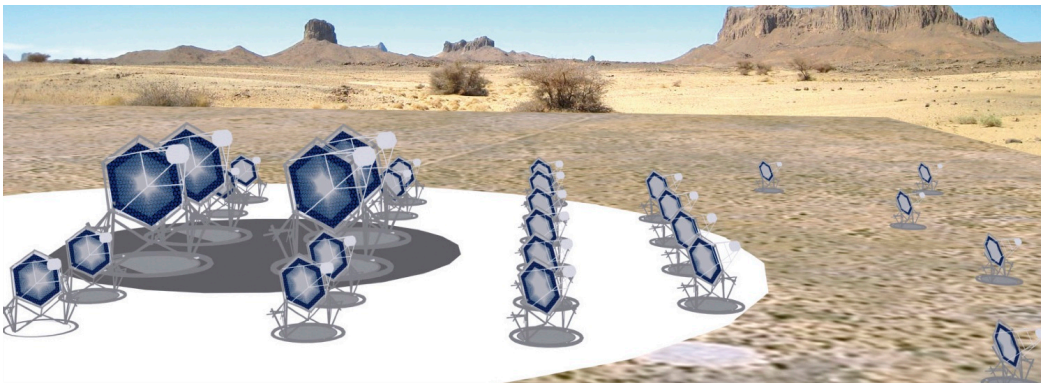

Figure 7.1: Conceptual layout of CTA consisting in three types of telescopes classes (CTA Consortium, 2010).

CTA Observatory will consist of three classes of telescopes (See Figure 7.1) with different reflector sizes in order to provide an extension of the observable range of energies (20 GeV to 100 TeV). CTA will achieve a factor of 10 improvement over the sensitivity of the present IACT arrays in the range between 100 GeV $-$ 10 TeV.

The preferred design solution to optimize the observations in the energy range between 100 GeV and 10 TeV is a 100 m square grid of telescopes of $10 - 15$ m diameter. Above 10 TeV, the limited rate of γ-ray showers per unit area requires a large IACT array that should be extended over an area of multiple kilometers squared. At these energies, the Cherenkov showers possess a 150 m radius light pool on the ground.

A widely spaced high-energy array of IACT telescopes, CTA, will have a relatively large field of view. Although this generally improves the uniformity of the camera and helps in reducing background systematics, it requires technically advanced telescope optics. It is mechanically difficult to realise telescopes with large field of views adopting a single-mirror configuration. An alternative solution, mainly presenting disadvantages in complexity and increased costs, is the adoption of a secondary mirror geometry configuration (Vassiliev *et al.*, 2007).

Even when observing faint objects, CTA will provide a very large amount of data that will easily provide the location of SED features. This will allow the compilation of lists of specific characteristics for different kinds of blazars, *e.g.*, validating or rejecting proposed unifying blazar categorizations and/or helping to extend them up to TeV energies (Ghisellini *et al.*, 2011; Giommi *et al.*, 2011; Plotkin *et al.*, 2012).

The upgrades of existing facilities and the construction of a next generation VHE observatory will radically increase our knowledge of the γ-ray sky.

Appendix A

UVOT and VERITAS Dataset

Here we provide the complete set of data that we have used in the present work.

Table 7.1 lists the UVOT observations recorded during the 2007-2008 observational season. The table has four columns in which we have included the identification number of each observation ("Obs ID"), the start time ("Start Time") and the total exposure time ("Total Exposure"). The fourth column provides the pointing offset between the Markarian 421 position and the centre of the field of view of the UVOT telescope ("Offset").

Table 7.2 provides the complete list of VERITAS datasets that we have utilized in this work. For consistency, we have provided a table structure to that for the UVOT dataset. A further column labeled "Weather" is displayed since the quality of the VERITAS analysis results depended on local weather conditions.

UVOT Observations

Obs ID	Start Time	Total Exposure	Search Offset
00030352099	2008-06-12 19:29:55	4802.55300	1.014 (166.11375 +38.208889)
00030352095	2008-04-13 04:59:01	2837.22500	3.073 (166.11375 +38.208889)
00030352070	2008-02-12 02:10:01	2413.51700	1.055 (166.11375 +38.208889)
00030352093	2008-04-09 23:59:01	2156.72700	0.553 (166.11375 +38.208889)
00030352080	2008-03-01 07:18:01	2067.35900	0.247 (166.11375 +38.208889)
00030352082	2008-03-31 13:18:32	1971.25200	0.171 (166.11375 +38.208889)
00030352098	2008-05-05 04:15:00	1895.25800	0.921 (166.11375 +38.208889)
00031202001	2008-05-02 20:11:45	1949.79300	1.122 (166.11375 +38.208889)
00030352068	2008-02-11 03:40:00	1843.29300	1.715 (166.11375 +38.208889)
00030352094	2008-04-11 01:33:00	1800.08800	0.743 (166.11375 +38.208889)
00030352064	2008-02-08 04:59:01	1704.66400	0.632 (166.11375 +38.208889)
00031202002	2008-05-06 04:03:01	1599.78500	2.194 (166.11375 +38.208889)
00030352077	2008-02-15 10:30:01	1575.01600	0.531 (166.11375 +38.208889)
00031202003	2008-05-07 04:09:00	1540.94600	1.733 (166.11375 +38.208889)
00030352075	2008-02-14 08:50:01	1515.54800	0.553 (166.11375 +38.208889)
00030352076	2008-02-15 02:28:01	1465.63400	0.703 (166.11375 +38.208889)
00030352071	2008-02-12 11:48:01	1451.34700	2.568 (166.11375 +38.208889)
00030352078	2008-02-16 02:34:00	1226.28800	0.586 (166.11375 +38.208889)
00030352074	2008-02-14 02:21:01	1205.50200	1.196 (166.11375 +38.208889)

Obs ID	Start Time	Total Exposure	Search Offset
00030352066	2008-02-10 03:34:01	1161.16000	0.514 (166.11375 +38.208889)
00030352086	2008-04-03 21:59:01	1145.79100	0.702 (166.11375 +38.208889)
00031202005	2008-05-08 22:03:00	1136.09300	0.681 (166.11375 +38.208889)
00030352085	2008-04-03 05:44:01	1125.09300	1.289 (166.11375 +38.208889)
00030352087	2008-04-04 04:16:01	1113.45400	0.827 (166.11375 +38.208889)
00030352088	2008-04-05 04:21:01	1113.43200	0.831 (166.11375 +38.208889)
00030352091	2008-04-08 04:26:01	1060.58400	0.594 (166.11375 +38.208889)
00030352081	2008-03-13 05:45:01	1024.86000	2.197 (166.11375 +38.208889)
00031202004	2008-05-08 06:15:01	1018.50500	0.809 (166.11375 +38.208889)
00030352089	2008-04-06 05:51:01	1006.34600	0.878 (166.11375 +38.208889)
00030352063	2008-02-06 20:49:47	988.37300	2.798 (166.11375 +38.208889)
00030352072	2008-02-13 03:52:00	965.35900	1.240 (166.11375 +38.208889)
00030352069	2008-02-11 10:14:01	943.80000	1.165 (166.11375 +38.208889)
00030352083	2008-04-02 00:42:01	880.88000	0.704 (166.11375 +38.208889)
00030352067	2008-02-10 10:10:00	810.53400	1.265 (166.11375 +38.208889)
00030352097	2008-05-04 05:33:01	686.87700	2.212 (166.11375 +38.208889)
00030352079	2008-02-16 10:49:01	699.26700	2.462 (166.11375 +38.208889)
00030352073	2008-02-13 08:49:01	619.75200	0.493 (166.11375 +38.208889)

Table 7.1: UVOT observations used to compute the seasonal lightcurve.

VERITAS Observations

Obs. ID	Date	Start Time	Duration	Weather
37640	2007-11-05	11:36:30	00:20:03	A
37641	2007-11-05	11:57:23	00:20:03	A
37847	2007-11-11	12:28:16	00:13:57	A
37918	2007-11-13	11:45:32	00:20:03	A
37919	2007-11-13	12:08:57	00:20:02	A
37957	2007-11-14	11:48:24	00:20:03	A
37958	2007-11-14	12:09:12	00:20:03	A
37959	2007-11-14	12:30:13	00:10:20	A
38045	2007-11-17	11:33:47	00:20:03	A-
38047	2007-11-17	12:01:05	00:06:55	A
38049	2007-11-17	12:31:20	00:16:18	A
38077	2007-11-18	11:57:52	00:20:03	A
38078	2007-11-18	12:18:40	00:20:03	A
38079	2007-11-18	12:39:33	00:08:04	A
38093	2007-11-19	11:44:20	00:20:04	A
38111	2007-11-20	12:04:28	00:02:28	A
38112	2007-11-20	12:07:51	00:20:03	A
38120	2007-11-21	11:38:48	00:20:02	A
38279	2007-12-06	10:00:34	00:20:03	A
38280	2007-12-06	10:24:00	00:20:03	A
38376	2007-12-14	11:32:02	00:01:01	A
38417	2007-12-15	11:02:09	00:20:02	A-
38477	2007-12-19	10:00:46	00:20:03	A
38487	2007-12-20	10:29:00	00:20:03	A
38488	2007-12-20	10:50:36	00:20:02	A
38549	2007-12-31	08:50:34	00:20:03	A
38574	2008-01-01	09:22:34	00:20:03	A

Obs. ID	Date	Start Time	Duration	Weather
38575	2008-01-01	09:44:05	00:20:03	A
38696	2008-01-10	08:39:48	00:20:03	A
38701	2008-01-10	10:21:31	00:20:02	A
38705	2008-01-10	11:50:00	00:25:03	A
38729	2008-01-11	08:53:29	00:20:03	A
38775	2008-01-12	09:06:33	00:20:02	A
38806	2008-01-13	09:01:06	00:20:03	A
38807	2008-01-13	09:21:39	00:20:03	A
38808	2008-01-13	09:42:38	00:20:02	A
38809	2008-01-13	10:03:33	00:12:24	A
38811	2008-01-13	10:19:04	00:00:21	A
38812	2008-01-13	10:20:17	00:20:03	A
38813	2008-01-13	10:41:18	00:20:03	A
38847	2008-01-14	10:38:47	00:20:03	A-
38864	2008-01-15	10:28:54	00:20:03	A
38892	2008-01-16	09:39:02	00:20:03	A
38893	2008-01-16	09:59:50	00:20:03	A
38906	2008-01-18	10:24:42	00:10:06	A
38969	2008-01-30	07:54:08	00:20:03	A-
39049	2008-02-02	07:29:53	00:09:50	A
39082	2008-02-03	07:39:00	00:10:26	A
39114	2008-02-06	05:36:05	00:20:03	A
39115	2008-02-06	05:59:36	00:20:02	A
39116	2008-02-06	06:21:11	00:20:03	A
39123	2008-02-06	08:47:42	00:20:02	A
39124	2008-02-06	09:09:08	00:20:03	A
39125	2008-02-06	09:30:22	00:20:03	A

Obs. ID	Date	Start Time	Duration	Weather
39126	2008-02-06	09:51:22	00:20:02	A
39127	2008-02-06	10:12:30	00:20:03	A
39128	2008-02-06	10:33:57	00:20:03	A
39129	2008-02-06	10:55:17	00:20:03	A
39130	2008-02-06	11:16:23	00:20:03	A
39131	2008-02-06	11:37:30	00:20:03	A
39150	2008-02-07	06:26:41	00:20:03	A
39151	2008-02-07	06:47:28	00:20:02	A
39160	2008-02-07	09:50:43	00:20:03	A
39196	2008-02-08	10:51:55	00:20:02	A
39231	2008-02-09	12:01:33	00:20:03	A
39247	2008-02-10	08:15:31	00:20:02	A
39309	2008-02-12	07:14:36	00:20:03	A
39349	2008-02-13	08:31:16	00:01:40	A
39351	2008-02-13	08:40:47	00:20:02	A
39352	2008-02-13	09:01:35	00:20:03	A
39515	2008-02-28	06:55:07	00:20:02	A
39529	2008-02-29	03:57:56	00:20:02	A
39550	2008-03-01	05:04:22	00:20:02	A
39570	2008-03-02	04:18:21	00:10:02	A
39593	2008-03-03	03:57:03	00:10:02	A
39621	2008-03-04	03:43:55	00:10:01	A
39673	2008-03-05	10:52:01	00:20:02	A
39694	2008-03-06	06:51:09	00:10:01	A
39698	2008-03-06	08:13:34	00:20:02	A
39699	2008-03-06	08:35:20	00:20:02	A
39700	2008-03-06	09:08:10	00:20:02	A
39763	2008-03-08	08:54:03	00:20:02	A

Obs. ID	Date	Start Time	Duration	Weather
39792	2008-03-09	08:37:47	00:10:01	A
39821	2008-03-10	08:35:11	00:04:00	A
39854	2008-03-11	10:03:30	00:10:02	A
39895	2008-03-13	09:59:32	00:10:13	A
40031	2008-03-27	06:35:54	00:10:01	A
40042	2008-03-28	06:36:01	00:10:02	A
40061	2008-03-29	04:34:22	00:10:01	A
40102	2008-03-30	09:02:54	00:10:01	A
40111	2008-03-31	05:09:48	00:10:01	A
40118	2008-03-31	06:31:32	00:10:02	A
40141	2008-04-01	05:09:49	00:01:10	A
40142	2008-04-01	05:12:12	00:10:01	A
40143	2008-04-01	05:23:04	00:20:02	A
40144	2008-04-01	05:44:05	00:20:02	A
40145	2008-04-01	06:05:25	00:20:03	A
40146	2008-04-01	06:26:31	00:20:02	A
40147	2008-04-01	06:47:57	00:20:02	A
40148	2008-04-01	07:09:10	00:20:03	A
40189	2008-04-03	05:41:59	00:10:01	A
40190	2008-04-03	05:53:25	00:20:03	A
40191	2008-04-03	06:14:19	00:20:03	A
40217	2008-04-04	05:50:39	00:10:02	A
40246	2008-04-05	05:59:38	00:10:05	A
40275	2008-04-06	06:02:45	00:00:03	A
40276	2008-04-06	06:03:25	00:10:02	A
40300	2008-04-07	04:31:12	00:10:11	A
40326	2008-04-08	04:28:52	00:20:03	A

Obs. ID	Date	Start Time	Duration	Weather
40353	2008-04-09	04:33:11	00:20:03	A
40386	2008-04-10	06:17:02	00:20:03	A
40420	2008-04-11	06:22:55	00:20:02	A
40441	2008-04-12	04:52:57	00:20:03	A
40481	2008-04-24	03:39:24	00:10:01	A-
40504	2008-04-26	04:54:21	00:10:01	A-
40529	2008-04-28	04:33:51	00:10:01	A-
40576	2008-04-30	04:03:38	00:20:03	A
40577	2008-04-30	04:24:57	00:20:03	A
40578	2008-04-30	04:45:38	00:20:03	A
40579	2008-04-30	05:07:18	00:20:03	A
40580	2008-04-30	05:28:36	00:20:03	A
40581	2008-04-30	05:49:28	00:20:02	A
40582	2008-04-30	06:10:26	00:20:03	A
40583	2008-04-30	06:31:22	00:20:03	A
40584	2008-04-30	06:52:12	00:20:03	A
40639	2008-05-02	06:50:58	00:00:22	A-
40640	2008-05-02	06:57:59	00:20:03	A-
40641	2008-05-02	07:19:04	00:20:03	A-
40672	2008-05-03	04:10:18	00:20:02	A
40673	2008-05-03	04:32:43	00:20:03	A
40674	2008-05-03	04:54:01	00:20:03	A
40675	2008-05-03	05:15:13	00:20:03	A
40676	2008-05-03	05:36:16	00:20:03	A
40678	2008-05-03	06:01:04	00:20:03	A
40679	2008-05-03	06:22:11	00:20:03	A

Obs. ID	Date	Start Time	Duration	Weather
40680	2008-05-03	06:43:25	00:20:03	A
40681	2008-05-03	07:04:27	00:20:03	A
40682	2008-05-03	07:25:48	00:20:03	A
40683	2008-05-03	07:47:43	00:20:03	A
40684	2008-05-03	08:08:57	00:20:02	A
40725	2008-05-05	03:19:44	00:20:02	A
40726	2008-05-05	03:40:59	00:20:03	A
40727	2008-05-05	04:02:36	00:20:03	A
40728	2008-05-05	04:23:56	00:20:02	A
40729	2008-05-05	04:45:33	00:20:03	A
40730	2008-05-05	05:06:35	00:20:03	A
40731	2008-05-05	05:27:33	00:20:03	A
40732	2008-05-05	05:48:30	00:20:03	A
40733	2008-05-05	06:10:16	00:20:03	A
40734	2008-05-05	06:31:00	00:20:03	A
40748	2008-05-06	03:36:01	00:20:02	A-
40749	2008-05-06	03:58:04	00:20:02	A-
40750	2008-05-06	04:19:00	00:20:03	A-
40752	2008-05-06	05:07:00	00:20:03	A-
40754	2008-05-06	05:59:21	00:20:03	A-
40954	2008-05-27	05:09:11	00:10:01	A
40970	2008-05-29	05:08:24	00:11:46	A
41042	2008-06-01	04:48:56	00:10:01	A
41087	2008-06-03	04:13:46	00:10:01	B+
41134	2008-06-05	04:06:06	00:00:21	A
41135	2008-06-05	04:29:17	00:00:56	A

Obs. ID	Date	Start Time	Duration	Weather
41136	2008-06-05	04:32:57	00:10:01	A
41158	2008-06-06	04:02:27	00:10:01	A
41159	2008-06-06	04:13:53	00:10:01	A
41160	2008-06-06	04:25:05	00:10:01	A
41161	2008-06-06	04:36:44	00:10:02	A

Table 7.2: VERITAS runs used to compute the seasonal lightcurve.

Appendix B

Selected Co-authored publications

Research Work in VERITAS

Veritas Observations of a Very High Energy γ-Ray Flare From the Blazar 3C66A

The VERITAS Collaboration

The intermediate-frequency peaked BL Lacertae (IBL) object 3C66A is detected during $2007 - 2008$ in VHE (very high energy; $E > 100$ GeV) γ-rays with the VERITAS stereoscopic array of imaging atmospheric Cherenkov telescopes. An excess of 1791 events is detected, corresponding to a significance of 21.2 standard deviations (σ), in these observations (32.8 hr live time). The observed integral flux above 200 GeV is 6% of the Crab Nebula's flux and shows evidence for variability on the timescale of days. The measured energy spectrum is characterized by a soft power law with photon index $\Gamma = 4.1 \pm 0.4\ stat \pm 0.6\ sys$. The radio galaxy 3C66B is excluded as a possible source of the VHE emission.

The Astrophysical Journal Letters, Volume 693, Issue 2, pp. L104-L108 (2009).

VERITAS Discovery of >200 GeV Gamma-ray Emission from the Intermediate-frequency-peaked BL Lac Object W Comae

The VERITAS Collaboration

We report the detection of very high-energy gamma-ray emission from the intermediate-frequency-peaked BL Lacertae object W Comae ($z = 0.102$) by VERITAS. The source was observed between January and April 2008. A strong outburst of gamma-ray emission was measured in the middle of March, lasting for only four

days. The energy spectrum measured during the two highest flare nights is fit by a power-law and is found to be very steep, with a differential photon spectral index of $\Gamma = 3.81 \pm 0.35\ stat \pm 0.34\ sys$. The integral photon flux above 200 GeV during those two nights corresponds to roughly 9% of the flux from the Crab Nebula. Quasi-simultaneous Swift observations at X-ray energies were triggered by the VERITAS observations. The spectral energy distribution of the flare data can be described by synchrotron-self-Compton (SSC) or external-Compton (EC) leptonic jet models, with the latter offering a more natural set of parameters to fit the data.

The Astrophysical Journal, Volume 684, Issue 2, pp. L73-L77, 2008.

Multiwavelength Observations of a TeV-Flare from W Comae

The VERITAS Collaboration and the AGILE Collaboration

We report results from an intensive multiwavelength campaign on the intermediate-frequency-peaked BL Lacertae object W Com ($z = 0.102$) during a strong outburst of very high energy gamma-ray emission in 2008 June. The very high energy gamma-ray signal was detected by VERITAS on 2008 June $7 - 8$ with a flux $F(> 200\text{GeV}) = (5.7 \pm 0.6) \times 10^{-11}$ cm^{-2} s^{-1}, about three times brighter than during the discovery of gamma-ray emission from W Com by VERITAS in 2008 March. The initial detection of this flare by VERITAS at energies above 200 GeV was followed by observations in high-energy gamma rays (AGILE; E $\gamma >= 100$ MeV), X-rays (Swift and XMM-Newton), and at UV, and ground-based optical and radio monitoring through the GASP-WEBT consortium and other observatories. Here we describe the multiwavelength data and derive the spectral energy distribution of the source from contemporaneous data taken throughout the flare.

The Astrophysical Journal, Volume 707, Issue 1, pp. 612-620 (2009).

Discovery of Very High Energy Gamma Rays from PKS 1424+240 and Multiwavelength Constraints on its Redshift

The VERITAS and the FERMI Collaboration

We report the first detection of very high energy γ-ray emission above 100 GeV. (VHE) gamma-ray emission above 140 GeV from PKS 1424+240, a BL Lac object with an unknown redshift. The photon spectrum above 140 GeV measured by VERITAS is well described by a power law with a photon index of $3.8 \pm 0.5\ stat \pm 0.3\ sys$ and a flux normalization at 200 GeV of $(5.1 \pm 0.9\ stat \pm 0.5\ sys) \times 10^{-11}$ TeV^{-1} cm^{-2} s^{-1}, where stat and sys denote the statistical and systematical uncertainties, respectively. The VHE flux is steady over the observation period between MJD 54881 and 55003 (from 2009 February 19 to June 21). Flux variability is also not observed in contemporaneous high-energy observations with the Fermi Large Area Telescope. Contemporaneous X-ray and optical data were also obtained from the Swift XRT and MDM observatory, respectively. The broadband spectral energy distribution is

well described by a one-zone synchrotron self-Compton model favoring a redshift of less than 0.1. Using the photon index measured with Fermi in combination with recent extragalactic background light absorption models it can be concluded from the VERITAS data that the redshift of PKS 1424+240 is less than 0.66.

The Astrophysical Journal Letters, Volume 708, Issue 2, pp. L100-L106 (2010).

Insights into the High-energy γ-ray Emission of Markarian 501 from Extensive Multifrequency Observations in the Fermi Era

The FERMI, MAGIC and VERITAS Collaborations

We report on the γ-ray activity of the blazar Mrk 501 during the first 480 days of Fermi operation. We find that the average Large Area Telescope (LAT) γ-ray spectrum of Mrk 501 can be well described by a single power-law function with a photon index of 1.78 ± 0.03. While we observe relatively mild flux variations with the Fermi-LAT (within less than a factor of two), we detect remarkable spectral variability where the hardest observed spectral index within the LAT energy range is 1.52 ± 0.14, and the softest one is 2.51 ± 0.20. These unexpected spectral changes do not correlate with the measured flux variations above 0.3 GeV. In this paper, we also present the first results from the 4.5 month long multifrequency campaign (2009 March 15 - August 1) on Mrk 501, which included the Very Long Baseline Array (VLBA), Swift, RXTE, MAGIC, and VERITAS, the F-GAMMA, GASP-WEBT, and other collaborations and instruments which provided excellent temporal and energy coverage of the source throughout the entire campaign. The extensive radio to TeV data set from this campaign provides us with the most detailed spectral energy distribution yet collected for this source during its relatively low activity. The average spectral energy distribution of Mrk 501 is well described by the standard one-zone synchrotron self-Compton (SSC) model. In the framework of this model, we find that the dominant emission region is characterized by a size $l_{sim} = 0.1$ pc (comparable within a factor of few to the size of the partially resolved VLBA core at 15-43 GHz), and that the total jet power (sime 10^{44} erg s^{-1}) constitutes only a small fraction ($\sim 10^{-3}$) of the Eddington luminosity. The energy distribution of the freshly accelerated radiating electrons required to fit the time-averaged data has a broken power-law form in the energy range 0.3 GeV -10 TeV, with spectral indices 2.2 and 2.7 below and above the break energy of 20 GeV. We argue that such a form is consistent with a scenario in which the bulk of the energy dissipation within the dominant emission zone of Mrk 501 is due to relativistic, proton-mediated shocks. We find that the ultrarelativistic electrons and mildly relativistic protons within the blazar zone, if comparable in number, are in approximate energy equipartition, with their energy dominating the jet magnetic field energy by about two orders of magnitude.

The Astrophysical Journal, Volume 727, Issue 2, article id. 129 (2011).

Multiwavelength Observations of the Previously Unidentified Blazar RX J0648.7+1516

The VERITAS Collaboration

We report on the VERITAS discovery of very high energy (VHE) gamma-ray emission above 200 GeV from the high-frequency-peaked BL Lac (HBL) object RX J0648.7+1516 (GB J0648+1516), associated with 1FGL J0648.8+1516. The photon spectrum above 200 GeV is fitted by a power law $dN/dE = F_0(E/E_0)^{-\Gamma}$ with a photon index Γ of 4.4 ± 0.8 *stat* ± 0.3 *sys* and a flux normalization F_0 of $(2.3 \pm 0.5$ *stat* $\pm$ 1.2 *sys*$) \times 10^{-11}$ TeV^{-1} cm^{-2} s^{-1} with $E_0 = 300$ GeV. No VHE variability is detected during VERITAS observations of RX J0648.7+1516 between 2010 March 4 and April 15. Following the VHE discovery, the optical identification and spectroscopic redshift were obtained using the Shane 3 m Telescope at the Lick Observatory, showing the unidentified object to be a BL Lac type with a redshift of $z = 0.179$. Broadband multiwavelength observations contemporaneous with the VERITAS exposure period can be used to subclassify the blazar as an HBL object, including data from the MDM observatory, Swift-UVOT, and X-Ray Telescope, and continuous monitoring at photon energies above 1 GeV from the Fermi Large Area Telescope (LAT). We find that in the absence of undetected, high-energy rapid variability, the one-zone synchrotron self-Compton (SSC) model overproduces the high-energy gamma-ray emission measured by the Fermi-LAT over 2.3 years. The spectral energy distribution can be parameterized satisfactorily with an external-Compton or lepto-hadronic model, which have two and six additional free parameters, respectively, compared to the one-zone SSC model.

The Astrophysical Journal, Volume 742, Issue 2, article id. 127 (2011).

Discovery of Very High Energy Gamma-ray Radiation from the BL Lac 1ES 0806+524

The VERITAS Collaboration

The high-frequency-peaked BL Lacertae object 1ES 0806+524, at redshift $z = 0.138$, was observed in the very high energy (VHE) gamma-ray regime by VERITAS between 2006 November and 2008 April. These data encompass the two- and three-telescope commissioning phases, as well as observations with the full four-telescope array. 1ES 0806+524 is detected with a statistical significance of 6.3 standard deviations from 245 excess events. Little or no measurable variability on monthly timescales is found. The photon spectrum for the period 2007 November to 2008 April can be characterized by a power law with photon index 3.6 ± 1.0 *stat* ± 0.3 *sys* between $\sim$ 300 GeV and $\sim$ 700 GeV. The integral flux above 300 GeV is $(2.2 \pm 0.5$ *stat* $\pm$ 0.4 *sys*$) \times 10^{-12}$ cm^{-2} s^{-1} which corresponds to 1.8% of the Crab Nebula flux. Non-contemporaneous multiwavelength observations are combined with the VHE data to produce a broadband spectral energy distribution that can be reasonably described using a synchrotron–self-Compton model.

The Astrophysical Journal Letters, Volume 690, Issue 2, pp. L126-L129 (2009).

Discovery of Variability in the Very High Energy γ-Ray Emission of 1ES 1218+304 with VERITAS

The VERITAS Collaboration

We present results from an intensive VERITAS monitoring campaign of the high-frequency peaked BL Lac object 1ES 1218+304 in 2008/2009. Although 1ES 1218+304 was detected previously by MAGIC and VERITAS at a persistent level of $\sim 6\%$ of the Crab Nebula flux, the new VERITAS data reveal a prominent flare reaching $\sim 20\%$ of the Crab. While very high energy (VHE) flares are quite common in many nearby blazars, the case of 1ES 1218+304 (redshift $z = 0.182$) is particularly interesting since it belongs to a group of blazars that exhibit unusually hard VHE spectra considering their redshifts. When correcting the measured spectra for absorption by the extragalactic background light, 1ES 1218+304 and a number of other blazars are found to have differential photon indices $\Gamma <= 1.5$. The difficulty in modeling these hard spectral energy distributions in blazar jets has led to a range of theoretical γ-ray emission scenarios, one of which is strongly constrained by these new VERITAS observations. We consider the implications of the observed light curve of 1ES 1218+304, which shows day scale flux variations, for shock acceleration scenarios in relativistic jets, and in particular for the viability of kiloparsec-scale jet emission scenarios.

The Astrophysical Journal Letters, Volume 709, Issue 2, pp. L163-L167 (2010).

Multiwavelength Observations of Markarian 421 in 2005-2006

The VERITAS Collaboration

Since 2005 September, the Whipple 10 m Gamma-ray Telescope has been operated primarily as a blazar monitor. The five northern hemisphere blazars that have already been detected at the Whipple Observatory, Markarian 421 (Mrk 421), H1426+428, Mrk 501, 1ES 1959+650, and 1ES 2344+514, are monitored routinely each night that they are visible. We report on the Mrk 421 observations taken from 2005 November to 2006 June in the gamma-ray, X-ray, optical, and radio bands. During this time, Mrk 421 was found to be variable at all wavelengths probed. Both the variability and the correlations among different energy regimes are studied in detail here. A tentative correlation, with large spread, was measured between the X-ray and gamma-ray bands, while no clear correlation was evident among the other energy bands. In addition to this, the well-sampled spectral energy distribution of Mrk 421 (1101+384) is presented for three different activity levels. The observations of the other blazar targets will be reported separately.

The Astrophysical Journal, Volume 695, Issue 1, pp. 596-618 (2009).

TeV and Multi-wavelength Observations of Mrk 421 in 2006-2008

The VERITAS Collaboration

We report on TeV γ-ray observations of the blazar Mrk 421 (redshift of 0.031) with the VERITAS observatory and the Whipple 10 m Cherenkov telescope. The excellent sensitivity of VERITAS allowed us to sample the TeV γ-ray fluxes and energy spectra with unprecedented accuracy where Mrk 421 was detected in each of the pointings. A total of 47.3 hr of VERITAS and 96 hr of Whipple 10 m data were acquired between 2006 January and 2008 June. We present the results of a study of the TeV γ-ray energy spectra as a function of time and for different flux levels. On 2008 May 2 and 3, bright TeV γ-ray flares were detected with fluxes reaching the level of 10 Crab. The TeV γ-ray data were complemented with radio, optical, and X-ray observations, with flux variability found in all bands except for the radio wave band. The combination of the Rossi X-ray Timing Explorer and Swift X-ray data reveal spectral hardening with increasing flux levels, often correlated with an increase of the source activity in TeV γ-rays. Contemporaneous spectral energy distributions were generated for 18 nights, each of which are reasonably described by a one-zone synchrotron self-Compton model.

The Astrophysical Journal, Volume 738, Issue 1, article id. 25 (2011).

Independent Research Work

The kinematic of HST-1 in the jet of M 87

Giroletti, M.; Hada, K.; Giovannini, G.; Casadio, C.; Beilicke, M.; Cesarini, A.; Cheung, C. C.; Doi, A.; Krawczynski, H.; Kino, M.; Lee, N. P.; Nagai, H.

Aims: We aim to constrain the structural variations within the HST-1 region downstream of the radio jet of M 87, in general as well as in connection to the episodes of activity at very high energy (VHE). Methods: We analyzed and compared 26 VLBI observations of the M 87 jet, obtained between 2006 and 2011 with the Very Long Baseline Array (VLBA) at 1.7 GHz and the European VLBI Network (EVN) at 5 GHz. Results: HST-1 is detected at all epochs; we model-fitted its complex structure with two or more components, the two outermost of which display a significant proper motion with a superluminal velocity around ~ 4 c. The motion of a third feature that is detected upstream is more difficult to characterize. The overall position angle of HST-1 has changed during the time of our observations from $-65°$ to $-90°$, while the structure has moved by over 80 mas downstream. Our results on the component evolution suggest that structural changes at the upstream edge of HST-1 can be related to the VHE events.

Astronomy & Astrophysics, Volume 538, id.L10 (2012).

Fermi Large Area Telescope Observations of Markarian 421: The Missing Piece of its Spectral Energy Distribution

The Fermi Collaboration

We report on the γ-ray activity of the high-synchrotron-peaked BL Lacertae object Markarian 421 (Mrk 421) during the first 1.5 years of Fermi operation, from 2008 August 5 to 2010 March 12. We find that the Large Area Telescope (LAT) γ-ray spectrum above 0.3 GeV can be well described by a power-law function with photon index $\Gamma = 1.78 \pm 0.02$ and average photon flux $F(> 0.3\mathrm{GeV}) = (7.23 \pm 0.16) \times 10^{-8}$ ph cm^{-2} s^{-1}. Over this time period, the Fermi-LAT spectrum above 0.3 GeV was evaluated on seven-day-long time intervals, showing significant variations in the photon flux (up to a factor ~ 3 from the minimum to the maximum flux) but mild spectral variations. The variability amplitude at X-ray frequencies measured by RXTE/ASM and Swift/BAT is substantially larger than that in γ-rays measured by Fermi-LAT, and these two energy ranges are not significantly correlated. We also present the first results from the 4.5 month long multifrequency campaign on Mrk 421, which included the VLBA, Swift, RXTE, MAGIC, the F-GAMMA, GASP-WEBT, and other collaborations and instruments that provided excellent temporal and energy coverage of the source throughout the entire campaign (2009 January 19 to 2009 June 1). During this campaign, Mrk 421 showed a low activity at all wavebands. The extensive multi-instrument (radio to TeV) data set provides an unprecedented, complete look at the quiescent spectral energy distribution (SED) for this source. The broadband SED was reproduced with a leptonic (one-zone synchrotron self-Compton) and a hadronic model (synchrotron proton blazar). Both frameworks are able to describe the average SED reasonably well, implying comparable jet powers but very different characteristics for the blazar emission site.

The Astrophysical Journal, Volume 736, Issue 2, article id. 131 (2011).

Bibliography

Abdo, A. A. (2010), Gamma-ray Light Curves and Variability of Bright Fermi-Detected Blazars, *ArXiv e-prints*. 144, 192

Abdo, A. A., J. Aleksić, and M. MWL partners (2011), Fermi-LAT Observations of Markarian 421: the Missing Piece of its Spectral Energy Distribution, *ArXiv e-prints*. 40, 124, 132, 135, 194

Abramowski, *et al.* (2011), The 2010 very high energy gamma-ray flare 10 years of multi-wavelength observations of M 87, *ArXiv e-prints*. 191

Acciari, V. A., *et al.* (2009a), Veritas Observations of a Very High Energy γ-Ray Flare From the Blazar 3C 66A, *ApJL*, *693*, L104–L108, doi:10.1088/0004-637X/693/2/L104. 28

Acciari, V. A., *et al.* (2009b), Simultaneous Multiwavelength Observations of Markarian 421 During Outburst, *ApJ*, *703*, 169–178, doi:10.1088/0004-637X/703/1/169. 136

Acciari, V. A., *et al.* (2009c), A connection between star formation activity and cosmic rays in the starburst galaxy M82, *Nature*, *462*, 770–772, doi:10.1038/nature08557. 3, 20

Acciari, V. A., *et al.* (2009d), Radio Imaging of the Very-High-Energy γ-Ray Emission Region in the Central Engine of a Radio Galaxy, *Science*, *325*, 444–, doi:10.1126/science.1175406. 145

Acciari, V. A., *et al.* (2011), TeV and Multi-wavelength Observations of Mrk 421 in 2006-2008, *ArXiv e-prints*. 40, 70, 73, 75, 131, 132, 135, 136, 159, 189

Acero, F., *et al.* (2009), Detection of Gamma Rays from a Starburst Galaxy, *Science*, *326*, 1080–, doi:10.1126/science.1178826. 20

Aharonian, F., *et al.* (2002), An unidentified TeV source in the vicinity of Cygnus OB2, *A&A*, *393*, L37–L40, doi:10.1051/0004-6361:20021171. 26

Aharonian, F., *et al.* (2004), Observations of 54 Active Galactic Nuclei with the HEGRA system of Cherenkov telescopes, *A&A*, *421*, 529–537, doi:10.1051/0004-6361:20035764. 123

Aharonian, F., *et al.* (2006), Observations of the Crab nebula with HESS, *A&A*, *457*, 899–915, doi:10.1051/0004-6361:20065351. 119

Albert, J., *et al.* (2008), VHE γ-Ray Observation of the Crab Nebula and its Pulsar with the MAGIC Telescope, *ApJ*, *674*, 1037–1055, doi:10.1086/525270. 87

Aleksić, J., *et al.* (2010), MAGIC TeV gamma-ray observations of Markarian 421 during multiwavelength campaigns in 2006, *A&A*, *519*, A32+, doi:10.1051/0004-6361/200913945. 124, 135

Aliu, E., *et al.* (2011), Detection of Pulsed Gamma Rays Above 100 GeV from the Crab Pulsar, *Science*, *334*, 69–, doi:10.1126/science.1208192. 25

Antonucci, R. (1993), Unified models for active galactic nuclei and quasars, *ARA&A*, *31*, 473–521, doi:10.1146/annurev.aa.31.090193.002353. 26

Arianos, S., and A. Carbone (2009), Cross-correlation of long-range correlated series, *Journal of Statistical Mechanics: Theory and Experiment*, *2009*(03), P03,037 (13pp). 169

Arimoto, N. (1996), The Iron Abundance Discrepancy in Ellipticals after ASCA, in *New Light on Galaxy Evolution*, *IAU Symposium*, vol. 171, edited by R. Bender & R. L. Davies, pp. 139–+. 73

Azarnia, G. M., J. R. Webb, and J. T. Pollock (2005), Noise Characteristics of Microvariations in Blazars, *International Amateur-Professional Photoelectric Photometry Communications*, *101*, 1–10. 193

Barrio, J. A. (1998), The Magic Telescope', design study, MPI-PhE 98-5, *internal*, *0*, 0–0. 86

Berge, D., S. Funk, and J. Hinton (2007), Background modelling in very-high-energy γ-ray astronomy, *A&A*, *466*, 1219–1229, doi:10.1051/0004-6361:20066674. 120

Blandford, R. D., and A. Konigl (1979), Relativistic jets as compact radio sources, *ApJ*, *232*, 34–48, doi:10.1086/157262. 28

Blandford, R. D., and M. J. Rees (1978), Some comments on radiation mechanisms in Lacertids, in *BL Lac Objects*, edited by A. M. Wolfe, pp. 328–341. 28

Błażejowski, M., *et al.* (2005), A Multiwavelength View of the TeV Blazar Markarian 421: Correlated Variability, Flaring, and Spectral Evolution, *ApJ*, *630*, 130–141, doi:10.1086/431925. 37, 40, 41, 135

Boettcher & Dermer (1995), Reverberation mapping of the central regions of active galactic nuclei using high-energy γ-ray observations., *A&A*, *302*, 37. 41

Böttcher, M., C. D. Dermer, and J. D. Finke (2008), The Hard VHE γ-Ray Emission in High-Redshift TeV Blazars: Comptonization of Cosmic Microwave Background Radiation in an Extended Jet?, *ApJL*, *679*, L9–L12, doi:10.1086/588780. 194

Breeveld, A. A., *et al.* (2010), Further calibration of the Swift ultraviolet/optical telescope, *MNRAS*, *406*, 1687–1700, doi:10.1111/j.1365-2966.2010.16832.x. 43, 72

Bretz, T. (2005), Comparison of On-Off and Wobble mode observations for MAGIC, in *International Cosmic Ray Conference*, *International Cosmic Ray Conference*, vol. 4, pp. 311–+. 104

Brown, R., and N. F. Rulkov (1997), Synchronization of chaotic systems: Transverse stability of trajectories in invariant manifolds, *Chaos*, *7*, 395–413, doi:10.1063/1.166213. 193

Buckley, J. H. (1998), ASTROPHYSICS: What the Wild Things Are, *Science*, *279*, 676–+, doi:10.1126/science.279.5351.676. 8

Catanese & Weekes, . (1999), Very High Energy Gamma-Ray Astronomy, *PASP*, *111*, 1193–1222, doi:10.1086/316435. 3

Celik, O. (2008), Crab Nebula and Pulsar with VERITAS, *PhD Dissertation, UCLA USA*, p. 294. 118

Chiaberge & Ghisellini (1997), Time dependent spectra of blazars, *MEMSAI*, *68*, 191. 41

Chiaberge & Ghisellini (1999), Rapid variability in the synchrotron self-Compton model for blazars, *MNRAS*, *306*, 551–560, doi:10.1046/j.1365-8711.1999.02538.x. 194, 195

Cogan, P. (2006), Nanosecond Sampling of Atnospheric Cherenkov Radiation Applied to TeV Gamma-Ray Observations of Blazars with VERITAS, *PhD Dissertation UCD Ireland*, p. 315. 99, 106

Cogan, P. (2008), VEGAS, the VERITAS Gamma-ray Analysis Suite, in *International Cosmic Ray Conference*, *International Cosmic Ray Conference*, vol. 3, pp. 1385–1388. 101, 114

Coleman & Glashow, . (1999), High-energy tests of Lorentz invariance, *Phys Rev D*, *59*(11), 116,008–+, doi:10.1103/PhysRevD.59.116008. 3

Commichau, S. C., *et al.* (2008), Monte Carlo studies of geomagnetic field effects on the imaging air Cherenkov technique for the MAGIC telescope site, *Nuclear Instruments and Methods in Physics Research A*, *595*, 572–586, doi:10.1016/j.nima.2008.07.144. 115

CTA Consortium, T. (2010), Design Concepts for the Cherenkov Telescope Array, *ArXiv e-prints*. 196

D'Ammando, F., *et al.* (2009), Blazars: the gamma-ray view of AGILE, *ArXiv e-prints*. 136

Daniel, M. K. (2008), The VERITAS standard data analysis, in *International Cosmic Ray Conference*, *International Cosmic Ray Conference*, vol. 3, pp. 1325–1328. 101

Daum, A., *et al.* (1997), First results on the performance of the HEGRA IACT array, *Astroparticle Physics*, *8*, 1–2, doi:10.1016/S0927-6505(97)00031-5. 116

Davies, J., and E. Cotton (1957), Design of the quartermaster solar furnace, *Sol. Energy;*, *1*(2-3), 16–22, doi:DOI:10.1016/S0927-6505(01)00152-9, 140909 – Solar Thermal Utilization– Miscellaneous Solar Applications– (1980-). 89

de la Calle Perez, I. (2006), Detection of High Energ Gamma rays from X-ray selected Blazar, *PhD Dissertation Leeds University UK*, p. 319. 117

Dermer, C. D., and R. Schlickeiser (2002), Transformation Properties of External Radiation Fields, Energy-Loss Rates and Scattered Spectra, and a Model for Blazar Variability, *ApJ*, *575*, 667–686, doi:10.1086/341431. 36

Donnarumma, I., *et al.* (2009), The June 2008 Flare of Markarian 421 from Optical to TeV Energies, *ApJL*, *691*, L13–L19, doi:10.1088/0004-637X/691/1/L13. 42, 124, 131, 135, 136

Edelson & Krolik (1988), The discrete correlation function - A new method for analyzing unevenly sampled variability data, *ApJ*, *333*, 646–659, doi:10.1086/166773. 160, 163, 168

Edelson, R., *et al.* (1995), Multiwavelength monitoring of the BL Lacertae object PKS 2155-304. 4: Multiwavelength analysis, *ApJ*, *438*, 120–134, doi:10.1086/175059. 159, 160

Edelson, R., *et al.* (2002), X-Ray Spectral Variability and Rapid Variability of the Soft X-Ray Spectrum Seyfert 1 Galaxies Arakelian 564 and Ton S180, *ApJ*, *568*, 610–626, doi:10.1086/323779. 149

Finkbeiner, D. P., M. Davis, and D. J. Schlegel (1999), Extrapolation of Galactic Dust Emission at 100 Microns to Cosmic Microwave Background Radiation Frequencies Using FIRAS, *ApJ*, *524*, 867–886, doi:10.1086/307852. 66

Finke, J. D., C. D. Dermer, and M. Böttcher (2008), Synchrotron Self-Compton Analysis of TeV X-Ray-Selected BL Lacertae Objects, *ApJ*, *686*, 181–194, doi:10.1086/590900. 136

Fitzpatrick, E. L. (1999), Correcting for the Effects of Interstellar Extinction, *PASP*, *111*, 63–75, doi:10.1086/316293. 68, 69, 72

Fitzpatrick, E. L., and D. Massa (1999), Determining the Physical Properties of the B Stars. I. Methodology and First Results, *ApJ*, *525*, 1011–1023, doi:10.1086/307944. 68

Ford, W. C. (1963), *The World of the Elementary Particles*, Blaisdale Publishing. 5

Fordham, J. L. A., *et al.* (1992), The MIC photon counting detector, in *Photon Detectors for Space Instrumentation*, *ESA Special Publication*, vol. 356, edited by T. D. Guyenne and J. Hunt, pp. 103–106. 47

Fordham, J. L. A., *et al.* (2000), High time-resolution spectroscopic imaging using intensified CCD detectors, *MNRAS*, *319*, 414–418, doi:10.1046/j.1365-8711.2000.03666.x. 50

Fossati, G., *et al.* (2008), Multiwavelength Observations of Markarian 421 in 2001 March: An Unprecedented View on the X-Ray/TeV Correlated Variability, *ApJ*, *677*, 906–925, doi:10.1086/527311. 38, 41, 42, 124, 145, 177, 178

Fukugita, M., K. Shimasaku, and T. Ichikawa (1995), Galaxy Colors in Various Photometric Band Systems, *PASP*, *107*, 945–+, doi:10.1086/133643. 73, 74

Gaidos, J. A., *et al.* (1996), Extremely rapid bursts of TeV photons from the active galaxy Markarian 421, *Nature*, *383*, 319–320, doi:10.1038/383319a0. 124

Galassi, M. (2009), Gnu scientific library reference manual (3rd ed.), in *GNU Scientific Library Reference Manual (3rd Ed.)*. 146

Gaskell & Peterson (1987), The accuracy of cross-correlation estimates of quasar emission-line region sizes, *ApJS*, *65*, 1–11, doi:10.1086/191216. 159

Gehrels, N., *et al.* (2004), The Swift Gamma-Ray Burst Mission, *ApJ*, *611*, 1005–1020, doi:10.1086/422091. 43, 44, 45, 46

Genzel, R., *et al.* (1998), What powers ultraluminous iras galaxies?, *The Astrophysical Journal*, *498*(2), 579–605. 28

George, I. M., R. S. Warwick, and G. E. Bromage (1988), X-ray and ultraviolet observations of Markarian 421, *MNRAS*, *232*, 793–808. 41

Ghisellini, G., F. Tavecchio, L. Foschini, and G. Ghirlanda (2011), The transition between BL Lac objects and flat spectrum radio quasars, *MNRAS*, *414*, 2674–2689, doi:10.1111/j.1365-2966.2011.18578.x. 197

Giommi, P., *et al.* (2011), Simultaneous Planck, Swift, and Fermi observations of X-ray and gamma-ray selected blazars, *ArXiv e-prints*. 197

Granger, C. W. J., and P. Newbold (2001), Spurious regressions in econometrics, *Essays in econometrics: collected papers of Clive W. J. Granger*, pp. 109–118. 168

Grebogi, C., E. Ott, and J. A. Yorke (1983), Crises, sudden changes in chaotic attractors, and transient chaos, *Physica D Nonlinear Phenomena*, *7*, 181–200, doi: 10.1016/0167-2789(83)90126-4. 193

Hanna, D. (2008), Calibration Techniques for VERITAS, in *International Cosmic Ray Conference*, *International Cosmic Ray Conference*, vol. 3, pp. 1417–1420. 110

Hays (2007), VERITAS Data Acquisition, *ArXiv e-prints*. 100

Hester, J., D. Burrows, and Crab Nebula Dynamics Collaboration (2002), Dynamics of the Crab Synchrotron Nebula, in *American Astronomical Society Meeting Abstracts #200*, *Bulletin of the American Astronomical Society*, vol. 34, p. 666. 25

Hillas, A. M. (1985), Cerenkov light images of EAS produced by primary gamma, in *International Cosmic Ray Conference*, *International Cosmic Ray Conference*, vol. 3, edited by F. C. Jones, pp. 445–448. 102, 111, 112

Hillas, A. M. (1996), Differences between Gamma-Ray and Hadronic Showers, *Space Science Reviews*, *75*, 17–30, doi:10.1007/BF00195021. 3, 79, 85

Hillas, M. A. (1981), Two Interesting Techniques for Monte-Carlo Simulation of Very High Energy Hadron Cascades, in *International Cosmic Ray Conference*, *International Cosmic Ray Conference*, vol. 8, pp. 193–+. 3

Hofmann, W., *et al.* (1999), Comparison of techniques to reconstruct VHE gamma-ray showers from multiple stereoscopic Cherenkov images, *Astroparticle Physics*, *12*, 135–143, doi:10.1016/S0927-6505(99)00084-5. 114

Holder, J., *et al.* (2006), The first VERITAS telescope, *Astroparticle Physics*, *25*, 391–401, doi:10.1016/j.astropartphys.2006.04.002. 89

Horan, D. (2001), Discovery of TeV Gamma-Ray from the BL Lacertae Object, 1H1426+428, *PhD Dissertation Harvard-Smithsonian CfA*, p. 216. 78, 83

Horan, D., and S. Wakely (2008), TeVCat: An Online Catalog for TeV Astronomy, in *AAS/High Energy Astrophysics Division*, *AAS/High Energy Astrophysics Division*, vol. 10, pp. 41.06–+. 20

Horan, D., *et al.* (2009), Multiwavelength Observations of Markarian 421 in 2005-2006, *ApJ*, *695*, 596–618, doi:10.1088/0004-637X/695/1/596. 41, 185

Hughes, P. A., H. D. Aller, and M. F. Aller (1992), The University of Michigan radio astronomy data base. I - Structure function analysis and the relation between BL Lacertae objects and quasi-stellar objects, *ApJ*, *396*, 469–486, doi:10.1086/171734. 173, 175

Hurst, H. (1951), Long Term Storage Capacity of Reservoirs, *Transactions of the American Society of Civil Engineers*, *01*, 770–799. 169

Kataoka, J. (1999), X-ray Study of Rapid Variability in TeV Blazars and the Implications on Particle Acceleration in Jets, *PhD Dissertation Tokio University*, p. 314. 192

Kataoka, J., *et al.* (2001), Characteristic X-Ray Variability of TeV Blazars: Probing the Link between the Jet and the Central Engine, *ApJ*, *560*, 659–674, doi:10.1086/322442. 144, 173, 192

Katarzyński, K., H. Sol, and A. Kus (2001), The multifrequency emission of Mrk 501. From radio to TeV gamma-rays, *A&A*, *367*, 809–825, doi:10.1051/0004-6361:20000538. 41

Kawakami, H., D. Bone, J. Fordham, and R. Michel (1994), The effect of event shape on controiding in photon counting detectors, *Nuclear Instruments and Methods in Physics Research A*, *348*, 707–712, doi:10.1016/0168-9002(94)90830-3. 47

Kieda, D. B. (2011), Status of the VERITAS Upgrade, *ArXiv e-prints*. 195, 196

Kihara, M., S. Ono, and P. Eskelinen (2002), *Digital Clocks for Synchronization and Communications*, Artech House, Inc., Norwood, MA, USA. 143

Kildea, J., *et al.* (2007), The Whipple Observatory 10 m gamma-ray telescope, 1997 2006, *Astroparticle Physics*, *28*, 182–195, doi:10.1016/j.astropartphys.2007.05.004. 89

Kino & Takahara (2008), On invisible plasma content in radio-loud AGNs: the case of TeV blazar Markarian 421, *MNRAS*, *383*, 713–719, doi:10.1111/j.1365-2966.2007.12579.x. 38

Krawczynski, H., *et al.* (2001), Simultaneous X-Ray and TeV Gamma-Ray Observation of the TeV Blazar Markarian 421 during 2000 February and May, *ApJ*, *559*, 187–195, doi:10.1086/322364. 40

Krawczynski, H., *et al.* (2004), Multiwavelength Observations of Strong Flares from the TeV Blazar 1ES 1959+650, *ApJ*, *601*, 151–164, doi:10.1086/380393. 37, 40

Krennrich, F., *et al.* (2000), Veritas: Very energetic radiation imaging telescope array system, in *GeV-TeV GAMMA RAY ASTROPHYSICS WORKSHOP: Towards a Major Atmospheric Cherenkov Detector VI*, vol. 515, edited by B. L. Dingus, M. H. Salamon, and D. B. Kieda, pp. 515–527, AIP, doi:10.1063/1.1291418. 89

Krennrich, F., *et al.* (2002), Discovery of Spectral Variability of Markarian 421 at TeV Energies, *ApJL*, *575*, L9–L13, doi:10.1086/342700. 124, 131

Krennrich, F., *et al.* (2007), Status report from VERITAS, *Journal of Physics Conference Series*, *60*, 34–39, doi:10.1088/1742-6596/60/1/006. 94

Kuin, N. P. M., and S. R. Rosen (2008), The measurement errors in the Swift-UVOT and XMM-OM, *MNRAS*, *383*, 383–386, doi:10.1111/j.1365-2966.2007.12549.x. 47, 52

Lainela & Valtaoja (1993), Structure Function Analysis of High Radio Frequency Variability in the Metsaehovi Monitoring Sample of Active Galactic Nuclei, *ApJ*, *416*, 485–+, doi:10.1086/173252. 174

Le Borgne, D., *et al.* (2004), Evolutionary synthesis of galaxies at high spectral resolution with the code PEGASE-HR. Metallicity and age tracers, *A&A*, *425*, 881–897, doi:10.1051/0004-6361:200400044. 74

Lessard, R. W. (1999), VERITAS: the Very Energetic Radiation Imaging Telescope Array System, *Astroparticle Physics*, *11*, 243–246, doi:10.1016/S0927-6505(99)00057-2. 89

Lessard, R. W., J. H. Buckley, V. Connaughton, and S. Le Bohec (2001), A new analysis method for reconstructing the arrival direction of TeV gamma rays using a single imaging atmospheric Cherenkov telescope, *Astroparticle Physics*, *15*, 1–18, doi:10.1016/S0927-6505(00)00133-X. 113

Levinson & Bromberg, O. (2007), Collimation and radiative deceleration of jets in tev agns, *Tech. Rep. arXiv:0712.2664*, comments: 5 pages. Proceedings of High Energy Phenomena in Relativistic Outflows, held in Dublin, Ireland, September 24-28, 2007. 41

Li, W., *et al.* (2006), The Calibration of the Swift UVOT Optical Observations: A Recipe for Photometry, *PASP*, *118*, 37–61, doi:10.1086/498356. 58, 70

Linnemann, J. (2003), Measures of Significance in HEP and Astrophysics, in *Statistical Problems in Particle Physics, Astrophysics, and Cosmology*, edited by L. Lyons, R. Mount, & R. Reitmeyer, pp. 35–+. 122

Little, M. A., *et al.* (2007), Exploiting Nonlinear Recurrence and Fractal Scaling Properties for Voice Disorder Detection, *ArXiv e-prints*. 155

Macomb, D. J., *et al.* (1995), Multiwavelength Observations of Markarian 421 During a TeV/X-Ray Flare, *ApJL*, *449*, L99+, doi:10.1086/309646. 135

Maier, G. (2008), Monte Carlo studies of the VERITAS array of Cherenkov telescopes, in *International Cosmic Ray Conference*, *International Cosmic Ray Conference*, vol. 3, pp. 1413–1416. 116

Mandelbrot & van Ness (1968), Fractional Brownian Motions, Fractional Noises and Applications, *SIAM Review*, *10*, 422–437, doi:10.1137/1010093. 192

Maraschi, L., *et al.* (1999), Simultaneous X-Ray and TEV Observations of a Rapid Flare from Markarian 421, *ApJL*, *526*, L81–L84, doi:10.1086/312370. 38

Mathis, J. S. (1990), Interstellar dust and extinction, *ARA&A*, *28*, 37–70, doi:10.1146/annurev.aa.28.090190.000345. 66

Michel, R., J. Fordham, and H. Kawakami (1997), Fixed pattern noise in high-resolution, CCD readout photon-counting detectors, *MNRAS*, *292*, 611–620. 48

Mohanty, G., *et al.* (1998), Measurement of TeV gamma-ray spectra with the Cherenkov imaging technique, *Astroparticle Physics*, *9*, 15–43, doi:10.1016/S0927-6505(98)00005-X. 122, 123

Molina, R. A., *et al.* (2010), Perspectives on 1/ f noise in quantum chaos, *Journal of Physics: Conference Series*, *239*(1), 012,001. 193

Mücke, A., *et al.* (2003), BL Lac objects in the synchrotron proton blazar model, *Astroparticle Physics*, *18*, 593–613, doi:10.1016/S0927-6505(02)00185-8. 40

Nagai, R. McKay, G. Sleege, and D. Petry (2007), Focal Plane Instrumentation of VERITAS, *ArXiv e-prints*. 94

Nilsson, K., *et al.* (2003), R-band imaging of the host galaxies of RGB BL Lacertae objects, *A&A*, *400*, 95–118, doi:10.1051/0004-6361:20021861. 73

Nilsson, K., *et al.* (2007), Host galaxy subtraction of TeV candidate BL Lacertae objects, *A&A*, *475*, 199–207, doi:10.1051/0004-6361:20077624. 41, 74

Paltani & Courvoisier (1997), Rest-frame variability of quasars and Seyfert galaxies in the ultraviolet: constraints on the discrete-event models., *A&A*, *323*, 717–726. 177

Paltani, S. (1999), Constraining BL Lac Models using Structure Function Analysis, in *BL Lac Phenomenon*, *Astronomical Society of the Pacific Conference Series*, vol. 159, edited by L. O. Takalo & A. Sillanpää, pp. 293–+. 173

Phillips, P. (1986), Understanding spurious regressions in econometrics, *Journal of Econometrics*, *33*(3), 311–340. 169

Pichel & Rovero, A. (2008), Monitoreo de blazares con el Telescopio Whipple de rayos gamma, *Boletin de la Asociacion Argentina de Astronomia La Plata Argentina*, *51*, 321–326. 124, 135, 159

Pittori, C., *et al.* (2008), AGILE detection of the blazar Mrk 421, *The Astronomer's Telegram*, *1583*, 1–+. 136

Plotkin, R. M., *et al.* (2012), The Lack of Torus Emission from BL Lacertae Objects: An Infrared View of Unification with WISE, *ApJL*, *745*, L27, doi: 10.1088/2041-8205/745/2/L27. 197

Poole, T. S., *et al.* (2008), Photometric calibration of the Swift ultraviolet/optical telescope, *MNRAS*, *383*, 627–645, doi:10.1111/j.1365-2966.2007.12563.x. 43, 49, 50, 51, 52, 54, 56, 57, 58, 59, 62, 70

Press, W. H. (1978), Flicker noises in astronomy and elsewhere, *Comments on Astrophysics*, *7*, 103–119. 141, 142, 143, 144

Punch, M., *et al.* (1992), Detection of TeV photons from the active galaxy Markarian 421, *Nature*, *358*, 477–+, doi:10.1038/358477a0. 38, 124, 135

Rebillot, P. F., *et al.* (2006), Multiwavelength Observations of the Blazar Markarian 421 in 2002 December and 2003 January, *ApJ*, *641*, 740–751, doi:10.1086/500653. 40

Reyes, L. C. (2008), VERITAS Observations of Mrk 421 during 2008 with Simultaneous X-ray Coverage, in *American Institute of Physics Conference Series*, *American Institute of Physics Conference Series*, vol. 1085, edited by F. A. Aharonian, W. Hofmann, & F. Rieger, pp. 581–584, doi:10.1063/1.3076739. 136

Roache, E., *et al.* (2007), Mirror Facets for the VERITAS Telescopes, in *International Cosmic Ray Conference 2007*. 91, 94

Roming, P. W. A., *et al.* (2003), The Swift Ultra-Violet/Optical Telescope, in *Bulletin of the American Astronomical Society*, *Bulletin of the American Astronomical Society*, vol. 35, pp. 765–+. 48

Roming, P. W. A., *et al.* (2005), The Swift Ultra-Violet/Optical Telescope, *Space Science Reviews*, *120*, 95–142, doi:10.1007/s11214-005-5095-4. 46, 47, 48

Rutman, J. (1978), Characterization of phase and frequency instabilities in precision frequency sources - Fifteen years of progress, *IEEE Proceedings*, *66*, 1048–1075. 177

Rybicki & Lightman (1979), *Radiative processes in astrophysics*. 10, 11, 14, 15

Sadgrove, M., S. Wimberger, S. Parkins, and R. Leonhardt (2008), Scaling law and stability for a noisy quantum system, *Phys. Rev. E*, *78*(2), 025206, doi:10.1103/PhysRevE.78.025206. 193

Sambruna, R. M., L. Maraschi, and C. M. Urry (1996), On the Spectral Energy Distributions of Blazars, *ApJ*, *463*, 444, doi:10.1086/177260. 38

Schlegel, D. J., D. P. Finkbeiner, and M. Davis (1998), Maps of Dust Infrared Emission for Use in Estimation of Reddening and Cosmic Microwave Background Radiation Foregrounds, *ApJ*, *500*, 525–+, doi:10.1086/305772. 66, 67, 68, 72

Simonetti, J. H., J. M. Cordes, and D. S. Heeschen (1985), Flicker of extragalactic radio sources at two frequencies, *ApJ*, *296*, 46–59, doi:10.1086/163418. 173, 174, 175, 177

Stecker & Glashow, . (2001), New tests of Lorentz invariance following from observations of the highest energy cosmic /γ-rays, *Astroparticle Physics*, *16*, 97–99, doi:10.1016/S0927-6505(01)00137-2. 3

Stetson, P. B., R. D. McClure, and D. A. VandenBerg (2004), A Star Catalog for the Open Cluster NGC 188, *PASP*, *116*, 1012–1030, doi:10.1086/426122. 52

Swordy, S. (2008), Discovery of greater than 100 GeV Gamma-ray Emission from the Blazar 3C66A by VERITAS, *The Astronomer's Telegram*, *1753*, 1–+. 28

Takahashi, T., *et al.* (1996), ASCA Observation of an X-Ray/TeV Flare from the BL Lacertae Object Markarian 421, *ApJL*, *470*, L89+, doi:10.1086/310302. 135

Takahashi, T., *et al.* (2000), Complex Spectral Variability from Intensive Multiwavelength Monitoring of Markarian 421 in 1998, *ApJL*, *542*, L105–L109, doi:10.1086/312929. 185

Tavecchio, F., L. Maraschi, and G. Ghisellini (1998), Constraints on the Physical Parameters of TeV Blazars, *ApJ*, *509*, 608–619, doi:10.1086/306526. 37

Terlevich, R., G. Tenorio-Tagle, J. Franco, and J. Melnick (1992), The starburst model for active galactic nuclei - The broad-line region as supernova remnants evolving in a high-density medium, *MNRAS*, *255*, 713–728. 28

Toner, J. (2008), MWL Observations of TeV Blazars 2006-07, *PhD Dissertation NUIG University Ireland*, p. 432. 5, 31, 177

Toner et al. (2007), Bias Alignment of the VERITAS Telescopes, in *International Cosmic Ray Conference 2007*. 92

Tramacere, A., *et al.* (2009), Swift observations of the very intense flaring activity of Mrk 421 during 2006. I. Phenomenological picture of electron acceleration and predictions for MeV/GeV emission, *A&A*, *501*, 879–898, doi:10.1051/0004-6361/200810865. 42

Urry & Padovani (1995), Unified Schemes for Radio-Loud Active Galactic Nuclei, *PASP*, *107*, 803–+, doi:10.1086/133630. 35

Valcarcel, I. (2008), VERITAS, 1ES1218 + 204 and the Extragalactic Background Light, *PhD Dissertation Mc-Gill University Canada*, p. 331. 90, 116, 122

Vassiliev, V., S. Fegan, and P. Brousseau (2007), Wide field aplanatic two-mirror telescopes for ground-based γ-ray astronomy, *Astroparticle Physics*, *28*, 10–27, doi:10.1016/j.astropartphys.2007.04.002. 197

Vassiliev, V. V., *et al.* (2003), Veritas CFDs, in *International Cosmic Ray Conference*, *International Cosmic Ray Conference*, vol. 5, pp. 2851–+. 96

Vaughan, S. (2005), A simple test for periodic signals in red noise, *A&A*, *431*, 391–403, doi:10.1051/0004-6361:20041453. 150

Vaughan, S., R. Edelson, R. S. Warwick, and P. Uttley (2003), On characterizing the variability properties of X-ray light curves from active galaxies, *MNRAS*, *345*, 1271–1284, doi:10.1046/j.1365-2966.2003.07042.x. 143, 148, 149, 169

Watanabe, S., *et al.* (2009), Suzaku Observations of the Extreme MeV Blazar SWIFT J0746.3+2548, *ApJ*, *694*, 294–301, doi:10.1088/0004-637X/694/1/294. 194

Weekes, T. C. (2003), *Very high energy gamma-ray astronomy*, AA. 18

Weekes, T. C., *et al.* (1989), Observation of TeV gamma rays from the Crab nebula using the atmospheric Cerenkov imaging technique, *ApJ*, *342*, 379–395, doi:10.1086/167599. 3

Weekes, T. C., *et al.* (2000), The very energetic radiation imaging telescope array system (veritas), in *THE FIFTH COMPTON SYMPOSIUM*, vol. 510, edited by M. L. McConnell and J. M. Ryan, pp. 637–641, AIP, doi:10.1063/1.1303279. 89

Weekes, T. C., *et al.* (2002), Veritas: the very energetic radiation imaging telescope array system, *Astroparticle Physics*, *17*(2), 221 – 243, doi:DOI:10.1016/S0927-6505(01)00152-9. 88

Weinstein, A. (2007), The VERITAS Trigger System, *ArXiv e-prints*. 97, 98

Welsh, W. F. (1999), On the Reliability of Cross-Correlation Function Lag Determinations in Active Galactic Nuclei, *PASP*, *111*, 1347–1366, doi:10.1086/316457. 159, 160, 169

White & Peterson (1994), Comments on cross-correlation methodology in variability studies of active galactic nuclei, *PASP*, *106*, 879–889, doi:10.1086/133456. 160

White, R. J. (2005), Rise Time of the Simulated VERITAS 12 m Davies-Cotton Reflector, in *High Energy Gamma-Ray Astronomy*, *American Institute of Physics Conference Series*, vol. 745, edited by F. A. Aharonian, H. J. Völk, and D. Horns, pp. 797–802, doi:10.1063/1.1878504. 89

Yang, J., J. Wang, B. Dai, and X. Gao (2009), Implications of Bulk Velocity Structures in AGN Jets, *PASJ*, *61*, 1153–. 40

You, J. H., T. Kiang, F. H. Cheng, and F. Z. Cheng (1984), Cerenkov line emission - Basic theory, *MNRAS*, *211*, 667–677. 84

Zhang, Y. H., *et al.* (1999), Rapid X-Ray Variability of the BL Lacertae Object PKS 2155-304, *ApJ*, *527*, 719–732, doi:10.1086/308116. 144

Zhang, Y. H., *et al.* (2002), Four Years of Monitoring Blazar PKS 2155-304 with BeppoSAX: Probing the Dynamics of the Jet, *ApJ*, *572*, 762–785, doi:10.1086/340349. 144, 173, 174, 176, 177, 184, 185, 192

Zhang, Y. H., *et al.* (2005), XMM-Newton View of PKS 2155-304: Characterizing the X-Ray Variability Properties with EPIC pn, *ApJ*, *629*, 686–699, doi:10.1086/431719. 135, 136, 149

Zhang, Y. H., *et al.* (2006), XMM-Newton View of PKS 2155-304: Hardness Ratio and Cross-Correlation Analysis of EPIC pn Observations, *ApJ*, *637*, 699–710, doi:10.1086/498498. 157

Zweerink, J. A., *et al.* (1997), The TeV Gamma-Ray Spectrum of Markarian 421 during an Intense Flare, *ApJL*, *490*, L141+, doi:10.1086/311036. 124, 131, 135